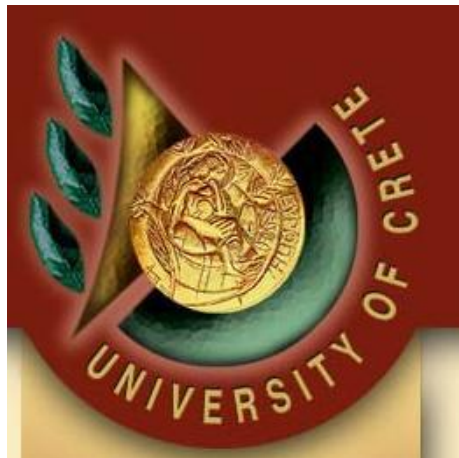


PhD Thesis

Marios Barberoglou

***Femtosecond laser micro/nano structuring of
solid surfaces:
Fundamentals and applications***



**Physics Department
University of Crete**

Heraklion, January 2012

Acknowledgments

I am greatly indebted to my advisor and supervisor *Prof. Costas Fotakis* who gave me the opportunity to work in the laboratories of the Institute of Electronic Structure and Laser of the Foundation for Research and Technology – Hellas and accomplish this Ph.D Thesis.

My most special thanks go to my friend and supervisor *Dr. Manolis Stratakis* with whom I had the fortune to work closely during the entire time of this work. I am truly grateful for the excellent collaboration for which without it, nothing would be realized.

I would also like to express my special thanks and gratitude to my friend and co-supervisors *Dr. Panagiotis Loukakos* with whom I had the opportunity to work and who closely supervised a Part Of this work. I am also grateful for the Kind and Excellent collaboration, the new techniques he taught me and the many Rich and stimulating discussions.

I want to express my gratitude to *Dr. Giorgos Tsibidis* for working closely together in a part of this work, for his contribution in the computational simulations and the plenty of interesting discussions. Furthermore I wish to thank *Dr. Anthi Ranella* for her expertise, contribution and our exciting discussions regarding the biological section. Also *Dr. Evi Papadopoulou* for her close collaboration in a part of this work.

Many thanks go to *Dr. David Gray* for his assistance and expertise in the pulse shaping techniques, to *Dr. Manolis Spanakis* for his assistance with the AFM measurements, *Aleka Manousaki* for her continuous help and patience with the SEM measurements as well as *Vaggelis Magoulakis* for his experimental assistance.

I would also like to thank all my friends and the post-graduate students at FORTH. Their continuous support has been invaluable to me.

Finally, many warm thanks go to my family for their continuous support over the years and their patience during the process. Without them I would not be the man I am today.

Thank You all - January 2011
Marios Barberoglou

Contents

Acknowledgments.....	3
Contents	5
Introduction and Overview	13
Chapter 1	17
Theoretical background	17
1.1 Introduction.....	17
1.2 Fundamental processes of laser-matter interaction	18
1.2.1 Primary processes - Absorption mechanisms	18
1.2.2 Secondary processes – Energy relaxation	18
1.3 The two temperature model	21
1.4 Thermal processes induced by laser irradiation	23
1.5 Periodic surface structures and surface plasmon waves.....	25
1.5.1 Laser induced periodic surface structures - Ripples.....	25
1.5.2 Surface plasmon waves: Coherent electron oscillations	27
1.5.3 Origin of HSFR.....	30
i. Interference with second harmonic generation (SHG) waves.....	30
ii. Gratin coupling effect.	31
1.6 Brief introduction to fluid dynamics	32
1.6.1 Simplified Navier–Stokes equations	32
1.6.2 Shallow water equations	33
Chapter 2	35
Experimental section.....	35
2.1 Introduction.....	35
2.2 The femtosecond Laser Source	35
2.2.1 The regenerative amplified Ti:Sapphire laser system	36

2.2.2 The multipass amplified Ti:Sapphire laser system	36
2.3 The Spatial Light Modulator (SLM) pulse shaper.	37
2.3.1 Introduction.....	37
2.3.2 Design of the SLM.....	37
• The 4f setup	38
2.4 Experimental setup.....	39
2.4.1 Silicon and ZnO processing setup.....	39
2.4.2 Double pulse experiments setup.....	40
2.4.3 Nananostructuring in liquids setup	41
2.5 Sample Preparation	42
2.5.1 Silicon samples treatment	42
2.5.2 Thermal Oxide growth and silanization process on Silicon.....	42
2.5.3 Zno films preparation.....	43
2.5.4 Thin Zno films on Si, prepared by plasma laser deposition (PLD).....	43
2.6 Sample characterization	44
2.6.1 Morphological characterization	44
2.6.2 Optical measurements	44
2.7 Wetting properties.....	45
2.8 Electrowetting on Dielectric (EWOD) setup	46
2.9 Field emission measurements	47
2.10 Methodology for biology experiments.....	48
2.10.1 Introduction.....	48
2.10.2 NIH/3T3 (Fibroblast) cells.....	48
• Cell culture methodology.....	48
• Cell viability assay	48
• Staining methodology for laser scanning confocal microscopy.....	49
2.10.3 Primary neuronal cells	50
• Cell culture methodology.....	50
• Immunofluorescence methodology for laser scanning confocal microscopy	50
Chapter 3.....	53
Fundamental processes upon Femtosecond laser micro/nano structuring of Si.....	53

3.1 Overview.....	53
3.2 Laser modification of silicon: The effect of single pulses	54
3.2.1 Introduction.....	54
3.2.2 Theoretical and experimental details.	56
I. Laser matter interaction process – implementation of the two temperature model	56
II. Liquid phase – implementation of the hydrodynamic equations (see also section 1.6).....	59
III. Interference of an incident with a surface plasmon wave	62
3.2.3 Simulation and experimental details	64
I. Simulations	64
II. Experimental details.....	67
3.2.4 Formation of ripples: Simulation and experimental results	68
3.2.5 Conclusion	80
3.3 Formation of micro/nano structures	82
3.3.1 Evolution of periodic surface structures	82
3.3.2 Surface structuring of Silicon in a reactive gas atmosphere	83
3.6 Conclusions.....	84
Chapter 4.....	85
Laser processing with temporally designed femtosecond pulses.....	85
4.1 Laser modification of semiconductors: The effect of temporally shaped pulses	85
4.1.1 Introduction.....	86
4.1.2 Methodology and double pulse examples	88
4.1.3 Experimental results on Silicon irradiated with Double laser pulses.....	89
4.1.4 Simulation results using double pulses	93
4.1.5 Investigation of spot area decrease.	95
4.2 High and Low Spatial frequency control of ripples on ZnO films with ultrashort double pulses.	96
4.2.1 Introduction.....	96
4.2.2 Methodology	98
4.2.3 Effect of laser fluence on ripple periodicity.....	98
III. Effect of laser fluence on ripple periodicity.....	98
IV. Pulse separation dependence ripple periodicity	101
3.3 Conclusion	105

Comparison of Si and ZnO results	105
Chapter 5	107
Application of Silicon micro/nano structured surfaces.....	107
Introduction.....	107
A) Field emission: Cold cathodes	109
Introduction.....	109
5.1 Fundamentals	110
I. Field emission from metals	110
II. Field emission from semiconductors	113
5.2 Stability and durability of metal-coated silicon spike cold-electron emitters.....	115
5.2.1 Methodology	115
5.3.2 Field emission of metal coated Si spikes - Improvement of performance with operation ..	117
5.2.3 Performance and saturation mechanisms analysis	119
5.2.4 Conclusion	122
5.3 Three-dimensional carbon nanowall field emission arrays.....	123
5.3.1 Introduction.....	123
5.3.2 Methodology	123
5.3.3 Field emission properties	124
5.3.4 Data analysis: FE enhancement factor	126
5.3.5 Screening effects and durability.....	127
I. Screening effects.....	127
II. Durability of carbon coated spikes.....	127
5.3.6 Conclusions.....	128
B) Dynamic control of the wetting properties.....	131
Introduction.....	131
5.4 Fundamentals	133
5.4.1 Young equation and contact angle	133
5.4.2 Wettability and Surface roughness: Wenzel and Cassie-Baxter states	134
5.5 Tailoring wetting response of silicon.....	136
5.5.1 Bio-inspired water repellent surfaces and self-cleaning applications	136
5.5.2 Silicon-based surface meets the water repellent performance of the lotus leaf	139

5.2.3	Methodology	140
5.2.4	Making Silicon superhydrophobic	140
5.5.3	Conclusions.....	144
5.6	Electrowetting Properties of Micro/Nanostructured Black Silicon.....	145
5.6.1	Introduction.....	145
5.6.2	Fundamentals of EWOD on flat and rough surfaces.	146
	• Flat surface.....	146
	• Structured Surface	147
5.6.3	Methods and Experimental Procedures.....	149
5.6.4	Morphology analysis.....	151
5.6.5	Electrowetting experiment	153
i.	Electrowetting on flat and hydrophobic surfaces.....	153
ii.	Electrowetting on superhydrophobic surfaces	156
5.6.6	Critical value of applied voltage – CA saturation.....	158
5.6.7	Reversibility of the electrowetting process.....	158
5.6.8	Alternative method for further investigation of the wettability transition via dynamic experiments.....	160
5.6.9	Conclusions.....	163
5.7	Reversible Photoinduced Wettability Transition of Hierarchical ZnO Structures.....	165
5.7.1	Introduction.....	165
5.7.2	Surface characteristics and measurements	165
5.7.3	Transition from Cassie – Baxter to Wenzel state.....	170
5.7.4	Mechanism of the transition.....	172
5.7.5	Conclusions.....	173
5.8	Smart Polymer-Functionalized Surfaces.....	175
5.8.1	Introduction.....	175
5.8.2	Functionalizing the silicon structured surfaces	176
5.8.3	Switching the hydrophobicity via the PH sensitive coating.....	177
5.8.4	Conclusions.....	181
C)	Biological Applications	183
	Introduction.....	183
5.9	Tuning cell adhesion of fibroblasts	185

5.9.1	Introduction.....	185
5.9.2	Methodology.....	186
5.9.3	Cell culture, spreading and viability	188
5.9.4	Cell adhesion.....	192
5.9.5	Conclusions.....	198
5.10	3D primary neuronal cells culture.....	199
5.10.1	Introduction.....	199
5.10.2	Methodology	199
5.10.3	Promoting neuron cell adhesion.....	200
5.10.3	Conclusions.....	204
Chapter 6	205
	Formation of metallic nanosurfaces and nanoparticles via fs laser ablation in liquid media.....	205
6.1	Introduction.....	205
6.2	Morphology of NS and NP under laser ablation of planar surfaces.....	207
6.3	Generation of Al nanoparticles and nanostructures via ablation of bulk Al in liquids with short laser pulses	211
6.3.1	Introduction.....	211
6.3.2	Methodology	212
6.3.3	Characterization of Al nanoparticles.....	213
6.4	Optical properties of nanostructures.	219
6.5	Applications of Nanostructures.....	222
6.6	Conclusion	224
	Concluding Remarks.....	225
	Relevant Publications.....	229
	Reference	231

Introduction and Overview

Introduction

Controlling the interactions of laser beams with matter is crucial for the success and scalability of materials processing applications. The optimal interplay between the laser irradiation and material parameters allows controlled modification of surface properties at different length scales adding a new dimension to materials properties optimization. For a given wavelength, the laser pulse duration is a critical parameter and processing by ultrashort (i.e. sub-picosecond) laser pulses opens new exciting possibilities. In comparison to ps and longer laser pulses, ultrafast laser processing provides two major advantages: (a) a net decrease of the ablation threshold for identical laser wavelength and focusing conditions^[1] and (b) an important decrease of the heat affected zone that can greatly reduce the extent of collateral damage to the surrounding area,^[2] allowing the production of sub-wavelength nanostructures. Such characteristics are due to the rapid energy deposition inside the target material and the subsequent non-linear processes induced at the focal point. Experimentally, it has been shown that the internal thermalization of the electron distribution following excitation by a femtosecond (fs) laser pulse takes place within one ps.^[3] Thermalization between the electron subsystem and the lattice is usually longer and is of the order of several ps, depending on the electron–phonon coupling strength.^[4] Thus, ultrafast laser excitation generates a hot electron gas which is in a highly non-equilibrium state with the lattice. As a consequence, direct irradiation of materials by ultrafast laser pulses induces modifications leading to complex micro- and nano- scale surface features, which are often found to have unique properties and cannot be realized by other, non-laser based techniques.

Laser micro- and nanostructuring of materials is important in many scientific, technological and biological applications, such as the fabrication of opto- and nanoelectronic devices, information storage systems, control over the mechanical and optical properties of solids, microfluidics and biomedical engineering.^[5,6,7,8,9,10] In this thesis we present the fabrication, and formation mechanisms of different kinds of micro- and nano- scale structures on the surface of semiconducting and metallic materials fabricated by means of ultrafast laser processing. Two distinct approaches are reviewed including laser surface modification in controlled gas and liquid media respectively. Emphasis will be placed on the

exploitation of the materials and structures attained to modern applications for which there is an increasing demand over the previous years. Besides presenting recent advances achieved by these techniques, it will also delineate existing limitations and discuss emerging possibilities and future prospects.

Overview

This thesis is organized as follows:

Chapter 1 reviews the basic processes taking place upon the interaction of intense laser pulses with solids and comments on the formation mechanisms proposed for the laser induced periodic surface structures.

Chapter 2 shows the experimental setup and instrumentation used for the surface structuring, sample preparation and characterization.

Chapters 3 and 4 investigate the fundamental processes occurring during femtosecond laser-material interaction, focusing in the normal boiling regime, where material removal is minimal and ablation does not take place. . In particular, we present experimental results on the surface modification observed upon irradiation of planar silicon surfaces with single and temporally delayed double pulses. A detailed theoretical model that takes into account heat transfer components and hydrodynamic equations describing the material melting and resolidification dynamics has been developed to predict the final surface profile attained . . Our study is then extended to femtosecond laser processing of transparent semiconductors and in particular to the study of the fundamentals of laser induced periodic structures (ripples) formation on ZnO surfaces irradiated with ultrashort delayed double pulses. In the last part of the chapter we present results from the experimental investigation of the evolution of the surface morphology upon increasing the laser energy. The formation mechanism and properties of microconical structures (spikes) on Silicon is subsequently discussed. Finally the role of laser processing in reactive gas atmosphere for the improvement of the spikes' aspect ratio, as well as for the realization of micro/nano morphology is demonstrated.

Chapter 5 presents the work on the practical applications of femtosecond laser processed micro/nano structured Si surfaces. . The chapter presents our study for three different types of

applications: **A)** *Field emission elements*, concerning the improvement of stability and durability of Si spikes-based cathode field emitters. **B)** *Responsive surfaces*, concerning applications where the wettability of a surface can be switched on demand under the action of various external stimuli. Depending on the conformal coating deposited onto micro/nano processed Si surfaces, electro-, photo- and pH- responsive surfaces are demonstrated. **C)** *Biological applications* where we demonstrate the ability to tune cell adhesion using laser textured biomimetic artificial Si substrates. .

Chapter 6 presents preliminary results on femtosecond laser-material processing in liquid media. It is shown that although such process also leads to surface texturing, in this case different mechanisms prevail, owing to the fact that the liquid adjacent to the melted surface undergoes a phase transition. The advantages of femtosecond laser processing for the formation of various types of nanostructures are presented and discussed.

Chapter 1

Theoretical background

1.1 Introduction

Surface processing of materials including metals, semiconductors and dielectrics, with ultra-short pulsed lasers has received considerable attention over the past decades due to its important technological applications, particularly in industry and medicine^[11,12,13,14,15,16,17,18,19,]. Rapid energy delivery and reduction of the heat-affected areas are the most pronounced advantages of the technique compared to effects induced by longer pulses^[20], which reflect the merit of the method as a potential tool for laser-assisted fabrication at micro- and nano-scales. These abundant applications require thorough knowledge of the laser interaction with the target material for enhanced controllability of the resulting modification of the target relief.

In this chapter, some fundamental processes that underlie laser matter-interactions will be reviewed: the formation of surface periodic structures and the mechanism associated with those structures' formation. We introduce the basic theory for a deep understanding of the mechanisms responsible for the laser structuring of materials. These will be later considered in a proposed theoretical framework describing ultrafast laser induced surface modification and compared with the experimental results obtained, (**Chapter 3**). Our final aim is to obtain a clearer picture of the physical processes governing ultrashort pulsed laser-surface interaction.

1.2 Fundamental processes of laser-matter interaction

1.2.1 Primary processes - Absorption mechanisms

Surface modification of materials by means of pulsed laser light requires the deposition of a certain amount of energy absorbed by the material. Different kinds of surface modification can be attained, depending on the laser parameters including energy, temporal and spatial distribution of the beam, and pulse repetition rate. Primary absorption processes involving interband transitions of electrons are: **(a)** single photon absorption, **(b)** multiphoton absorption, **(c)** interband transitions by free-carrier excitation and **(d)** impact ionization. Detailed information on these processes can be found elsewhere.^[12]

1.2.2 Secondary processes – Energy relaxation

Following the primary absorption mechanisms the energy absorbed by the electron is relaxed through a variety of processes which can eventually end in modification of the material structure. **Figure 1.1** summarizes the most important processes involved after the absorption of the laser energy, its redistribution and transport through the target and the resulting structural and thermal effects, together with their typical timescales.^[21,22] The governing processes are the following:

- (i) Carrier excitation:** Carrier (electrons in metals or electron-holes in semiconductors) excitation is the movement of an electron to a higher energy state due to absorption of photons by a laser beam. Single or multiphoton absorption are the dominant mechanisms for exciting electrons in the valence band provided that the energy gap is smaller or greater respectively than the photon energy. If some of the carriers are excited well above the band gap (or Fermi level in metals), impact ionization can generate additional excited states.
- (ii) Thermalization:** On a time scale of about $10^{-14} - 10^{-12}$ sec described as the *electron phonon relaxation time*, the initial energy distributed among the electrons is transferred to the lattice via carrier-carrier and carrier-phonon scattering. In metals and semiconductors scattering occurs during a few hundreds of femtoseconds after excitation and it takes several picoseconds for the carrier and lattice to reach thermal equilibrium.
- (iii) Carrier removal:** After carriers and lattice have reached equilibrium the material has a well-defined temperature but there is still an excess of free carriers compared to thermal equilibrium. These are removed by recombination or carrier diffusion processes.

- (iv) **Thermal and structural effects:** On the time scale of 10^{-11} sec and below carriers and lattice come to an equilibrium temperature and heat is diffused from the material's surface to the bulk. If the laser pulse intensity exceeds the melting or boiling point thresholds, melting or vaporization of the material occurs. As the deposited optical energy is converted to kinetic energy of the lattice ions, material removal via ablation can occur in the form of individual atoms, ions, molecules or clusters. Finally solidification of the material occurs in timescales from nanosecond through microseconds.

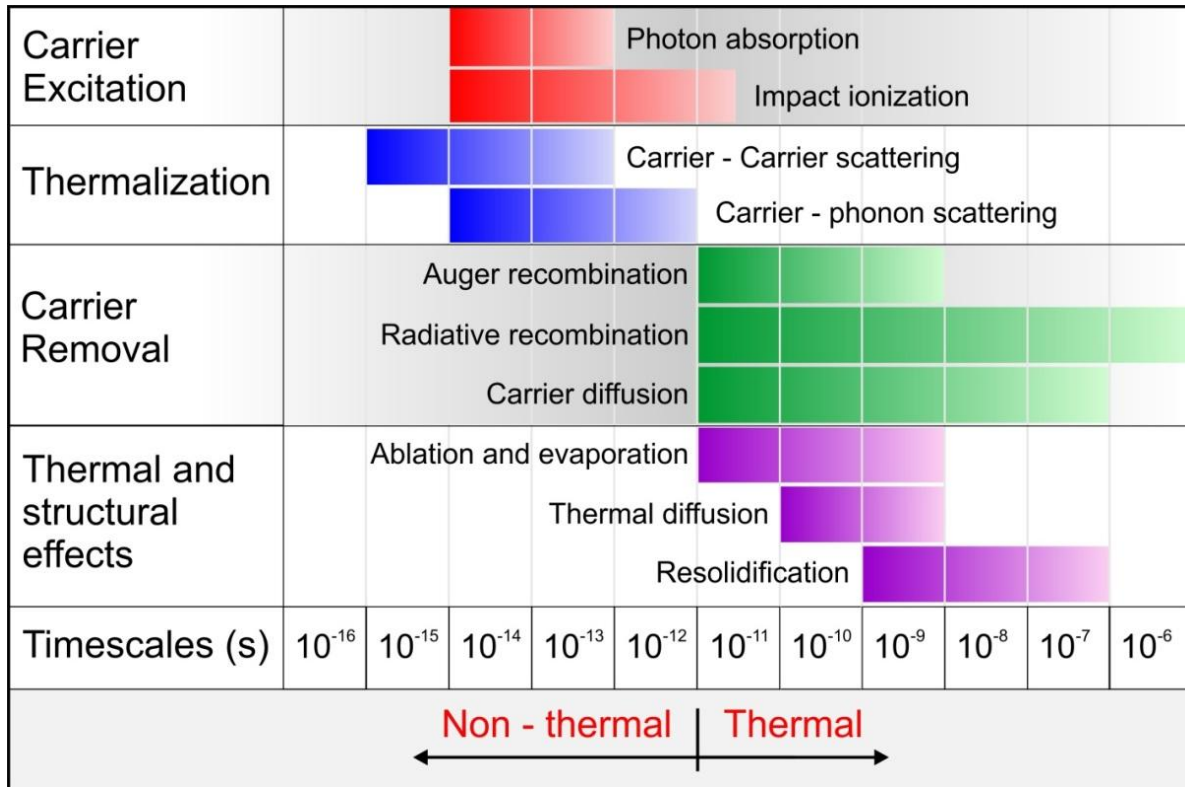


Figure 1.1 Processes (and associated timescales) taking place in the target following the absorption of the laser pulse. Ablation typically takes place on a timescale of ps to a fraction of a ns. (Adapted from [12])

There is a distinct line at about 10^{-12} - 10^{-11} s which distinguishes the regimes between non-thermal and thermal processes. Mechanisms leading to structural modifications using picosecond and longer laser pulses are predominantly thermal. By contrast, exposure to ultrashort (femtosecond) pulses leads to a different type of modification. As illustrated in **Figure 1.1**, for pulse durations that are significantly less than electron-to-lattice (ions) non-thermal pathways may be accessed that take place on a timescale shorter than a picosecond, hence before thermal processes are initiated. Nevertheless, there are still several aspects of femtosecond laser induced modification of solids yet to be interpreted.

1.3 The two temperature model

For pulse duration longer than the electron-phonon relaxation time there is a significant transfer of energy from the laser-excited electrons to the lattice on the time scale of the pulse duration. Therefore, in this case electrons and lattice are in thermal equilibrium and acquire the same temperature.^[23] On the contrary, when the pulse duration is shorter than the electron-phonon relaxation time, non-equilibrium occurs between the carrier and lattice temperatures. Electrons in the conduction band are heated by the laser pulse much faster than they can cool by phonon emission and thus electrons and lattice have to be described by a set of separate temperatures.

The two temperature model (TTM) first reported by Anisimov et al.^[24] described mathematically the evolution of the temperature increase due to the absorption of a short laser pulse beam. Two sets of coupled heat diffusion equation describe the evolution of the electron T_e and lattice temperature T_l and are given by the following expressions:

$$\text{Carrier} \quad C_c \frac{\partial T_c}{\partial t} = \underbrace{\vec{\nabla} \cdot}_{\text{Temporal evolution of Electron Temp.}} \underbrace{\left[(k_e + k_h) \vec{\nabla} T_c \right]}_{\text{Heat diffusion due to carriers}} - \underbrace{\frac{C_c}{\tau_e} (T_c - T_l)}_{\text{Energy transfer carrier-phonons}} + \underbrace{S(\vec{r}, t)}_{\text{Heat source}} \quad (\text{eq. 1.1})$$

$$\text{Lattice} \quad C_l \frac{\partial T_l}{\partial t} = \underbrace{\vec{\nabla} \cdot}_{\text{Temporal evolution of Lattice Temp.}} \underbrace{\left[K_l \vec{\nabla} T_l \right]}_{\text{Heat diffusion due to lattice}} + \underbrace{\frac{C_c}{\tau_e} (T_c - T_l)}_{\text{Energy transfer carrier-phonons}} \quad (\text{eq. 1.2})$$

$$\text{Number Density Of Carriers} \quad \frac{\partial N}{\partial t} = \underbrace{\frac{\alpha}{h\nu} \Omega I(\vec{r}, t)}_{\text{Number density}} + \underbrace{\frac{\beta}{2h\nu} \Omega^2 I^2(\vec{r}, t)}_{\text{One Photon absorption}} - \underbrace{\gamma N^3}_{\text{Two Photon absorption}} + \underbrace{\theta N}_{\text{Auger recomb.}} - \underbrace{\theta N}_{\text{Impact ionization}} - \underbrace{\vec{\nabla} \cdot \vec{J}}_{\text{Carrier current vector}} \quad (\text{eq. 1.3})$$

$$\Omega = \frac{1 - R(T_l)}{\cos \varphi} \quad (\text{eq. 1.4})$$

where C_c and C_l are the heat capacity of electron-hole pairs and lattice, respectively, ν is the frequency of the laser beam, k_e and k_h are the thermal conductivity of the electrons and holes, respectively, K_l is the thermal conductivity of the lattice, h is the Planck's constant, γ is the Auger recombination coefficient, θ is the impact ionisation coefficient, α and β are the one-photon and two-photon absorption coefficients, φ is the angle of the incident beam with respect to the normal axis on the irradiated surface, $R(T_l)$ is the reflectivity of the laser beam on the silicon surface (which is a function of the material temperature), τ_e is the energy relaxation time, \vec{J} is the carrier current vector and $S(\vec{r}, t)$ is provided by the following expression:

$$S(\vec{r}, t) = (\alpha + \Theta N) \Omega I(\vec{r}, t) + \beta \Omega^2 I^2(\vec{r}, t) - \frac{\partial N}{\partial t} (E_g + k_B T_c) - N \frac{\partial E_g}{\partial T_l} \frac{\partial T_l}{\partial t} - \vec{\nabla} \cdot \left[(E_g + 4k_B T_c) \vec{J} \right] \quad (\text{eq. 1.5})$$

where Θ stands for the free-carrier absorption cross section, k_B is the Boltzmann's constant and E_g the band-gap energy. The contribution of the current vector in the balance equation for the electron-hole carriers depends largely on the pulse duration. Experiments in which laser induced modification of Si has been investigated suggest that the divergence of the carrier current for pulses shorter than 600fs can be neglected.^[25] The laser intensity in **Eqs. 1-5** is obtained by considering the propagation loss due to one-, two-photon and free carrier absorption^[26]

$$\frac{\partial I(\vec{r}, t)}{\partial z} = -(\alpha + \Theta N) I(\vec{r}, t) - \beta I^2(\vec{r}, t) \quad (\text{eq. 1.6})$$

assuming that the laser beam is Gaussian both temporally and spatially and the transmitted laser intensity at the incident surface is expressed in the following form:

$$I(r, z = 0, t) = \frac{2\sqrt{\ln 2}}{\sqrt{\pi} \tau_p} E_p e^{-\left(\frac{r^2}{R_0^2}\right)} e^{-4\ln 2 \left(\frac{t-t_0}{\tau_p}\right)^2} \quad (\text{eq. 1.7})$$

where E_p is the fluence of the laser beam and τ_p is the pulse duration (i.e. full width at half maximum), R_0 is the irradiation spot-radius (distance from the centre at which the intensity drops to I/e^2 of the maximum intensity).

1.4 Thermal processes induced by laser irradiation

Femtosecond pulsed laser interaction with matter triggers a variety of timescale-dependent processes (see **Section 1.2**), influenced by the laser fluence and pulse duration;^[27] different combinations of those parameters are capable of inducing phase transition and/or material removal. For instance, a solid material subjected to ultrashort pulsed laser heating at sufficiently high fluences undergoes a phase transition to a superheated liquid whose temperature reaches $\sim 0.90T_{cr}$ (T_{cr} being the thermodynamic critical temperature).^[23] Subsequent bubble nucleation leads to a rapid transition of the superheated liquid to a mixture of vapour and liquid droplets that are ejected from the bulk material leading to material removal via ablation. **Figure 1.2** shows an example of the phase diagram of a metallic material^[28,29] in the neighbourhood of T_{cr} . Here we summarize some details regarding the phase diagram.

- The “*normal heating*” line indicates the heating process of a liquid metal when the temperature is below the boiling temperature. The system (provided it is liquid and provided also that the heating is slow enough) undergoes normal boiling at T_b . At the boiling temperature, the liquid and the vapor phases are in equilibrium, which is shown as the “*binodal line*”.
- “*Superheating*” refers to heating which is carried out sufficiently rapidly (i.e. with a characteristic time of $\leq \sim 1000$ ns according to,^[30] but perhaps a shorter time is preferable) so that the system passes beyond T_b and is therefore metastable (superheated).
- That marked “*vaporization in vacuum*” differs mainly in that a so-called Knudsen layer forms at the liquid surface.^[30, 31] This is the region in which the vaporized particles, initially having only positive velocities normal to the surface, develop negative velocities, but, in order that momentum to be conserved, the particles also develop a positive center-of-mass (or flow) velocity.
- The “*spinodal*” is the limit to which the metastable liquid can be heated.
- The curve marked “*equilibrium vaporization*” is that corresponding to liquid metal in equilibrium with saturated metal vapor at pressure p_0 .
- The curve marked “*onset of anomalies*” indicates the approximate temperature at which anomalous behavior is found for a number of properties for $T/T_{lc} > \sim 0.80$. Indeed, major fluctuations in volume and enthalpy are found to occur^[34,31] which imply dramatic changes in the specific heat, C_p (very high), and in the resistance (very high).

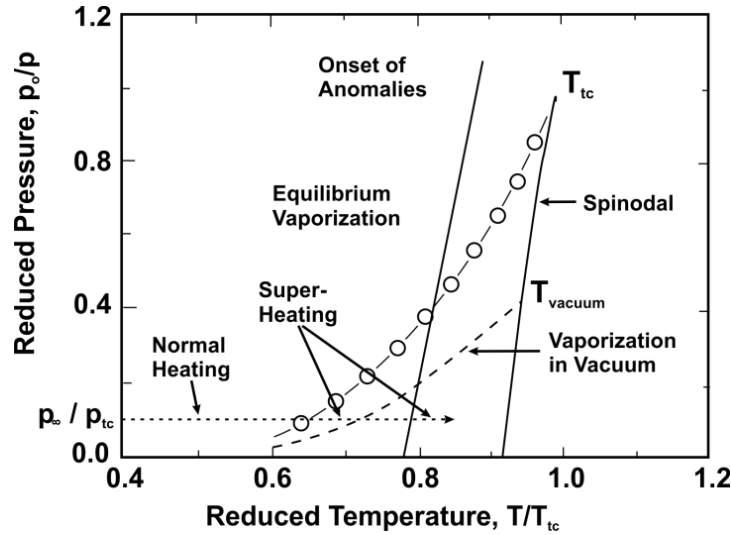


Figure 1.2: p - T phase diagram of a metal (Cs) in the neighborhood of T_{tc} (Adapted from [29])

- By “*normal vaporization*” we refer to the passage from a condensed phase (solid or liquid) to vapor by virtue of the emission of particles (atoms or molecules) from the extreme outer surface under conditions of electron–phonon coupling.
- “*Normal boiling*” involves heterogeneous nucleation. These are vapor bubbles which, in the case of liquids, initiate heterogeneously from a variety of disturbances such as gas or solid impurities, or defects, or an underlying or enclosing solid surface. Once formed, the bubbles tend to diffuse and may, given enough time together with the inequality $T > T_b$, escape from the outer surface of the liquid. Bubbles may form in either solids (as in nuclear fuel) or liquids, but given the problem of mobility only liquids need to be considered for short timescale processes investigated here. Bubbles may form: 1. at the outer surface of the liquid 2. in the bulk of the liquid 3. at an underlying or enclosing solid surface

1.5 Periodic surface structures and surface plasmon waves

1.5.1 Laser induced periodic surface structures - Ripples

Surface structuring of materials with lasers has been of great interest in the past years due to its various exciting applications arising from the new properties of the modified area. Researchers studying the laser-matter interaction are familiar with almost a universal phenomenon occurring close to the damage threshold of a material. This is the so called “**Laser induced periodic surface structures**” (LIPPS) or “**ripples**”. Birnbaum^[32] was the first to observe the formation of a laser-induced periodic surface structure (LIPSS) after irradiation of semiconductor surfaces with a CW Ruby laser. He explained this ripple formation as the result of light diffraction effects at the focal region. These patterns exhibit a grating-like morphology with a periodicity close to the laser wavelength and have been observed at the surface of many materials including semiconductors^[33,34,35] metals^[36,37,38,39] and dielectrics^[40]. For a normally incident laser beam ripples are formed perpendicular to the electric field polarization. **Figure 1.3** shows a spot created on a Si surface irradiated by 4 femtosecond pulses at a wavelength of 800 nm. Ripples formation perpendicular to the light polarization is observed while the measured periodicity is measured to be close to laser wavelength and around 710 nm. However, as reported by other groups^[41,42,43,44] ripple periodicity can decrease upon increasing the number of laser shots. This is attributed to the fact that the spots diameter and depth are increasing upon increasing the number of laser shots, which affect the ripple formation mechanism. For circular polarization no ripples are observed. Ripples can be produced by a single or many laser shots and are independent of the irradiation atmosphere and of the crystallographic direction of the surface.

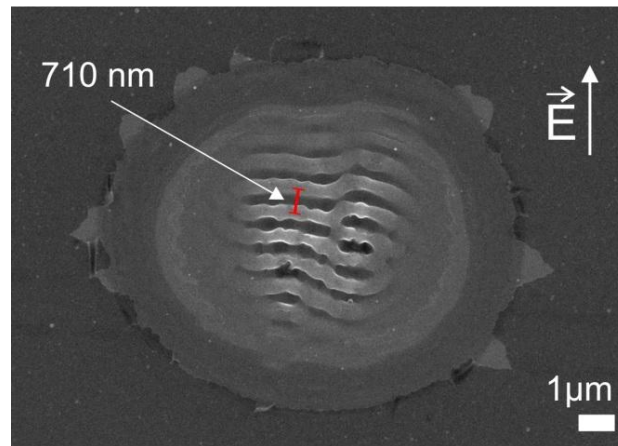


Figure 1.3: Spot created on silicon with a 800nm femtosecond laser beam and 4 laser pulses. The formation of ripples can be observed having a periodicity of 710 nm. Ripples are formed perpendicular to the laser polarization.

Emmony et al.^[45] irradiated germanium surfaces and suggested that interference between the incident and a scattered surface wave may explain the formation of the observed ripples. The ripple wavelength Λ due to the proposed mechanism was calculated to be equal to

$$\Lambda = \frac{\lambda}{1 \pm \sin\theta} \quad (\text{eq. 1.8})$$

where λ is the laser wavelength and θ is the angle of the incidence laser beam and the \pm accounts for the scattered wave co-propagating and counter-propagating to the surface projection of the incident wave. For normal incidence Eq. 1 gives $\Lambda \sim \lambda$ therefore such ripples are called **Wavelength- or Low-Spatial-Frequency- Ripples (LSFR)**". Similar theoretical and experimental investigations provided a systematic and improved analysis towards the estimation of the periodicity of LSFRs on rough surfaces^{[46] [47]}. All approaches predicted ripple wavelengths in the order of the beam wavelength ($\Lambda \sim \lambda$).

Despite the successful interpretation of LSFR formation, a large number of experimental observations showed that ripple periodicity can be much smaller than the laser wavelength ($\Lambda \ll \lambda$); in this case we have **High-Spatial-Frequency-Ripples (HSFR)**^[48,49,50,51,52,53,54], while their formation could not be explained by the aforementioned mechanism. A widely accepted mechanism that accounts for **HSFR** formation is based on the laser induced excitation of surface plasmon waves and this process will be considered throughout the thesis.

1.5.2 Surface plasmon waves: Coherent electron oscillations

In 1907 Zenneck^[55] proposed that electromagnetic waves in the radiofrequency regime can ride along the planar interface between air and either ground or water. This idea was later reintroduced in 1957 by R. H. Ritchie^[56] to the visible portion of the electromagnetic spectrum at the interface of a metal and a dielectric, leading to the concept of **surface-plasmon-polaritons S-PP**.

Surface plasmons (S-P), are coherent electron oscillations that exist at the interface between any two materials (**Figure 1.4**) where the real part of the dielectric function changes sign across the interface (e.g. a metal-dielectric interface, such as a metal sheet in air). S-Ps have lower energy than bulk (or volume) plasmons which quantize the longitudinal electron oscillations about positive ion cores within the bulk of an electron gas (or plasma).

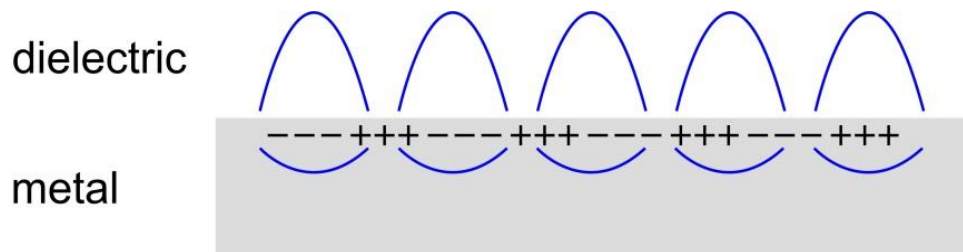


Figure 1.4: Schematic representation of an electron density wave propagating along a metal - dielectric interface. The charge density oscillations and associated electromagnetic fields are called surface plasmon-polariton waves.

When S-Ps couple with a photon, the resulting hybridized excitation is called a **surface plasmon polariton (S-PP)**. This S-PP can propagate along the surface of a metal until energy is lost either via absorption in the metal or radiation into free-space. Surface plasmons can be excited by both electrons and photons.

It should be noted that semiconducting surfaces irradiated by ultrashort pulsed bandgap laser light, at fluences close to the damage threshold, should also exhibit metallic behaviour.. This is due to the laser-induced excitation of a large number of electrons in the conduction band. As a result, the electronic properties of ultrashort laser-excited semiconductors are similar to those of a *degenerate semiconductor*. Therefore S-PPs can potentially be excited along a semiconductor - dielectric interface as well.

If we consider a S-PP wave excited by a laser beam, its plasmon wavelength, λ_s is related to the wavelength of the incident beam, λ , through the relation: ^[57]

$$\Lambda = \frac{\lambda}{\frac{\lambda}{\lambda_s} \pm \sin\theta} \quad (\text{eq. 1.8})$$

λ_s can be obtained by the dispersion relation on metal/dielectric interface assuming $\varepsilon'' < |\varepsilon'|$ and a real ε_d ,

$$\lambda_s = \lambda \left(\frac{\varepsilon' + \varepsilon_d}{\varepsilon' \varepsilon_d} \right)^{\frac{1}{2}} \quad (\text{eq. 1.9})$$

$$\varepsilon' = \text{Re} \left(1 + (\varepsilon_g - 1) \left(1 - \frac{N}{n_0} \right) - \frac{N}{N_{cr}} \frac{1}{\left(1 + i \frac{1}{\omega \tau_e} \right)} \right) \quad (\text{eq. 1.10})$$

where λ is the laser wavelength, λ_s is the plasmon wavelength, ε' is the real part of ε of a laser-induced high excited and ε_d is the dielectric constant of the dielectric material (for air, $\varepsilon_d = 1$), ω is the frequency of the incident beam, n_0 is the valence band density.

The process whereby the excitation of surface-plasmon waves lead to the formation of periodic structures is not yet fully understood. The following mechanism is generally proposed: the interference of the incident laser beam with the propagating plasmon wave gives rise to the generation of local, periodically charged areas onto the material surface. Areas that become positively charged are exploded

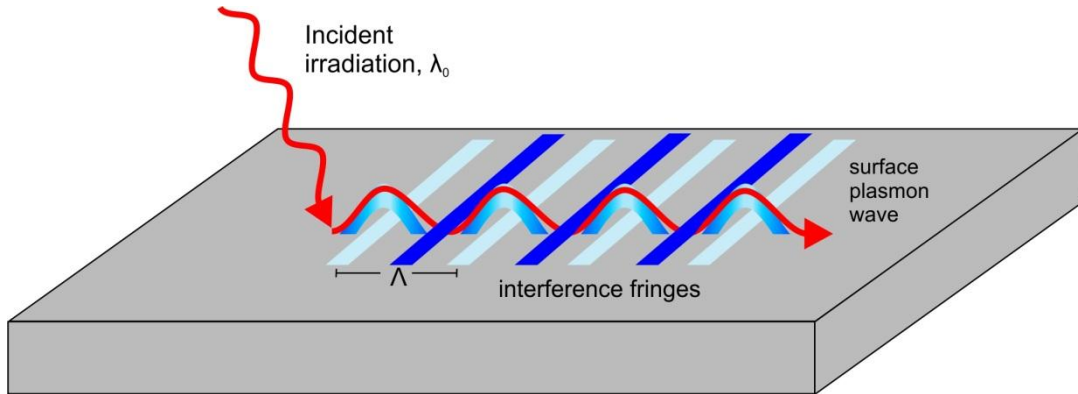


Figure 1.5: Schematic representation of an interference of the incident beam with the surface plasmon wave (blue wave).

towards free space by the Coulomb repulsive force (Coulomb explosion); consequently, a thin layer located at such areas is ablated and a periodic pattern is imprinted. According to the above mechanism, the periodicity of the surface patterns attained depends only on the frequency (electron density) of the surface plasmon wave.^[58] **Figure 1.5** illustrates a schematic representation of the interference mechanism. The laser beam with wavelength λ_0 excites a S-P wave on the material (gradient blue colour). During material heating and melting (**Section 1.4.1**) process, the interference of the incident with the surface plasmon wave gives rise to periodic fringes (red colour) which are subsequently “printed” on the material after resolidification. Therefore, the structures formed exhibit the periodicity of the interference pattern which is close to the incident beam wavelength.

1.5.3 Origin of HSFR

As previously mentioned, there are many reports of periodic surface structure formation with spatial periods much smaller than the laser wavelength (see also **Section 1.4.1** and **Section 3.4.3**). The following mechanisms had been proposed to explain the origin of HSFRs.

i. Interference with second harmonic generation (SHG) waves

The first mechanism suggests that second harmonic generation is involved in the HSFR formation.^[59,60] A study^[61] performed on crystalline ZnO surface, using a 800nm femtosecond laser beam, shows that in a narrow excitation range, the peak intensity of the laser pulse is large enough to efficiently generate SHG at 400 nm. This radiation interacts with a highly excited material which is still transparent for this SHG wavelength. The intrapulse interference effect of the incident SHG and the surface electromagnetic wave scattered at 400 nm is then finally generating the HSFL structures. **Figure 1.6(a)** illustrates the above mechanism and how the interference of a generated SHG wave (light blue line) with a scattered wave (dark blue line) at $\lambda/2$ leads to LSFR. An example of HSFRs created on ZnO surfaces can be seen in **section 4.2.3** showing spatial periods in the range of 150 - 280 nm.

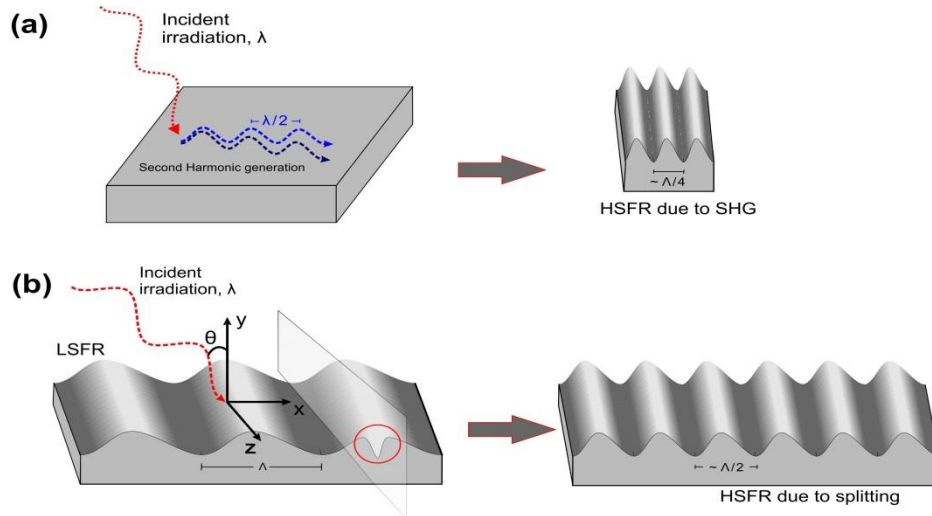


Figure 1.6: (a) Schematic representation of the interference of a generated SHG wave (light blue wave) with a scattered wave (dark blue wave) at $\lambda/2$ leading to HSFR. (b) Example of the splitting of the LSFR due to the grating coupling mechanism leading to HSFR

ii. Grating coupling effect.

When the initial ripples are formed the physical picture should be changed due to the effect of grating coupling. This mechanism is proposed in order to explain the observed splitting of ripples into smaller ones.^[62] R.W. Wood^[63] first observed coupled S-PPs using the grating configuration in 1902. Incident radiation at an angle θ with respect to the normal plane of the surface can scatter from the grating, increasing or decreasing the component of its wave vector by integer multiples of the grating wave vector k_g ($k_g = 2\pi / \Lambda$). This gives rise to diffracted orders which lead to the formation of HSFR. **Figure 1.6(b)** presents an example of the splitting (red circle) of the LSHR due to the grating coupling mechanism leading to HSFR. LSHR is always initially observed in the crater periphery, where the energy for a Gaussian beam is lower, which indicates the important role of the excited carrier density that is monotonously dependent on the irradiation fluence.

1.6 Brief introduction to fluid dynamics

The laser induced creation of a melted layer and its subsequent solidification (see also **Section 1.4**) entails on further investigation of the molten material dynamics. The melted material should be regarded as an incompressible Newtonian fluid and thereby a more complete theoretical model requires to be enriched by hydrodynamics equations. In this section we briefly introduce some fundamental aspects of fluid dynamics used in **Chapter 3** to describe the motion of the molten material. Fluid dynamics is a sub-discipline of fluid mechanics that deals with fluid flow - the natural science of fluids (liquids and gases) in motion. Fluid dynamics has a wide range of applications, including calculating forces and moments on aircraft, determining the mass flow rate of petroleum through pipelines. The solution to a fluid dynamics problem typically involves calculating various properties of the fluid, such as velocity, pressure, density, and temperature, as functions of space and time.

1.6.1 Simplified Navier–Stokes equations

The **Navier–Stokes equations**, named after Claude-Louis Navier and George Gabriel Stokes, describe the motion of fluid substances. These equations arise from applying Newton's second law to fluid motion, together with the assumption that the fluid stress is the sum of a diffusing viscous term (proportional to the gradient of velocity), plus a pressure term.

A simplification of the Navier–Stokes equations flow equations is obtained when considering an incompressible flow (material density is constant within an infinitesimal volume that moves with the velocity of the fluid) of a Newtonian fluid. The assumption of incompressibility rules out the possibility of sound or shock waves to occur. In this sense the Navier–Stokes equations will read, in vector form:

$$\rho \left(\underbrace{\frac{\partial \mathbf{v}}{\partial t}}_{\text{Unsteady acceleration}} + \underbrace{\mathbf{v} \cdot \nabla \mathbf{v}}_{\text{Convective acceleration}} \right) = \underbrace{-\nabla p}_{\text{Pressure gradient}} + \underbrace{\mu \nabla^2 \mathbf{v}}_{\text{Viscosity}} + \underbrace{\mathbf{f}}_{\text{Other body forces}} \quad (\text{eq. 1.11})$$

Inertia (per volume) Divergence of stress

where v is the flow velocity, ρ is the fluid density, p is the pressure, f represents body forces (per unit volume) acting on the fluid, such as gravity or centrifugal force, ∇ is the del operator, $\mu \nabla^2 \mathbf{v}$ is the viscosity of the fluid and μ is the (constant) dynamic viscosity.

1.6.2 Shallow water equations

To account for the morphology of the melt profile attained following the resolidification process, the evolution of the capillary height (rises or falls) should also be calculated. Considering that the height of the molten material is small compared to its lateral size the shallow water equations are applied. The shallow water equations^[64] (also called *Saint Venant* equations) is a set of hyperbolic partial differential equations that describe the propagation of disturbances in water and other incompressible fluids. The underlying assumption is that the depth of the fluid is small compared to the wave length of the disturbance. The equations are derived from depth-integrating the Navier–Stokes equations, in the case where the horizontal length scale is much greater than the vertical length scale. Under this condition, conservation of mass implies that the vertical velocity of the fluid is small.

$$\frac{\partial H(\vec{r}, t)}{\partial t} + \vec{\nabla} \cdot (H(\vec{r}, t) \vec{u}) = 0 \quad (\text{eq. 1.12})$$

where, H is the mean height of the horizontal liquid surface and u is the velocity. Gravitational forces are here neglected.

Or

$$\frac{\partial H(\vec{r}, t)}{\partial t} + \vec{u} \vec{\nabla} H(\vec{r}, t) + H(\vec{r}, t) \vec{\nabla} \vec{u} = 0 \quad (\text{eq. 1.13})$$

This equation expresses the local rate of change of surface height in terms of two contributions:

- (i) by advection of height $\vec{u} \vec{\nabla} H(\vec{r}, t)$
- (ii) by volume convergence $H(\vec{r}, t) \vec{\nabla} \vec{u}$

Chapter 2

Experimental section

2.1 Introduction

This chapter includes a description of the laser sources and the experimental setups employed for surface structuring, sample preparation and characterization. Furthermore, a description of the apparatus used for the implementation of pulse shaping techniques, field emission measurements, wetting and electrowetting experiments is demonstrated. Finally, regarding the biological investigations, the methodologies followed for cell culture, viability and imaging are presented.

2.2 The femtosecond Laser Source

The laser sources employed for the experiments were:

- A regenerative amplified Ti:Sapphire laser system ($\lambda = 800nm$, $\tau_{FWHM} = 180 fs$, $1KHz$)
- A multipass amplified Ti:Sapphire laser ($\lambda = 800nm$, $\tau_{FWHM} = 35 fs$, $1KHz$)

A more detailed discussion follows

2.2.1 The regenerative amplified Ti:Sapphire laser system

This laser system is based on a Spectra Physics Tsunami oscillator, which delivers 80-100 fs pulses at a repetition rate of 81 MHz with a power of 500 to 600 mW and a FWHM of 10 nm. The pump laser used for this system is a Spectra Physics Millennia Nd:YLF, which pumps the oscillator with a power of 5 W. A “Thales Laser System” (stretcher, amplifier, compressor) amplifies the beam by using another Ti:Sapphire crystal and a 12 W Q-switched Nd:YLF pump laser (B. M. Industries). During the chirped pulse amplification the repetition frequency is lowered from 81 MHz to 1 kHz by a pulse picker (pockels cell) inside the cavity of the amplifier. After being amplified the pulse is linearly polarized, it has a length of 180 fs with a repetition rate of 1 kHz and a power of 500 to 600mW, respectively.

2.2.2 The multipass amplified Ti:Sapphire laser system

This laser (FEMTOPOWERTM COMPACTTM PRO) is a kHz-repetition rate, multi-pass titanium-sapphire amplifier which is seeded by a broadband femtosecond pulses from a mirror-dispersion controlled titanium-sapphire oscillator and uses a modified version of the chirped-pulse-amplification scheme.

The FEMTOPOWERTM COMPACTTM PRO requires two laser energy sources for operation:

- ✓ A *continuous wave (cw)*, frequency-doubled Nd:YVO₄ laser for pumping the oscillator.
- ✓ A kHz-repetition rate, Q-switched, frequency-doubled Nd:YAG laser for pumping the amplifier.

A mirror-dispersion controlled oscillator generates broadband (>100nm), ultrashort (~10 fs) pulses at 76 MHz repetition rate. The pulses are stretched to a safe value amplification by a traversing a suitable amount of optical glass. Third-order dispersion pre-compensation is archived by a certain number of reflections from TOD-dispersion compensating mirrors. The pulses are then amplified by the multiple pass through a kHz-pumped amplifier assembly to ~ 1 mJ. After the first four passes a single pulse is selected from the MHz-pulse train to be further amplified in another five passes. After amplification the pulses are recompressed to less than 40 fs by a prism compressor.

2.3 The Spatial Light Modulator (SLM) pulse shaper.

2.3.1 Introduction

A **spatial light modulator** (SLM) is an electrically programmable device that modulates light according to a fixed spatial (pixel) pattern. SLMs have an expanding role in several optical areas where light control on a pixel-by-pixel basis is critical for optimum system performance. SLMs are typically used to control incident light in amplitude-only, phase-only or the combination (phase-amplitude).

2.3.2 Design of the SLM

The Spatial Light Modulator (SLM-S640d) displayed in **Figure 2.1** is suitable for modulation of femtosecond laser pulses. By coupling two Liquid Crystal Modulators in a sandwich-like configuration an independent and simultaneous modulation of phase and amplitude is reached by assembling in a 4f arrangement or in a CPA-system (chirped pulse amplification). Any of the 640 strips (**Figure 2.2b**) of each separate LC display can be controlled in activity by 12-bit resolution.

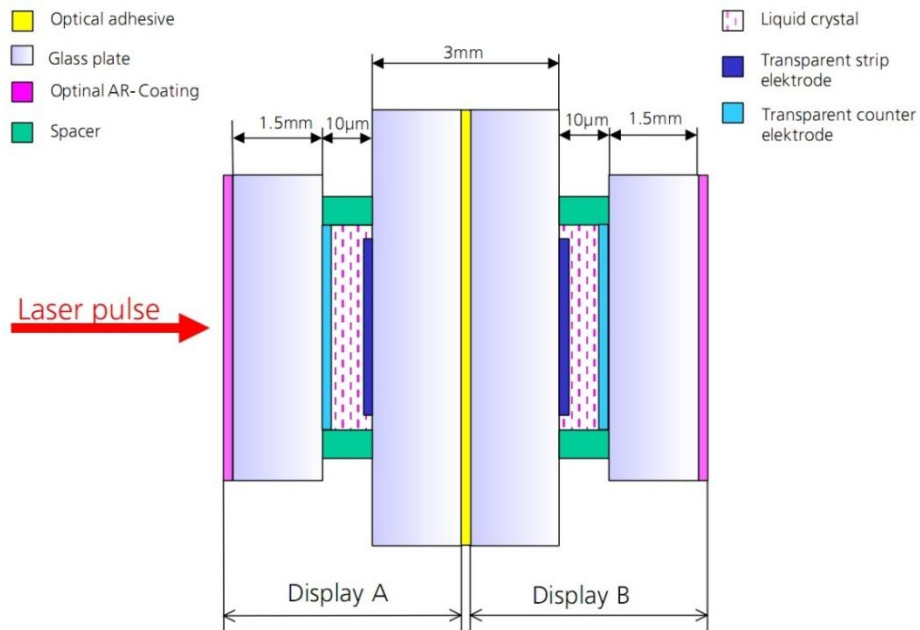


Figure 2.1 : Design of the LC modulator SLM-S640d

• The 4f setup

In 1983, Froehly and co-workers^[65] proposed a new design of versatile pulse shaper, the so-called zero dispersion line or 4f-line.

A 4f-line is a particular spectrometer composed of two diffraction gratings and two lenses arranged in a 4f set-up (**Figure 2.2b**). Each spectral component is angularly dispersed by the first grating and then focused to a small diffraction spots in the Fourier plane by the first lens (or mirror). Thus, in this plane, all the spectral components are spatially separated and focused. Then a second combination of lens (or curved mirror) and grating allows the recombination of all the frequencies into a single collimated beam. If nothing is placed in the Fourier plane then the device is dispersion free (zero dispersion line) and the output pulse shape is identical to the input one. By putting a specific mask in the Fourier plane (as in the case of the SLM), one can modify the optical path and/or optical density for each spectral component and thus shape the output pulse. For ultrashort pulses (broad spectral bandwidth), the lenses are often replaced by cylindrical or spherical mirrors to avoid unwanted dispersion and chromatic aberrations. Depending on the mask, a 4f pulse shaper controls the phase^[66], both phase and amplitude^[67], the polarization^[68] and also the transverse spatial profile^[69].

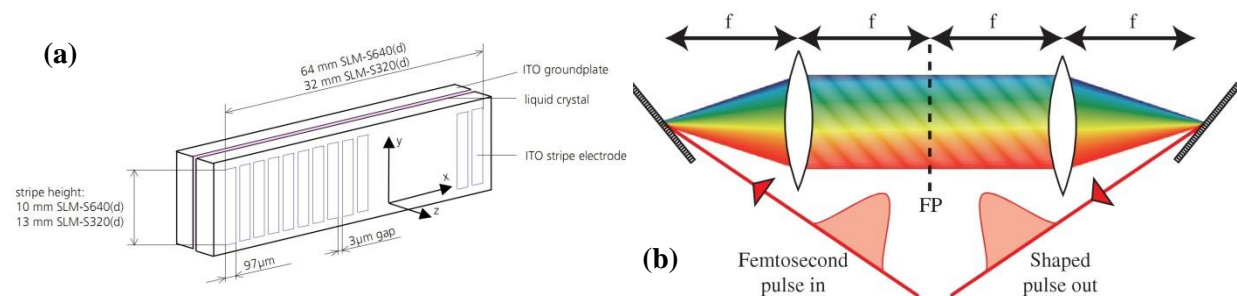


Figure 2.2: (a) Layout of the Indium Tin Oxide (ITO) strip-electrode of a single LC-cell. (b) A zero dispersion line composed of two gratings and two lenses of focal length f , arranged in a 4f set-up. The output pulse is identical to the input pulse. In the Fourier plane, all the spectral components are spatially separated and focused.

FOR MORE DETAILS AND REVIEWS CAN BE FOUND IN:

1. Documentation of Jenoptic SLM-S640d-320d
2. A. M. Weiner, Rev. Sci. Instrum. **71**, 1929-60, (2000)
3. A. Monmayrant, S. Weber, B. Chatel, J. Phys. B **43**, 103001 (2010)

2.4 Experimental setup

2.4.1 Silicon and ZnO processing setup

Single crystal n-type Si (1 0 0) wafers were used for microstructuring which took place in a vacuum chamber (**Figure 2.3 (a),(b)**) evacuated down to a residual pressure of $\sim 10^{-2}$ mbar by means of a rotary pump (Alcatel). The background pressure was measured using a pirani gauge. A micro valve system attached to the chamber enabled a precise backfilling of a halogen-containing ambient gas (SF_6). The pressure of the backfilling gas was measured with a baratron gauge (MKS Instruments).

The laser beam was focused with a quartz lens on the sample, mounted to a sample holder inside the vacuum processing chamber. The laser fluence was varied by using filters or attenuators. The laser beam entered the chamber through a quartz entrance window, while the irradiation process could be monitored through a Plexiglas window, which was laterally mounted on the vacuum chamber.

The processing chamber was placed on a computer driven high precision X-Y translation stage (Standa) with spatial resolution of 1 μm allowing sample displacement with regard to the laser beam up to 100 mm.

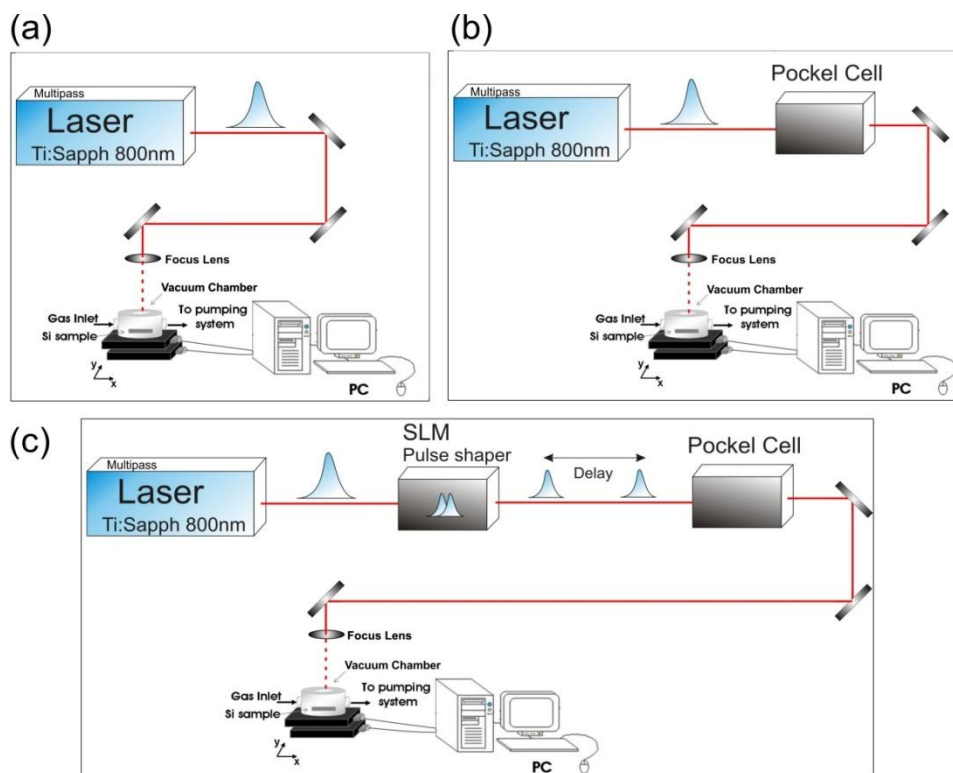


Figure 2.3: Experimental setups for the silicon processes. (a),(b) For creation of structured surfaces and spots, and (c) experimental arrangement for double pulse experiments.

Samples inside the chamber can be processed in two ways:

1. **Creation of micro-structured surfaces:** When large areas of microstructures are required we scan the beam (**Figure 3.2(a)**) across the sample by also controlling (via PC software) the amount of overlap between consecutive scans. A constant SF₆ pressure of 500 Torr was maintained during the process through a precision micro-valve system. Different laser fluences can be used by introducing filters in the laser beams path.
2. **Creation of single spots:** A pockel cell device (electro-optical shutter) (**Figure 3.2(b)**) which gives us the ability to control the number of pulses irradiated on a material, was introduced in the laser beams path. It is triggered by the laser beam and controlled by a computer. In this way single spots on the material can be created, with desirable number of pulses.

2.4.2 Double pulse experiments setup

Experiments (**Figure 2.3 (c)**) were performed with a the multipass femtosecond Ti:Sapph laser system (**section 2.2.2**). The pulse duration could be varied from 35fs to 430fs and measured by means of cross correlation techniques.^[70] A 4/F pulse shaper (**section 2.3**) configuration using a Spatial Light Modulator (SLM) was used in order to filter the Fourier spectrum of the laser pulses and create double pulse sequences of equal fluence with pulse separations varying from 0 to 14 ps. A pockels cell (electro-optical shutter) controlled the repetition rate and the number of the double pulse sequences that irradiated the silicon surface. The beam was subsequently focused with a 5cm lens normally onto the silicon substrate giving a spot diameter of 50μm² located inside a vacuum chamber evacuated down to a residual pressure of 10⁻² mBar.

2.4.3 Nananostructuring in liquids setup

The experimental setup for material processing inside liquids is illustrated in **figure 2.4**. The ablation was performed using the beam of the femtosecond Ti:sapphire laser emitting at 800nm, focused onto the target through a liquid layer. The target was placed into a Pyrex cell and covered by a liquid layer (usually water or ethanol) with typical thickness above the target being of the order of 2-3 mm. The cell was mounted on a computer-driven X-Y stage and translated during laser exposure. The free surface of liquid was exposed to air.

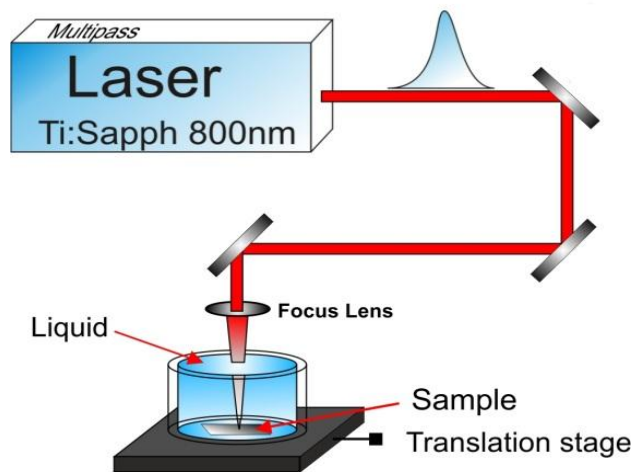


Figure 2.4: Experimental setup for the nanostructuring of materials in liquid environment.

2.5 Sample Preparation

2.5.1 Silicon samples treatment

The samples used were single crystal n-type Si(100) wafers with a resistivity of 2-8 Ohm from The samples were cleaned in an ultrasonic acetone bath prior to irradiation, followed by isopropanol and deionized water baths. Following the irradiation process, the samples were first cleaned in ultrasonic baths of trichloroethylene, acetone and methanol followed by a 10% HF aqueous treatment in order to remove the oxide grown on the surface.

2.5.2 Thermal Oxide growth and silanization process on Silicon.

- **Oxidation**

A method to alter the wettability of the surface making it super-hydrophobic is to grow an oxide layer onto the silicon samples. For this reason, the samples were placed in a box furnace and heated at 1000 °C for 30 min in air, resulting in a ~100nm thick oxide layer.

- **Silanization**

In the cases where silanization was required, the samples were placed in a flask containing 0.5 ml of dimethyldichlorosilane ((CH₃)₂SiCl₂, DMDCS) reagent. Hydrophobic DMDCS monolayers were subsequently deposited on the sample's surface through adsorption reactions. The vapor-phase reactions were carried out overnight at room temperature. The hydrophobized wafers were rinsed with toluene (two aliquots), ethanol (three aliquots), 1:1 ethanol/water (two aliquots), deionized water (two aliquots), ethanol (two aliquots), and deionized water (three aliquots) and were finally dried in a clean oven at 120 °C for 30 minutes.^[71]

2.5.3 ZnO films preparation

ZnO thick films with thickness up to 4 μm were deposited onto Corning glass (1737F) in an Alcatel D.C. magnetron system by a 99.999% pure metallic zinc target of 15 cm diameter. The base pressure of the ultra-high vacuum (UHV) chamber was below 5×10^{-7} mbar while during the deposition the pressure was 8×10^{-3} mbar and the substrate temperature at 27 °C (RT). All the films were done at constant plasma current settings of $I=0.45$ A. In order to achieve a high uniformity throughout the substrate area the distance between target and substrate was set to 20 cm. The thickness was measured using an Alphastep profilometer.

2.5.4 Thin ZnO films on Si, prepared by plasma laser deposition (PLD)

A thin ZnO film can be deposited on Silicon structured surfaces thorough PLD in a flowing oxygen environment. A KrF excimer laser (Lambda Physik, λ) 248 nm, τ) 34 ns pulse duration, 600 mJ/pulse maximum) was used for the ablation of a ZnO target, delivering 2500 pulses at a repetition rate of 10 Hz. The beam was incident on a rotating target at an angle of 45° with respect to the target normal and was focused with a spherical lens to yield an energy fluence of 1.5 J/cm² per pulse. The base pressure prior to deposition was more than 10^{-6} mbar, while the partial oxygen pressure during deposition was kept constant at 5×10^{-2} mbar. The Si substrate was placed parallel to the target at a distance of 4 cm and heated to 650 °C using a resistive heater. The samples were cooled to room temperature in the same oxidized environment used during deposition.

2.6 Sample characterization

2.6.1 Morphological characterization

The structured samples were characterized morphologically from top and side view by a Scanning Electron Microscopy (SEM) from JEOL. Image analysis software (Media cybernetics-Image Pro Plus) were utilized in order to get quantitative information concerning the structural characteristics formed i.e. height density, cone tip radius and distribution. For periodicity measurements a Fast Fourier Transform (FFT) (OriginLabs) has been implemented on the images to get distinct information.

In order to determine the depth and morphology of samples in more detail a high resolution atomic force microscopy (AFM) was utilized. Detailed information about the roughness is of the order of a few nm and can be obtained by an image processing algorithm.

The morphology of nanoparticles was characterized by Transmission Electron Microscopy (TEM) with a Philips CM20 equipment. High Resolution Field Emission Transmission Electron Microscopy (HRTEM) was performed with a Jeol JEM 2100F UHR at 200 kV equipped with a field emission electron source.

2.6.2 Optical measurements

Optical absorption of the samples can be measured with a spectrometer through reflectance and transmittance. In the case of samples with high roughness it is hard to obtain measurements due to the high scattering of the incident beam which enhances the diffusive component of the reflectance and transmittance. A common way to measure reflectance and transmittance from strongly scattering materials is to use an integrating sphere; a hollow sphere coated internally with a matte finish, diffusing type of material. In this way the light that enters the sphere can be scattered uniformly around its interior through multiple reflections, before it is detected. The measurements were performed using a UV/VIS/IR spectrophotometer equipped with an integrating sphere (PerkinElmer Lambda-950). An all-reflecting, double monochromator optical system was used, for the UV/Vis and NIR range. The two radiation sources, a deuterium lamp and a halogen lamp covered the working range of the spectrometer. The beam diameter on the sample surface was $\sim 0.3 \times 0.3 \text{ cm}^2$. The interior of the integrating sphere was constructed of Spectralon, a material which exhibits high diffuse reflectance across the 250-2500 nm wavelength range. The transmitted and reflected light was detected by a UV/Vis detector (R955 photomultiplier tube (PMT)) and a NIR lead sulphide (PbS) photocell detector mounted inside the integrating sphere.

2.7 Wetting properties

For the static and dynamic contact angle measurements an automated tensionmeter (Material Interface Associates Inc.) was used as shown in **Figure 2.5**. The liquid drop was gently deposited on the samples using a micro liter plunger-operated pipette (Transferpette-BRAND (1-10 μ l)). A software analysis algorithm determined the static contact angle of the liquids drop image captured by a CCD camera.

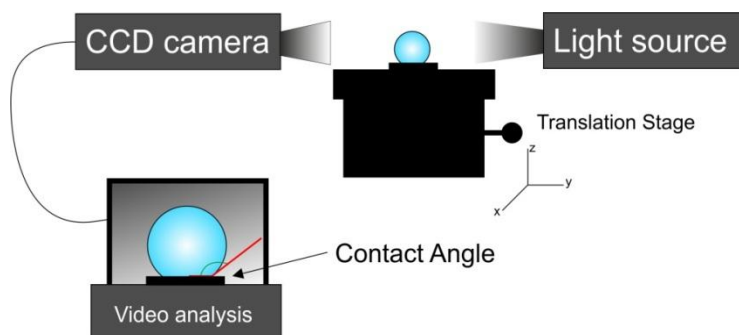


Figure 2.5: Experimental setup used for the determination of static and dynamic contact angle on structured surfaces.

A similar experimental setup was used for the determination of contact angle hysteresis and the sliding angle experiments. Inclination of the sample up to 30° could be achieved with the use of a rotational stage. A CCD camera (30 fps), vertically positioned recorded the profile of the drops either in digital images or videos, from which certain frames were captured. The contact angle formed in each case was determined through a best circle fit approximation (ImageJ). A best circle fit can be safely used to determine the contact angle formed at the liquid-solid interface in our case, since for small drop volumes, typically < 5 μ l, gravitational forces are negligible, and the drop is not significantly deformed.

For the water repellence experiments, where high temporal resolution was required, a Casio Exilim EX F1 high speed camera with a high magnification focus lens was used. In this way up to 1200 fps could be captured. For these experiments the drop was not deposited on the surface, but was left to perform free fall from different heights.

2.8 Electrowetting on Dielectric (EWOD) setup

The electrowetting setup used here is illustrated in **Figure 2.6**. The sample to be tested was placed on a XYZ translational stage, and a liquid droplet was then deposited on its surface. During the electrowetting experiments, a DC voltage was applied between a thin Au wire in contact with the droplet and a metallic contact at the back of the Si substrate. In order to avoid phenomena related to liquid

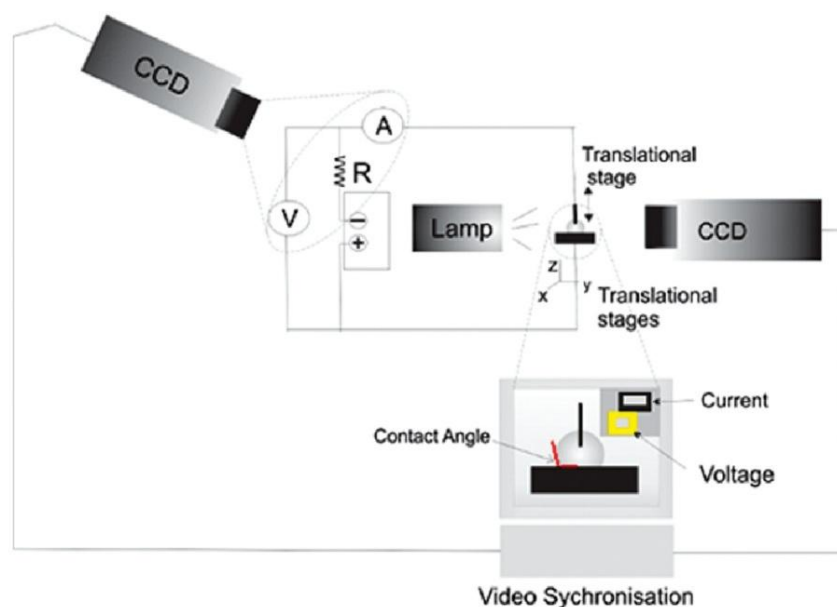


Figure 2.6: Experimental setup used for the electrowetting measurements

electrolysis, the leakage current through the dielectric was always recorded using a Keithley 485 picoameter. A computer controlled CCD camera with an optical lens system for magnification positioned vertically with regard to the system, allowed monitoring of the change in the contact angle with time. A second CCD camera recorded simultaneously the changes in the applied voltage and the current variations as a function of time. Video synchronization was used in order to perform the analysis and extract the information on the contact angle change as a function of applied voltage and current. In order to obtain the values of the contact angle, the best fit to the droplet profile was determined using image processing software with the values of the left and the right contact angles being independently evaluated.

2.9 Field emission measurements

Figure 2.7 illustrates the experimental setup used for the field emission experiments in **section 5.2-3**. The samples were tested under vacuum ($<10^{-5}$ Torr), as cold cathode field emitters in a, short-circuit protected, planar diode system. Each sample was used as the cathode and the emitted electrons were collected on a CuSn anode. The distance was always set at least three times the height of the highest observable spike of each sample to ensure that the emission field was not influenced by the anode

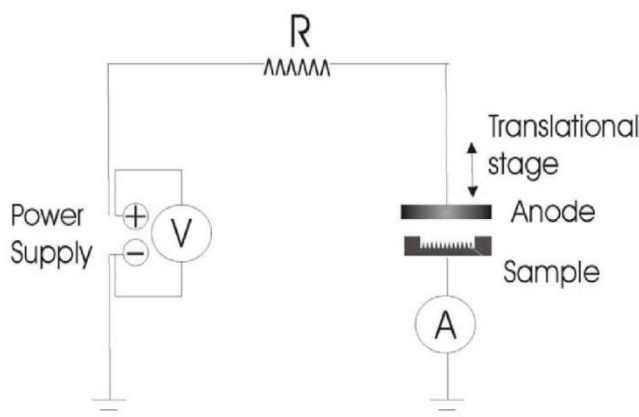


Figure 2.7: Experimental setup used for the field emission measurements on structured Silicon

location.^[72] The distance between the anode and the cathode was determined with a $10\mu\text{m}$ resolution, using a translational stage. A voltage was applied between the anode and the cathode ((SRS-PS350) power supply, 5000V max) to extract the electrons out of the microspikes. A current-limiting resistance of $R = 41\text{ M}\Omega$, was placed after the power supply, in order to protect the circuit and the sample from possible damage. The emitted current was recorded during the increase and decrease of the applied voltage using a Keithley 617 Electrometer.

2.10 Methodology for biology experiments

2.10.1 Introduction

Some applications demonstrated in **Section 5.9** are associated with cell culture on Silicon surfaces. For this reason the methodology used for cell culture, viability and imaging is presented in the next sections. Silicon surfaces used for cell cultured were fabricated as described in **section 2.3.1-1**.

2.10.2 NIH/3T3 (Fibroblast) cells

- **Cell culture methodology**

Prior to cell culture the structured surfaces were sterilized and then transferred onto sterile 6 well plates (Sarstedt; Numbrecht, Germany).

The NIH/3T3 cells were suspended to a concentration of 105 cells/mL in Dulbecco's modified Eagle's medium (DMEM) supplemented with 10% fetal bovine serum (FBS), and 1% antibiotic solution (GIBCO, Invitrogen, Kalsruhe, Germany) and 3 ml of cell suspension was added in the 6 well plate and cultured at 37 °C, for 72 h in an atmosphere of 5% CO₂. Before seeding the cells on the different surfaces, cells were grown to confluency, detached with 0.05% trypsin/EDTA (GIBCO, Invitrogen, Kalsruhe, Germany) and diluted in complete medium at an appropriate density. All experiments were done in triplicates to ensure reproducibility and obtain better statistics.

- **Cell viability assay**

In order to assess cell viability, the Live-Dead Cell Staining Kit (BioVision) was used. The kit utilizes Live-Dye, a cell-permeable green fluorescent dye ($E_x/E_m = 488/518$ nm), to stain live cells. Dead cells can be easily stained by propidium iodide (PI), a cell non-permeable red fluorescent dye ($E_x/E_m = 488/615$). At the end of the incubation time (72 h), structured surfaces with the cells were covered with the staining solution and incubated for 15 min at 37 °C. Cells were observed immediately under a fluorescence microscope. Stained live and dead cells can be visualized by fluorescence microscopy using a band-pass filter (detects FITC and rhodamine). Healthy cells stain only with the cell-permeable Live-Dye, fluorescing green. Dead cells can stain with both the cell-permeable Live-Dye and the cell non-permeable PI (red), the overlay of green and red appears to be yellow-red. The experiments were done in triplicates and for each surface the mean number of live cells was calculated.

- **Staining methodology for laser scanning confocal microscopy**

For the double staining of F-actin and Vinculin the focal adhesion staining kit (Chemicon International Inc., Temecula, CA, USA) was used. The cells were fixed with 4% paraformaldehyde for 15 min and permeabilized with 0.1% Triton X-100 (Merck KGaA, Darmstadt, Germany) in PBS for 3–5 min on ice. The non-specific binding sites were blocked with 1% BSA in PBS for 30 min. Actin and focal adhesion complexes were stained by incubating cells in diluted primary antibody (anti-vinculin) in blocking solution (1:200) for 1 h and subsequently labelling them with diluted secondary antibody (1:200) (mouse–anti-mouse FITC conjugate) (Sigma–Aldrich Chemie GmbH, Munich, Germany) for 45 min, with simultaneous incubation with diluted tetramethyl rhodamine isothiocyanate-conjugated phalloidin. The samples were then washed with PBS and stored in 10% glycerol in PBS in dark.

Confocal microscopy was performed using a ‘Zeiss Axios Kop 2 plus’ laser scanning confocal microscope.

2.10.3 Primary neuronal cells

- **Cell culture methodology**

Fetal brains were obtained from timed pregnant mice at embryonic day 14. After removing duraarachnoid membranes, whole brains were isolated and incubated in Hank's balanced salt solution medium (Biochrom, Germany). After a series of washings at low centrifugation speed, with the supernatant discarded, the pellets were resuspended in a small volume of Dulbecco's modified Eagle's medium (DMEM=F12:1=1) (Biochrom) medium. After vigorous trituration the cells were resuspended to a final volume, in DMEM=F12 supplemented with penicillin (100U=mL), streptomycin (100 mg=mL), and B-27 (Gibco)(DMEM=F12: B-27¼50:1). Finally, the neurons were plated on polyornithine-precoated dishes. The primary neuronal cultures were kept at 37°C, in a 5% CO₂ humidified incubator for 3 days and then were enzymatically (Trypsin–Gibco, 0.05% Trypsin–ethylene-diaminetetra-acetic acid) detached and plated on the substrates under study. The density with which cells were plated on the substrates was 2.5106 cells=well.

- **Immunofluorescence methodology for laser scanning confocal microscopy**

Cells grown on the substrates under study were fixed at 5 days in vitro in 4% paraformaldehyde in 0.1 M phosphate buffer for 5min and permeabilized in phosphate-buffered saline containing 0.1% Triton X-100 (PBST). The cells were blocked in PBST with 10% serum for 10min, and all subsequent reactions were carried out in PBST with 2% serum. A monoclonal anti-beta III tubulin primary antibody (Promega G712A; 1:1000), a rabbit polyclonal anti-GFAP (Abcam-AB7260;1:3000), Cy5-conjugated anti-mouse secondary antibody (1:500), and an AMCA-conjugated anti-rabbit secondary antibody (1:500) obtained from Jackson Immuno research Laboratory were used for the immunostaining. Beta III tubulin was used as a neuronal marker because its initial expression begins during or immediately after the completion of mitosis in neuroblasts.¹⁴

The digital images were acquired on Leica TCS SP5 confocal microscope using the LAS AF software. The 488 and 633 nm laser lines were used to view spikes (at reflection mode) and cell immunofluorescence, respectively.

Chapter 3

Fundamental processes upon Femtosecond laser micro/nano structuring of Si

3.1 Overview

In this chapter An investigation of ultrashort pulsed laser induced surface modification due to conditions that result in a superheated melted liquid layer and material evaporation are considered. To describe the surface modification occurring after cooling and resolidification of the melted layer and understand the underlying physical fundamental mechanisms, a unified model is presented to account for crater and subwavelength ripple formation based on a synergy of electron excitation and capillary waves solidification. The proposed theoretical framework aims to address the laser-material interaction in sub-ablation conditions and thus minimal mass removal in combination with a hydrodynamics-based scenario of the crater creation and ripple formation following surface irradiation with single and multiple pulses, respectively. The development of the periodic structures is attributed to the interference of the incident wave with a surface plasmon wave. Details of the surface morphology attained are elaborated as a function of the imposed conditions and results are tested against experimental data.

It is important to stress out that part of this work is done in collaboration with Dr. G. Tsididis who carried out the simulation part presented in this Chapter.

3.2 Laser modification of silicon: The effect of single pulses

3.2.1 Introduction

Silicon surface processing with ultra-short pulsed lasers has received considerable attention over the past decades due to its important technological applications, in particular in industry and medicine.^[73,74,75,76,77,78,79,80,81,82,83] Rapid energy delivery and reduction of the heat-affected areas are the most pronounced advantages of the technique compared to effects induced by longer pulses,^[84] which reflect the merit of the method as a potential tool for fabrication at micro- and nano-scales.^[85] These abundant applications require thorough knowledge of the laser interaction with the irradiated material for enhanced controllability of the resulting modification of the target relief.

Femtosecond pulsed laser interaction with matter triggers a variety of timescale-dependent processes, influenced by the fluence and pulse duration;^[86] different combinations of those parameters are capable to induce phase transition or material removal. A solid material subjected to ultrashort pulsed laser heating at sufficiently high fluences undergoes a phase transition to a superheated liquid whose temperature reaches $0.90T_{cr}$ (T_{cr} being the thermodynamic critical temperature).^[87] A subsequent bubble nucleation leads to a rapid transition of the superheated liquid to a mixture of vapour and liquid droplets that are ejected from the bulk material (phase explosion). This has been proposed as a material removal mechanism.^[88,89] By contrast, the interpretation of a possible surface modification due to evaporation has been related to the presence of a Knudsen layer adjacent to the liquid-vapor interface and the process has been analysed in numerous works.^[90,91,92] The proposed scenario of modelling material removal is based on a combination of evaporation of material volumes that exceed upon irradiation lattice temperatures close to $0.90T_{cr}$ and evaporation due to dynamics of Knudsen layer, which is a scenario that is yet to be elaborated. Hence, the applied conditions are proposed to be sufficient enough to lead to minimal mass removal while the rest of the material is treated as an incompressible Newtonian fluid. It has to be emphasised that throughout this manuscript the term ‘mass removal’ is associated with ‘mass loss’ rather than ‘displaced mass’ or ‘mass ejection’.

A very significant aspect that will be investigated is the development of rippled structures (see also **section 1.4**) on the semiconductor surface after exposure to repetitive laser pulses. Previous theoretical approaches or experimental observations related to the formation mechanism of these periodic structures were performed in submelting^[93] or ablation conditions.^[94,95,96,97,98,99,100] The proposed theoretical framework will elaborate both optical (the interference of the incident and plasmon waves) and

hydrodynamical (capillarity-driven ripple formation) effects. To the best of our knowledge, there is no theoretical interpretation of surface patterning in an intermediate regime, in conditions that lead to a superheated liquid, describe surface modification due to mass redistribution and present surface morphological changes that originate from a phase transition process (resolidification). Although there exists a number of models that investigate short pulsed laser welding processes of metals,^[101,102,103] our approach aims to provide a detailed description of the underlying mechanisms of semiconductor surface patterning after irradiation with ultrashort pulses and link ripple formation with development of surface plasmon waves.

The purpose of this article is to introduce a unifying theoretical framework that is capable to describe ultrafast laser induced surface modification and ripple formation by considering that hydrodynamic, and not the so far believed mass removal, effects constitute the main agent that govern the initial morphological changes. Compared to previous established approaches,^[104,105,106,107] the proposed theory aims to provide an extension based on the spatial dependence (i.e. radial) of the intensity distribution that induces bending of the isothermal lines. The proposed model comprises: i) a heat transfer component that accounts for the particle dynamics and heat conduction phenomena, and (ii) a hydrodynamics component which describes the molten material dynamics and the resolidification process. The laser fluences modelled and experimentally tested were chosen and restricted to lie within the onset of material evaporation, avoiding conditions of mass removal due to ablation. This enabled us to shed light on the key mechanisms governing the embryonic stages of material modification.

3.2.2 Theoretical and experimental details.

I. Laser matter interaction process – implementation of the two temperature model

Ultrashort-pulsed lasers first excite the charge carriers (electron-hole pairs) in semiconductors while their energy is subsequently transferred to the lattice. The relaxation time approximation to Boltzmann's transport equation^[108] is employed to determine the number density, carrier energy and lattice energy. The model assumes an equal number of electron and holes in the solid and no electron photoemission is considered after the laser irradiation.^[109] The evolution of the number density N , carrier temperature T_c and lattice temperature T_l are derived using the carrier, carrier energy and lattice heat balance equations. Based on this and on the discussion made with more details in **section 1.3** the following set of equations determine the temperature and particle dynamics^[110,111,112,113]

$$\text{Carrier} \quad C_c \frac{\partial T_c}{\partial t} = \vec{\nabla} \cdot \left((k_e + k_h) \vec{\nabla} T_c \right) - \frac{C_c}{\tau_e} (T_c - T_l) + S(\vec{r}, t) \quad (\text{eq. 3.1})$$

$$\text{Lattice} \quad C_l \frac{\partial T_l}{\partial t} = \vec{\nabla} \cdot \left(K_l \vec{\nabla} T_l \right) + \frac{C_c}{\tau_e} (T_c - T_l) \quad (\text{eq. 3.2})$$

$$\text{Number Density} \quad \frac{\partial N}{\partial t} = \frac{\alpha}{h\nu} \Omega I(\vec{r}, t) + \frac{\beta}{2h\nu} \Omega^2 I^2(\vec{r}, t) - \gamma N^3 + \theta N - \vec{\nabla} \cdot \vec{J} \quad (\text{eq. 3.3})$$

$$\Omega = \frac{1 - R(T_l)}{\cos \varphi} \quad (\text{eq. 3.4})$$

where \mathbf{S} is:

$$S(\vec{r}, t) = (\alpha + \Theta N) \Omega I(\vec{r}, t) + \beta \Omega^2 I^2(\vec{r}, t) - \frac{\partial N}{\partial t} \left(E_g + k_B T_c \right) - N \frac{\partial E_g}{\partial T_l} \frac{\partial T_l}{\partial t} - \vec{\nabla} \cdot \left((E_g + 4k_B T_c) \vec{J} \right) \quad (\text{eq. 3.5})$$

And

$$\frac{\partial I(\vec{r}, t)}{\partial z} = -(\alpha + \Theta N) I(\vec{r}, t) - \beta I^2(\vec{r}, t) \quad (\text{eq. 3.6})$$

$$I(r, z=0, t) = \frac{2\sqrt{\ln 2}}{\sqrt{\pi}\tau_p} E_p e^{-\left(\frac{r^2}{R_0^2}\right)} e^{-4\ln 2 \left(\frac{t-t_0}{\tau_p}\right)^2} \quad (\text{eq. 3.7})$$

where E_p is the fluence of the laser beam and τ_p is the pulse duration (i.e. full width at half maximum), R_0 is the irradiation spot-radius (distance from the centre at which the intensity drops to $1/e^2$ of the maximum intensity).

In the present work, we assume conditions that lead to temperatures greater than $\sim 0.90T_{cr}$ (for silicon, $T_{cr}=5159^0\text{K}$ ^[114]) for a small part of the material. While this portion is evaporated, a superheated liquid still remains in the system which undergoes a slow cooling. Furthermore, to introduce the phase transition that causes the bulk temperature to exceed the silicon melting temperature T_m ($\sim 1687^0\text{K}$), the second equation in **Eq.3.3** has to be modified properly to include the phase change in the solid-liquid interface

$$\left(C_l + L_m \delta_{\pm}(T_l - T_m)\right) \frac{\partial T_l}{\partial t} = \vec{\nabla} \cdot (K_l \vec{\nabla} T_l) + \frac{C_c}{\tau_e} (T_c - T_l) \quad (\text{eq. 3.8})$$

where L_m is the latent heat of fusion. A suitable representation of the δ -function should accomplish (for numerical calculations) a smooth transition between solid and liquid phases, ^[115] therefore the following expression is used

$$\delta_{\pm}(T_l - T_m) = \frac{\pm 1}{\sqrt{2\pi}\Delta} e^{-\left[\frac{(T_l - T_m)^2}{2\Delta^2}\right]} \quad (\text{eq. 3.9})$$

where Δ is in the range of $10\text{-}100^0\text{K}$ depending on the temperature gradient. The sign of the δ -function depends on whether melting or solidification takes place. Unlike the solid phase of the irradiated material, liquid silicon behaves as a metal and thereby, for temperatures above T_m , **Eqs. 3.1-3.2** need to be replaced by the following two equations that describe electron-lattice heat transfer

$$C_e \frac{\partial T_e}{\partial t} = \vec{\nabla} \cdot (K_e \vec{\nabla} T_e) - \frac{C_e}{\tau_E} (T_c - T_L) \quad (\text{eq. 3.10})$$

$$C_L \frac{\partial T_L}{\partial t} = \vec{\nabla} \cdot (K_L \vec{\nabla} T_L) + \frac{C_e}{\tau_E} (T_c - T_L) \quad (\text{eq. 3.11})$$

where C_e and C_L are the heat capacity of electrons and lattice (liquid phase), K_e and K_L are the thermal conductivity of the electrons and lattice, respectively, while τ_E is the energy relaxation time for the liquid phase. Since $K_L \ll K_e$ in metals, the first term of the second part of the second equation is usually ignored. In Eqs. 3.10-3.11, no source term is included because it is assumed that laser energy deposition has been completed before the onset of the material melting.

II. Liquid phase – implementation of the hydrodynamic equations (see also section 1.6)

Following heat transfer from electrons to the lattice, a spatio-temporal variance of temperature distribution takes place on the molten material and variation of the surface tension and gravitational force result in the development of flow and capillary waves.^[116] The governing equations for the incompressible Newtonian fluid flow (see also **section 1.6.1**) and heat transfer in the molten material are defined by the following equations:

(i). for the mass conservation (incompressible fluid):

$$\vec{\nabla} \cdot \vec{u} = 0 \quad (\text{eq. 3.12})$$

(ii). for the energy conservation

$$C_L \left(\frac{\partial T_L}{\partial t} + \vec{\nabla} \cdot (\vec{u} T_L) \right) = \vec{\nabla} \cdot (K_L \vec{\nabla} T_L) \quad (\text{eq.3.13})$$

where K_L is the thermal conductivity of the lattice. The presence of a liquid phase and liquid movement requires a modification of the second of **Eq.3.13** to incorporate heat convection. Furthermore, an additional term is presented in the equation to describe a smooth transition from the liquid-to-solid phase (i.e. it will help in the investigation of the resolidification process)

$$C_L \left[\frac{\partial T_L}{\partial t} + \vec{\nabla} \cdot (\vec{u} T_L) \right] - L_m \delta(T_L - T_m) \frac{\partial T_L}{\partial t} = \vec{\nabla} \cdot (K_L \vec{\nabla} T_L) \quad (\text{eq. 3.14})$$

(iii). for the momentum conservation:

$$\rho_L \left(\frac{\partial \vec{u}}{\partial t} + \vec{u} \cdot \vec{\nabla} \vec{u} \right) = \vec{\nabla} \cdot \left(-P \mathbf{1} + \mu (\vec{\nabla} \vec{u}) + \mu (\vec{\nabla} \vec{u})^T \right) \quad (\text{eq. 3.15})$$

where \vec{u} is the velocity of the fluid, μ is the liquid viscosity, P pressure. C_L and K_L stand for the heat capacity and thermal conductivity of the liquid phase, respectively. It is evident that the transition between a purely solid to a completely liquid phase requires the presence of an intermediate zone that contains material in both phases. In that case, **Eq.3.15** should be modified accordingly to account for a

liquid-solid two phase region (i.e. mushy zone) where the total velocity in a position should be expressed as a combination of the fraction of the mixtures in the two phases.^[117] Nevertheless, to avoid complexity of the solution of the problem and given the small width of the two phase region with respect to the size of the affected zone a different approach will be pursued where a mushy zone is neglected and transition from solid-to-liquid is indicated by a smoothened step function of the thermophysical quantities. Furthermore, as it will be explained in the Simulation section, the flow will be assumed to occur for two liquids of significantly different viscosity.

While a complete description would also require the inclusion of buoyancy forces,^[118,119,120] its contribution is expected to be minimal and therefore the relevant term will be eliminated. Vapour ejected creates a back (recoil) pressure on the liquid free surface which in turn pushes the melt away in the radial direction. The recoil pressure and the surface temperature are usually related according to the equation^[121,122]

$$P_r = 0.54P_0 \exp\left(L_v \frac{T_L^s - T_b}{RT_L^s T_b}\right) \quad (\text{eq. 3.16})$$

where P_0 is the atmospheric pressure (i.e. equal to 10^5 Pa), L_v is the latent heat of evaporation of the liquid, R is the universal gas constant, and T_L^s corresponds to the surface temperature. Given the radial dependence of the laser beam, temperature decreases as the distance from the centre of the beam increases; at the same time, the surface tension in pure molten silicon decreases with growing melt temperature (i.e. $d\sigma/dT < 0$), which causes an additional depression of the surface of the liquid closer to the maximum value of the beam while it rises elsewhere. Hence, spatial surface tension variation induces stresses on the free surface and therefore a capillary fluid convection is produced. Moreover, a precise estimate of the molten material behaviour requires a contribution from the surface tension related pressure, P_σ , which is influenced by the surface curvature and is expressed as $P_\sigma = K\sigma$, where K is the free surface curvature. The role of the pressure related to surface tension is to drive the displaced molten material towards the centre of the melt and restore the morphology to the original flat surface. Thus, pressure equilibrium on the material surface implies that the pressure in **Eq.3.15** should outweigh the accumulative effect of $P_r + P_\sigma$.

As the material undergoes a solid-to-liquid-to-solid phase transition, it is important to explore the dynamics of the distribution of the depth of the molten material and the subsequent surface profile change when solidification terminates. The generated ripple height is calculated from the Saint-Venant's shallow water equation^[123]

$$\frac{\partial H(\vec{r}, t)}{\partial t} + \vec{\nabla} \cdot (H(\vec{r}, t) \vec{u}) = 0 \quad (\text{eq. 3.17})$$

where $H(\vec{r}, t)$ stands for the melt thickness. Hence, a spatio-temporal distribution of the melt thickness is attainable through the simultaneous solution of **Eqs. 3.11-3.17**).

III. Interference of an incident with a surface plasmon wave

Due to an inhomogeneous deposition of the laser energy on the semiconductor as a result of the exposure to a Gaussian-shape beam, the surface of material is not expected to be perfectly smooth after resolidification; further irradiation of the non-planar profile will give rise to a surface scattered wave.^[124] According to theoretical predictions and experimental studies, the interference of the incident and the surface wave results in the development of periodic ‘ripples’ with orientation perpendicular (*p*-polarisation) to the electric field of the laser beam.^[125,126,127] A revised process that leads to the formation of the surface wave has been also proposed that involves surface plasmons^[128,129] where the ripple periodicity is provided by the expression $\lambda/(\lambda/\lambda_s \pm \sin\phi)$. Surface plasmons are excited on metals due to abundant free electrons and they explain rippled development upon intense laser excitation of a variety of semiconductor, metal and dielectric materials. Further information about ripples and surface plasmons can be found in section 1.5. The involvement of plasmon wave related mechanism in the generation of ripples will be employed in this work as the metallic behaviour of silicon at large temperatures allows excitation of surface plasmon waves. The plasmon wavelength, λ_s , is related to the wavelength of the incident beam through the relations^[130]

$$\lambda_s = \lambda \left(\frac{\epsilon' + \epsilon_d}{\epsilon' \epsilon_d} \right)^{1/2} \quad (\text{eq. 3.17})$$

$$\epsilon' = \text{Re} \left(1 + (\epsilon_g - 1) \left(1 - \frac{N}{n_0} \right) - \frac{N}{N_{cr}} \left(\frac{1}{1 + i \frac{1}{\omega \tau_e}} \right) \right) \quad (\text{eq. 3.18})$$

where ϵ_d ($\epsilon_d=1$) is the dielectric constant of air, ϵ_g stands for the dielectric constant of unexcited material ($\epsilon_g=13.46+i0.048$), ω is the frequency of the incident beam, n_0 is the valence band density ($n_0=5 \times 10^{22} \text{ cm}^{-3}$), $N_{cr}=m_e \epsilon_0 \omega^2 / e^2$.

Although the equations presented in the previous section are still valid, some modification has to be performed to the form of the laser intensity beam due to the interference of the incident and the surface plasmon wave. The average intensity of the superposition of the two waves on the surface of the material

is derived by computing the Poynting vector and integrating it over the laser period (λ/c). Then, the final intensity on the surface is provided by the following expression

$$I_{surf}(\vec{r}, t) = \left\langle \left| \vec{E}_i + n_{mat} \vec{E}_s \right|^2 \right\rangle e^{-\left(\frac{r^2}{R_0^2}\right)} e^{-4 \ln 2 \left(\frac{t-t_0}{\tau_p}\right)^2} \quad (\text{eq. 3.19})$$

where n_{mat} is the refractive index of silicon, $\vec{E}_i = \vec{E}_{i,o}(\vec{r}) \exp(-i\omega_i t + \vec{k}_i \bullet \vec{r})$ and $\vec{E}_s = \vec{E}_{s,o}(\vec{r}) \exp(-i\omega_s t + \vec{k}_s \bullet \vec{r})$ and ω_i ω_s are the frequencies of the incident beam (equal to ω) and the surface plasmon wave, respectively. The magnitude of the electric field of the incident wave can be calculated by the expression

$$\frac{E_d}{\tau_p} = \frac{c\epsilon_0 \sqrt{\pi} \left\langle \left| \vec{E}_i \right|^2 \right\rangle}{2\sqrt{\ln 2}} \quad (\text{eq. 3.20})$$

while the magnitude of the electric field of the longitudinal surface plasmon wave ⁴² is taken to be of the order of the electric field of the incident wave. The computation of the time averaged quantity in the final intensity on the surface (**Eq. 3.19**), yields a contribution proportional to $\cos\left(\sqrt{\vec{k}_i^2 + \vec{k}_s^2 - 2\vec{k}_i \bullet \vec{k}_s} (\sin \varphi) x\right) \vec{E}_{i,o} \bullet \vec{E}_{s,o}$ (x -axis is along the direction of the electric field of the incident beam, see Simulation Section), where \vec{k}_i and \vec{k}_s are the wavevectors of the incident and surface plasmon waves, respectively. The above expression indicates that the polarisation of the incident beam is crucial for the determination of the form of the total intensity distribution. Due to the curvature of the initially modified surface after irradiation with one laser pulse, the direction of the surface plasmon waves is geographically correlated. Nevertheless, the energy deposition will be highest in the direction of the laser electrical field and lowest in the perpendicular direction because the electric field of the surface plasmon wave has a larger component along the polarisation of the incident beam. Hence, the energy deposition is strongly correlated to the polarisation of the laser beam and it yields a highest component along the incident electric field polarisation. As a result, for an incident beam with polarisation on the xz -plane (**Figure 3.9(a)**), the periodic function produces an optical interference pattern which propagates in parallel to the polarisation vector and it is followed by a spatially and periodically modulated energy deposition. The proposed model suggests that spatial energy deposition will lead to temperature gradients which accounts for the capillarity-driven ripple formation when material is melted and then resolidified.

3.2.3 Simulation and experimental details

I. Simulations

It is important to stress out that all simulation were performed by Dr. G. Tsibidis and here we provide some further information about the simulation characteristics.

The proposed model aims to determine the time-dependent surface profile by solving both momentum and energy equations introduced in the previous paragraphs. It takes into account: (i). a solid-to-liquid phase transition with an energy transfer to the lattice equal to the latent heat (**Eqs.3.3, 3.10, 3.11**), (ii). the Marangoni effect which describes liquid flow due to temperature gradients,^[131] (iii). the contribution of recoil pressure and pressure due to surface tension, and (iv) a resolidification process that is quantifiable by computing the liquid-solid interface velocity. Due to a small vertical anticipated surface modification with respect to the size of the laser beam, a finite difference method to solve the **Eqs.(3.3-3.20)** will suffice to produce accurate results. The coordinate system used in the analysis is defined as follows: the z -axis is normal to the material surface, the x -axis is on the surface with a direction based on that the electric field of the incident beam must reside on the xz -plane, and the y -axis, again on the material surface (**Figure 9(a)**). Due to the axial symmetry (for single pulse irradiation), cylindrical coordinates (r and z) can be employed to obtain the carrier and lattice temperatures and the surface modification details. As a result, we can perform a simulation on a rectangular subregion of thickness $W=5\mu\text{m}$ and length $L=30\mu\text{m}$ is selected. The simulation runs for timepoints in the range from $t=0$ to 15ns in time intervals that vary from 10fs to 50fs to integrate nonequilibrium time history while a substantially larger time step (i.e. 5ps) is followed for post equilibrium evolution. Carriers and lattice temperatures are set to $T=T_0=300^0\text{K}$ (room temperature) at $t=0$ while the initial concentration of the carrier is set to $N=1\mu\text{m}^{-3}$.^[132]

The hydrodynamic equations will be solved in the aforementioned subregion that contains either solid or molten material. To include the ‘hydrodynamic’ effect of the solid domain, material in the solid phase is modelled as an extremely viscous liquid ($\mu_{\text{solid}}=10^5 \mu_{\text{liquid}}$), which will result into velocity fields that are infinitesimally small. An apparent viscosity is then defined with a smooth switch function similar to **Eq.3.9** to emulate the step of viscosity at the melting temperature. A similar step function is also introduced to allow a smooth transition for the rest of temperature dependent quantities (i.e. heat conductivity, heat capacity, density, etc) between the solid and liquid phases. For time-dependent flows, a

common technique to solve the Navier-Stokes equations is the projection method and the velocity and pressure fields are calculated on a staggered grid (**Figure 3.1(a)**) using fully implicit formulations.^[133,134] The inset in **Figure 3.1(a)** illustrates the different locations at which the velocity (v, u) and pressure P fields are calculated at a timepoint $t=t'$. More specifically, the horizontal and vertical velocities are defined in the centres of the horizontal and vertical cells faces, respectively where the pressure and temperature fields are defined in the cell centres. Similarly, all temperature dependent quantities (i.e. viscosity, heat capacity, density, etc) are defined in the cell centres. An explicit solution method is employed to solve **Eq. 3.20** and compute temperature values at subsequent time points. The size of the horizontal side of the computation grid is 0.1nm while the vertical side is taken to be equal to 0.01nm.

During the ultrashort period of laser heating, heat loss from the upper surface of target is assumed to be negligible. As a result, the heat flux boundary conditions for carriers and lattice are zero throughout the simulation while a zero flux at $r=0$ must be also imposed. Furthermore, it is assumed that only the top surface is subjected to the Gaussian-shape laser beam of an irradiation spot-radius $R_0=15\mu\text{m}$. Regarding the momentum conditions at the boundaries, we impose the following constraints:

1. $u_r=0$, on the symmetry axis $r=0$,
2. $\vec{u} = 0$, on the solid-liquid interface (non-slipping conditions),
3. $\mu \frac{\partial u_r}{\partial z} = \frac{\partial \sigma}{\partial T_s} \frac{\partial T_s}{\partial r}$, on the upper flat free surface (T_s is the surface temperature),^[135] and $\mu \frac{\partial u_\tau}{\partial n} = \frac{\partial \sigma}{\partial T_s} \frac{\partial T_s}{\partial \tau}$,
on the rest curved free surface,^[136] where τ and n are the surface tangent direction and normal component, respectively.

The aforementioned boundary conditions are valid when the first incident pulse irradiates the initial planar surface. The first boundary condition excludes transverse component of the velocity on the symmetry axis ($r=0$). The last expression describes the shear stress which is due to the surface tension gradient and it is exerted on the free surface and it is important to incorporate the effect of Marangoni flow. The temperature-dependent parameters that are used in the numerical solution of the governing equations are listed in **Table I**. In order to increase accuracy, the model geometry is divided into two regions: a subdomain in which solid phase dominates and velocity fields are minimal and another subdomain where both momentum and energy equations are solved with an increased tolerance level.

For irradiation with subsequent pulses, we note that the incident beam is not always perpendicular to the modified profile, therefore the surface geometry influences the spatial distribution of the deposited laser energy. Hence, the laser irradiation reflected from the profile slopes can lead to light entrapment

among the formed structures where the laser fluence is modified. Typical Fresnel equations are used to describe the reflection and transmission of the incident light. Due to multiple reflection, absorption of the laser beam is modified^[137] and thereby a ray tracing method is employed to compute the absorbed power density while a similar methodology is ensued to estimate the proportion of the refraction by applying Snell's law. With respect to the numerical scheme used to simulate dynamics of velocity and pressure fields and all thermophysical quantities in **Eqs .(3.1-3.17)**, a similar procedure is ensued in the event of subsequent pulses, however in this case the interaction with the modified surface profile induced by the first pulse due to the hydrodynamic motion of the molten material and its subsequent resolidification, should be taken into account. While second order finite difference schemes appear to be accurate for $NP=1$ where the surface profile has not been modified substantially, finer meshes and higher order methodologies are performed for more complex and profiles.^[138,139] The calculation of the pressure associated to the surface tension requires the computation of the temporal evolution of the principal radii of surface curvature R_1 and R_2 that correspond to the convex and concave contribution, respectively.^[140] Hence the total curvature is computed from the expression $K=(1/ R_1 +1/ R_2)$. A positive radius of the melt surface curvature corresponds to the scenario where the centre of the curvature is on the side of the melt relative to the melt surface.

Regarding the material removal simulation, in each time step, lattice and carrier temperatures are computed and if lattice temperature reaches $\sim 0.90T_{cr}$, mass removal through evaporation is assumed. In that case, the associated nodes on the mesh are eliminated and new boundary conditions of the aforementioned form on the new surface are enforced. In order to preserve the smoothness of the surface that has been removed and allow an accurate and non-fluctuating value of the computed curvature and surface tension pressure, a fitting methodology is pursued. **Figure 3.1(b)** illustrates simulating data and the resulting curve after data fitting to produce a smoothed curve. To facilitate assessment of data fitting accuracy, the resulting smoothing is sketched in an enlarged rectangular region of **Figure 3.1(b)** (**Figure 3.1(c)**).

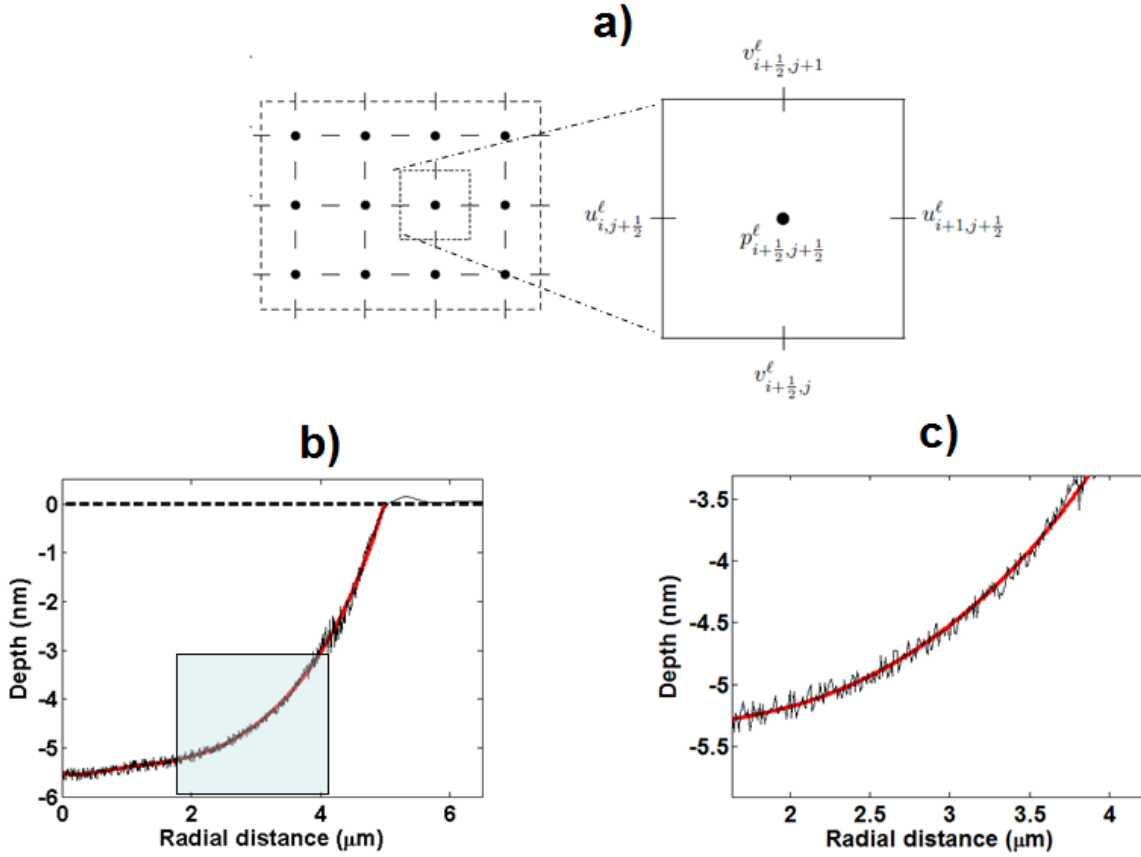


Figure 3.1 (Color online): (a) Staggered grid: pressure-nodes are shown as black dots, while u -component and v -component of the velocity are computed at the centre of the horizontal and vertical solid lines, respectively, (b) Smoothing of simulating data after a single illumination, (c) An inset of the enlarged area (rectangular region in (b)).

II. Experimental details

Experiments were performed with a femtosecond Ti:Sapphire laser system operating at a wavelength of 800 nm and repetition rate of 1 kHz as described in **section 2.2.2**. The pulse duration was set to 430 fs and measured by means of cross correlation techniques. A pockels cell controlled the repetition rate and the number of the pulses that irradiated the silicon surface (**section 2.4.1(2)**). The beam was perpendicular to the silicon substrate giving a spot diameter of 50 μm (beam waist of 30 μm) located inside a vacuum chamber evacuated down to a residual pressure of 10^{-2} mBar. The laser fluence calculated from the beam waist ($1/e^2$) was 0.37 J/cm², chosen to assure a minimal mass removal for a SP

irradiation. This is performed by means of atomic force (AFM) and Field emission scanning electron microscopy (FESEM images of the profiles of the various modification spots obtained.).

3.2.4 Formation of ripples: Simulation and experimental results

The theoretical model is firstly examined to derive the time evolution of carrier (electron-hole for semiconductors and electrons for metals) and lattice temperatures for one laser shot ($NP=1$) of fluence $E_p=0.37\text{J/cm}^2$ and pulse duration $\tau_p=430\text{fs}$. The fluence value used in the simulation is appropriate for investigation of thermophysical effects when minimal mass loss removal is assumed and the selection was based on the requirement of exploration of morphological changes in sub-ablation conditions. **Figure 3.2(a)** depicts the evolution of the temperatures that occur at $r=0$, $z=8.2\text{nm}$, which corresponds to lattice points that have reached temperatures higher than $0.90T_{cr}$. **Figure 3.2(b)** illustrates the lattice temperature spatial distribution at $t=5\text{ps}$, which indicates that the material is divided in three regions: the first region

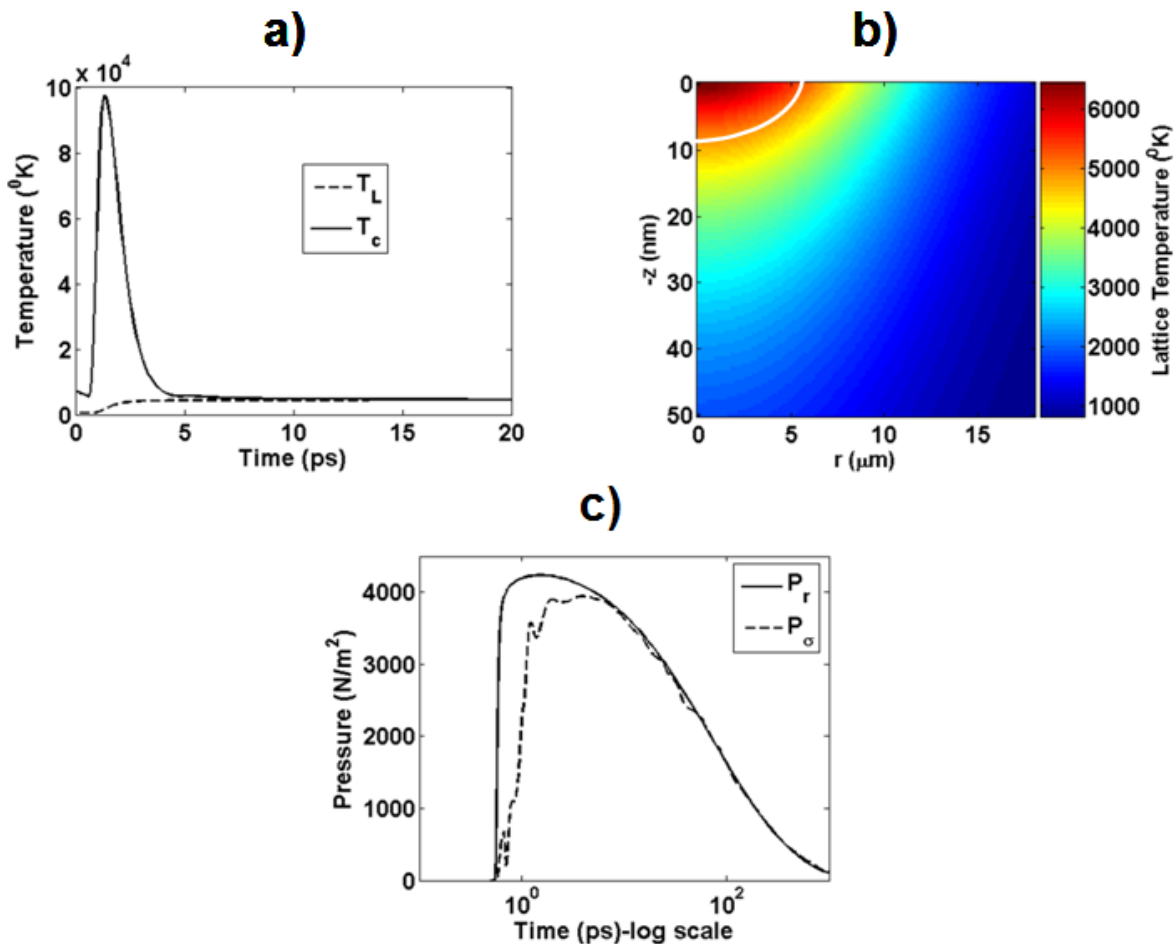


Figure 3.2 (Color online): **(a)** Time evolution of carrier and lattice temperatures at $r=0$ and $z=8.2\text{nm}$, **(b)** Spatial distribution of lattice temperatures at $t=5\text{ps}$ (white line represents boundary of evaporated region), **(c)** temporal evolution of recoil (P_r) and surface tension (P_σ) pressures.

(inside the region defined by the boundary in *white*) corresponds to material that has been evaporated due to the fact that it reaches temperatures above that of $0.90T_{cr}$; the second one refers to a superheated liquid with temperatures in the range $[T_m, 0.90T_{cr}]$; the third region corresponds to material in solid phase with temperatures less than T_m . The choice of $t=5\text{ps}$ was based on the fact that it corresponds to the maximum calculated material removal (as the attained temperature reaches a maximum value) for the aforementioned laser beam characteristics and the radial size of the approximate removed portion is equal to $6.5\mu\text{m}$. According to **Figure 3.2(b)**, the theoretically calculated depth of the evaporated material is approximately equal to 8.2nm .

To estimate surface modification due to the cooling mechanism of the superheated liquid, a detailed investigation of the liquid-to-solid phase transition is required. It is noted that other works focused on the consideration that the onset of melting involves homogeneous or heterogeneous nucleation of the molten phase at lattice defects.^[141,142] According to these works, atomistic simulations predict an increased melting front speed dependent on the degree of overheating which potentially has an impact on the simulation results. It is evident that the incorporation of a model with molecular dynamics simulations and lattice instabilities potentially results in a complementary description of the general case of material especially in cases where material has structural instabilities. Nevertheless, the aim of the present investigation is aimed to characterize a simpler scenario in which melting is basically associated with a homogeneous nucleation once melting temperature has been reached and compare theoretical results to experimental observations.

Melting of material entails elaboration of the solidification process and therefore hydrodynamics effects influenced by recoil pressure, surface tension pressure and surface tension gradient have been investigated. To examine the interplay of the various types of pressure and their resulting effect on the surface modification, the evolution of the melt recoil pressure and surface tension pressure and their relation are assessed. To determine which is the dominant mechanism of surface modification and the hill formation process, the contribution of each term is required to be estimated and it known that the speed of the melt flow is related to the recoil pressure through the expression $P_r = 1/2\rho_m(u_m)^2$ (i.e. the subscript m characterizes the molten material).^[143] Furthermore, the exponential dependence of the recoil pressure on surface temperature causes a large radial gradient for the recoil pressure and this gradient accounts for the melt flow in the radial direction. Moreover, the outward melt leads to the creation of a small protrusion at the edge of the affected region that undergoes melting whose curvature varies substantially with respect to the curvature of the surface closer to the beam centre. **Figure 3.2(c)** shows the temporal evolution of all types of pressure at the edge of the zone that undergoes melting. The

illustration indicates that the recoil pressure effect is larger than the pressure due to surface tension in the early stages of resolidification that produces a small melt ejection towards the edge of the zone. By contrast, at later stages and before the end of the resolidification process the recoil pressure is outweighed by the increase of the pressure due to surface tension. Hence, the resulting pressure will produce a protrusion of size that increases in a way that forces due to recoil pressure and surface tension will balance one another. Therefore, material ejection out of the irradiated zone will not further occur till the material cools to temperatures below the melting point

Figures 3.3(a)-(c) illustrate the evolution and the transient behaviour of the movement of the molten volume of the material while the thick arrows show the direction of the associated velocity fields at $t=0.1, 1$, and 10ns , respectively. Recoil pressure has initially an important impact in the surface depression. **Figures 3.3(a)-3.3(c)** show that molten material displacement due to the combination of recoil pressure and surface tension gradient results in a decrease of the melt thickness and melting of a new portion of the material. Temperature gradient coupled with surface tension gradient induces an outward and upward flow (i.e Marangoni flow). Furthermore, recoil pressure makes the molten material flow upwards. Simulation results show that upward melt flow delivers both heat and molten material towards the edge of the depressed zone. The displaced material will produce a convex profile that will undergo two oppositely directed pressures (one due to the surface tension and another from decreasing recoil pressure) that will collide and a protrusion will be formed at the edge of the affected region. A liquid temperature decrease at larger distances from the laser beam centre leads to increasing liquid surface tension which is an additional reason why liquid is pulled away from the centre. Furthermore, a surface tension variance leads to the development of clockwise flow and capillary waves which eventually results into surface depression in regions of higher temperatures.^[144,145] **Figures 3.3(d)-3.3(f)** illustrate the temperature distribution at different time-points which is associated to the heat flow inside the molten material.

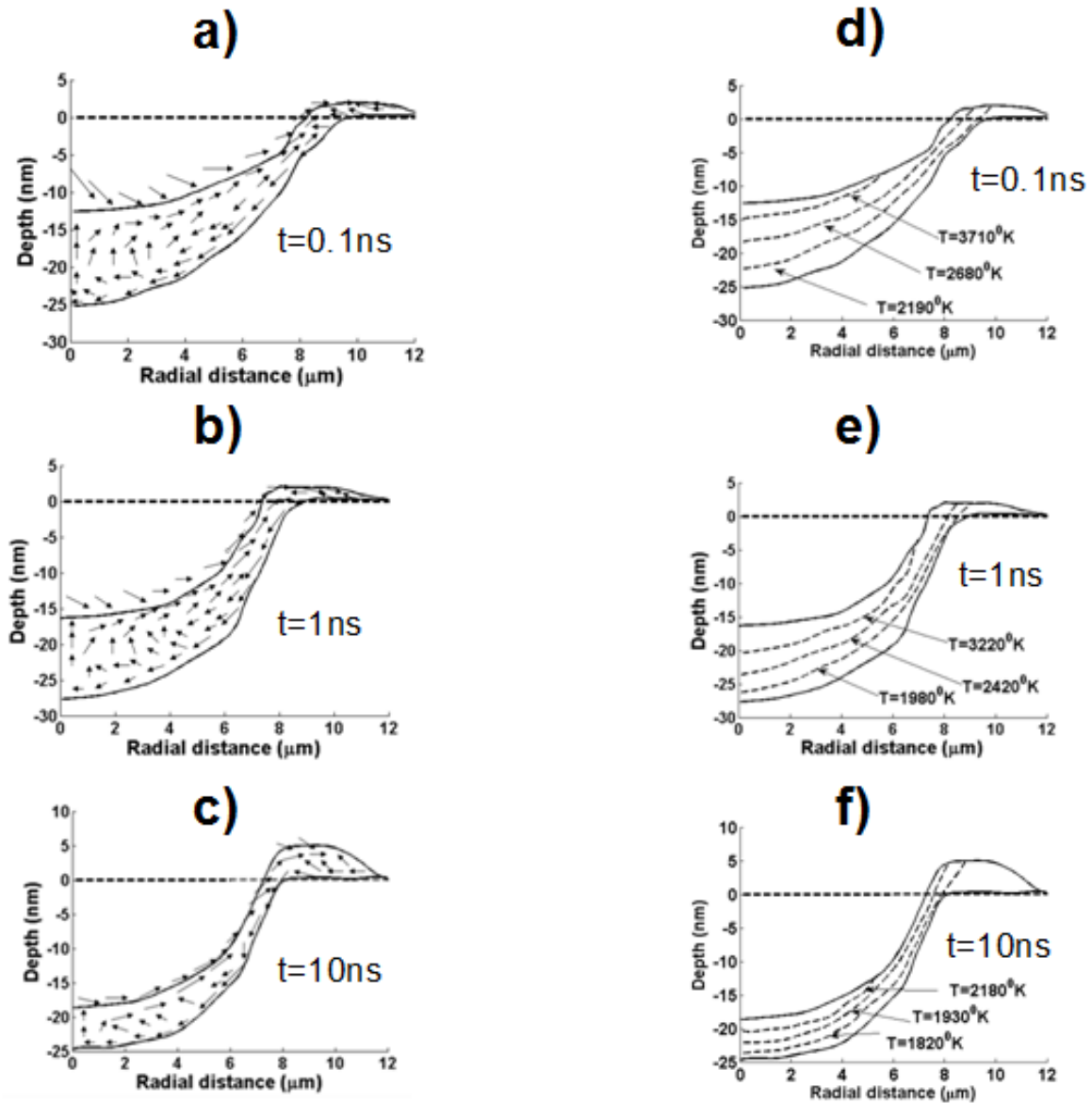


Figure 3.3: Surface profile and flow pattern (a-c) and temperature distribution (d-f) at $t=0.1, 1, 10\text{ ns}$ after first irradiation (theoretical results).

The employment of the Navier-Stokes equation and estimation of the liquid-solid interfacial location leads to the surface profile illustrated in **Figure 3.4** which shows that there exists an increased surface depression with respect to the initially flat profile. In comparison to the surface profile resulted from mass evaporation, phase transition of the molten material induces an enhanced radially dependent depression and for mass conservation reasons a hill protrusion is pronounced above the surface.

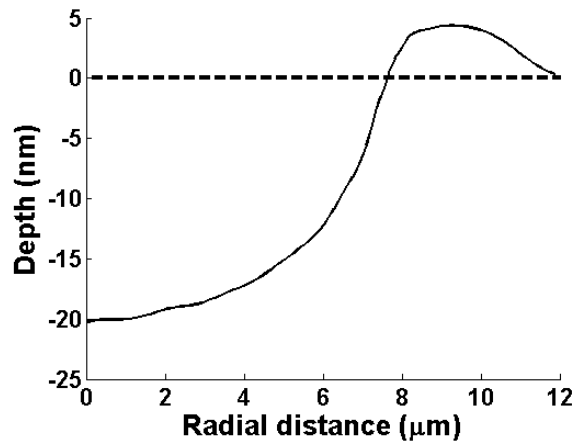


Figure 3.4: Surface profile and flow pattern (a-c) and temperature distribution (d-f) at $t=0.1, 1, 10$ ns after first irradiation (theoretical results).

Figure 3.4 illustrates the theoretically predicted crater formation after a single pulse irradiation and the maximum depth of the crater is estimated to be equal to about 20 nm. Due to axial symmetry a similar process and a symmetric profile is expected for the other half of the material (results not shown). Both experimental observations and the theoretically predicted value (i.e. 8.2 nm) are very low compared to the laser beam penetration depth which ranges from 2.6 μm to 4.4 μm for the range of lattice temperatures during the laser pulse illumination (i.e. penetration depth is estimated from the inverse interband absorption coefficient and it decreases monotonically with increasing

temperature). Furthermore, a top view of the SEM image of the spot attained after irradiation with one pulse is illustrated in **Figure 3.5(a)** where enhancement of the crater formation is performed by reversing the contrast of the intensity image (decreasing depth is represented by darker pixels). A cross-line (*dashed* line in **Figure 3.5(a)**) exhibits a roughened and steep crater with a precise mass removal and a small pronounced hill protrusion (**Figure 3.5(b)**). Although similar observations including ablated material and a protruding hill in the periphery of the affected region (attributed to recoil pressure of the ablated material) have been observed in ablation experiments,^[146,147] the proposed model predicts similar results in sub-ablation conditions. A significant conclusion inferred from **Figure 3.5(b)** is that there is a minimal (but existing) mass removal from the material as a result of the irradiation. To avoid misinterpretation or mass removal underestimation and exclude any preferential orientation of mass displacement, image analysis was performed in the whole region that depicts surface modification in **Figure 3.5(a)** (and similar images produced from a single irradiation) and similar profiles (**Figure 3.5(b)**) were attained. Hence, quantification of the image provides a justification that a simple mass redistribution is not capable to explain the process. The depth of the evaporated material computed from the simulation (i.e. equal to 8.2 nm), is comparable to the average depth measured in the AFM image of the single-pulse spot (i.e. approximately equal to 5.4 nm). More specifically, **Figure 3.5(c),(d)** illustrate a portion of the modified profile and a cross section, respectively.

Irradiation of the non-flat surface with a second pulse (which is performed after completion of surface solidification due to the first pulse) give rises to a plasmon wave excitation which interferes with

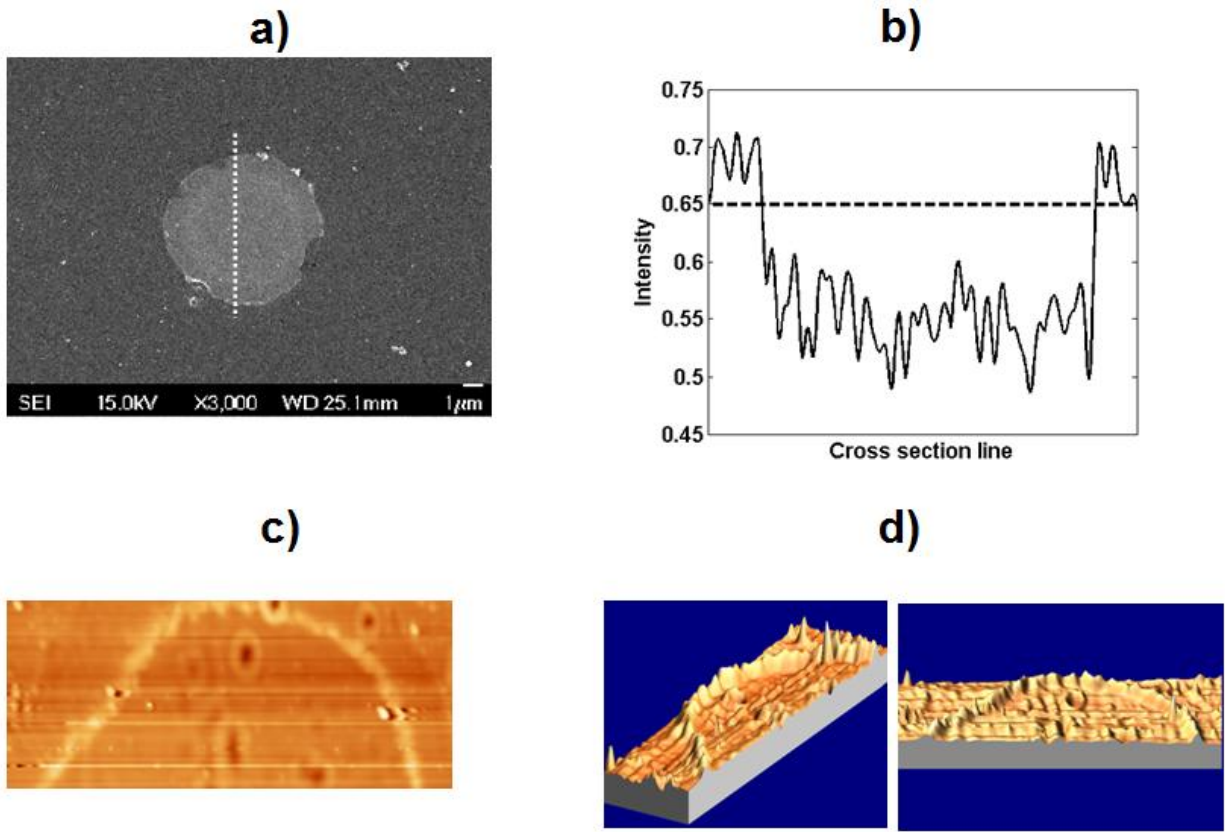


Figure 3.5: Surface profile and flow pattern (a-c) and temperature distribution (d-f) at $t=0.1, 1, 10\text{ns}$ after first irradiation (theoretical results).

the incident field and produces a spatially modulated energy deposition as explained in **Section 3.2.2(iii)**. A non uniform temperature distribution along the modified surface produces again locally surface tension gradients that in combination of a balance between recoil pressure and surface tension pressure are responsible for the rise and depression of molten surface. However, interference of the incident beam with surface plasmon waves leads to a periodic melting of the initially formed profile. The transient behaviour of the molten portion of the material is characterised by a clockwise flow of molten material and periodic structures are developed with an orientation perpendicular to the electric field. The interference of the initial beam with the surface plasmon wave will destroy the axial symmetry of the system and thereby surface morphology will not exhibit a cylindrical symmetry. As a result, for $NP = 2$, a three dimensional solution of **Eqs (3.1-3.20)** was employed as explained in the Simulation section. Calculation of the absorbed energy due to multiple reflection and application of Fresnel expressions shows an enhanced energy density locally. In order to interpret the morphological changes and associate them to thermophysical processes, the effect of the nonuniform energy density deposition has to be investigated. It

is evident that a higher recoil pressure is exerted on a modified surface profile which results in an increased flow velocity and force applied to the molten material. On the other hand, due to a periodic deposition of the laser density, a recoil pressure will also be a periodic function and spatially modulated. Moreover, the values of local maxima decrease towards the edge of the affected region which indicates that at positions where the recoil pressure function has local maxima, upward flow will be stronger on the side which is closer to the centre. By contrast, close to the points which are related to local minimum for the recoil pressure, the profile is characterised by an increased curvature that results to higher pressure due to surface tension. Hence, the collision of the two opposing types of pressures yields pronounced protrusions.

Figures 3.6(a)-(d) illustrate the transient behaviour of the movement of the molten volume and the distribution of the temperature fields after a second pulse irradiates the material ($NP=2$) at $t=1$, and 10ns, respectively. To elucidate the behaviour and facilitate the process observation, figures are restricted only to a small portion of the affected zone (equal to a $2.1\mu\text{m}$ size along the x -axis). The thick arrows in **Figures 3.6(c)-(d)** show the direction of the associated velocity fields. The flow of the molten material in **Figures 3.6(c)-(d)** demonstrates that the aforementioned interpretation of ripple wavelength with respect to the number of pulses is more evident during the formation of the ripple profile. **Figures 3.6(e)-(f)** illustrate the periodic behaviour of the spatial dependence of the recoil pressure at two different timepoints, $t=1$ and 10 ns, respectively. According to the illustrations, at the bottom of each well, recoil pressure exhibits local maxima and it is stronger on the left side of the well.

To investigate incubation effects and the evolution of the ripple periodicity, the surface profile modification is probed after irradiating the material with more pulses. **Figure7(a)** illustrates the ripple formation for 2, 4, and 8 pulses on the xz -plane at $y=0$ and it is evident that the spot size, depth and amplitude increase monotonically with number of pulses. We notice that for $NP = 4$, ripples develop above the initial level of the surface profile (i.e flat surface) while for smaller values of NP , ripples form below $z=0$. An increase of the spot depth with an increase in the number of pulses is explained by the evaporation of the top layer of the surface profile after irradiation with subsequent pulses (i.e. every new pulse irradiates a modified surface profile and it will cause a further mass removal). Furthermore, a repetitive exposure to pulses leads to ripples with larger amplitude due to an increased gradient of energy deposition as number of pulses grows which causes the ripples to be more pronounced. Ripple height is spatially dependent due to the periodic variation of the gradient of the surface tension and temperature gradient that generates the creation of the periodic structures. Bigger variations are expected closer to the centre of the laser beam yielding structures with bigger peaks.

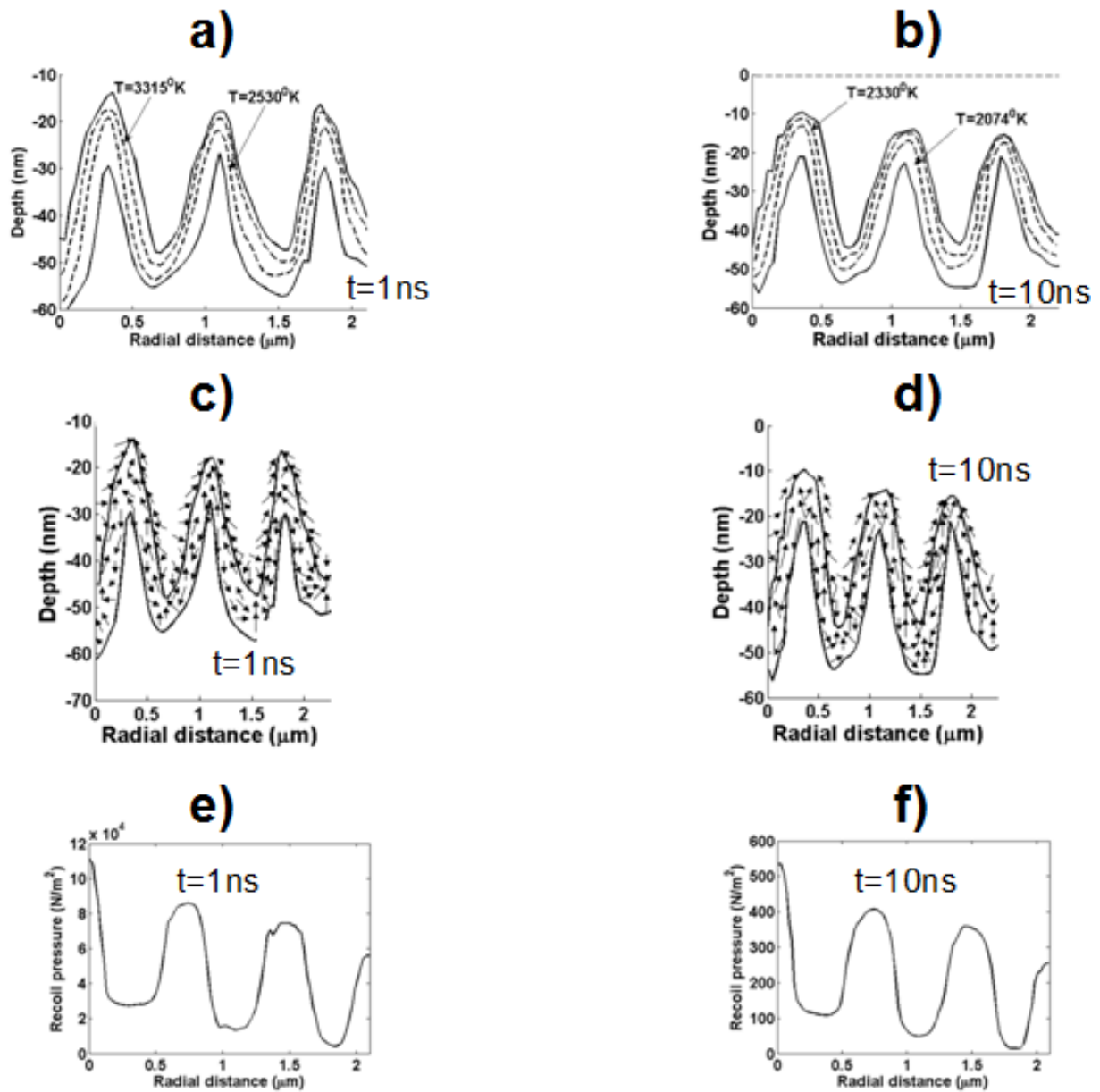


Figure 3.6: Simulations for temperature distribution (a,b) and flow pattern (c,d) at $t = 1, 10\text{ns}$ after irradiation with two pulses ($NP=2$). Radial dependence of recoil pressure at $t=1\text{ns}$ (e) and $t=10\text{ns}$ (f), respectively.

The average ripple period after laser irradiation with four pulses is estimated to be equal to 736nm. **Figure7(b)** illustrates the theoretically predicted three dimensional spatial dependence of the surface patterning for $NP=8$ in one quadrant where there is a pronounced rippled surface. Ripple horizontal profile resembles the result illustrated in **Figure7(a)**. A cross section (*dotted line* in **Figure7(b)**) along a ripple indicates a spatial decrease followed by an increasing behaviour while along the well (*dashed line*

in **Figure7(b)**) it increases monotonically before the occurrence of a small protrusion at the edge of the affected region. The two distinct types of behaviour are exhibited in **Figure7(c)** and **Figure7(d)**, respectively where fluctuations have been removed by filtering simulation results using a mean filter.

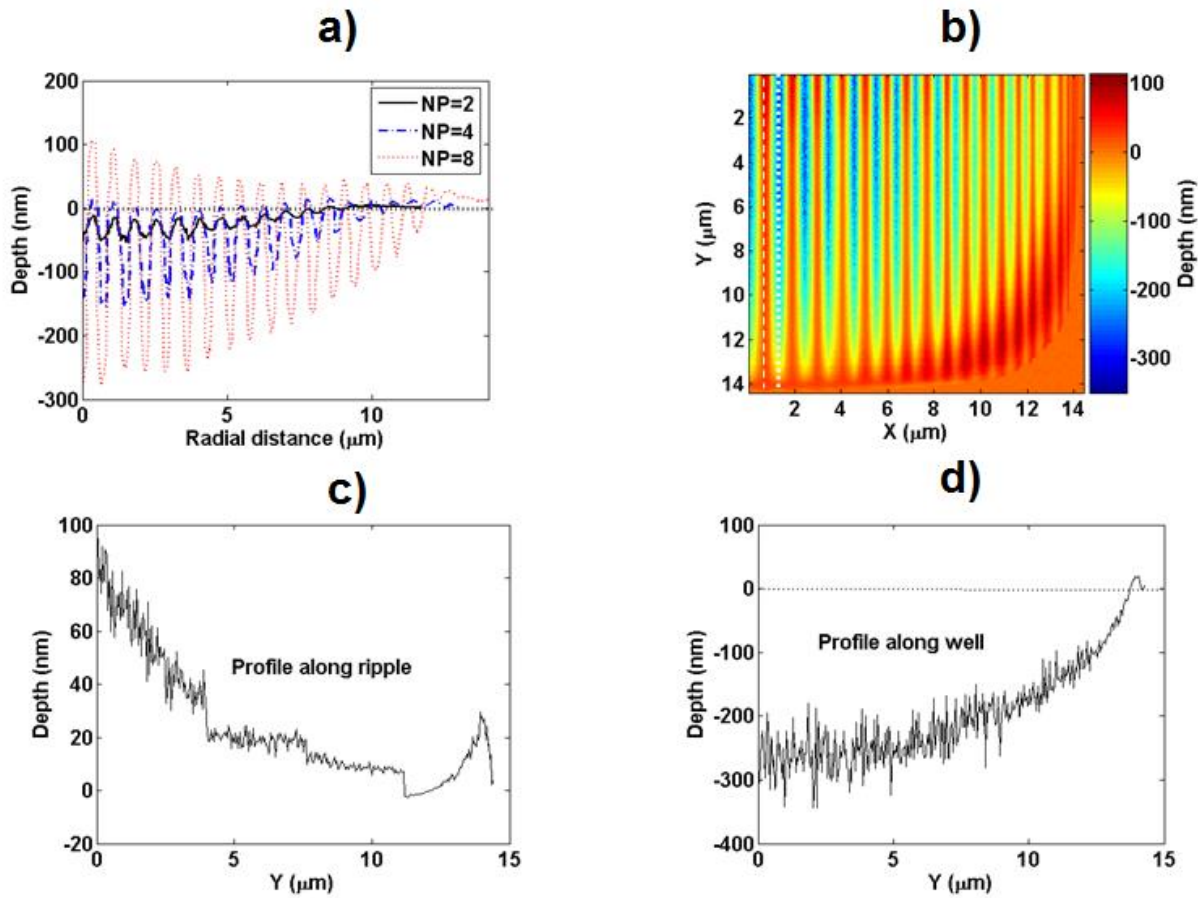


Figure 3.7 (Color online): Theoretical results for: **(a)** Ripple formation after repetitive irradiation ($NP=2$, solid line) with $NP=4$ (dashdot line), $NP=8$ (dashed line) at xz -plane ($y=0$), **(b)** Ripple formation (simulation results) for $NP=8$, **(c)** Spatial dependence of depth along ripple (dotted line in **(b)**), **(d)** Spatial dependence of depth along well (dashed line in **(b)**).

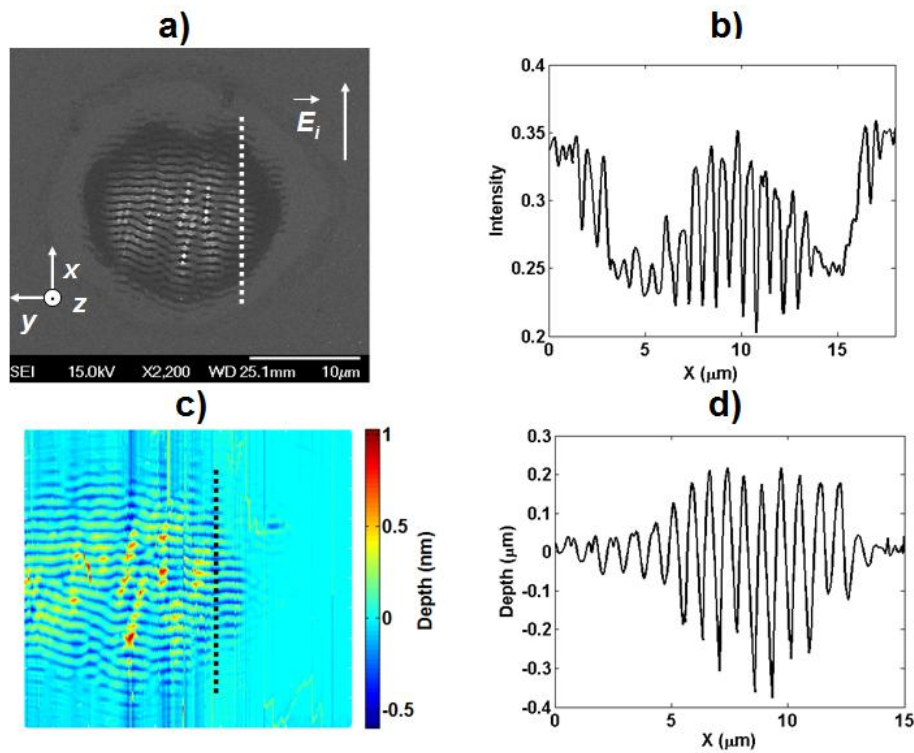


Figure 3.8 (Color online): Experimental results for $NP=4$: **(a)** SEM intensity image (shows the polarization of the incident beam-on the x - z plane and parallel to x), **(b)** Intensity profile spatial dependence along *dashed* cross-line shown in **(b)**, **(c)** AFM intensity image, **(d)** Intensity profile spatial dependence along *dashed* cross-line shown in **(c)**.

In order to measure and investigate quantitatively the modifications in the surface morphology, theoretical simulations are tested against the experimental data. **Figure 3.8(a)** illustrates a top-view SEM image of the spot attained after irradiation with four pulses and the intensity profile along a perpendicular to ripples direction (*dashed* line) was used to estimate ripple periodicity. Interestingly, due to spot or laser beam irregularities, periodicity is not obvious and thereby attention has been restricted to areas where some conclusive measurements are obtainable. Therefore the selected region (*dashed* crossline in **Figure 3.8(a)**) based on that it is characterised by small intensity variances and a well-defined ripple profile can be attained. It is evident that for a p -polarised beam the ripples develop perpendicularly to the electric field of the incident beam which also has been reported in laser induced welding, hardening and annealing.^[148,149] Image analysis techniques including a fast Fourier transform (FFT) low pass filter were performed to remove noise and produce the intensity profile without significant fluctuation. Estimation of ripple periodicity is achievable through the computation of the horizontal distance between the pronounced local minima (**Figure 3.8(b)**) which yields an average experimental value of 738 ± 6 nm. The

analysis of the SEM image along the cross-line exhibits a morphology with a crater in the centre of the heat affected region, a small protrusion in the periphery and an interference pattern which is similar to the theoretically predicted profile (**Figure 3.7(a)**). It should be noted, though, that this intensity-based profile provides accurate information only for the dimensions on the sample plane, while in the vertical direction it gives relative rather than the absolute dimensional values. A depth-related analysis approach through a processing of the AFM image and plot of the radial dependence of the depth across selected cross sections (*dashed* line in **Figure 3.8(c)**) yields a similar value for the period. Although the ripple period is more accurate by analysing the AFM-obtained surface features, the image acquisition procedure performed by the pointed tip produces estimation errors in computing the correct depth and thereby the peak of the ripples is used to compute periodicity. **Figure 3.8(d)** illustrates the ripple amplitude along a cross section (*dashed* line in **Figure 3.8(c)**) which shows a surface patterning with protruded ripples above the unaffected flat surface of the material which conforms to the theoretical results for $NP=8$ rather than $NP=4$ (**Figure 3.7(a)**). The difference can be attributed to the discrepancy between the experimental and theoretical laser beam fluence values. It is evident that an increased energy deposition induces larger temperature gradients and ripple amplitudes which means that a possibly larger experimental fluence value can account for the observed profile at a lower number of pulses.

Figure 9(a),(b) illustrate a correlation between the surface plasmon wavelength, ripple wavelength, carrier density and number of pulses. It is evident (**Eq. 3.19**) that an increase of the carrier density causes an increase in the surface plasmon wavelength (**Figure 9(a)**). By contrast, as the number of pulses increase, the absorbed energy due to multiple reflection increases locally (in the neighborhood of the wells), however, due to a larger surface roughness in other parts of the surface energy deposition decreases which influences the material dielectric constant. The resulting decrease of the absorbed energy will lead to a lower carrier density distribution and lattice temperatures. Furthermore, with respect to the molten material dynamics, the contribution of the recoil pressure in conjunction with surface tension pressure will push the fluid back towards the centre of the irradiated zone which leads to an enhanced decrease of the ripple wavelength compared to the surface plasmon wavelength (**Figure 9(b)**). More specifically, it is evident that as the profile becomes deeper and steeper (with increasing number of pulses), pressure due to surface tension near the protrusions play an increasingly predominant role and the displacement of molten material towards to the positions of local maxima of the recoil pressure is expected to be more pronounced. Hence, irradiation of the material with a higher number of pulses lowers the ripple wavelength as protruded hills are pushed towards the wells. As a result, an interpretation of the correlation between the ripple wavelength and the number of pulses is proposed which is based completely on hydrodynamics grounds. Despite an apparent small discrepancy between the ripple and the

surface plasmon wavelengths, the change has to be emphasised and flow dynamics appear to explain the trend. Moreover, the resulting ripple wavelength and the proximity of its value to the surface plasmon wavelength indicate that although the surface structure periodicity is determined predominantly by optical effects (i.e. interference), our simulations signify that hydrodynamics and the evolution of the melt flow are capable to maintain surface structures (subwavelength ripples). Hence, the influence of the recoil pressure, surface tension pressure, capillary effects and the subsequent solidification fail to lead to the destruction of a patterned surface with an optically prescribed wavelength.

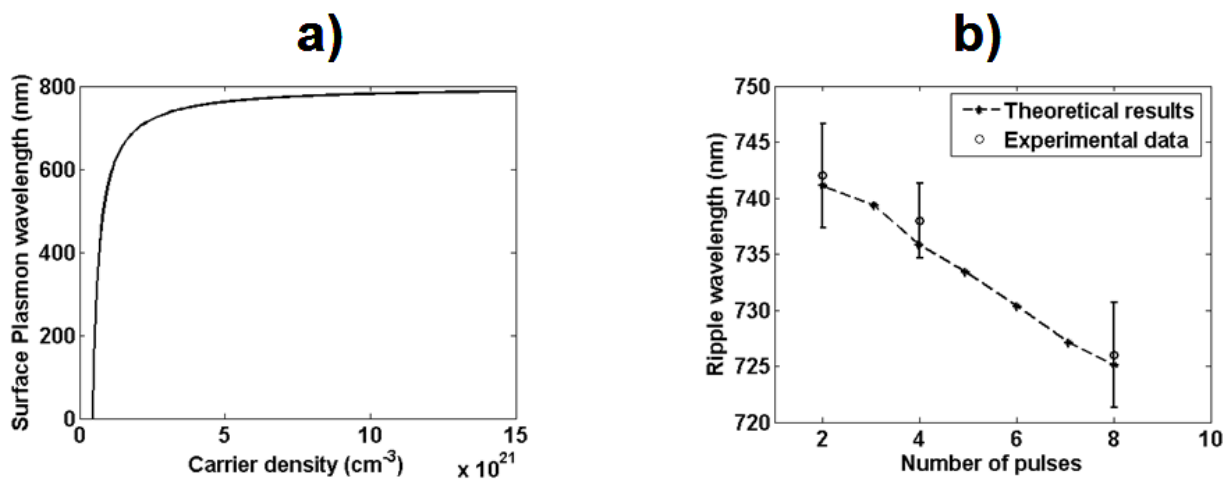


Figure 3.9: (a) Theoretical results for surface plasmon wavelength as a function of carrier density, (b) Theoretical results and experimental observations of the ripple wavelength's dependence on number of pulses.

The monotonic decrease of the ripple subwavelength periodicity with increasing pulse number (**Figure 9(b)**) has also been reported in other works that assume ablation[150]²³, however, variance is minimal around the estimated value for $NP < 8$. Furthermore, **Figure 9(b)** illustrates a comparison between the theoretically computed ripple period and the experimentally observed values for $NP \leq 8$. The sketch indicates that the theoretical results are within the experimental error and therefore the model offers an adequate description of the underlying mechanism. Certainly, the discrepancy of the results can be partly attributed to the difficulties to create in the laboratory the exact conditions of the simulations (i.e. eradication of experimental errors). Nevertheless, the theoretical framework reveals with a good accuracy the tendency of the expected results.

The results presented in this work suggest that our model provides a very good insight into the process that dictates the formation of ripples and yields significant quantitative details of the underlying mechanism. Our approach provides a detailed characterisation of the morphology change, ripple characteristics, spot size and propose the hydrodynamic factor to be of predominant importance. In comparison with alternative approaches regarding the interpretation of the ripple formation,^[151,152,153] our theoretical framework aims to provide a complementary methodology by incorporating a variety of ultrashort-pulsed induced effects. It is capable to incorporate a surface plasmon wave-induced ripple formation mechanism by considering a plasmon wave interference with the incident beam, the spatial modulation of the deposited energy on the material surface and the influence of the hydrodynamic factor. Furthermore, a revised version of the theoretical model that incorporates ablation and hot electron explosion effects potentially could provide a smooth transition to understand the underlying mechanism of a yet unjustified groove formation^[154] or spike development.^[155]

3.2.5 Conclusion

A detailed theoretical unified model was presented which is aimed to account for the surface modification and the plasmon-generated-periodic surface structure formation (ripples) observed during semiconductor irradiation with ultrashort laser pulses in sub-ablation conditions. It contains heat transfer and hydrodynamics components that describe the particle dynamics, carrier excitation conduction phenomena and the morphology modification, respectively. By choosing beam characteristics that result in minimal mass loss, we demonstrated that it is likely to modulate the surface profile upon laser irradiation. Theoretical simulations and experimental observations indicate that temperature dependent surface tension gradients and recoil pressure are capable to generate molten material movements that lead to the observed morphology changes after capillary wave freezing. Elucidation of the underlying mechanism that dictates surface modification in semiconductors will allow control and alteration of their optoelectronic properties. A similar approach can be ensued to investigate related phenomena in other types of materials such as metals and dielectrics which enhance the applicability of the model.

TABLE I. Model parameters for Si.

Solid Phase		
Quantity	Symbol (Units)	Value
Initial temperature	T_0 (°K)	300
Electron-hole pair heat capacity	C_c (J/ μm^3 K)	$3Nk_B$
Electron-hole pair conductivity	K_c (W/ μm K)	$10^{-6} \times (-0.5552 + 7.1 \times 10^{-3} \times T_c)$
Lattice heat capacity	C_l (J/ μm^3 K)	$10^{-12} \times (1.978 + 3.54 \times 10^{-4} \times T_l - 3.68 T_l^{-2})$
Lattice heat conductivity	K_l (W/ μm K)	$0.1585 T_l^{-1.23}$
Band gap energy	E_g (J)	$1.6 \times 10^{-19} \times (1.167 - 0.0258 T_l / T_0 - 0.0198 (T_l / T_0)^2)$
Interband absorption (800nm)	α (μm^{-1})	$0.112 e^{T_l/430}$
Two-photon absorption (800nm)	β (sec $\mu\text{m}/\text{J}$)	9×10^{-5}
Reflectivity (800 nm)	$R(T_l)$	$0.329 + 5 \times 10^{-5} T_l$
Auger recombination coefficient	γ ($\mu\text{m}^6/\text{sec}$)	3.8×10^{-7}
Impact ionisation coefficient	θ (sec $^{-1}$)	$3.6 \times 10^{10} e^{-1.5E_g/k_B T_c}$
Free carrier absorption cross section (800nm)	Θ (μm^2)	$2.9 \times 10^{-10} T_l / T_0$
Energy relaxation time	τ_e (sec)	$\tau_{e0} \left[1 + \left(\frac{N}{N_{cr}} \right)^2 \right]$, $\tau_{e0} = 0.5\text{ps}$, $N_{cr} = 2 \times 10^9 \mu\text{m}^{-3}$
Molten Phase		
Electron heat capacity	C_e (J/ μm^3 K)	$10^{-16} \times T_e$
Electron conductivity	K_e (W/ μm K)	67×10^{-6}
Lattice heat capacity	C_L (J/ μm^3 K)	$1.06 \rho_L$
Density	ρ_L (gr/ μm^3)	$10^{-12} \times (3.005 - 2.629 \times 10^{-4} T_L)$
Dynamic viscosity	μ (gr/ μm sec)	$3.53 \times 10^5 \rho_L$
Thermal Expansion coefficient	β_l (K $^{-1}$)	1.32×10^{-4}
Surface tension	σ (N/m)	(1) $0.7835 - 0.65 \times 10^{-13} (T - T_m)$, for $T < 1773\text{K}$ (2) $-1.94789 \times 10^{-11} (T - 5108.13)^3 + 0.00238748$, for $T > 1773\text{K}$ and $T < 0.9 T_{cr}$ (3) $3.70923 \times 10^{-7} (T_{cr} - T)$, for $T > 0.9 T_{cr}$
Energy relaxation time	τ_E (sec)	10^{-12}
Melting temperature	T_m (K)	1687
Boiling temperature	T_b (K)	3514
Critical point temperature	T_{cr} (K)	5159
Latent heat of melting	L_m (J/ μm^3)	4206×10^{-12}

3.3 Formation of micro/nano structures

3.3.1 Evolution of periodic surface structures

Further irradiation of Si with increasing number of pulses gives rise to various types of structural morphologies which finally lead to microconical structures' formation.

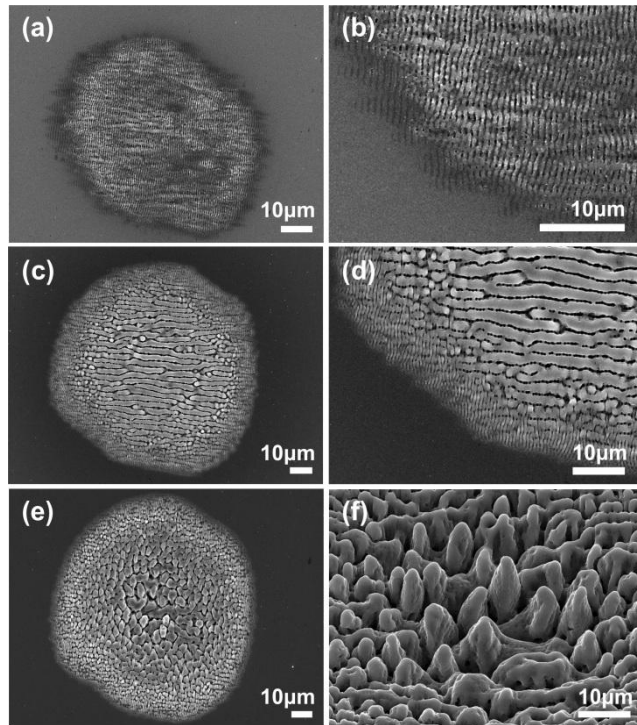


Figure 3.6: Silicon spots irradiated with a femtosecond, 800nm laser and a fluence of 0.3 J/cm^2 . (a),(b) Ripple formation after irradiation with 10 pulses. (c),(d) Increasing the number of pulses (here 40 pulses) leads to the formation of parallel surface waves with periodicity 2-3 times bigger. (e),(f) When further increasing the number of pulses the waves break, leading to the formation of micro-sized columns/cones.

Figure 3.6, shows the three different stages of evolution of the same silicon spot irradiated with a femtosecond laser, at 800nm laser, a fluence of 0.3 J/cm^2 and increasing number of pulses. **Figure 3.6 (a),(b)** show the formation of ripples, discussed previously, after irradiating the sample with 10 pulses. **Figure 3.6(c),(d)** shows that upon increasing the number of pulses to 40, formation of a new type of periodic structures (grooves) created on top of the initial ripples but are oriented perpendicular to them, i.e parallel to the beam polarization. The periodicity of grooves is 2-3 times higher than the laser wavelength, here at the order of 2-2.5 μm . Ripples are simultaneously observed, located in the spot periphery. Although extensively observed, the physical mechanism behind the formation of these periodic structures still remains unclear. Upon further irradiation grooves break apart into micro-columns as can

be seen in **Figure 3.6(e),(f)**. For higher number of pulses the height of the columns/cones is increased as there is preferential material removal mostly in those areas of the target that are oriented normally to the laser beam axis ^[156,157]. Moreover the laser beam reflected from the cone slopes can lead to light entrapment in between the high roughness areas, where the local laser fluence is sequentially increased.

3.3.2 Surface structuring of Silicon in a reactive gas atmosphere

3.3.2 Surface structuring of Silicon in a reactive gas atmosphere

Silicon structuring has been examined over the past few years, by using several different laser sources [18,158,159,160,22,161,162,163,164,165,166,167], including ArF laser (193nm, 23ns),^[20,21] KrF (248 nm, 25 ns)^[19,22,23] and Cu vapor laser (510.6nm, 20ns).^[25,26] Mazur and co-workers also performed experiments in the presence of different ambient gasses including vacuum, Cl₂, SF₆ and studied morphological structural and optical properties.^[18,168] One of the most extensively used gases for etching of semiconductors, and in particular Si with which it is very active, is SF₆. At the laser beam focus where the optical intensity reaches pretty high values, the dissociation of SF₆ leads to the formation of fluorine radicals which is well known in plasma etching applications.^[169,170] Etching of Si can then occur through the formation of such radicals, which eventually react with Si to form volatile Si-containing fluorine compounds. Briefly, SF₆ molecules decompose into SF₅ and F atoms. SF₅ (being very unstable) decomposes into SF₄ and another F atom, which both diffuse into the Si surface and react to form SiF₄. **Figure 3.7(a), (b), (c)** presents the shape on the silicon cones produced in the presence of vacuum and in SF₆ respectively. As it can be clearly observed much sharper and well defined cones can be obtained when irradiating in the presence of an etching gas. Furthermore the formation of nanoscale roughness on the cones' surface becomes more pronounced. In particular, protrusions with size from tens to a few hundreds of nanometres, which provide the double length-scale pattern on the Si surface, are formed (**Figure 3.7(c)**). The micrometer-scale features generated by the spikes landscape together with the nano-scale features generated by the surface prongs on the cones result into a significant increase of the overall roughness. In chapter 5 we will show that such hierarchical morphology is desirable for a range of practical applications.

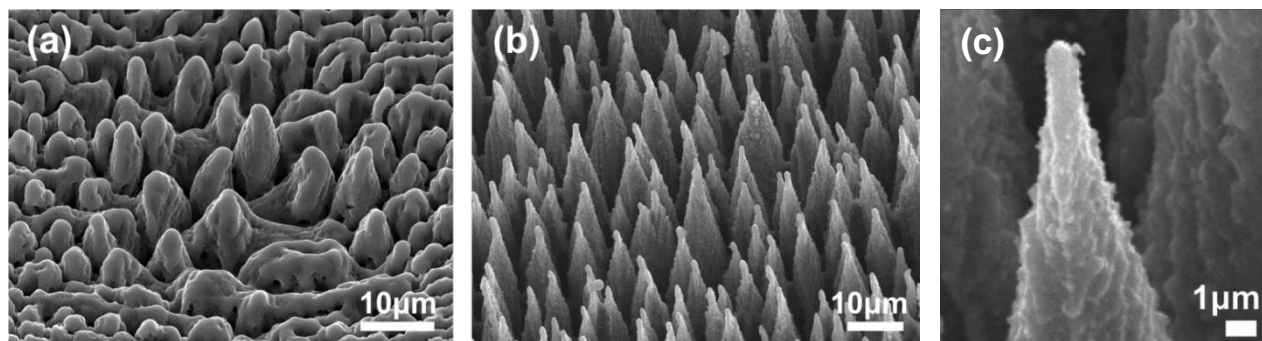


Figure 3.7: (a) Cones obtained irradiating crystalline silicon in vacuum and (b) SF₆ (c) a magnification of a single Si tip where the nanoscale roughness is evident.

3.6 Conclusions

A detailed theoretical hybrid model was presented which is aimed to account for the surface modification and the periodic surface structure formation (ripples) observed during semiconductor irradiation with ultrashort laser pulses. It contains heat transfer and hydrodynamics components that describe the particle dynamics and conduction phenomena and the morphology modification, respectively. By choosing beam characteristics at the onset of material evaporation, we demonstrated that it is likely to modulate the surface of the material upon laser irradiation. Theoretical simulations and experimental observations indicate that temperature dependent surface tension gradients are capable to generate molten material movements that lead to the observed morphology changes. Elucidation of the underlying mechanism that dictates surface modification in semiconductors may allow control over the final surface micro/nano morphology attained which is a key issue for practical applications.

Chapter 4

Laser processing with temporally designed femtosecond pulses

4.1 Laser modification of semiconductors: The effect of temporally shaped pulses

In this Chapter we present an experimental study on the surface modification of two semiconductors namely Si and ZnO irradiated with two sequential ultrashort pulses that are separated by a certain time delay lying in the range from hundreds of femtoseconds to tens of picoseconds. Using a Spatial Light Modulator (**section 2.3**) to produce *double pulses (DP)*, several spots using various numbers of pulses and time delays were obtained and analysed. In the case of Si we study the effect of double-pulse irradiation for fluences close to the boiling point where minimum mass removal occurs. Furthermore the theoretical model developed for single-pulse irradiation, presented in the previous chapter, is expanded to include the case of double-pulse irradiation as well. In the case of ZnO we show that double-pulse irradiation can be used as a mean to control the periodicity of the final surface pattern attained.

4.1.1 Introduction

Laser pulses with a defined temporal shape, used in the majority of laser-surface processing experiments, limit the control over the final morphological features. On the contrary, temporal pulse shaping of a laser beam used for controlling the timescale over which the energy on a material is deposited, may be promising in this respect.

A variety of timescale-dependent processes (see also **section 1.2**) are triggered following ultrashort pulsed laser interaction with matter: **(a)** Carrier generation, **(b)** internal thermalization of free carriers, **(c)** carrier-lattice thermalization, **(d)** energy transport via carrier transport **(d)** thermal and surface modification.^[171] A desirable effect in laser-mater processing applications is to achieve control and influence the morphology of the final interaction product by regulating the way of energy delivery from the laser into the various degrees of freedom of the system. This may be partly achieved by exploiting or controlling the aforementioned fundamental processes, with the utilization of the temporal pulse shaping methodology.^[172] A primitive form of pulse shaping is simply (but not necessarily easily) done by splitting the initial pulse in two equal components and vary the temporal pulse separation in the time range from hundreds of fs to tens of ps, thus attempting to manipulate ultrafast electron interaction and cooling processes that take place in this temporal range.

Several studies have demonstrated the advantages of DP irradiation concerning material processing. One of the advantages was realized in the mass removal rate by means of ablation efficiency. For example an increase of the ablated mass of steel up to a factor of 8 was demonstrated with the use of DP.^[173] In laser ablation it was also suggested that DP series, increases the rate of mass removal in drilling process.^[174,175] Plasma re-heating and ablation was also studied by ultrafast double pulses as a function of pulse delay on the picosecond delay scale for Cu and Al target.^[176] In this case a crater depth decrease was observed with increasing pulse delay.

Furthermore simulations with femtosecond pulses and picosecond time delays were performed in order to investigate the DP ablation processes in metals.^[177,178] During the first pulse, simulations revealed that the induced pressure of ions, results in a formation of a shock and rarefaction wave propagating into the target. For DP experiments when the delay is on the order of the electron-phonon relaxation time, the second pulse reduces the intensity of the rarefaction^[128] wave resulting in the decrease of the ablated crater depth.

In this chapter we study the effect of double-pulse irradiation on Si surfaces for fluences close to its boiling point.. Under these conditions, melting of the target and minimum mass removal is considered, while explosive mass removal is excluded. The pulse separation used ranged from 0 to 14 ps.. In particular, laser-induced periodic surface structures (ripples) with periodicity close to the laser wavelength are formed, showing no dependence on pulse separation. On the contrary, a decrease of the irradiated spot area and spot depth with increasing pulse delay is observed. Those results are discussed in the framework of the hybrid two-temperature/hydrodynamic model developed for single pulse and expanded to include DP irradiation.

4.1.2 Methodology and double pulse examples

Experiments were performed with a femtosecond Ti:Sapphire laser system operating at a wavelength of 800 nm and repetition rate of 1 kHz. Two pulse durations were used 90 fs and 430 fs (**Figure 4.1(a)**) and measured by means of cross correlation techniques. A 4/F pulse shaper configuration using a Spatial Light Modulator (SLM) was used in order to filter the Fourier spectrum of the laser pulses and create double pulse sequences^[179] (see **Figure 4.1**) of equal fluence (0.24 J/cm^2 each) with pulse separations varying from 0 to 14 ps. A pockels cell controlled the repetition rate and the number of the double pulse sequences that irradiated the silicon surface. The beam was subsequently focused normally onto the silicon substrate giving a spot diameter of $15 \mu\text{m}^2$ measured with a CCD camera. The spots are located inside a vacuum chamber evacuated down to a residual pressure of 10^{-2} mBar . The maximum energy delivered onto the silicon target was $1.2 \mu\text{J}$ per pulse corresponding to a laser fluence of 0.48 J/cm^2 . Finally various numbers of shots were used ranging from 12 – 1000 laser shots. More details about the setup can be found in section 2.3 and 2.4.1-2

Field emission scanning electron microscopy (FESEM) was used for imaging analysis and spot diameter characterization. In addition, atomic force microscopy (AFM) was used to evaluate the depth profiles of several spots at different time delays.

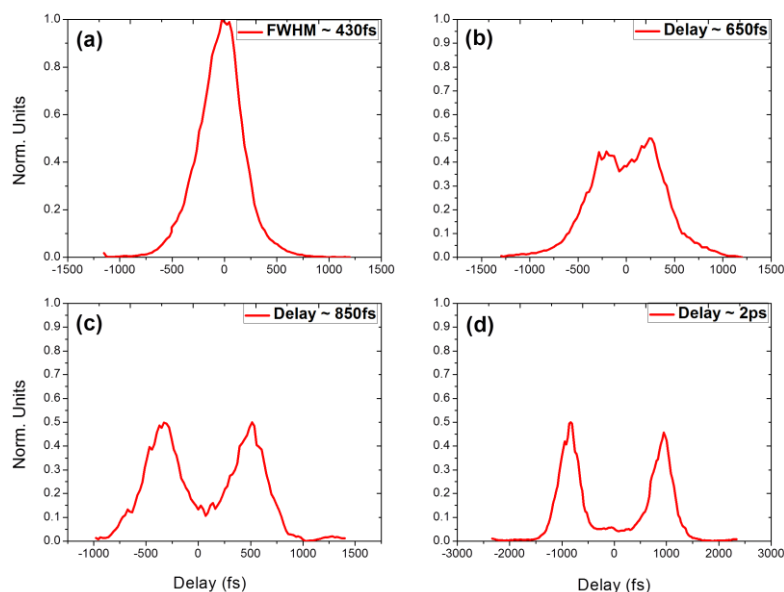


Figure 4.1: Example of double pulses as measured by cross correlation technique. (a) single pulse with FWHM=430fs, (b) 650fs delay, (c) 850fs delay and (d) 2ps delay

4.1.3 Experimental results on Silicon irradiated with Double laser pulses

Crystalline silicon was irradiated using various numbers of laser shots up to 1000 pulses, and different pulse separations ranging from 0.5 to 14 ps. The choice of the number of pulses was based on the fact that $NP=12$ corresponds to a number of pulses that produces pronounced measurable morphology characteristics with minimum mass removal. The two pulse duration used (90 fs and 430 fs) showed

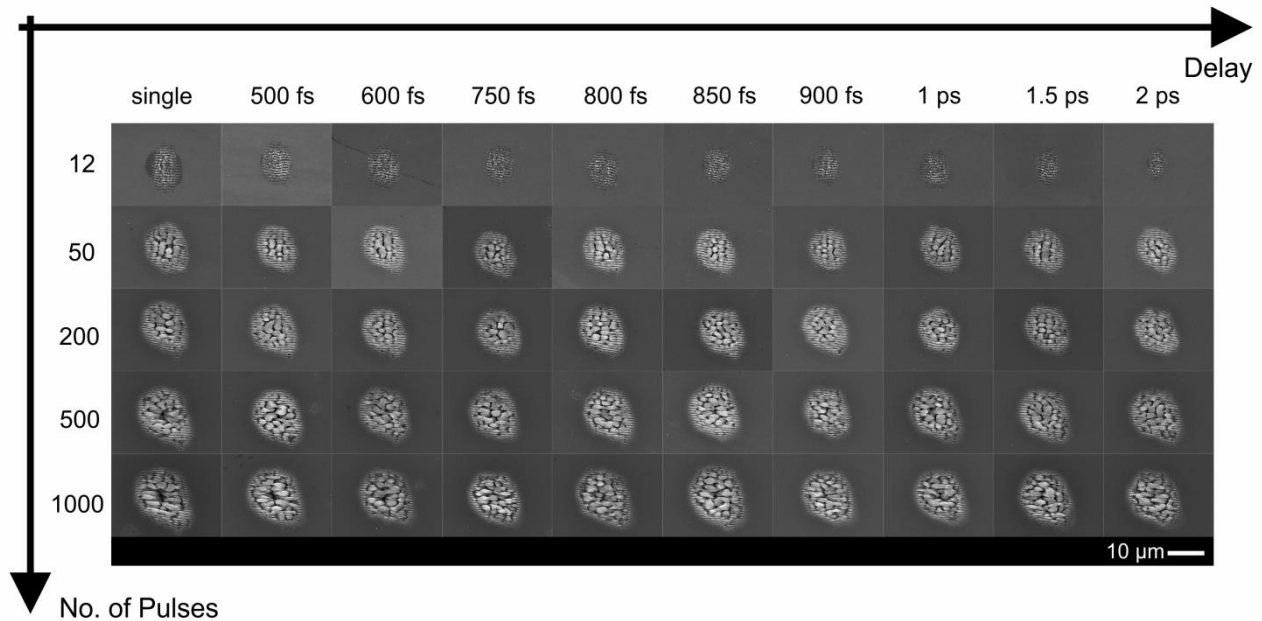


Figure 4.2: SEM image of silicon spots irradiated with various number of pulses and time delay between the double pulse. Fluence used for all spots was calculated 0.5 J/cm^2 .

similar results and no differences on the final surface morphology could be found between them. The fluence of 0.48 J/cm^2 was chosen so that surface modification occurs when irradiated with *single pulses* (SP, zero delay between pulses), but no modification occurs upon irradiation with half of this fluence. When using *double pulses* (DP) the fluence of each individual double pulse is half of that of the SP (compare **Figure 4.1(a) and (d)**).

Figure 4.2 presents an example of SEM images of the Silicon spots and provides an overview of the spot size variation as a function of the number of pulses and the pulse separation. Spots are created using increasing number of pulses, so as to cover a wide range of surface modification stages. For the lowest number of pulses used, minimum mass removal can be obtained whereas for higher number of pulses ablation phenomena become more pronounced due to intense irradiation.

The *electron-phonon relaxation time* (τ_{e-p}) of Silicon which is the characteristic time for a distribution of electrons in a solid to “relax” to equilibrium after a disturbance (i.e. absorption of laser light) is removed, is measured to be ~ 500 fs.^[180] Therefore the temporal separation of the DP is important since it can cover a range below and above this characteristic value. The initial structures observed upon

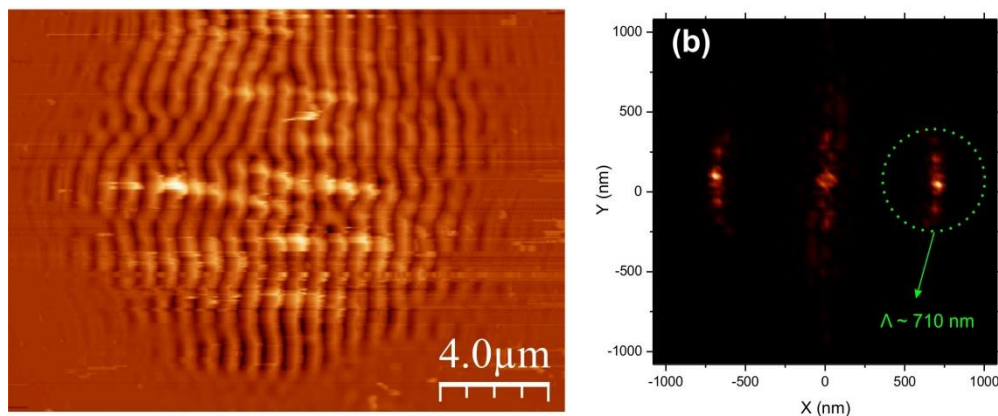


Figure 4.3: (a) AFM of a Silicon spot at zero pulse delay. (b) Fourier transform of the AFM image. A distinct area marked with the green circle corresponds to a ripple periodicity of 710 nm

irradiation with a fluence close to the surface modification threshold are periodic surface structures (ripples, see also **section 1.5** and **3.2**). **Figure 4.3(a)** shows an AFM profile of a Silicon spot attained. In order to calculate the special frequency of the ripples a *Fast Fourier Transform* (FFT) was used. The Fourier Transform is an important image processing tool which is used to decompose an image into its sine and cosine components. The output of the transformation represents the image in the *Fourier* or frequency domain, while the input image is the spatial domain equivalent. In the Fourier domain image, each point represents a particular frequency contained in the spatial domain image. Using this algorithm for image processing an accurate measurement of the periodicity of ripples can be obtained. **Figure 4.3(b)** presents an FFT spectrum based on the AFM image. Analysis shows a peak corresponding to a spatial separation of 710 nm close to the laser wavelength. Similar measurements of the ripple periodicity were performed for all time delays used in this study. Results show that regardless the time delay used the ripples periodicity is preserved close to that of SP irradiation (i.e. ~ 710 nm); therefore DP irradiation does not affect the ripples spacing observed for SP..

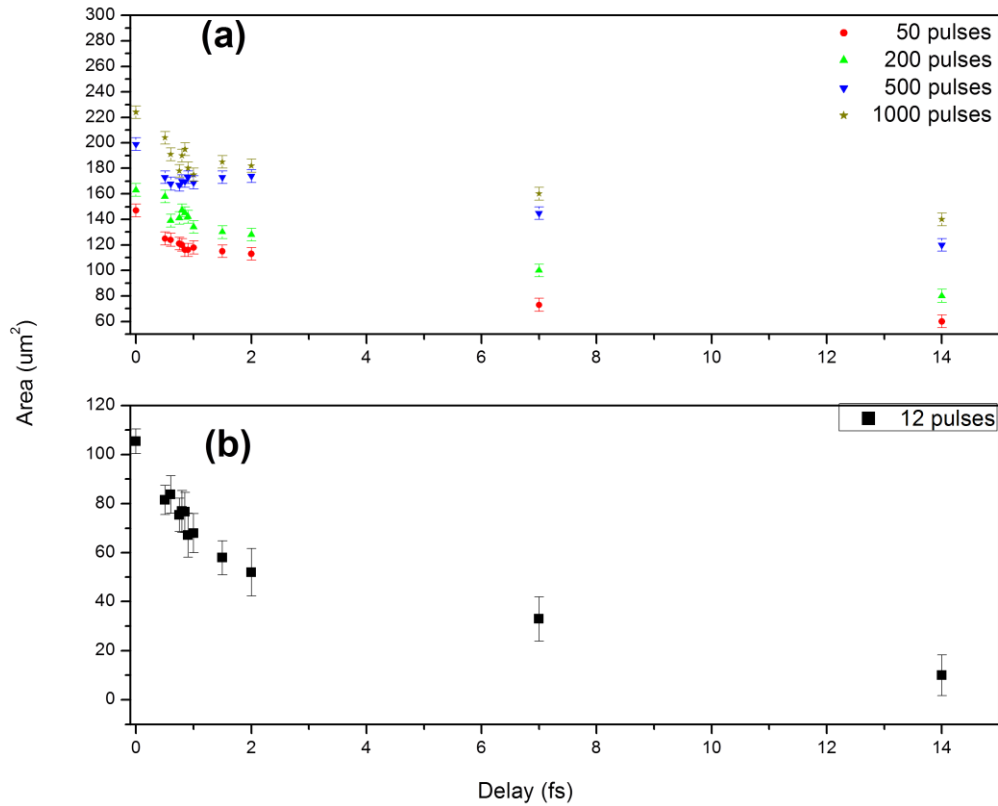


Figure 4.4: The relationship between the pulse separation and the spot area from (a) 50, 200, 500, 1000 number of pulses and (b) 12 pulses. Pulse separation ranges from zero pulse delay to 14 ps

On the other hand, quantitative analysis of the spots characteristics performed using the corresponding SEM images show a pronounced decrease of the spot area with increasing pulse separation as illustrated in **Figure 4.4(a), (b)**. Nearly half of the initial spots' area created with SP remains after irradiation with DP of 14 ps time delay. Furthermore, the spot is not detectable with SEM and AFM imaging for delay times that are longer than 14 ps. The temporal separation of the DP pulse sequence in this case is large enough for the material to realize one pulse with half the fluence. Indeed, as mentioned earlier, half the fluence of the SP (0.24 J/cm^2) is not sufficient to modify the material. The same trend for the spot area is observed upon irradiation with 90 fs pulses (**Figure 4.4**). It should be emphasized that no distinct information could be obtained for time delays close to the τ_{e-p} , in the case of 430 fs pulses. On the contrary, the experiments performed using 90 fs pulses showed that the spot areas for time delays in the range of 0 – 400 fs decrease very slowly. This is in accordance with previous results in metals, showing that irradiation with DP below the τ_{e-p} give similar results with SP irradiation.^[181] For this delay range the

energy which is first delivered into the electronic system is transferred to the lattice only after a time scale associated to the τ_{e-p} (0.5 ps). Lattice temperatures in this case should have a similar value leading to a similar spot area. For higher pulse separation the second pulse realizes a system which already undergoes a relaxation process. Lattice temperature in this case is thus decreased with increasing time-delay, leading to a decrease in the respective spot area. More on this issue will be discussed in **Section 4.1.5**.

Next we investigate the suppression of the crater located at the center of the irradiated spot, marked with the red circle in **Figure 4.5(a)** during single and double pulse irradiation. An example of this crater formed at the center of the Si spot is best observed upon irradiation with 1000 laser shots and for time delays between SP and 0.5 ps (**Figure 4.5(a), (b)**). The size of this crater is decreasing with increasing pulse delay until it disappears for higher delays an example of which is presented in **Figure 4.5(c)** for 600fs time separation. Subsequently, when using higher pulse delays and higher number of pulses we have a combined decrease of the spot area and the crater formed in the center. Furthermore disappearance of the crater was observed to shift to higher pulse delays upon increasing the number of pulses. . Further experiments focusing on the properties of crater formation and disappearance may provide more valuable information regarding the dynamics involved during the DP irradiation.

Similar information is obtained from the spots irradiated with 12 pulses. **Figure 4.5(d),(e)** presents a contour analysis of the depth as measured from the AFM images. In **Figure 4.5(d)** we notice the formation of a crater with a mean depth of around 200nm appearing for SP at the center of the spot. The inset shows the image profile across the center and the mean depth plotted with the red line. **Figure 4.5(e)** shows the same contour analysis for a spot created again at 12 DP with a delay of 600fs. In this case a much smaller crater is formed.

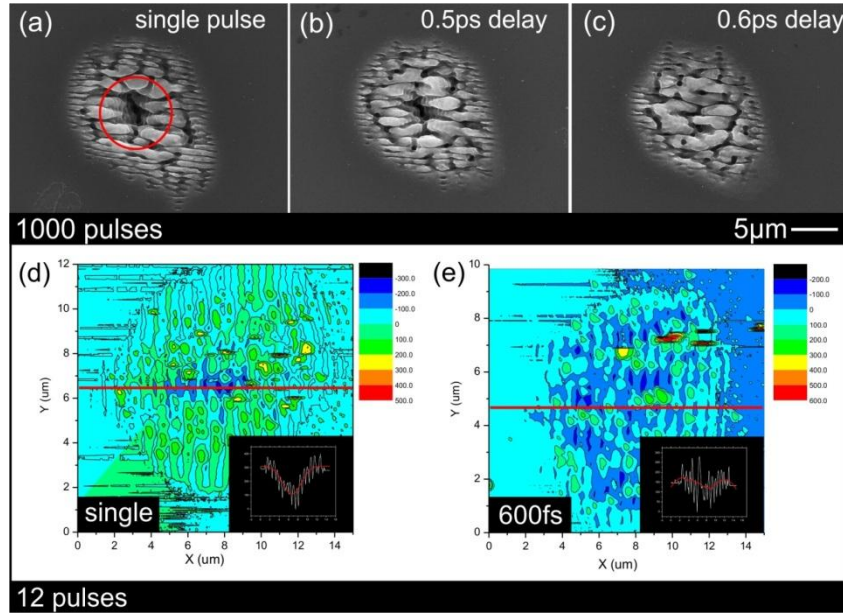


Figure 4.5: (a)-(c) Suppressions of the crater formed in the case of irradiating the silicon target with 1000 pulses for (a) zero pulse delay, (b) 0.5 ps and (c) 0.6 ps. Contour analysis of AFM images from the spots irradiated with 12 pulses for (d) zero pulse delay and (e) 600fs delay which shows the same crater suppression. Insets in (d),(e) illustrate a mean value of the crater plotted for easier crater observation.

4.1.4 Simulation results using double pulses

In this part we will present our effort to expand the applicability of the theoretical model described in **section 3.2** to the double-pulse irradiation case. Our aim is to show that the same model can be applied to predict the findings presented in this section.

Irradiation with a temporally tailored double pulse is described by the following expression which yields the intensity beam profile on the surface of the material.

$$I(r, z=0, t) = \frac{2\sqrt{\ln 2}}{\sqrt{\pi}\tau_p} \frac{F_d}{2} e^{-\left(\frac{r^2}{R_0^2}\right)} \left(e^{-4\ln 2 \left(\frac{t-t_0}{\tau_p}\right)^2} + e^{-4\ln 2 \left(\frac{t-t_0-t_{delay}}{\tau_p}\right)^2} \right) \quad (\text{Eq. 4.1})$$

Note also that **Eq. 4.1** is similar to **Eq. 3.19** with an additional term where t_{delay} corresponds to the temporal separation between the two pulses. It is assumed that the total laser beam fluence is equally shared by the two constituent pulses. F_d stands for the fluence of the laser beam and τ_p is the pulse duration (i.e. full width at half maximum), R_0 is the irradiation spot-radius (distance from the centre at which the intensity drops to $1/e^2$ of the maximum intensity); t_0 is chosen to be equal to $3\tau_p$. The choice of the value of t_0 is based on the requirement that at $t=0$, the intensity of the incident beam is practically

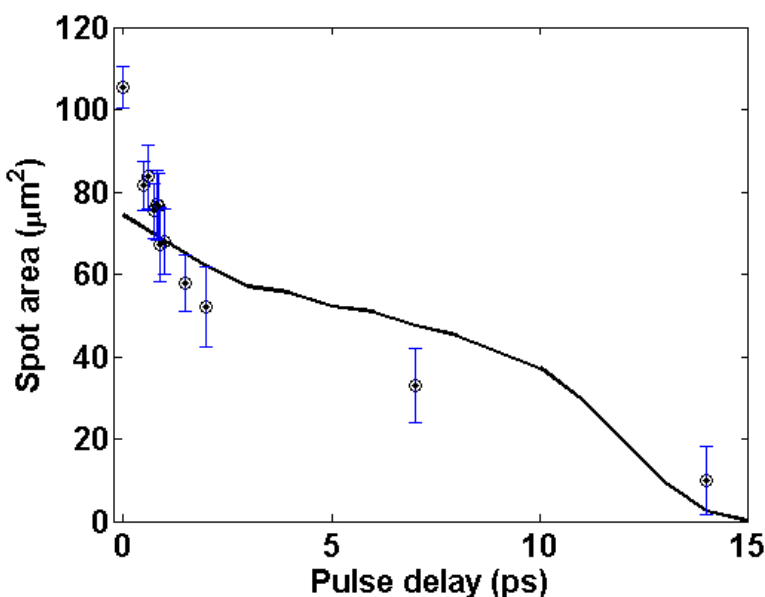


Figure 4.6: Comparison of experimental data (dots) with theoretical simulation (line) for the pulse separation dependence of spot area, for $NP=12$.

zero, at $t= t_0$ it reaches the maximum power while laser irradiation vanishes at $t=2t_0$.

Simulations reveal a monotonic decrease of the maximum area of the modified profile with increasing pulse delay. Furthermore, the spot area vanishes for $t_{delay}=16ps$ where the laser beam energy is not sufficient to melt the material and thereby no surface modification occurs. **Figure 4.6** shows the calculated theoretical line and the experimental results for $NP=12$. A fairly good trend is achieved while the spot disappears after 16 ps.

However there is a discrepancy between experiment and simulation for small time delay values. This may be partially attributed to the exclusion thermomechanical effects which are shown to give rise to additional routes of surface modification[REF]. However, it is beyond the scope of the present work to analyse phenomena of this nature. Furthermore there might be a discrepancy between the fluences used in the experiments and simulation due to calculation errors involved during the measurements, leading to higher crater areas.

4.1.5 Investigation of spot area decrease.

Previous theoretical models, try to explain the physical mechanisms occurring during DP laser-matter interaction in ablation conditions. When sub-ablation regimes is considered one must include the fact that the arrival of the second pulse, realizes a modified material (i.e. temperature, morphology) produced by the first pulse. This modified material will have different optical properties by means of reflectivity and absorptivity. Based on the electron phonon-relaxation time (τ_{e-ph}) of the material we can divide the physical mechanism in three parts.

- i) $t_{del} < \tau_{e-ph}$: For delays shorter than the τ_{e-ph} the energy is delivered into the electronic system with its temperature rising, leaving the lattice cold.
- ii) $t_{del} \sim \tau_{e-ph}$: For time delays close to the τ_{e-ph} , this initial energy distributed among the electrons is following distributed via carrier-carrier and carrier-phonon scattering and energy is transferred to the lattice. If the laser pulse intensity exceeds the melting or boiling point temperature threshold, melting, vaporization and ablation can occur. In our case the fluence of each individual pulse is not sufficient to modify the material, but is sufficient enough to heat the surface. This means that in a sequence of DP, the arrival of the second pulse interacts with a heated surface. This heated surface exhibits different optical properties from the non-irradiated surface. Reviewing **Table I** in the previous section, we can see that the interband absorption coefficient for Silicon is proportional to $a_{coef} = 0.112 e^{T_i/430}$. This means that the absorption increases exponentially and as a consequence the penetration depth ($1/a$) becomes smaller. Due to this, the second pulse arriving onto a heated material does not penetrate with the same rate leading to smaller modification. In combination with the fact that the fluence of the individual DP is not sufficient to induce modification, the spot area is decreasing gradually with increasing pulse separation. Finally after a certain delay (here $> 15ps$) the DP are sufficient far apart in order for the material not to be modified.
- iii) $t_{del} \gg \tau_{e-ph}$: For delays much higher than the τ_{e-ph} either the energy of the second pulse is not sufficient to modify the material and/or the pulse is completely shielded by the plasma formation of the first pulse leading to no further surface modification.

4.2 High and Low Spatial frequency control of ripples on ZnO films with ultrashort double pulses.

4.2.1 Introduction

Femtosecond pulsed lasers have received considerable attention as tools for materials structuring at micro and nano scale. Among the distinct advantages of fs laser sources are the rapid energy delivery, the minimization of the total energy deposition into the material and hence the reduction of the heat-affected zone^[182,183] As a consequence, fs lasers allow precise removal of the material, while the optimal interplay between the laser and material parameters allow the fabrication of features with dimensions beyond the diffraction limit.^[184,185] In particular, excitation of solid surfaces in air or liquid media by a fs laser beam close to ablation threshold may lead to periodic surface nanostructures in the form of near or sub wavelength ripples (also called laser-induced periodic surface structures, LIPSS).^[186,187,188] LIPSS have been extensively studied and observed in many types of materials including metals,^[189] semiconductors,^[190] ceramics^[191] and polymers^[192] and have revealed new interesting properties for optical, electronic, wetting and biological applications.^[193,194] The periodicities reported are either close to or multiple times lower than the laser beam wavelength, corresponding to low spatial-frequency (LSFR) and medium to high spatial-frequency (M/HSFR) ripples respectively. It is shown that the most critical parameters affecting ripples periodicity are the laser energy and number of pulses.^[195]

At the same time, there are other emerging possibilities of ultrafast laser-based modification techniques which may be exploited for expanding the breadth and novelty of applications. In particular fs pulsed irradiation induces fast energy deposition into the electronic system, temporally decoupled from the relaxation to the lattice and subsequent material modification. Hence it allows a realistic attempt towards understanding the fundamental mechanisms of the interaction. The use of temporally designed pulses appears in this context to be a feasible way of taking advantage of the materials specific response and to determine an optimum energy coupling required for controlling the outcome of processing.^[196,197,198] For instance, a desirable effect in laser processing applications is to control the surface morphology by modulating the energy deposited onto the material. Temporally shaped pulses provide the ability to temporally control such energy delivery. Indeed, various experimental studies have been performed to explore the effect of temporally shaped pulses on the morphology of metallic^[199,200,201,202] and dielectric surfaces.^[203,204,205] Although nanoripples' formation and related mechanisms had been extensively studied under single-pulse irradiation conditions, the physical processes

occurring upon irradiation with simple pulse shapes, as well as the consequences to the surface morphology, have been rarely investigated. Specifically, the influence of temporal control of laser energy delivery on the nanoripples' formation is yet to be explored.

In this work we present a simple and effective way of controlling the formation of high spatial-frequency (HSFR) or low spatial-frequency (LSFR) ripples on ZnO surfaces through irradiation with double fs laser pulses, tailored on a sub-picosecond time scale. It is shown that by proper choice of pulse separation one can switch from HSFR to LSFR formation and in this way control the final surface nanomorphology. Exploring novel techniques to fabricate and control nanostructures on ZnO is of high technological interest, considering the numerous applications of nanopatterned ZnO surfaces, inexpensive transistors^[206,207] for disposable electronics and low-cost LEDs,^[208] thin-film batteries^[209] and ITO replacement for displays and photovoltaic panels.^[210] Apart from the importance of practical applications it is concluded that, our results may provide further insight on the mechanism of nanoripples' formation, since the characteristic delay range in which the switch of ripple periodicity is observed is possibly related to the electron-phonon relaxation time of the material.

4.2.2 Methodology

The experimental setup used for the experiment is similar to the one in **section 3.3.1**. The laser pulse duration used was measured to be 120fs, and pulse delays range from 0-7 ps. Various numbers of laser shots and fluences were used ranging from 15 - 1000 and 0.55 - 4.5 J/cm² respectively. Information about the ZnO film preparation can be found in **section 2.5.3**.

4.2.3 Effect of laser fluence on ripple periodicity

III. Effect of laser fluence on ripple periodicity

Experiments have been performed on two separate ZnO films with thickness 1.7 and 3.2 μm , however similar results were obtained in both cases. Here we focus on the experiments performed using seven different fluences, at a constant number of 15 pulses. **Figure 4.7(a)** and (b) show SEM images of the spots obtained upon irradiation of the surface using two fluences, one close to the damage threshold and the other well above, being 0.55 J/cm² and 0.92 J/cm² respectively. Three distinct ripple periodicities are clearly observed on the spot obtained at the higher fluence (**Figure 4.7(b)**), while their periodicity decreases from the spot center towards the outer periphery. The respective values, calculated via a Fourier transform algorithm, are ~650nm (Low Surface Frequency Ripples - LSFR), ~221nm (Medium SFR - MSFR) and ~160nm (High SFR - HSFR). On the contrary, LSFRs are absent on the spot obtained when irradiating with the lower fluence (**Figure 4.7(a)**). **Figure 4.7(c)** summarizes the fluence dependence of the ripples period indicating that while HSFRs and MSFRs are generated at all fluences, LSFRs disappear below a critical fluence value that is close to the damage threshold of the material. It should be noted that for fluences above ~1.5 J/cm², the LSFRs disappear from the spot center while only MSFR and HSFR are visible at the spot periphery.

The physical mechanism behind the formation of LSFR is attributed to the optical interference of the incident laser beam with the excited surface plasmon at the solid air interface.^[211,212] Surface plasmons, are traveling waves of collective longitudinal oscillating electrons at optical frequencies that can be excited at the interface of a material-dielectric. An effective coupling of the incident electromagnetic radiation with the plasmon oscillation, leads to periodic modulation of the absorbed intensity. This interference effect propagates perpendicular to the electric field and is followed by a spatial and periodical modulation of energy deposition, generating finally the LSFR.

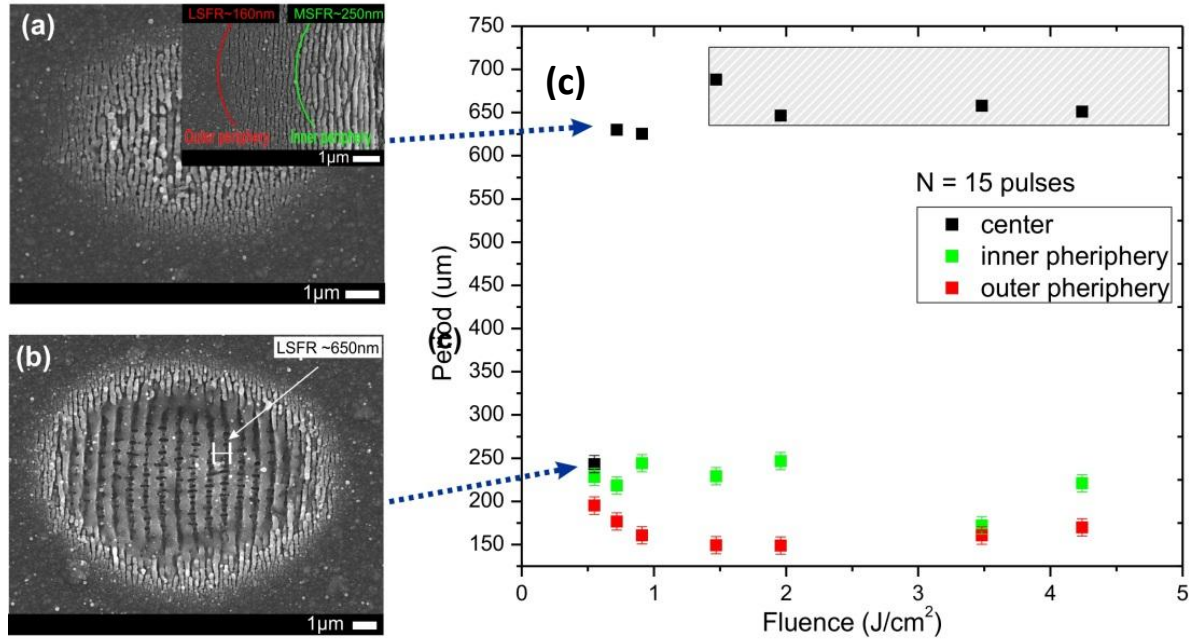


Figure 4.7: SEM images of the ZnO spots obtained upon irradiation (a) close to the damage threshold using a fluence of 0.55 J/cm² and (b) above the damage threshold using a fluence 0.92 J/cm². (c) Graph of the ripples period versus the irradiation fluence. The blue line connects the SEM images with the two points on the graph.

Two are the dominant mechanisms proposed and reviewed below for the creation of subwavelength ripples (M/HSFR). The first one is attributed to the generation and interference of a second harmonic wave^[213] while the second to a grating-assisted surface plasmon-laser coupling effect.^[214] For high laser fluencies N_e (here fluence higher than ~ 0.9 J/cm²) the excited carrier density can reach above 10^{-21} cm⁻³ and as a result, the refractive index of ZnO changes significantly. As a result, the initial transparent material turns into one with a metallic character. As a consequence the surface reflectivity of the ZnO film increases and starts to significantly absorb the incident radiation. In this case the formation of LSFR occurs. On the other hand, for carrier densities in the range $10^{-20} < N_e < 10^{-21}$, (fluence of $0.5 - 0.8$ J/cm²) the peak intensity is high enough to generate a second harmonic wave on the material surface. The interference of this wave with the surface electromagnetic wave scattered at 400 nm gives rise to the HSFR with periodicity close to ~ 200 nm. The second mechanism is attributed to a grating coupling effect. R.W. Wood^[215] was the first to propose coupled surface plasmon polaritons using the grating configuration. In particular, incident radiation at an angle θ with respect to the normal plane of the surface

can be scattered from the grating, increasing or decreasing the component of its wave vector by integer multiples of the grating wave vector k_g ($k_g = 2\pi / \Lambda$). This gives rise to diffracted orders which lead to the formation of HSFR. When the fluence is high, the strong thermal effects are dominating over the grating-coupling effect and the generation of LSFR occurs due to the interference mechanism. In contrast, for fluences when non thermal ablation effects take place, the grating coupling effect becomes dominant and assists the generation of HSFRs. Accordingly, the above mechanism is able to describe the generation of ripples with periodicities multiple times lower than the laser wavelength.

IV. Pulse separation dependence ripple periodicity

A proper way to control the flow of laser energy deposition on the material is the use of temporally shaped laser pulses. A simple pulse shape is created by splitting the initial Gaussian pulse in two equivalent pulses of the half intensity/same duration, separated by a delay time, τ_d . **Figure 4.8** presents an example of SEM images of different spots attained, following irradiation with 15, 20 and 50 sequences of two identical pulses of 1.1 J/cm^2 , at various τ_d . The respective spots obtained after irradiating the surface with 15, 20 and 50 double laser shots of 0.55 J/cm^2 fluence are also shown, which are almost identical to those obtained using no pulse separation (**Figure 4.7(a)**). It is clear that using a fluence of 1.1 J/cm^2 for single

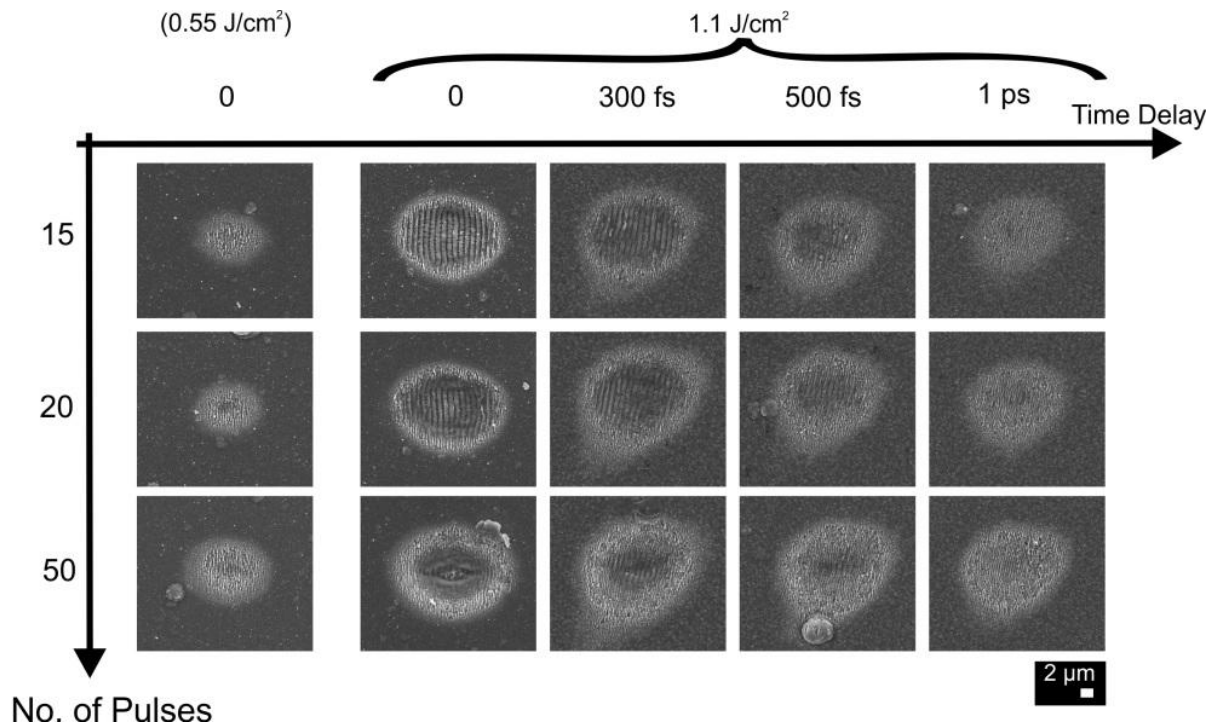


Figure.4.8: SEM images of different spots for irradiation with 15, 20 and 50 sequences of two identical pulses of 1.1 J/cm^2 , at various time delays.

or double pulse irradiation with small time delays ($\tau_d < 500 \text{ fs}$), all three types of ripples are generated. On the contrary, after double-pulse irradiation with $\tau_d > 500 \text{ fs}$ the LSFRs disappear from the spot center, being replaced by MSFR and HSFR at the periphery. Similar to **Figure 4.7**, the corresponding dependence of the different ripple periodicities observed on τ_d is presented **Figure 4.9(b),(c)** for zero

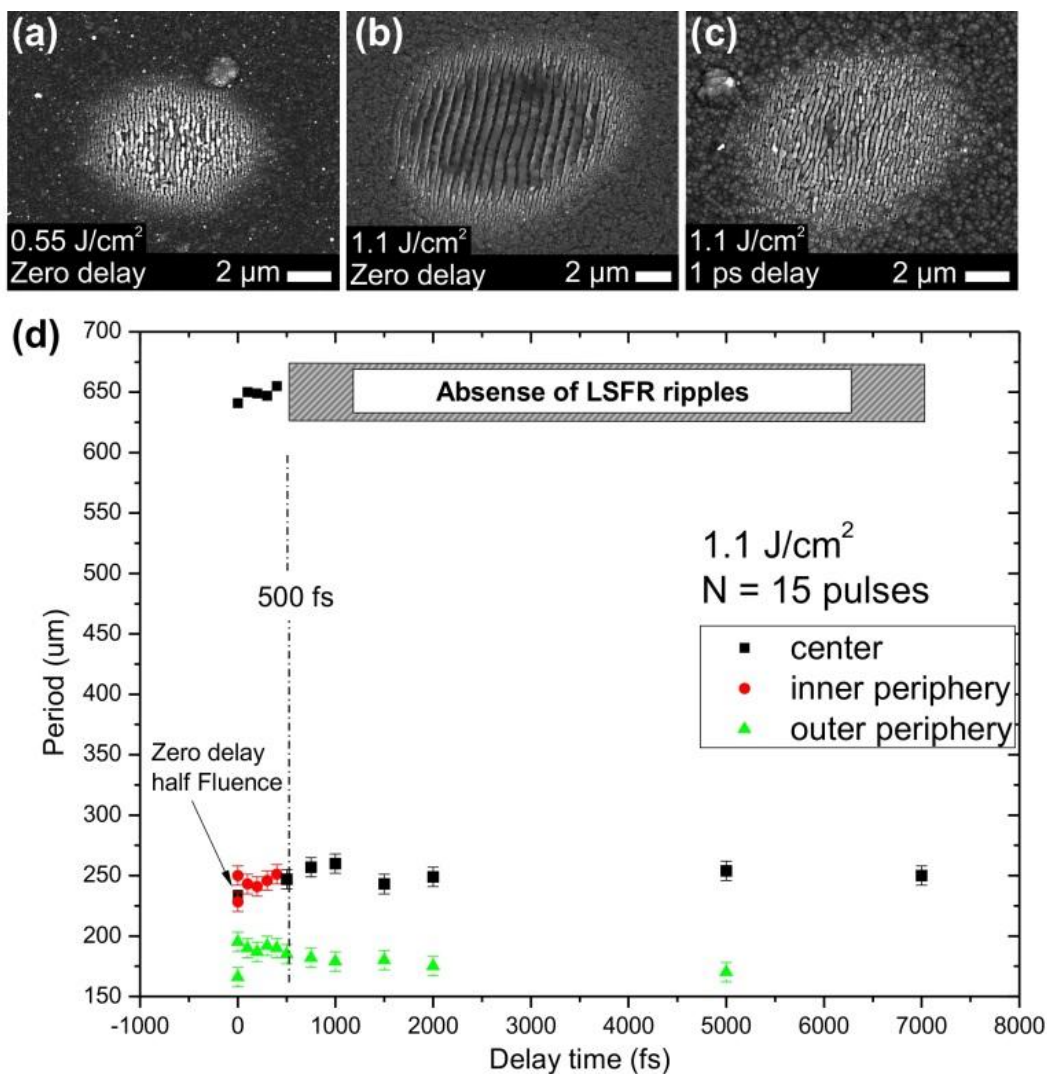


Figure. 4.9: The corresponding dependence of the different ripple periodicities on pulse delay time. Switch between LSFRs and MSFR/HSFRs occurs via proper variation of the pulse separation time. **(a)** Spots irradiated with a fluence of 0.55 J/cm^2 and zero pulse delay. **(b), (c)** fluence of 1.1 J/cm^2 with and zero pulse and 1 ps time delay respectively. **(d)** Ripples period vs pulse delay for 15 laser pulses and fluence of 1.1 J/cm^2 . Around 500 fs periodicity changes from LSFR to MSFR

pulse and 1 ps time delay, indicate that one can switch between LSFRs and MSFR/HSFRs via proper variation of the pulse time separation.

The characteristic time delay of around 500 fs as shown in the graph in **Figure 4.9(d)**, for which the change from LSFR to M/HSFR occurs, may possibly be related to the electron-phonon relaxation time (τ_{e-ph}) of the material. Experimental studies on the ultrafast dynamics of crystalline ZnO films reported carrier cooling times of $\sim 0.8 \text{ ps}$ ^[216] and 1 ps . ^[217] Furthermore theoretical studies ^[218] predict that $\tau_{e-ph} \sim 0.7$

ps. The above values are close to the characteristic τ_d for which the switching of the ripple periodicity occurs in our experiments. In particular, for $\tau_d < \tau_{e-ph}$ the second pulse arrives before the energy absorbed by the first pulse is transferred to the lattice. Considering that material modification takes place after the energy is transferred to the lattice, the final ripple profile should be similar to that of the single pulse of the same total fluence of 1.1 J/cm^2 . Therefore, according to the fluence dependence of the ripple periodicity presented in the previous section, LSFRs are generated. On the other hand, for $\tau_d > \tau_{e-ph}$ the second pulse arrives when the energy of the first pulse is already transferred from the electronic system to the lattice. Accordingly, M/HSFRs are generated due to the action of the first pulse, which has half the intensity compared to that corresponding zero τ_d , while the second pulse interacts with the already formed ripple profile.

The above effect may be exploited for tailoring the outcome of fs laser nanopatterning of ZnO surfaces. This is presented in **Figure 4.10** showing two scan lines fabricated at zero (**Figure 4.10 (a)**) and 1 ps (**Figure 4.10 (b)**) delay times respectively. In accordance to the switching effect described above, the periodicity of the respective nanopatterns changes from $\sim 650\text{nm}$ to $\sim 220\text{nm}$. This further demonstrates the control over different nanopattern formation upon changing the pulse separation which can expand the breadth and novelty of applications of nanopatterned ZnO surfaces. Experiments are currently in progress to further explore the properties of large area ZnO surfaces, which are nanopatterned using different time delays.

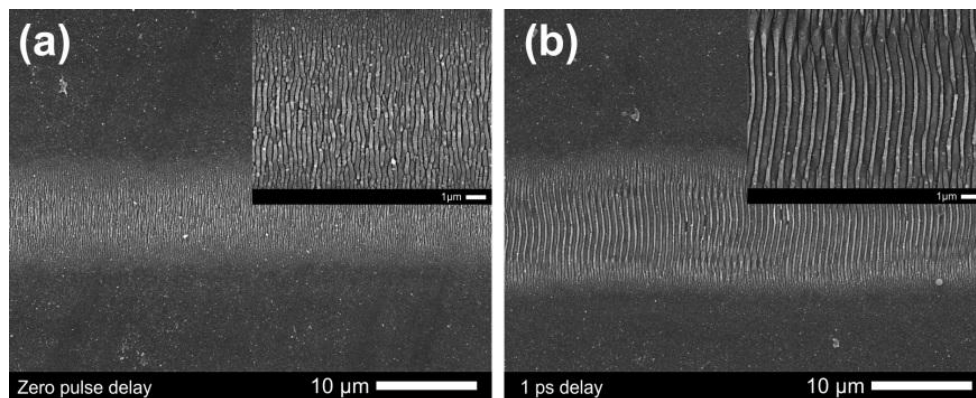


Figure 4.10: Two scan lines fabricated at (a) zero and (b) 1 ps delay times. The periodicity of the respective nanopatterns changes from $\sim 650\text{nm}$ to $\sim 220\text{nm}$.

Finally, the surface modification attained at the highest τ_d is very similar to that induced by a single pulse of the half fluence, not only in terms of the ripple characteristics but also in terms of the affected area. Indeed, a gradual decrease of the modified area is observed upon increasing the pulse separation, indicating that for long delay times the material responds as if it receives only half of the fluence. This is indicated in **Figure 4.11** presenting the LSFR, HSFR+MSFR and total spot areas as a function of τ_d . Furthermore, it is clear that for $\tau_d < 500$ fs the LSFR area decreases at the expense of that of HSFR+MSFR while the total area gradually decreases upon increasing pulse separation. A spot area decrease has been previously studied for certain semiconductors and metals both experimentally^[219,220] and theoretically.^[221]

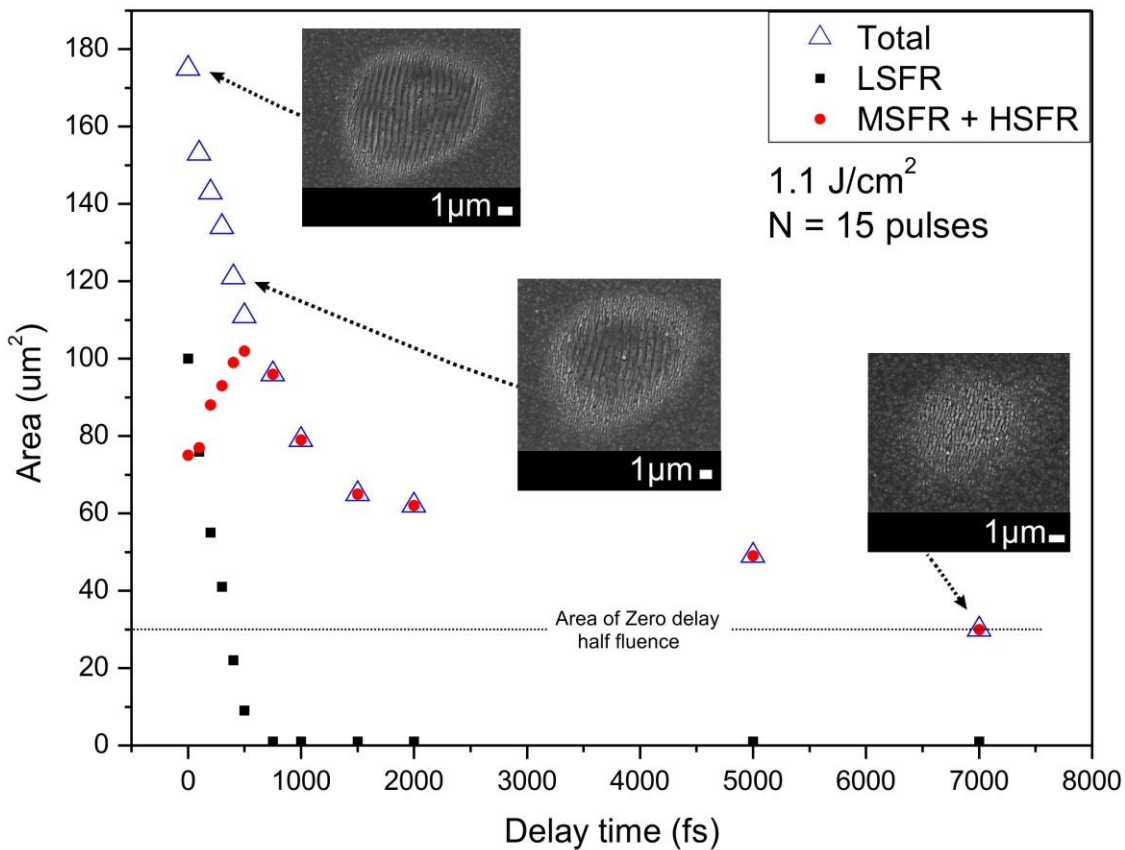


Figure 4.11: Graph of the LSFR, HSFR+MSFR and total spot areas versus the delay time.

3.3 Conclusion

Comparison of Si and ZnO results

From the discussed results it is obvious that certain ripple types (M/HSFR) are not formed, or at least are formed much harder on Silicon. This is attributed to the fact that the generation of non-linear phenomena (like SHG, multiphoton absorption, etc.) which are responsible for the formation of M/HSFR are not easily generated in metallic and in low-bandgap materials. Silicon which has a relatively low bandgap behaves similar to a metal where the formation of LSFR is typically observed. This is also confirmed by A. Borowiec et al.^[222] showing that HSFR are created more easily on semiconductors with band gaps higher than $\sim 2\text{eV}$. In ZnO with a bandgap of 3.3eV , the formation of M/HSFR is favored due to the fact that non-linear phenomena like SHG can be generated more easily,. Nevertheless recent studies have demonstrated the formation of HSFR in metals^[223,224] and Silicon^[225] at fluences very close to the damage threshold number of pulse. The authors showed that the reduced period is caused by an increase of the real part of the effective refractive index of the air-metal interface when nanostructures develop and affect the propagation of surface plasmons.

Chapter 5

Application of Silicon micro/nano structured surfaces.

Introduction

Silicon is a very well studied material used in a variety of applications. Extending and researching for new ones is always challenging and might lead to a variety of new possibilities. Surface structuring of the material plays a key role towards this direction as the remarkable new and altered properties offer not only insight for understanding fundamental processes but also finding new novel application.

In this chapter we present our work on how silicon structured surfaces can be used as basis for novel applications. We divide our work in three major fields: **A)** Field emission, **B)** Wetting properties and **C)** Biological applications.

Field emission refers to the emission of electrons from a solid cathode (generally in the shape of a sharp tip) into vacuum under the influence of a strong electric field.^[226] The pointed or conical shape of the cathode strongly enhances the electric field at the tip, originating from biasing the cathode negatively with respect to a nearby anode. Field emission occurs when electrons tunnel through the potential energy barrier at the interface between the cathode and the vacuum. This is in contrast to the more familiar phenomenon of thermionic emission, wherein electrons are emitted from a cathode when they acquire

sufficient thermal energy to overcome this potential barrier. Here we will present results concerning the stability and durability of metal coated Silicon spikes

Wetting refers to the ability of a liquid to maintain contact with a solid surface, resulting from intermolecular interactions when the two are brought together. The degree of wetting (wettability) is determined by a force balance between adhesive and cohesive forces. Fundamentals will be discussed at the beginning of this section. Following a basis for novel application taking advantage of the wetting properties will be presented. Our main interest here concerns applications where we can dynamically control a liquid drop by means of switching the wettability of a surface on demand.

Biological applications refer to the fabrication of artificial cell culture scaffold designed to mimic the natural extracellular environment features, in a way that cells can function as if they are in vivo. In this respect, designing surfaces for controlling cell–material interactions is a considerably interesting subject, highly significant in the development and eventual success of implantable medical devices and engineered tissues^[227,228]. Using different approaches, various materials have been surface engineered in order to guide cell adhesion and modulate cell–biomaterial interactions^[229,230], indicating that cell growth, division and migration are highly dependent on their immediate culture substrate. In this section we demonstrate the ability to tune cell adhesion using biomimetic artificial Silicon substrates in a 3D-design, comprising hierarchical micro- and nanostructures.

A) Field emission: Cold cathodes

Introduction

In the last few years a considerable amount of research effort is being devoted towards a technology that could supersede liquid crystals in flat panel displays. Some of the goals are thinner self-luminous and energy efficient screens that will have larger viewing angles, higher contrast and a better response time per pixel. This would allow faster scan rates by eliminating blurring effects. *Field-Emission Devices* (FEDs) contain structures that emit electrons when charged to a low (negative) potential under vacuum; the electrons excite light emission from fluorescent screens. Such devices could serve as flat-panel displays with good picture quality at low power consumption and low cost.^[231] The key to these properties is to produce cathodes that will emit as high current density at as low voltage as possible and the only way to achieve both is by producing oriented tip or needle type structures^[232]. FEDs of this type have also to overcome another obstacle before they become useful for consumer applications. The emitters have to become stable to within less than 1% and durable for long-life operation (of the order of at least 10000 hrs), under moderate vacuum conditions (of the order of 10^{-4} Pa or more), which are feasible for their miniaturized sandwich design, under current vacuum technology capabilities.^[233]

5.1 Fundamentals

I. Field emission from metals

Field emission is a quantum-mechanical phenomenon in which electrons tunnel through a potential barrier at the surface of a solid as a result of the application of a large electric field. Field emission is distinct from thermionic emission (**Figure 5.1(a)**) and Shottky emission (**Figure 5.1(b)**) in which electrons acquire sufficient energy via heating or energy exchange with photons, respectively, to overcome (go over) the potential barrier. In field emission an external electric fields of the order of 10^7 V cm^{-1} are required for appreciable electron currents. This is true for emitter materials with work functions of approximately 4.5 eV such as Si, W and Mo. **Figure 5.2** shows a typical test configuration employed for measuring the emission current of a field emitter diode. The presence of the electric field makes the width of the potential barrier finite and therefore permeable to the electrons. This can be seen with the help of **Figure 5.1(c)** which presents a diagram of the electron potential energy at the surface of a metal.

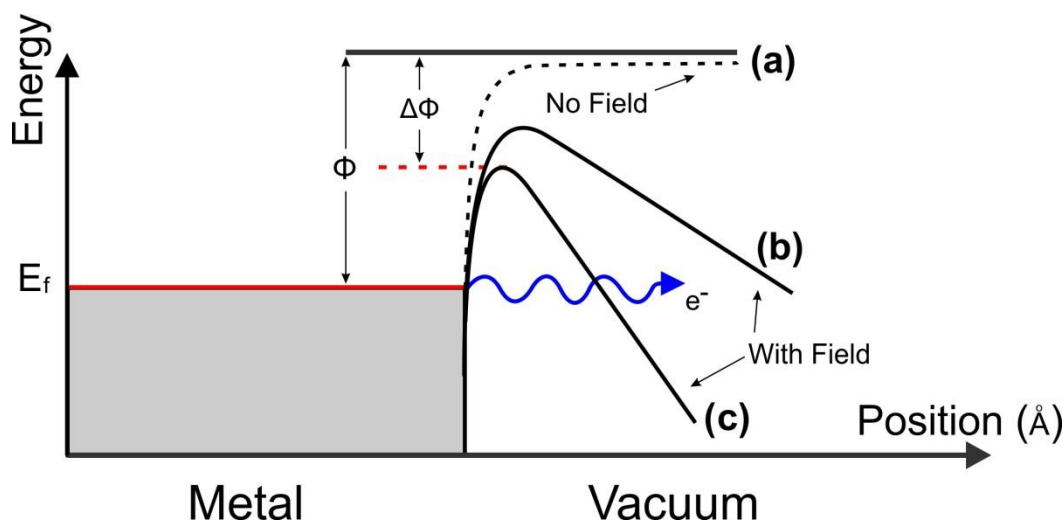


Figure 5.1: Diagram of the potential energy of electrons at the surface of a metal. (a) thermionic emission, (b) Shottky mission and (c) Field emission. E_f is the Fermi level of the metal and Φ is the barrier height or the work function

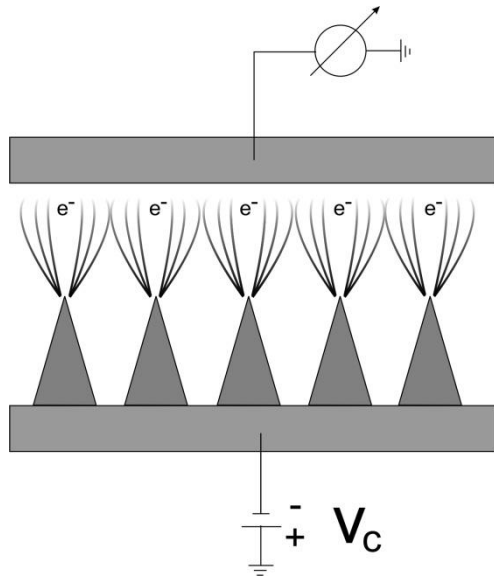


Figure 5.2: Schematic of a test configuration for obtaining $I - V$ characteristics of a field emitter array diode

The height of the barrier is equal to the work function of the metal, Φ , which is defined as the energy required to remove an electron from the Fermi level E_F of the metal to a rest position just outside the material (the vacuum level). The solid lines ((a),(b),(c)) in **Figure 5.1** correspond to the shape of the barrier in the presence of the external electric field. As can be seen, in addition to the barrier becoming triangular in shape, the height of the barrier in the presence of the electric field E is smaller, with the lowering given by

$$\Delta\Phi = \left(\frac{\varepsilon E}{4 \pi \varepsilon_0} \right)^{1/2} \quad \text{Eq. 5.1}$$

where e is the elementary charge and ε_0 is the permittivity of vacuum.

In order to reach higher fields at reasonable voltages, fabrication of field emitters with protruding objects to take advantage of field enhancement from the regions with high curvature is required. The current of an array of emitters is governed by the equation:

$$J = naJ_{FN} \quad \text{Eq. 5.2}$$

where n is the number of emitters in the array, a the emitting area per tip in cm^2 and J_{FN} the Fowler-Nordheim current density. It can be also shown from the time-independent Schrödinger equation that:

$$J_{FN} = a_{FN} \cdot (\beta V)^2 \cdot \exp\left(-\frac{b_{FN}}{\beta V}\right) \quad \text{Eq. 5.3}$$

$$\text{Where } a_{FN} = \frac{A}{1.1 \cdot \Phi \cdot e \sqrt{\Phi}} \quad \text{and } b_{FN} = 0.94 \cdot B \cdot \Phi^{\frac{3}{2}}$$

with $A = 1.54 \cdot 10^{-6} \text{ AV}^{-2}\text{eV}$ and $B = 6.83 \times 10^7 \text{ Vcm}^{-1}\text{eV}^{-3/2}$. Finally β is the field enhancement factor ($\beta \geq 1$), describing the amplification of the electric field (e.g. on a sharp tip).

It is usual to express the local field at the tip by:

$$E_{loc} = \beta E = \beta \frac{V}{d} \quad \text{Eq. 5.5}$$

with β the field enhancement factor in cm^{-1} . The Fowler – Nordheim current of an array is then given by:

$$J = na \frac{1.54 \times 10^{-6} (\beta V)^2}{\Phi} \exp \left(-6.87 \times 10^7 \frac{\Phi^{\frac{3}{2}} v(y)}{\beta V} \right) \quad \text{Eq. 5.6}$$

Where $v(y) = \cos(\frac{1}{2}\pi y)$

The Fowler – Nordheim can be rewritten as

$$\ln \left(\frac{J}{V^2} \right) = \ln \left(1.54 \times 10^{-6} \frac{n a \beta^2}{\Phi} \right) - 6.87 \times 10^7 \frac{\Phi^{\frac{3}{2}} v(y)}{\beta V} \quad \text{Eq. 5.7}$$

Or, if \log is preferred, as

$$\log \left(\frac{J}{V^2} \right) = \log \left(1.54 \times 10^{-6} \frac{n a \beta^2}{\Phi} \right) - 2.98 \times 10^7 \frac{\Phi^{\frac{3}{2}} v(y)}{\beta V} \quad \text{Eq. 5.8}$$

By plotting the emission current in the form of $\log(J/V^2)$ versus J/V a straight line should be obtained with the slope proportional to the $\Phi^{3/2} v(y)/\beta$ and an intercept proportional to $n\beta^2/\Phi$.

II. Field emission from semiconductors

The fundamental processes regarding field emission in semiconductors can be derived parallel to the theory in metals. Field emission from semiconductors like Silicon consist of two processes: a) flux of electron to the surface and b) the transmission of electrons through a surface barrier by tunneling when

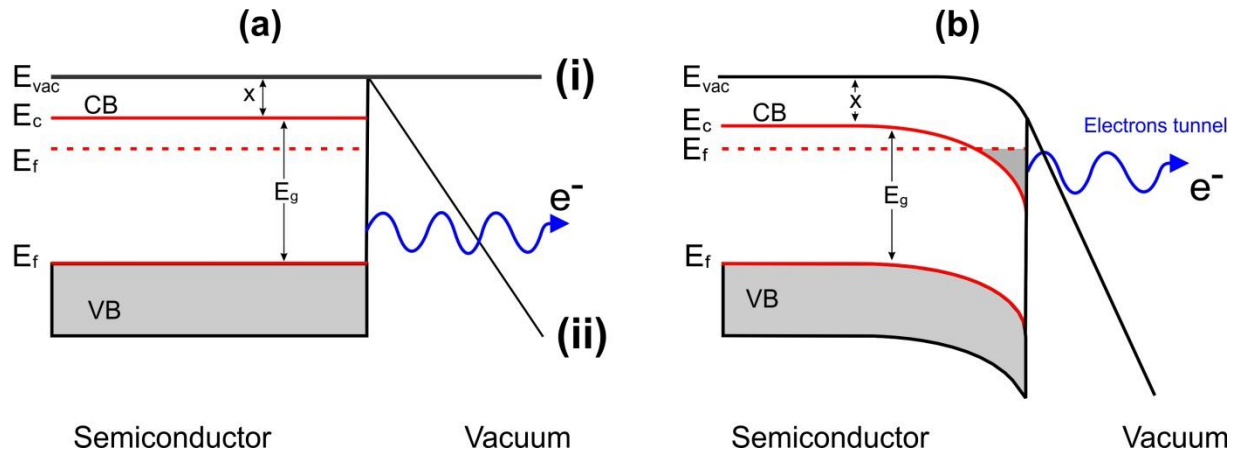


Figure 5.3: Schematic of the band diagram of silicon near the semiconductor-vacuum interface. **(a)**, (i) without applying an electric field, (ii) in the presence of an applied field and **(b)** in the presence of an applied field with its penetration into the surface taken into account.

the the barrier width at the surface is reduced. When the penetration of the applied electric field is neglected, tunneling can occur from the valence band if the applied field is sufficiently intense as illustrated in **Figure 5.3 (a)-ii**. If the penetration of the applied electric field into the semiconductor is taken into account, the picture becomes somewhat more complicated. The electric field in this case can cause the deformation of the potential experienced by the electrons (**Figure 5.3(b)**).

The surface electric field is E_s , is again related to the applied gate voltage V_g through $E_s = \beta V_g$, where β is again the field enhancement factor. For the “ball-in-a-sphere model”^[234,235] which relates the field factor to the tip radius r and the aperture R is given by:

$$\beta = \left[\frac{1}{r} - \frac{1}{R-r} \approx \frac{1}{r} \right]$$

The I-V characteristics of Si field-emitters arrays obey the following FN equations to the first order:

$$J = a_{FN} V_g^2 \exp\left(\frac{-b_{FN}}{V_g}\right) \quad \text{Eq. 5.9}$$

Where: $a_{FN} = \frac{a \cdot A \cdot \beta^2}{1.1\varphi} \left(B \frac{-1.44 \times 10^7}{\varphi^{1/2}} \right)$

$$b_{FN} = 0.95 \cdot B \cdot \varphi^{3/2}$$

$$V_g = bE$$

φ : surface barrier height of the emitter tip

$$A = 1.54 \times 10^{-6},$$

$$B = 6.87 \times 10^7$$

5.2 Stability and durability of metal-coated silicon spike cold-electron emitters.

In this section our aim is to evaluate the evolution of the performance of high aspect ratio Si-spike field emission cathodes, passivated with different metallic coatings. In particular, we take advantage of the unique morphology of femtosecond laser fabricated Si spikes as a mean to improve the stability and durability of Si-based field emission cathodes. A major problem of Si-based cathodes is the degradation of performance upon prolonged operation attributed to local oxidation of field emission sites. We demonstrate that passivation of the emitters with a thin metallic coating is an effective solution to this issue. The metallic coating we have employed for the experiments span a range of work functions from 2.9eV (Gd) to 5.4eV (Au). Tungsten and Molybdenum were chosen because they are commonly utilized as single tip cathodes in electron guns.^[236] Chrome and Titanium were also chosen as metallic alternatives, with similar work function, to n-type silicon.

5.2.1 Methodology

A $2 \times 1 \text{ cm}^2$ Silicon structured surface was fabricated at a fluence of 0.9 Jcm^{-2} as described in **section 2.4.1-1** following a cleaning process (**section 2.5.1**). The typical morphology of the structured area is shown in **Figure 5.4**. After irradiation, the surface of silicon exhibits high aspect ratio spikes, which have conical shapes of about $5 \text{ }\mu\text{m}$ height and 40 degrees angle opening. The density of the spikes is $13 \times 10^6 \text{ cm}^{-2}$ and remains approximately uniform across the total processed area of $2 \times 1 \text{ cm}^2$. Close investigation of the apex of the spikes reveals that they end to approximate hemispheres with diameters of $\sim 600 \text{ nm}$. Furthermore the surface of each spike is rough, full of secondary protrusions which have an approximate diameter of less than 100 nm or a mean height that is lower than 50 nm . This image shows that fs laser structuring of the silicon surface results in the production of salient features that differ from each other by two orders of magnitude; $5 \text{ }\mu\text{m}$ spikes that are overlaid by $50 - 100 \text{ nm}$ high protrusions. This homogeneous template was then diced to result to 12 similar substrates that were subsequently coated with metals. Au, Ti and Cr were sputter coated with a Baltec MED-020 dc magnetron system pumped to below $5 \times 10^{-3} \text{ Pa}$ by a turbomolecular pump. Gd, W and Mo were thermally evaporated under a base pressure of 10^{-4} Pa . All thickness values were measured in-situ by a quartz crystal thickness monitor. All coatings were performed simultaneously on flat silicon and glass substrates and were found uniform with no visible signs of cracks when imaged with a high resolution JEOL JSM-JSF700F Field Emission

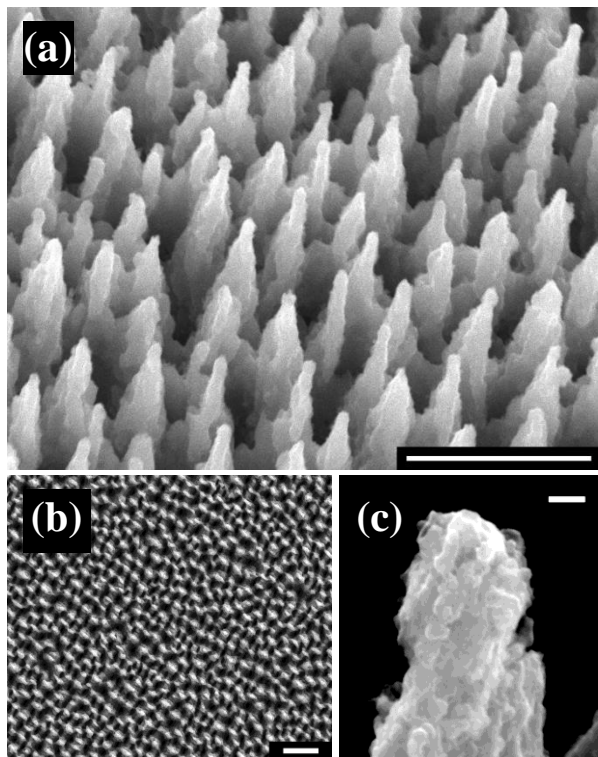


Figure 5.4: Scanning Electron Microscopy images of laser patterned spike arrays on Silicon. **(a)** 45° view (scale bar 10 μm) **(b)** top view (scale bar 10 μm) and **(c)** FE-SEM magnification of the apex of a single, relatively sharp spike (scale bar 200 nm).

against high voltage surges by a MOSFET limiter.^[238] All current density values given throughout this section refer to the ratio of current measured divided by the actual area covered by the incoming electrons at the anode. This area was determined for each metal separately by imaging the very thin deposit of organic contaminants induced by the highly energetic e-beam at the anode after the measurements in time were taken.^[239] The pressure was kept constant to a value of $4 \pm 1 \times 10^{-4}$ Pa during the temporal characterization of all samples.

It was observed (**Figure 5.4(b)**) that a serious change in spike geometry appeared upon metal deposition above 50nm. At first, the spikes appear wider compared to the bare Si ones due to the presence of the thick gold film. Secondly each spike is observed to acquire a sponge like morphology which is full of large protrusions of the order of 200 nm on top of which salient, nanoparticle-like, features can be resolved. This would have an impact on field emission behavior that is not wanted in the present study.

Scanning Electron Microscope (FE-SEM). All structured surfaces were characterized morphologically by normal SEM images. The samples were tested as cold cathode field emitters in a short-circuit protected planar diode system, under high vacuum conditions (5×10^{-4} Pa or lower). The experimental setup can be found in **section 2.9**. Current – voltage (I-U) curves were taken by means of a voltage source, which applied sufficient voltage between the anode and the cathode to extract the electrons out of the microtips. Several emission cycles were initially taken in order for the I-U curves to become relatively stable and reproducible. Each curve presented is the average of at least five consecutive I-U sweeps after the aforementioned seasoning^[237] of the emitting surfaces and each current value is the mean of 10 consecutive current samples per voltage. The substrate-to-anode distance was always set to 100 μm . The emission current was monitored during I-U experiments and temporal characterisation using an electrometer protected

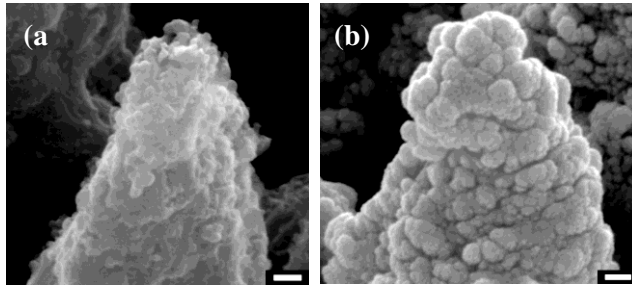


Figure 5.4: SEM image of a 10 nm (a) and a 200 nm (b) thick Au covered Si spike. Very thick metal films result in a prominent change of spike surface morphology (scale bar 200 nm).

For this reason the deposited thickness was limited to 10 nm for which no apparent change in morphology is observed as can be seen in comparing **Figures 5.4(a)** and **5.4(b)**. **Table I** below summarized the work functions of the metal used for coating the Si spikes.

Table I

Metal	Si	Gd	Ti	Cr	Mo	W	Au
Φ (eV)	4.05	2.9	4.3	4.5	4.5	4.5	5.4

5.3.2 Field emission of metal coated Si spikes - Improvement of performance with operation

In **Figure 5.5(a)** we plot on a logarithmic diagram the dependence of the measured current density from the applied average field for all metal deposits and the bare Si spikes in the pristine state.

The total field range can be divided in three main regions: a) one of no emission at low bias, b) the field emission region between 8 and 20 V/ μm where a steep rise of the current is observed and c) the “saturation” region where the current still increases with bias voltage but with a markedly lower slope.

We observe that there is no significant change in the turn-on field for emission, F_{to} , with the work function, Φ , of the emitting surface, for Φ_s spanning from 2.9 eV (Gd) to 5.4 eV (Au). Only Ti resulted in an observable decrease of F_{to} . **Figure 5.5(b)** shows the same data in a Fowler-Nordheim (FN) plot in which the slope, b_{FN} , of a linear fit of the field emission region is proportional to the ratio $\Phi^{1.5}/\beta$, where Φ is the work function of the emitting surface and β is the field enhancement factor associated with the densification of the equipotentials in the vicinity of the emitting spikes. The absolute values of the slopes, b_{FN} , of these fits lie in the range of 220 – 280 $\mu\text{m}/\text{V}$, with the exception of Cr for which $b_{FN} = 380 \mu\text{m}/\text{V}$; they are thus similar to each other showing no systematic trend with Φ .

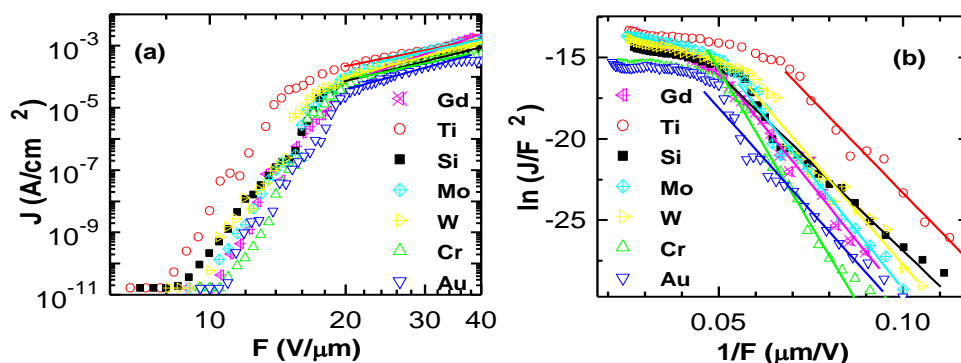


Figure 5.5 (a) Logarithmic plot of the emission current density, J , observed for the silicon spikes covered with 10 nm of various metals as a function of the mean applied field, F . The “Si” data stand for bare Si spikes. **(b)** Fowler-Nordheim plot of the data of **(a)**. The solid lines represent linear least square fits of the data.

Current densities are similar for all metal coatings and are close to those found in the literature for bare silicon field emitter arrays. These are, however, orders of magnitude lower than those routinely observed from metallic field emitters.^[240] In the saturation region the data can be fitted by power law curves as shown by the linear least square fits of the corresponding data in the log plot of **Figure 5.5(a)**. The power law exponent does not show any systematic dependence on the work function of the metal coating; its mean value is 3.4 ± 0.4 . Gd is the only exception with a markedly higher slope of 5.2. Finally it was verified by secondary conductivity experiments that the back contact of each cold cathode was able to supply at least three orders of magnitude higher current than that observed in our experiments thus eliminating the possibility of current saturation originating from a potential blocking effect.

The long term durability of the emitted current density, J , was tested for all samples at a bias voltage (or average electric field) that gave an initial current of approximately 5 μA. In **Figure 5.6** we plot J as a function of time for the bare and the metal coated silicon spikes. The marked different aging of different samples is evident. Bare silicon has the worst durability of all, closely followed by tungsten and molybdenum which do not last a day. Gadolinium and titanium also turn off after a little more than a day of operation. Gold and chromium on the other hand did not stop emitting electrons within the 3-day time scale of our experiments. Moreover these two metal coatings show a clear increase of the emitting current with time, which points to a potentially much longer operational life than that covered by our experiments.

Gold and chromium coated spikes were tested electrically after the 72h operation in order to detect any changes in their current-voltage behavior caused by prolonged operation. **Figure 5.7** presents the current density, J vs. average field, F data and the corresponding Fowler-Nordheim (FN) plots for both metal coatings in the pristine and final state for comparison.

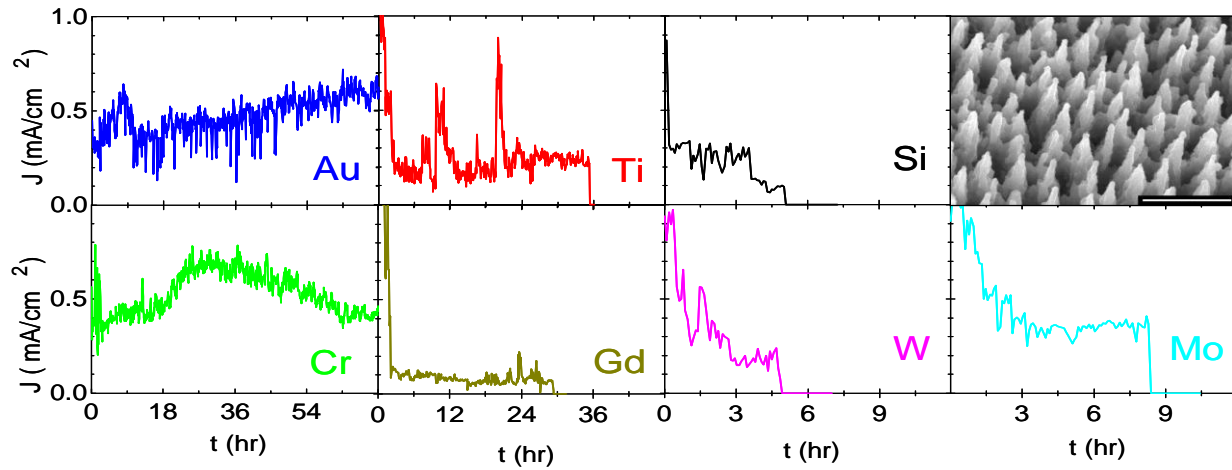


Figure 5.6: Current density vs. time under continuous operation at constant voltage and background pressure for the bare and coated Si spikes. The upper right picture is a SEM micrograph of the structured surface. Scale bar is 10 μm .

The J - F plot shows a drop of the turn-on field for emission for both metals. This improvement is more pronounced in the case of chromium coated spikes, which start to emit electrons at half the field that was initially necessary. The absolute slope of the FN plot of the gold surface is $280 \pm 30 \mu\text{m/V}$ initially and remains exactly the same at the end of the experiment. On the other hand Cr shows a pronounced decrease in the slope by more than a factor of 2, from $380 \pm 30 \mu\text{m/V}$ to $160 \pm 30 \mu\text{m/V}$.

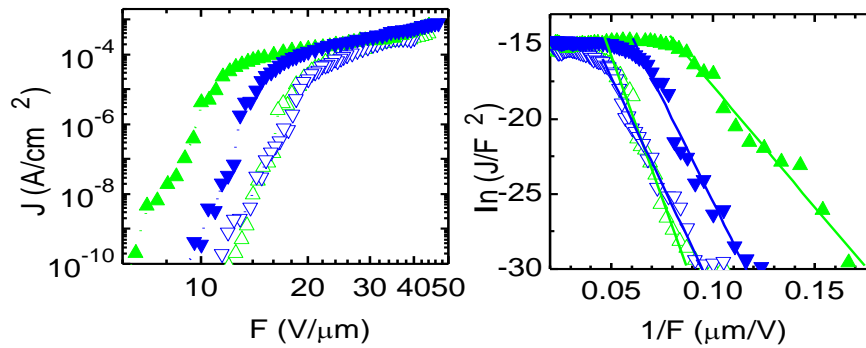


Figure 5.7: Logarithmic plot of the emitted current density as a function applied average field for the chromium (up triangles) and gold (down triangles) coated surfaces in the pristine (open symbols) and long-term operated (solid symbols) state respectively. The inset presents the Fowler-Nordheim plots of the corresponding data (see text). The dotted lines are guides to the eye. The solid lines are linear least square fits of the data.

5.2.3 Performance and saturation mechanisms analysis

Both results of this study were unexpected: a) thin coatings with metals of different work function do not have a significant effect on the cold-electron emission behavior of silicon spikes in their pristine state and under moderate vacuum conditions and b) coating with specific metals results in marked enhancement of the emitters' long-term performance. Furthermore, Si spikes emitters coated with gold or chromium show field emission characteristics improving with time in typical working conditions.

The similarity of the FN slopes of all metal coatings in the pristine state suggests that the actual potential barrier for electron emission is different from the work function of the metal coatings or of bare silicon and is roughly independent of the material of the emitting surface. We are considering two effects behind this finding. One is the presence of adsorbates on the surface of the spikes originating from the moderate vacuum conditions of our experiments. As a result an electric dipole field can built up at each adsorption site, which modifies the work function of the underlying surface.^[241,242] The other is that emission is governed by the tunneling probability through localized states lying either below the metal-silicon interface or through a thin residual silicon oxide layer between the spikes' core and the coated metal and not by the potential barrier imposed by the metallic surface itself. Whatever its origin, this result suggests that one should avoid using the value of Φ for the clean surface in estimating field enhancement factors from FN analysis of emission curves in moderate vacuum conditions.

Next we consider the “saturation” regime of the curves of **Figure 5.5(a)**. This regime is characterized by similar values of the saturation current and of the power law exponent among all metal coatings and the bare silicon surface. This excludes any contribution of the metal coating to this effect. Similar saturation effects have been observed also in Si microtip arrays fabricated by other techniques and have been attributed to either limitation of the supply of carriers at the maximum attainable current from the conduction band of Si^[243] or to limitation due to space charge accumulated somewhere inside the silicon core probably near the emitting surface.^[244] We have verified that the onset of saturation occurs at the same current density irrespective of dopant concentration for n-type resistivities varying from 0.002 – 100 Ω -cm, thus current saturation is unlikely to originate from a limited supply of carriers from the semiconductor. Space charge limitation near the emitting surface cannot be verified or excluded based on our results but it is usually described by a second order power law^[245] which is not observed in our samples. An exponent greater than two however could arise from either some geometrical effect having to do with the 3-D geometry of the tips, or from charge-limited conduction through traps of a solid with exponential band tails.^[246]

Oxidation of the surface is the mechanism to which emission degradation and final termination is most commonly attributed.^[247,248] In our case it is compatible to air being the residual gas on the chamber (and not some inert gas) and to the fact that one of the coatings that do not show any signs of degradation is gold, which is the most inert metal among those utilized. The increase of current in gold coated emitters with time, shown in **Figure 5.6**, may result from the increase of the contributing emitters to the observed total current probably due to surface cleaning by incoming ions. This is supported by the fact that the slope of the Fowler-Nordheim (FN) plot of the long-term operated surface remains exactly the same as that of the pristine sample, which implies that neither the apparent potential barrier nor the geometry of the emitters change with time. The most intriguing result however is the unexpected durability of the chromium coated surfaces. The remarkable reduction of the turn-on field for emission and especially of the slope of the FN plot shown in **Figure 5.7**, reveal that a major change on the characteristics of the emission surface has taken place during operation. As there is no change of morphology observable with the high resolution FE-SEM, one could conclude that a reduction of the apparent potential barrier of the actually emitting spikes has occurred. The reason for this reduction cannot be identified at present. It may originate from insertion of chromium atoms into the silicon matrix of the underlying spikes favored by a) a collision cascade process, imposed by ion bombardment, known to occur in sputtering of layered targets and usually referred to as “ion-mixing” and b) the diffusivity of chromium into silicon which, along with that of gold, is the highest among the metals of this study.^[249,250] Hot spots for current emission are very likely to occur^[251] and to have significantly higher temperature than neighboring surface areas in operation favoring the diffusion of these atoms. Si implantation may result in the creation of a more refractory surface and/or the introduction of tunneling states in the gap of the oxide formed in operation.^[252,253]

5.2.4 Conclusion

In this section we have studied for the first time in a consistent manner cold electron emission from fs-laser nanostructured silicon spikes coated with several different metals. We found that the current–voltage characteristics of this cathode are not significantly altered by metal coating provided that it is thin enough so as not to alter their morphology. Continuous operation of the cathodes revealed that chromium and gold coated silicon spikes are most durable, showing no signs of degradation even after 3 days of continuous operation. Resistance against oxidation is one of the key technological issues for sustainable emission but the case of chromium points to the presence of additional processes, yet to be identified, that could prolong operational life of the emitters.

5.3 Three-dimensional carbon nanowall field emission arrays

5.3.1 Introduction

Owing to their unique geometries of small curvature radius, one-dimensional graphitic nanostructures like carbon nanotubes (CNTs) and nanofibers have attracted significant interest for their potential *Field Emission* (FE) applications. Two-dimensional carbon nanostructures such as carbon nanowalls (CNWs) have also been grown and used as FE materials.^[254,255] However, there is a growing research effort to develop three-dimensional (3D) graphitic FE structures and good FE properties have been obtained.^[256,257] Those results indicate that the emission performance might be effectively improved by a hierarchical development of field emitters starting from microstructured substrates and subsequently growing graphitic nanostructures onto them.

In this section we report on the hierarchical fabrication and FE performance of large scale regular arrays of 3D CNW field emitters produced by growing CNWs on forests of micro-conical Si spikes CNW/ μ Si. The results indicate that the FE performance and stability of 3D CNW structures is by far superior to that of planar CNW mats and comparable to that reported for optimized CNT-based emitters.

5.3.2 Methodology

CNW mats were grown by Hot Filament CVD (HFCVD) as described here.^[258] All the CNW samples were grown for 20 min in 30 mbar CH₄/He atmosphere, substrate temperature of 700 °C and gaseous precursors' ratio of 3/100. In particular, for FSi sample, CNW mats were grown over planar n-type Si substrates, while for CNW/ μ Si samples HSi (High aspect ratio Si) and LSi (Low aspect ratio Si), CNW mats were grown on laser etched Si substrates comprising 3D arrays of high- and low-aspect ratio microspikes respectively. For the production of spikes arrays, Si wafers (resistivity of 1–20 Ω cm) were subjected to femtosecond (fs) laser irradiation in a SF₆ atmosphere as described in **section 2.4.1**. Samples were characterized by scanning electron microscopy (SEM) and micro-Raman spectroscopy. The latter revealed typical spectra (not shown) of nanocrystalline CNWs with the ordered graphitic G peak at 1584 cm⁻¹ and the disorder-induced D peak at 1362 cm⁻¹. The intensity ratio of the two peaks is $I_G/I_D \sim 1.3$ for all samples indicating that the quality of the deposited CNWs is similar.

5.3.3 Field emission properties

Figure 5.8 shows the high-aspect ratio spike array obtained after the laser structuring process, showing a forest of Si spikes, which are well-separated and perpendicular to the substrate surface, forming a highly aligned array. **Figures 5.8(b)–(f)** depict the corresponding SEM images after the CVD process for the HSi and LSi, samples respectively. It is observed that nanowalls follow the surface and decorate the microspikes forming a flower-like coating. As a result the final surface exhibits a 3D structure comprising arrays of CNW-spikes with hierarchical micro and nanomorphology. The nanowalls on the LSi sample are slightly larger than those on HSi, because the respective Si tip morphologies were different and locally the effect of the electric field induced plasma is different, even though the process parameters are kept constant. Structural features for both CNW/ μ Si samples are summarized in **Table I**.

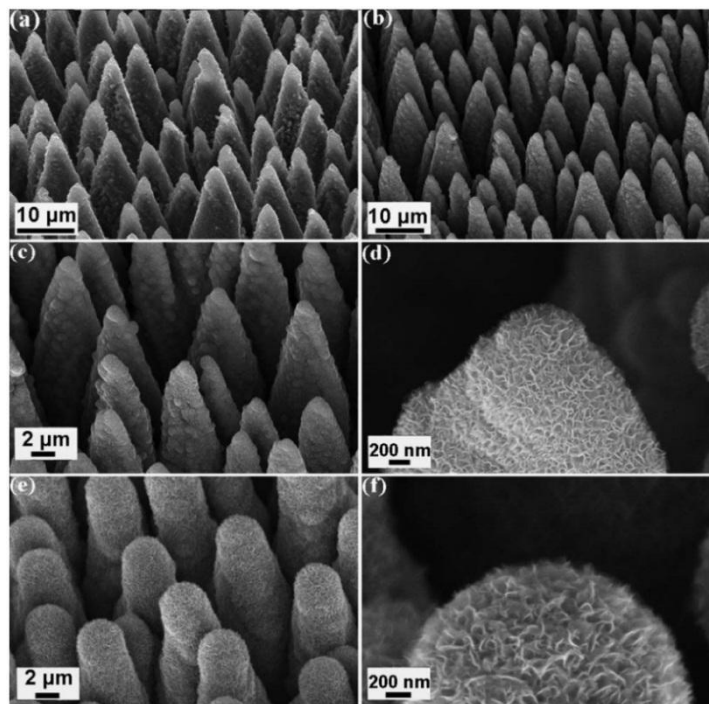


Figure 5.8: SEM view (45°) of: **(a)** The high-aspect ratio Si microspike array, **(b)** high-aspect ratio CNW/ μ Si emitters (HSi sample) 2.25 J/cm², 500 pulses at the rate 1 kHz, 500 Torr SF₆) **(c)** higher magnification image of **(b)**, **(d)** image of an emitter tip showing the decorating CNWs, **(e)** low-aspect ratio CNW/ μ Si emitters LSi sample (0.9 J/cm², 500 pulses at the repetition rate of 1 kHz, 500 Torr SF₆).

The spike tip radius, r , represents the best fitting sphere radius, as measured by 45° tilted SEM images and the spike height, h , was measured from the base of the spike's cone using cross-sectional SEM micrographs. The spike density, measured from top view SEM images, is $\sim 5 \times 10^6/\text{cm}^2$ for both CNW/ μ Si samples. FE measurements were performed under 5×10^{-6} Mbar vacuum, using the samples as cold cathode emitters in a planar diode system. Current-voltage (I-V) curves were taken at a sample-to-anode distance, d , equal to $d=200 \mu\text{m}$. Details for the setup can be found elsewhere.^[259,260] **Figure**

5.9(a) shows a plot of the current density-field (J-E) emission characteristic curves. Several emission cycles were taken in order for the J-E curves to become relatively stable and reproducible. Error bars are a measure of the emission stability in each case.

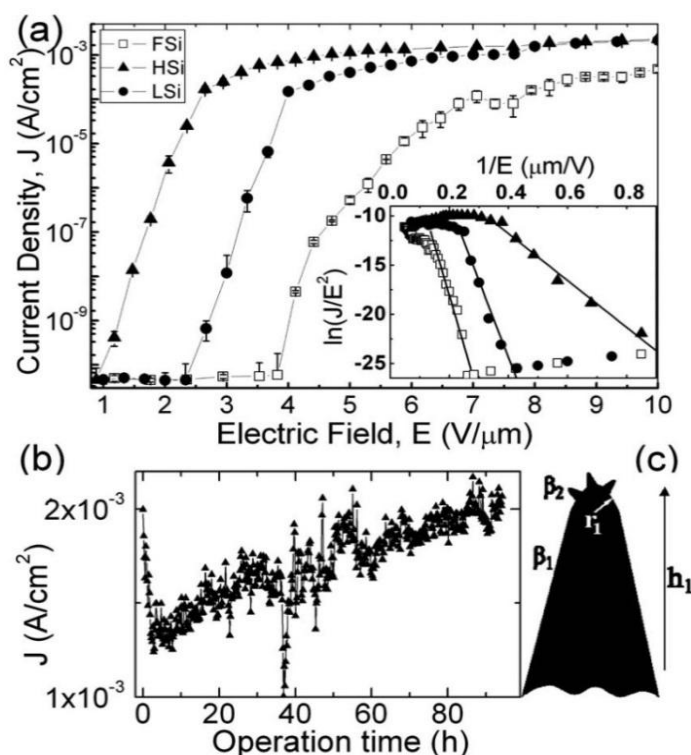


Figure 5.9: (a) Plot of J-E FE characteristics for the CNW/μSi samples studied. The solid lines are guides to the eye. The corresponding FN [$\ln(J/E^2)$ vs E^{-1}] plots are shown in the inset. The solid lines represent linear fits to the FN equation. (b) Emission current stability over time for the HSi CNW/μSi sample. (c) Geometry of a CNW/μSi emitter, assumed by the TSFE model.

The threshold field, E_{th} , which we define as the macroscopic field where the emission current is 60 pA/cm², is measured to be lowest for the HSi—CNW/μSi, sample, reaching a value of ~0.9 V/μm. This value is more than four times lower from that measured on the FSi sample prepared at identical growth conditions. Interestingly, the FE performance is greatly improved, when the CNW mat is deposited on top of the 3D structured substrate compared to the same mat on planar substrate. On the other hand, for the lower aspect ratio sample, LSi, E_{th} increases to 2.4 V/μm indicating that as the spike aspect ratio decreases, E_{th} becomes higher. Increase of bias voltage above the threshold dramatically increases the FE current according to a Fowler–Nordheim (FN) tunneling process, until saturation is reached. A similar saturation behavior was observed in other graphitic emitters and attributed to a large voltage drop along the emitter and/or at

the emitter/substrate interface.^[261,262] On the contrary Wang et al.^[263] measured current densities of up to 10 mA/cm² without observing any saturation, probably due to the much lower resistivity of the substrates used and thus the absence of a substantial voltage drop (low contact resistance) at the emitter/substrate interface. At high fields current tends to saturate at about the same level for all samples, possibly because it becomes limited by the CNW/substrate contact resistance. The latter should be equal among samples, considering that the CNW quality is similar and the deposition conditions and substrate types were kept constant.

5.3.4 Data analysis: FE enhancement factor

In analyzing our FE data, we adopted the FN analysis^[264] of field-assisted tunneling, as described in **section 5.2.1 ii (Eq. 5.9)**. Within this frame the FN law is expressed as:

$$J = a_{FN} \cdot (\beta E)^2 \cdot \exp\left(\frac{-b_{FN}}{\beta E}\right)$$

where $A=1.54 \cdot 10^{-6} \text{ A V}^{-2} \text{ eV}$, $b_{FN}=0.94 \text{ B} \cdot \Phi^{3/2}$, with $B=6.83 \cdot 10^7 \text{ V cm}^{-1} \text{ eV}^{-3/2}$, while Φ is the work function in electron volt. **Figure 5.9(a) (inset)** shows FN plots [$\ln(J/E^2)$ versus E^{-1}] of the FE data. The corresponding β values also shown in **Table I** are determined by fitting the linear part of the data, following **Eq. 5.9**, assuming a typical work function for graphite of 5.0 eV.

Sample	Spike height, h_1 (μm)	Spike tip radius, r_1 (nm)	E_{th} (V/ μm)	β	$\beta \times E_{th}$ (V/ μm)	$\beta_{1\text{single}}$	$\beta_{1\text{exp}}$	$\beta_{1\text{single}}/\beta_{1\text{exp}}$
FSi	3.8	800	3040
HSi	20.8 ± 3.0	590 ± 100	0.9	3533	3180	35.2	4.4	8.0
LSi	10.9 ± 2.0	1010 ± 300	2.4	1221	2930	10.8	1.5	7.2

TABLE 1: Morphological characteristics and FE properties of the planar and CNW/ μSi emitters. The values denote the standard deviation of each measured or estimated quantity.

The FE results can be explained in the framework of the “two-step field enhancement (TSFE)” approach.^[265] According to this model, the emitting surface may be thought of as a number of primary structures corresponding to Si spikes in our case with height of h_1 and sharpness of r_1 , decorated by tiny emitters, corresponding to CNWs (**Figure 5.9(c)**). The local field on the primary tip is $E_1 = \beta_1(V/d)$ while that on the very end of the secondary protrusions is

$$E_2 = \beta_2 E_1 = \beta_2 \beta_1 (V/d)$$

If the nature of emitting sites is the same in all samples measured, then according to **Eq. 5.5**, the local field at the threshold, βE_{th} , should be constant.^[266] As shown in **Table I**, βE_{th} is indeed found constant among samples, indicating that CNW emission sites are of the same nature and thus $\beta_2 = 800$ in all samples; it also suggests that the small difference in the nanowall length does not have a significant impact on the β_2 value. By placing $\beta_2 = 800$ in **Eq. 5.9** one can calculate the corresponding β_1 values obtained experimentally in the framework of the TSFE approach, i.e., $\beta_{1\text{exp}}$. Assuming now a point-to-

plane geometry, the far field value of β_1 for a single isolated spike can be calculated, i.e., $\beta_{1\text{single}} = h_1 / r_1$,^[267] and compared with $\beta_{1\text{exp}}$.

5.3.5 Screening effects and durability

I. Screening effects

The poor emission of high density films or dense structures as in our case, is explainable by an electrostatic screening effect provoked by the proximity of neighboring spikes. The presence of many spikes per unit area (u.a.) means that there is more charge per u.a. and the charge reduces the potential drop perpendicular into the film. The limit of zero distance between the spikes would correspond to a flat Si surface without field penetration and poor emission.

The results are presented in **Table I** and show that the enhancement effect of the primary tips, $\beta_{1\text{exp}}$, is lower than the far field value predicted by geometrical considerations, $\beta_{1\text{single}}$. This discrepancy can be attributed to the fact that the local field at one spike is considerably reduced due to the shielding effect by the neighboring ones.^[268,269] Screening effects are found to be substantial when the average distance of emitters is in the order of few microns,^[270] as it is in our case. As the ratio $\beta_{1\text{exp}} / \beta_{1\text{single}}$ remains fairly constant, the TSFE model predicts that the β reduction caused by screening effects is equal for the two CNW/ μSi samples, which is reasonable considering that the respective spike densities are equal.

II. Durability of carbon coated spikes

The stability of the FE current over time is crucial and of equal importance to E_{th} and β for practical device applications. **Figure 5.9(b)** presents the evolution of the saturated emission current density over a long period of continuous operation for the best emitting sample HSi. No degradation of emission performance was observed, even after four days of continuous operation. It should be noted that stable emission was in the saturated limit and was therefore controlled by the CNW/substrate resistance, not the emission process.

5.3.6 Conclusions

In this section we have prepared a large scale Si-based graphitic cathode (CNW/ μ Si), exhibiting high FE performance, by a simple hierarchical growth process. CNWs were grown radially on the surface of laser fabricated Si microspikes to form a 3D regular array of micro/nano structured field emitters. The threshold field, enhancement factor and the remarkable stability of FE current is comparable to that of optimized CNT emitters^[271], demonstrating that CNW/ μ Si is a promising FE cathode with potential applications in vacuum microelectronics and FEDs.

B) Dynamic control of the wetting properties

Introduction

The understanding and fabrication of functional and responsive surfaces with wetting properties that can be controllably altered on demand has attracted the interest of the scientific community due to their wide variety of potential applications,^[272] including microfluidic and “lab-on-chip” devices,^[273,274] drug delivery,^[275] enzyme immobilization,^[276] bioseparation,^[277] cell adhesion,^[278] chemical and biochemical gates,^[279] sensor development,^[280] and self-cleaning surfaces.^[281] These surfaces are able to reversibly switch their hydro-phobicity/hydrophilicity in response to external stimuli.^[282,283,284,285,286,287]

The development of water repellent surfaces^[288,289,290] has been the focus of current research. The strategy employed consists in mimicking superhydrophobic biosurfaces,^[291] like insects as Cicada orni^[292] and Rhinotermitidae^[293] and plants like those of *Nelumbo nucifera* leaves (the sacred Lotus),^[291] by designing rough substrates out of hydrophobic materials.^[294,295,296] It is generally understood that the microstructured rough surface enhances the effect of hydrophobic surface chemistry into superhydrophobicity and water repellency. In fact the lotus leaf surface has been considered as a “model” superhydrophobic, water repellent surface. The properties of the lotus leaf have been ascribed to the complex morphology present on its surface, consisting of hierarchical structuring, at two different lengthscales. As a consequence, the main strategy for the fabrication of any artificial superhydrophobic and water-repellent surface has been to mimic its surface topology. Simplified schemes of micro-nanomanufacturing, enabling the reproducible creation of such complex surface topologies with different lengthscales are therefore very desirable.

Several different physical and chemical patterning approaches have been employed for structuring surfaces, so as to tailor their wettability, including photolithography^[297] templated electrochemical deposition^[298] plasma treatments.^[299] Microstructuring by lasers in specific ambient

environments is particularly attractive, because it may result into structuring of solid substrates at two length scales through a simple one-step production, without a clean room facility and high-vacuum equipment requirements. The resulting surface in Si^[300] consists of self-organized conical spike forests with characteristic size from a few to tens of μm , decorated by fine features between tens and a few hundreds of nm. Among the advantages of this technique, is that it can be applied in a wide range of materials, such as polymers^[301] ceramics^[302], or metals^[303] in order to control surface topology, and thus open the way to controlling their wettability.

In the first section we will study the fundamental theory of water repellency, by defining the contact angle, the Cassie-Baxter and Wenzel. The next 4 sections present some novel methods for the dynamic control of the wetting properties of Silicon structured surfaces.

5.4 Fundamentals

5.4.1 Young equation and contact angle

When a small water drop is deposited on a plane surface its shape is defined by the volume of the liquid, and the surface tensions between the solid liquid and air interface. The static contact angle is strongly defined by the morphology of the surface. If the surface is ideal, meaning plane and homogeneous then the contact angle is defined as the angle at which a liquid-gas interface meets the solid surface is called the equilibrium or Young contact angle (θ_0) and for this, the energy of the system reaches a local minimum.^[304,305] Gravitational forces don't play a roll here as long as the water drop is between 1-5 μl , and the shape of the water drop is approximately a sphere.

The force balance leads to the well-known Young equation:

$$\gamma|_{lv} \cos \theta_Y = \gamma|_{sv} - \gamma|_{sl} \Leftrightarrow$$

$$\cos \theta_Y = \frac{\gamma|_{sv} - \gamma|_{sl}}{\gamma|_{lv}} \quad (\text{Eq. 5.10})$$

where the subscripts (sg), (sl), and (lg) refer to solid-gas, solid-liquid, and liquid gas interfaces respectively (**Figure 5.10**)

The contact angle is a measure of the wetting behavior of a given surface and depending on its value a surface can be characterized as hydrophilic ($\theta_0 < 90^\circ$) (**Figure 5.10(a)**) or hydrophobic ($\theta_0 > 90^\circ$) (**Figure 5.10(b)**)

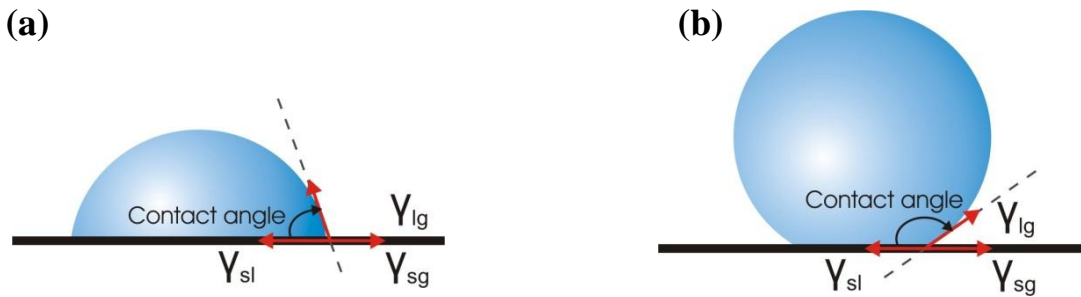


Figure 5.10: A sessile liquid drop on **(a)** a hydrophilic and **(b)** a hydrophobic surface.

The surface tension γ is a manifestation of the intermolecular forces at a surface (or interface), of a liquid on a surface, and is defined as the energy W needed to increase the surface area per increase in surface area A :

$$\gamma = \frac{dW}{dA} \quad (\text{Eq. 5.11})$$

Surface tension has dimensions of force per unit length (N/m), or of energy per unit area (J/m²). According to Young's equation the higher the surface tension of a liquid on a surface, the higher the contact angle.

5.4.2 Wettability and Surface roughness: Wenzel and Cassie-Baxter states

The effect of the macroscopic surface roughness on the wettability of surfaces has been theoretically approached by two different models. In the *Wenzel* model,^[306] the liquid is assumed to completely penetrate within the entire rough surface, described as “homogeneous wetting regime” without leaving any air pockets underneath it (**Figure 5.11(a)**). The apparent contact angle, θ_w , is then given by the following equation:

$$\cos\theta_w = r \cos\theta_o, \quad (\text{Eq. 5.12})$$

where r is the ratio of the unfolded surface to the apparent area of contact under the droplet, and θ_o is the apparent contact angle on a flat surface of the same nature as the rough (Young contact angle). Since r is always greater than unity, this model predicts that the contact angle will decrease/increase with surface roughness for an initially hydrophilic ($\theta_o < 90^\circ$) / hydrophobic ($\theta_o > 90^\circ$) surface.

When dealing with a heterogeneous surface, the Wenzel model is not sufficient. *Cassie and Baxter*^[307] (CB) (**Figure 5.11(b)**) assumed that the liquid does not completely permeate the rough surface because air gets trapped underneath it. As a result a droplet will form a composite solid-liquid/air–liquid interface with the sample in contact. In this case, the apparent contact angle, θ_{CB} , is an average of the flat surface, θ_o , and the value for full hover over the flat surface (that is, 180°) and is given by:

$$\cos \theta_{CB} = -1 + f + r_f f \cos \theta_o \quad (\text{Eq. 5.13})$$

where f is the ratio of flat projection of solid-liquid contact area, to the total flat geometrical area of the composite substrate under the drop and r_f is the roughness ratio of the wet surface area.

When the liquid drop is lying on the top of the rough surface without sinking into the features at all (**Figure 5.11(b)**), the roughness factor will equal one ($r_f=1$) and **Eq. 5.5** becomes the widely used simplified form of the Cassie-Baxter equation.

$$\cos \theta_{CB} = -1 + f(1 + \cos \theta_o) \quad (\text{Eq. 5.14})$$

As f is always lower than unity, this model always predicts enhancement of hydrophobicity, independently of the value of the initial contact angle θ_o . The lower the value of f , the higher the contact angle measured. In contrast, when $f=1$ and $r_f=r$, **Eq. 5.4.4** turns into the Wenzel equation.

Assessment of the preferred state of the droplet in contact with a rough surface is not always a

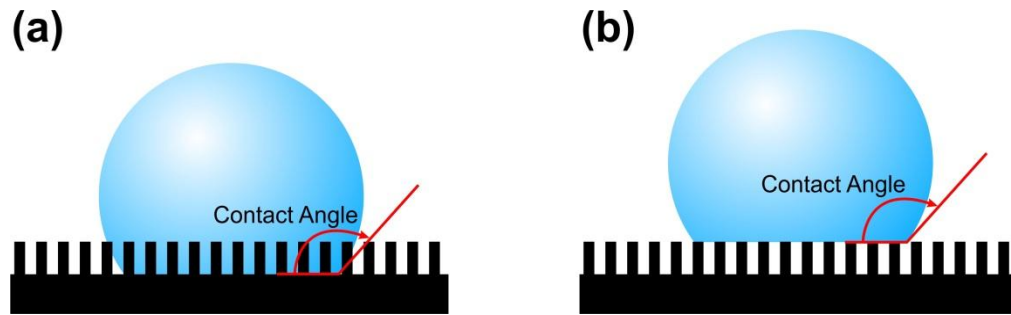


Figure 5.11: The two different wetting models. **(a)** Wenzel model, **(b)** Cassie-Baxter Model

trivial task. On the other hand, the apparent contact angle of a drop in contact with a structured surface, is a result of surface energy minimization of the drop. It has been found[308] that the most energetically favourable state will be the CB one when the contact angle of the flat surface, θ_o , is less than a critical value θ_c determined by:

$$\cos \theta_c = \frac{f-1}{r-f} \quad (\text{Eq. 5.15})$$

Eq. 5.6 is deduced by equating θ_w of **Eq. 5.3** with θ_{CB} of **Eq. 5.5**. When $\theta_o > \theta_c$, then complete or partial wetting occurs as a result of the liquid penetration into the rough solid surface.

5.5 Tailoring wetting response of silicon.

5.5.1 Bio-inspired water repellent surfaces and self-cleaning applications

In this part of our work we study the effect of different surface morphologies on the wettability of processed Si surfaces. Textured Si surfaces have been fabricated (experimental setup in [section 2.4.1](#)) by employing the same number of laser pulses (an average of 500) at different fluences ([Figure 5.12](#)). Increasing the incident energy per unit area causes remarkable changes in the structures shape, dimension and density. At low irradiation fluences laser heating induces melting of the surface producing a rippled landscape, with structures not completely physically separated ([Figure 5.12\(a\)](#)). Upon increasing the fluence ([Figure 5.12\(b\)](#) and [5.12\(c\)](#)), conical microstructuring is promoted on the Si surface, with structures becoming more pronounced and spatially separated. In this regime the average spikes spacing, base diameter and height increase with laser fluence. For larger fluence values (above $\sim 1.0 \text{ J/cm}^2$), the spikes growth reaches a plateau, where the base diameters stabilize around $8 \mu\text{m}$, while the height stabilizes around $15\mu\text{m}$. Further information can be found in [section 2.4.1\(i\)](#).

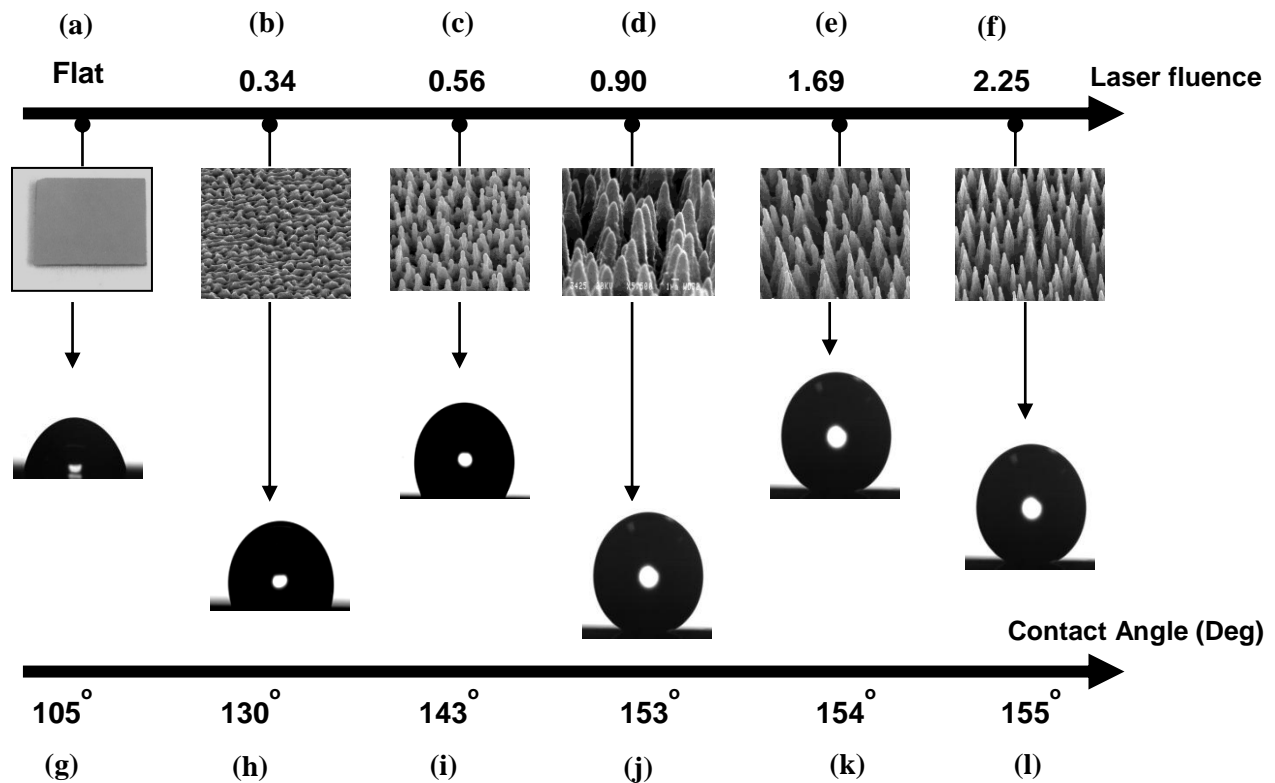


Figure 5.12: (a)-(f): Side scanning electron microscope view of Si surfaces structured by fs-irradiation at different laser fluences. (g)-(l): Images of water droplets on the corresponding structured Si surfaces.

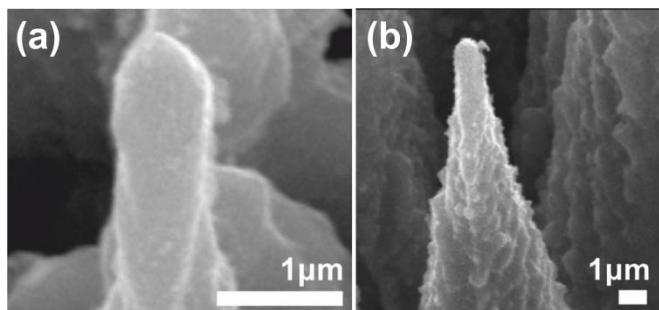


Figure 5.13: (a) Silicon spike tip at low fluence (0.34 J/cm^2) and smoother surface. (b) Silicon tip at high fluence (1.6 J/cm^2) with secondary scale roughness in the nm scale.

Besides directly affecting the micrometer-scale surface topology, increasing fluence is also crucial to induce a more pronounced sub-micrometer decoration on the spikes walls. In particular, the protrusions with size from tens to a few hundreds of nanometers, which constitute the second length-scale pattern on the Si surface, become more evident as the laser fluence increase

(compare **Figure 5.13(a)** with **(b)**). The micrometer-scale cones together with the nano-scale features, generated on high fluences result into a significant increase of the overall roughness.

Images of the water drops lying on the structured Si surfaces are shown in **Figure 5.12(g)-(l)** under the Si structured surfaces. Changes in the observed wettability may be attributed to a synergy of surface chemistry and roughness. It is known that the formation of a native oxide layer is initiated on the Si surface immediately after the HF treatment.^[309,310] Its thickness changes very slowly in the first few hours (an increase of $\sim 2 \text{ \AA}$ in the first hour). For this reason particular care was given in our experiments, in performing the CA measurements only a few minutes after the HF treatment, therefore ensuring the presence of similar native oxide thicknesses in all the samples. Based on the above findings, the structured Si surfaces are considered to maintain a similar chemical composition and the observed changes in the wettability may be attributed primarily to the morphological changes obtained at different laser fluences.

On the lower axis of **Figure 5.12** we measure the changes in the static CA of a $2 \mu\text{l}$ nanopure water drop. The CA increases rapidly even for the surfaces with low roughness starting at 104° structured at energies around 0.34 J/cm^2 (**Figure 5.12(g)**). Starting from flat Si with a CA of 67° we observe a gradual increase and reaches a plateau at 153° . Using the general Cassie – Baxter equation (**Eq. 5.14**) one can obtain information about the wettability of the structured surface. For the samples exhibiting the pronounced two-lengthscale surface roughness, namely those obtained by irradiation fluences larger than 1.0 J/cm^2 , the CA values reach a plateau around 155° (**Figure 5.12(e),(f)**). Therefore, for these samples the liquid is in contact with a practically constant solid surface, and thus, the factors f and r_f in **Eq. 5.13** remain constant. Assuming that at these irradiation regimes the formed structures roughly resemble cones (the nanometer scale formed features are integrated into the cone structure), a simple geometric equation correlates the factor r_f with the angle of the formed cones, which is evaluated by the scanning electron

microscopy pictures. Finally, by **Eq. 5.14** the factor f is calculated ~ 0.13 . Namely, the surface of the base of the wetted Si cone is about 13% of the total base of the formed Si cones.

Figure 5.14 presents a time sequence of snapshots of a water droplet rolling on a slightly tilted artificially structured surface. In order to investigate its self-cleaning ability, the surface is covered with carbon particles (**Figure 5.15(a)**) and a 10 ml water droplet was left to roll across it. One can clearly observe that the droplet leaves a clean path behind it (**Figure 5.15(b),(c)**) with nearly no particles as it rolls down the slightly tilted structured surface. **Figure 5.15(d)** shows that at the end of its path, the droplet is surrounded by the carbon particles which were collected by it.



Figure 5.14: Selected frames of a water drop rolling on a tilted laser structured and silanized Si surface. The artificial surface was structured in the presence of 500 Torr SF_6 at a laser fluence of 2.47 J/cm^2 with an average of 500 pulses

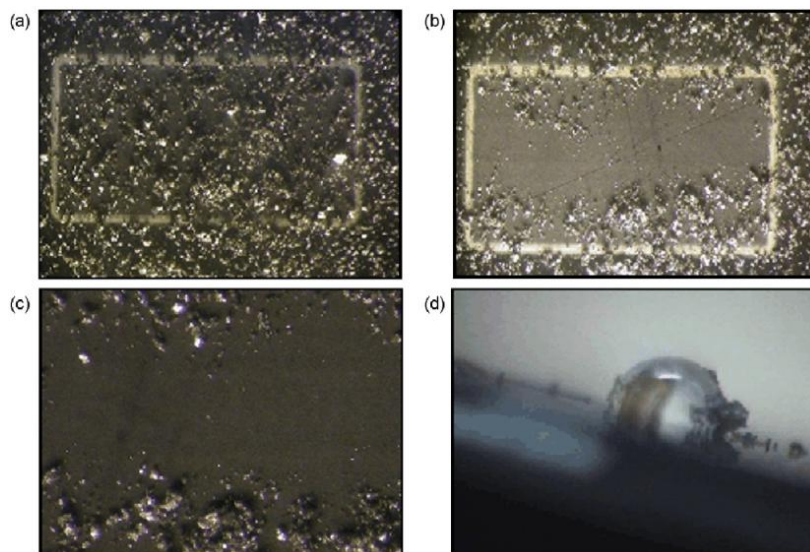


Figure 5.15: (a) Macro-view of a silicon structured surface covered with carbon particles. The size of the surface is 3 mm x 8 mm. (b), (c) Image of the path left behind by the rolling droplet and (d) image of the drop with the carbon particles collected on it. The surface was structured in the presence of 500 Torr SF_6 at a laser fluence of 2.47 J/cm^2 with an average of 500 pulses.

5.5.2 Silicon-based surface meets the water repellent performance of the lotus leaf

Water repellent surfaces demonstrate a range of remarkable wetting properties; from droplet impact with a time of contact independent of speed^[311] to drops rolling down these surfaces at a speed faster than a solid sphere would roll under gravity.^[312] The goal of the study is to prepare an artificial surface comprising both the surface morphology and chemistry to meet the repellence performance of the lotus leaf (*Nelumbo nucifera*)^[313] and thus provide insight into the design of efficient water repellent materials. when water lands on the surface of a natural lotus leaf (**Figure 5.16(a)**) it beads up to form nearly spherical drops (**Figure 5.16(b)**) that immediately roll off, removing dust particles and surface contaminants. **Figure 5.16(c)** and **(d)** show scanning electron microscopy (SEM) pictures of the sacred lotus leaf surface, comprising micrometer-sized papillae decorated with nanometre-sized branch like protrusions.

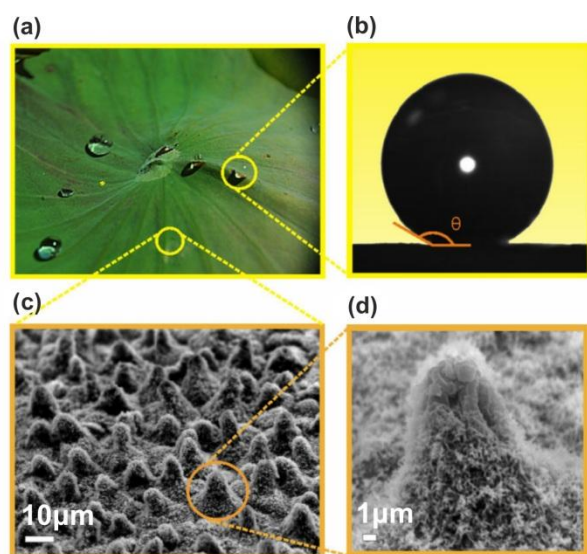


Figure 5.16: (a) Picture of water droplets lying on a lotus leaf, (b) static contact angle ($\theta=153^\circ$) of a water droplet of 0.78 mm radius on the leaf, (c) SEM image of the leaf surface comprising micrometer-sized papillae and (d) high magnification SEM image of a single papilla depicting nanometer-sized branch like protrusions.

A surface is called repellent when an incoming drop bounces away from the surface upon impact. Then the lowest velocity sufficient for a complete rebound gives a proper measure of repellence. The second step is to choose a material and a method to modify its surface in a way that it resembles that of the lotus leaf. Microstructuring by ultrafast Lasers^[314,315] in specific ambient environments is specifically attractive, because a) it produces morphology exhibiting two length scales through a simple one-step production, without a clean room facility and high-vacuum equipment requirements and b) it can be applied to a wide variety of materials.^[316,317,318] The final step is to control the surface chemistry of the structure towards an even better performance. The easiest known way to do

this is by growing a self-assembled coating that is known to produce or increase hydrophobicity on a flat surface. We show that the implementation of the above steps resulted in the production

of one of the most water repellent surfaces ever reported. We quantify the repellence of this surface and we directly compare it, for the first time, to that of the natural lotus leaf, to find a remarkable similarity in the overall performance.

5.2.3 Methodology

Microstructuring of the flat Si surfaces was performed by femtosecond (fs) laser irradiation under reactive gas (SF_6) atmosphere. Following the irradiation process, the patterned surfaces were covered by low surface energy organosilane layers, which are known to assemble high quality conformal coatings to flat Si surfaces.^[319] Dichlorodimethylsilane ($(\text{CH}_3)_2\text{SiCl}_2$, DMDCS) is chosen among other hydrophobic silanes due to its lower tendency to polymerise on Si surfaces, and its excellent stability, allowing it to maintain its hydrophobic properties for long time and wide temperature range.^[320] More experimental details can be found in **section 2.4.1-1** and **2.5.2**.

5.2.4 Making Silicon superhydrophobic

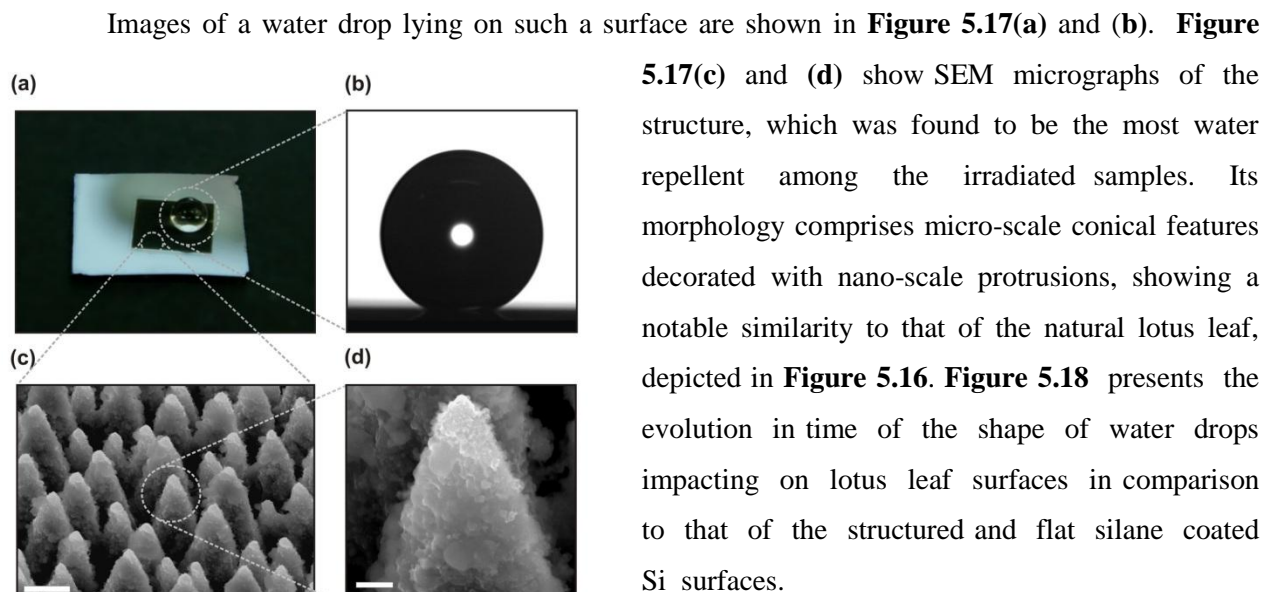


Figure 5.17: **(a)** Picture of a water droplet lying on a silane coated Si surface (dark area), **(b)** static contact angle ($\theta=154^\circ$) of a water droplet of 0.78 mm radius on the surface, **(c)** SEM image of the surface comprising micrometer-sized cones and **(d)** high magnification SEM image of a single cone depicting nanometer-sized protrusions. The surface was structured in the presence of 500 Torr SF_6 at a laser fluence of 2.47 J/cm^2 with an average of 500 pulses.



Figure 5.18: Selected snapshots of a millimetric water drop impact on: **(a)** a laser structured silane coated Si surface with a Weber number, We , of 3.5, **(b)** on a lotus leaf surface with $We = 3.5$, **(c)** on a laser structured silane coated Si surface with $We = 0.7$ **(d)** on a lotus leaf surface with $We = 0.7$ and **(e)** on an unstructured silane coated Si surface with $We = 3.5$.

In particular, **Figure 5.18(a)** and **(b)** show a selected time sequence of snapshots showing a 10 μ l water drop free-falling on the structured surface and on a lotus leaf respectively. The drop has a radius of $R=1.35$ mm and is released from a height of 10mm so that the impact velocity is ~ 0.44 m/s. The behaviour of the falling droplet is quite similar in the two surfaces. In particular, we observe that the drop's shape changes significantly during impact as its kinetic energy transforms into energy stored in surface deformation. In this case, the deformation is strong, because the Weber number, We , defined as the ratio of the arriving kinetic energy to the intrinsic surface energy, is higher than unity. Despite this deformation, both surfaces are so water-repellent that the drop bounces back numerous times. **Figure 5.18(c)** and **(d)** show similar series of video frames for the structured Si and the lotus leaf surface respectively, in the case of $We < 1$, where the drop is lightly deformed. On the other hand, as shown in **Figure 5.18(e)**, no rebound is observed when the drop impacts on the silanized flat region of the Si sample. In this case the surface is not repellent and the drop has insufficient momentum to leave the sample. As a result it remains stuck to the surface. The elasticity of the collisions observed on both natural lotus and laser structured surfaces is remarkable, indicating a high degree of repellence. A direct measure of this elasticity is the restitution coefficient, $\varepsilon = V'/V$, defined as the

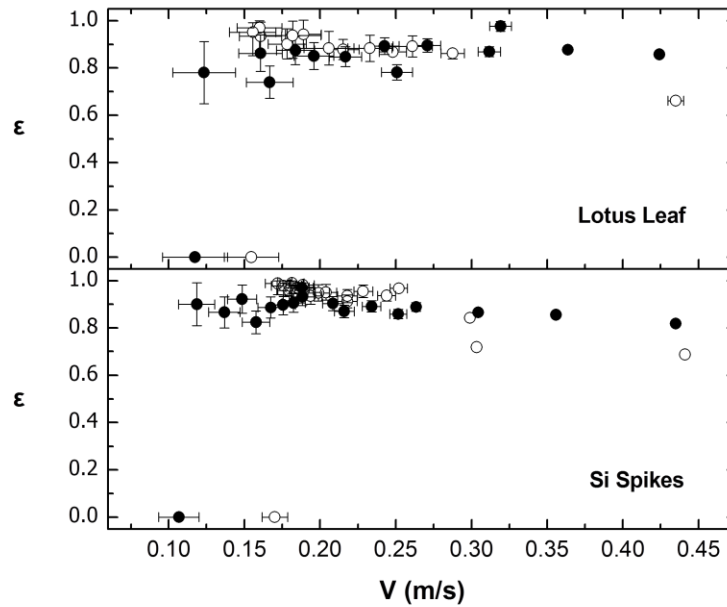


Figure 5.19: Restitution coefficient ϵ as a function of the impact velocity V for a lotus leaf and a laser structured silanized Si surface. The solid and open symbols represent data taken for water drops having a radius of 0.84 mm and 1.35 mm respectively.

ratio of the center of mass velocity just after impact, V' , to that just before impact, V . This coefficient was deduced from the recorded video clips and is plotted in **Figure 5.19** as a function of V for a series of experiments, performed with drops of different volumes. The highest elasticity is observed at intermediate velocities, from ~ 0.15 m/sec to ~ 0.25 m/sec, where the restitution coefficient is found to exceed 0.90. Its value matches that of lotus and to our knowledge is among the highest ever reported.^[321] Elasticity arises from the efficient interchange between kinetic and surface potential energy during drop deformation. According to Richard and Quere,^[322] even in the ideal case of zero energy loss during collision there is a limit in elasticity, $\epsilon < 1$, due to the transfer of a part of kinetic energy into drop vibrations. In all cases we observed that the drop vibrates after leaving the surface. Thus, part of the initial kinetic energy of the drop is transferred into vibrational energy after the impact, and subsequent damping of the bouncing motion occurs due to viscous dissipation.

Although full rebounds occur at moderate impact velocities, the situation is different at small and large V . For small velocities, ϵ decreases abruptly with decreasing V and reaches zero at some velocity that depends on the droplet volume. This is the threshold that quantifies the water repellence of the surface;^[323] the smaller this velocity, the more water repellent the surface. We find this velocity for our surface to be comparable to that of the lotus leaf (**Figure 5.19**). The bouncing to non-bouncing

transition arises from the presence of surface defects that become the main source of kinetic energy dissipation.^[324] The contact line pins on such defects resulting in a difference between the advancing, θ_a and receding, θ_r contact angles. This phenomenon is called hysteresis. The bigger the droplet, the longer this line is, resulting to higher hysteresis and therefore to an increase of the threshold velocity anticipated. This is exactly what we observe in **Figure 5.19** for both surfaces examined. For a drop of radius R and density, ρ , the pinning force per unit length is^[325] $\gamma \Delta \cos \theta$, where $\Delta \cos \theta = \cos(\theta_a) - \cos(\theta_r)$, and γ is the liquid-air surface tension. The energy dissipated will scale as $\gamma R^2 \Delta \cos \theta$. The drop will bounce provided that its kinetic energy, which scales as $\rho R^3 V^2$, overcomes this dissipation. Equation of these two energies, gives an estimate of the velocity threshold for repulsion. We have measured $\theta_a = 157^\circ$ and $\theta_r = 152^\circ$ for the laser structured surface and for the drop of $R \sim 0.84$ mm and we have calculated this velocity to be ~ 6 cm/sec, a value close to the one observed experimentally. Finally, in the high velocity regime, ε slowly decreases with V because of the large drop deformation followed by increased internal vibration after impact. It has been observed in other structured surfaces that there exists an upper velocity above which significant impalement of the drop occurs resulting in part of it getting captured to completely wet the surface.^[326] The value of the highest velocity for which the surface remains dry, has also been used as a measure of the surface resistance against wetting. In this context, we have examined the behavior of water droplets with impact velocities up to 5 m/s, a typical value for the terminal velocity of millimetric raindrops. In this high velocity regime, the drop brakes apart into numerous smaller droplets. This behavior was never observed in the flat region of the Si sample, indicating that structuring favors the creation of tiny droplets in an effort to resist penetration by the falling drop. After each experiment, the surface was thoroughly examined, with a high resolution CCD optical system, for signs of water impalement. We found the lotus leaf as well as the laser structured surface to be impervious to water penetration over the entire range of attainable impact velocities (0.2 - 5 m/s). It should finally be emphasized that the low-adhesion and high repellence of the laser structured surfaces are maintained even after rinsing and complete immersion in water for long periods of time. Long-term endurance against wetting is a feature that is always desirable in relevant applications.

5.5.3 Conclusions

Silicon-based water repellent and self-cleaning surfaces have been fabricated by femtosecond laser structuring combined with a proper hydrophobic chemistry, which follows the guide-lines given by nature for the lotus leaf. The laser processed surfaces produced at high fluences possesses a hierarchical morphology with two length-scale roughnesses. The water repelling characteristics of the surfaces were quantified by investigating the bouncing of free-falling water droplets impacting onto them as a function of impact velocity. This repellency of the artificial surface can be very favorably compared to that of the Lotus leaf in terms of the threshold velocity sufficient to avoid sticking of the droplets, the collision energy loss and the remnant wetting of the surfaces at high velocities. The great similarities observed in the water repellency between the artificial and Lotus leaf surfaces are indicative of the critical role of the two-scale hierarchical morphology, which combines microscale and nanoscale features. Our results provide insight into the design of stable water repellent surfaces in other materials as well, for various related applications.

5.6 Electrowetting Properties of Micro/Nanostructured Black Silicon

5.6.1 Introduction

Droplet based microfluidics is a rapidly emerging technology aiming to actuate and manipulate micro- to picoliter liquid or biofluid volumes, with potential application in “lab-on-chip” diagnostic and health care devices.^[327] Liquid actuation and manipulation using electrowetting on dielectric (EWOD) is becoming a promising tool toward the realization of modern microfluidic devices.^[328,329] Indeed, EWOD has been used to demonstrate a variety of microfluidic operations such as droplet actuation,^[330,331] dispensing,^[332] mixing,^[333] and splitting.^[334] Apart from “lab-on-chip” devices,^[335,336,337] applications related to adjustable lenses,^[338] display technology,^[339] fiber optics,^[340] and microelectromechanical systems^[341] have been demonstrated.

In this Section we present reversible EWOD of liquid droplets on dual rough superhydrophobic black silicon (Si) surfaces, produced by pulsed laser micro/nano structuring. Superhydrophobicity is achieved by the synergy of dual rough surface morphology and control over the surface chemistry through the deposition of low surface energy coatings. The role of the surface water repellence properties on the reversibility of the EWOD process is investigated and discussed.

5.6.2 Fundamentals of EWOD on flat and rough surfaces.

- **Flat surface**

Typically, an electrowettable surface consists of a conductive lower layer with a dielectric layer sandwiched between the lower electrode and an upper hydrophobic material, which lowers the surface energy and confers a larger initial hydrophobicity (**Figure 5.20(a)**). A slightly conductive droplet creates a capacitance defined by the contact area of the droplet and the substrate. When a voltage, V , is applied between the conductor and insulator an electric charge is created and this alters the surface free energy balance. The additional energy per unit area due to the capacitance is given by $1/2CV^2$, where for a simple planar surface the capacitance per unit area is $C = \epsilon_r \epsilon_0 / d$, where ϵ_r is the dielectric constant of the layer, d is its thickness and ϵ_0 is the dielectric constant of air.

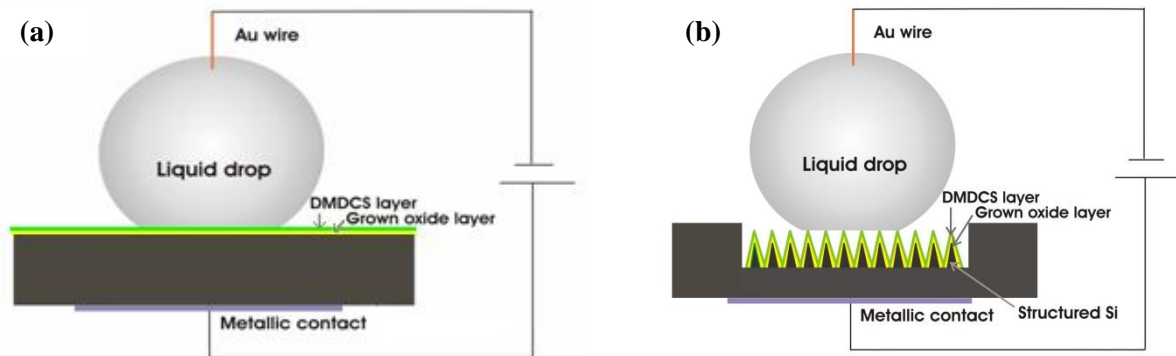


Figure 5.20: Electrowetting-on-dielectric system for (a) flat and (b) structured Si substrates.

It is found that on a flat surface the equilibrium contact angle θ_e for a given voltage V , is given by the expression:

$$\cos\theta = \cos\theta_0 + \frac{1}{2} \frac{\epsilon_0 \epsilon_r}{\gamma_{lv} d} V^2 = \cos\theta_0 + \frac{\gamma_{esl}}{\gamma_{vl}} \quad (\text{Eq.5.15})$$

otherwise known as the Lippmann-Young equation. Here γ_{lv} is the liquid-air interfacial tension, γ_{esl} is the electric-field induced surface tension, θ_0 the CA prior to application of the electric field. The prediction of this equation is that a voltage will cause the CA of a droplet to decrease so that a reduction in hydrophobicity occurs. Although this effect is seen in practice there is a problem of CA saturation after a threshold voltage.^[342] The phenomenon is also reversible, although hysteresis is often observed.

- **Structured Surface**

Figure 5.20(b) illustrates the experimental setup for electrowetting on a structured surface. In order to describe the EWOD behavior on superhydrophobic surfaces we follow the approach proposed by Torkelli.^[343] We assume that the wettability of the structured surfaces is described by the Cassie Baxter model, where air is trapped underneath the water droplets inside the spikes and the proportional areas of solid and air are f and $1 - f$ respectively. The corresponding surface tensions γ in the contact line between the droplet and the surface are presented in **Figure 5.21**, where the subscripts γ_{sv} , γ_{sl} , and γ_{lv} refer to solid-vapor, solid-liquid, and liquid-vapor interfaces respectively.

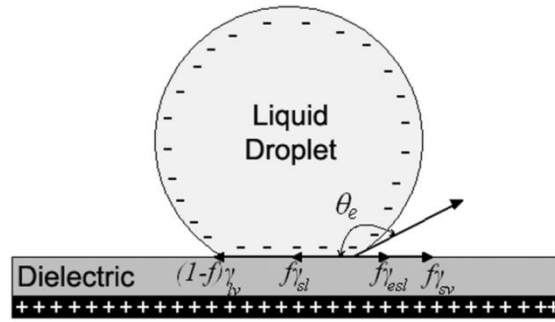


Figure 5.21 Interfacial tensions at the bottom of the droplet placed on a heterogeneous surface under an electric field.

The change in the apparent CA can be calculated by introducing the electric-field induced surface tension, γ_{esl} , into the force balance equation of the contact line. As γ_{esl} is effective only in the solid-liquid interface, it should be multiplied by f . From **Figure 5.21** we obtain the following force balance equation:

$$\gamma_{lv} \cos \theta_e + (1 - f) \gamma_{lv} + f \gamma_{sl} = f \gamma_{sv} + f \gamma_{esl} \quad (\text{Eq. 5.16})$$

where θ_e is the CA under the application of an electric field and $(1-f)$ is the non wetted fraction of the projected area. Substituting Young's equation, $\gamma_{lv} \cos \theta_o = \gamma_{sv} - \gamma_{sl}$, in **Eq 5.6.2** we get

$$\cos \theta_e = f \cos \theta_o + f - 1 + \frac{f \gamma_{esl}}{2 \gamma_{lv}} \quad (\text{Eq. 5.17})$$

Using **Eq. 5.4.5** $\cos \theta_{CB} = -1 + f(1 + \cos \theta_o)$ describes in **section 5.4.2** we obtain

$$\cos \theta = \cos \theta_{cb} + f \frac{1}{2} \frac{\epsilon_0 \epsilon_r}{\gamma_{lv} d} V^2 \quad (\text{Eq. 5.18})$$

It is important to note that **Eq. 5.18** is otherwise identical to **Eq 5.15**, but the Young angle has been replaced by the initial CA of the hydrophobic surface, and there is the fractional area f in the voltage term.

There are many factors which affect the performance of an electrowettable surface, such as the surface energies and tensions of the materials. In order to reduce voltage requirements, which is desirable for microfluidic chip technology, the basic strategy is to use a thinner dielectric film with higher dielectric constant and dielectric strength. However, it is understood that a more important limiting factor is the small range of the actuated CAs before the electric charge saturation in the dielectric occurs. This range depends on the surface CA at zero voltage, and the higher its value the greater the attainable CA variation. Although hydrophobicity can be enhanced by a chemical modification that lowers the surface energy, contact angles larger than 120° have never been achieved for water on a smooth planar surface.^[344] For higher hydrophobicity and superhydrophobicity, the combination of micro- and nanoscale surface roughness with low surface energy chemical coatings is required. This strategy is widespread in natural systems and is well-known as the “lotus effect” (see also **Section 5.5.2**). This surface is composed of micro and nanostructures covered with a hydrophobic wax layer. The high roughness leads to a reduced contact area between the surface and a liquid drop, with droplets residing only on the surface tips, whereas the hydrophobic coating lowers the free surface energy. Superhydrophobic surfaces demonstrate a range of remarkable wetting characteristics originating from very high contact angles (in excess of 150°) and very low flow resistance. Artificial superhydrophobic surfaces can be achieved by a variety of bottom-up or bottom-down approaches, including generation of rough surfaces coated with low surface energy molecules, roughening the surface of hydrophobic materials, and creating well-ordered structures using micromachining and etching methods.

Exploitation of these principles for the fabrication of electrowettable superhydrophobic surfaces would be highly advantageous to fabricate electrowettable superhydrophobic surfaces. Up to now, there are few reports in the literature demonstrating EWOD on superhydrophobic nanostructured surfaces.^[345,346,347,348,349] The main difficulty is caused by the high degree of roughness exhibited by superhydrophobic surfaces, which leads to substantial spatial separation between the liquid and the underlying electrode, strongly impeding the electrowetting effect.^[350] Among them, only one has demonstrated reversibility,^[351] this is attributed to the fact that when the drop wedged in the structures it does not go up, leading to an irreversible EWOD effect. It is thus evident that achieving reversible electrowetting on superhydrophobic surfaces is not only a technical challenge but also a real asset for potential applications.

5.6.3 Methods and Experimental Procedures.

Similar structures as described in **Section 5.3.1** were fabricated for the EWOD experiments. The laser pulse fluence was varied from 0.17 to 1.69 J/cm². Then the patterned surfaces were covered with a thin layer of thermally grown (1000 °C ambient conditions) silicon oxide (**section 2.4.2**); this would serve as the dielectric layer for the EWOD experiments. The thickness of this layer was determined by means of spectroscopic ellipsometry performed on the flat part of the oxidized Si wafer, outside the irradiated area. However, the oxidized surface became superhydrophilic and as a result a water droplet wetted completely the patterned area. To perform EWOD experiments and achieve superhydrophobicity, the oxidized surfaces were silanized (details in **section 2.5.2**), which can assemble into high quality conformal coatings on flat Si surfaces^[352] resulting in a material with a low surface energy that can maintain its hydrophobic properties for long periods of time and for a wide temperature range.^[353] The same surface treatment was used for flat Si samples that were not microstructured.

Static contact angle measurements were performed by an automated tensionmeter (details in **section 2.7**), using the sessile drop method. A 5 µL glycerol droplet, 85% in water solution (γ_{lv} = 65.7 mN/m, conductivity: 0.040 µS/cm), was gently positioned on the surface using a microsyringe and images were captured to measure the angle formed at the liquid-solid interface. The mean value was calculated from at least five individual measurements. Successive measurements were reproducible within $\pm 1^\circ$. Contact angle hysteresis was quantified by measuring the sliding angle which is the lowest angle at which a 5 µL glycerol drop starts to move on a surface. A tilt stage assembly, with an extendable lever arm that permitted continuous inclination of the surface from horizontal, was used in order to determine this angle. Depending on the variability of the data, a mean sliding angle value was calculated from five to ten individual measurements. For the highly hydrophobic surfaces, contact angle hysteresis was also determined by measuring the advancing, θ_a , and receding, θ_r , angles from the drop-snapshot just before slippage occurred. On a 5 µL water drop about to slide, the wetting angle on the lower edge is the θ_a , whereas that on the upper edge is the θ_r . The dynamic behavior of 10 µL water droplets free falling on patterned surfaces was examined using a high-speed camera at a frame rate of up to 1000 Hz.

Figure 5.20(a), (b), illustrates a schematic representation of the experimental method used to investigate the electrowetting behavior of droplets deposited on the planar and structured Si surfaces respectively. The corresponding experimental setup is described in **Section 2.8**. For the experiments, droplets of 85% glycerol in water solution were used. All measurements were performed in air and at room temperature. In this work we have used four types of specimens, namely **sample A** (based on the Si microstructure prepared at 0.34 J/cm²), **sample B** (based on the Si microstructure prepared at 0.90 J/cm²),

sample C (based on the Si microstructure prepared at 1.69 J/cm^2), and a sample prepared on a flat Si surface. **Table 1** summarizes structural, wetting and EWOD characteristics of the different samples studied.

Table 1. Morphological Characteristics, Wetting, and Electrowetting Properties of the Si Surfaces Studied

sample	spike density (cm^{-2})	spike height, h (μm)	d (nm)	contact angle (deg)	sliding angle (deg)	θ_a (deg)	θ_r (deg)	f	critical angle, θ_c (deg)	threshold velocity, v_t (m/sec)	critical velocity, v_c (m/sec)	critical pressure, P_c (kPa)
A	2×10^6	1	210 ± 5	128 ± 1	> 30			0.20	90	0.18 ± 0.01	3.10	9.60
B	5×10^5	7	205 ± 5	150 ± 1	14 ± 2	157 ± 1	148 ± 1	0.19	96	0.16 ± 0.01	3.83	14.70
C	3×10^5	10	190 ± 5	151 ± 1	7 ± 2	157 ± 1	152 ± 1	0.21	108	0.16 ± 0.01	> 5.0	> 25.00
Flat Si			210 ± 5	94 ± 1	> 30							

5.6.4 Morphology analysis

In this section we present our results regarding the EWOD experiments. First we analyze the Si laser structured morphology and the static contact angle measurement for glycerol drops. FESEM pictures of surfaces made at different incident laser fluences and constant shot number are presented in **Figure 5.22**. The micrometer-scale structures generated by the spike forest together with the nano-scale features decorating the cones result into a significant increase of the overall roughness. In particular, protrusions with size from tens to a few hundreds of nanometers, which constitute the second length-scale pattern on the Si surface, become more evident, as the laser fluence increases.

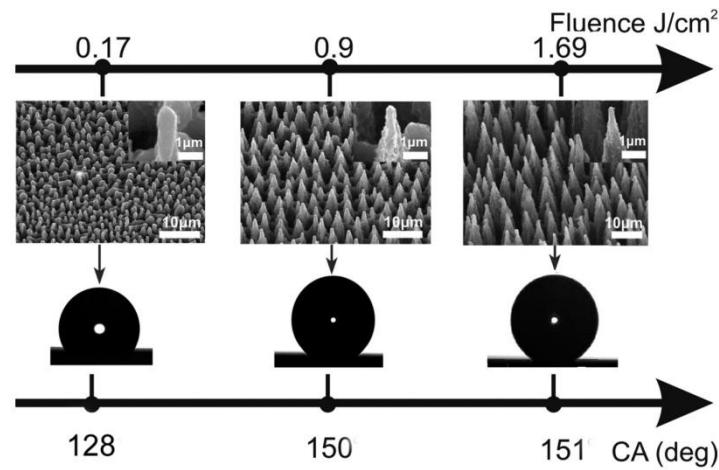


Figure 5.22: Side scanning electron microscope view of black Si surfaces structured by fs irradiation at different laser fluences: (a) 0.17, (b) 0.90, and (c) 1.69 J/cm². The insets are higher magnifications of the obtained structures. Images of a glycerol droplet placed on the surfaces, after being thermally oxidized and coated with a DMDCS layer.

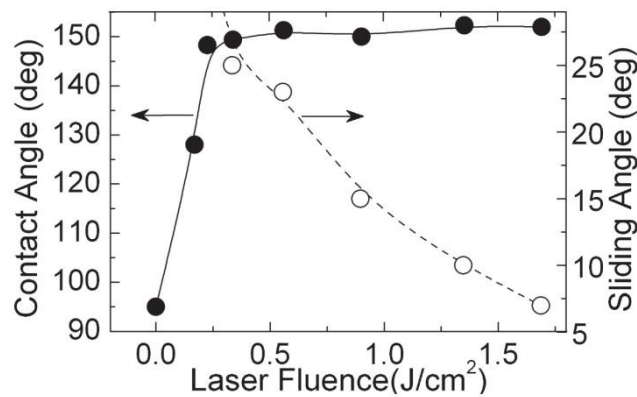


Figure 5.23: Static contact angle (●) and sliding angle (○) measurements of a glycerol drop on black Si surfaces plotted as a function of laser fluence. For fluences below 0.25 J/cm², the sliding angles are higher than 30°. The lines are guides for the eye.

The respective pictures of glycerol droplets lying on the surfaces after being thermally oxidized and terminated with a DMDCS layer are also shown. The highest CA reached is 151° , corresponding to an increase of 56° with respect to the flat surface. The corresponding dependence of CAs and SAs on laser fluence is presented in **Figure 5.23**, indicating an abrupt transition to superhydrophobicity as the laser energy increases. At high fluences, the apparent contact angle remains fairly constant, though the nanometre scale morphology changes significantly. Furthermore, glycerol droplets roll off the structured area at tilt angles lower than 10° for samples treated at fluences higher than $\sim 1.4 \text{ J/cm}^2$. Interestingly, such samples exhibit the most pronounced second length-scale surface roughness. Samples in the mid fluence range ($0.3 - 1.4 \text{ J/cm}^2$) do not meet the criteria for superhydrophobicity; they exhibit high sliding angles although they show similar contact angle to their high-fluence counterparts. On the contrary, glycerol drops remain pinned on surfaces structured at fluences lower than $\sim 0.3 \text{ J/cm}^2$. It is concluded that, the surfaces obtained at high fluences are superhydrophobic exhibiting high glycerol CAs and low hysteresis. In the case of water droplets, the fluence dependence of the respective CAs and SAs shows qualitatively the same characteristics,^[354] though the CAs measured are slightly higher and the SAs lower due to the small increase of the liquid surface tension.

5.6.5 Electrowetting experiment

i. Electrowetting on flat and hydrophobic surfaces

In this section flat silicon, **sample A** prepared at low fluence and also **Sample B** are tested. During the EWOD experiments, the apparent contact angle of a glycerol droplet on modified flat and structured surfaces was measured as a function of the applied voltage. The detailed evolution of the CAs for flat Si and **sample A** as a function of the bias voltage is plotted in **Figure 5.24(a), (b)**, respectively. For the flat surface the CA decreases as the bias voltage increases until it saturates when the CA change becomes $\sim 20^\circ$. CA saturation is not uncommon in EWOD systems; however, its origin is still undetermined and usually attributed to a specific leakage mechanism.^[355,356] It was recently shown^[357] that contact angle saturation can be explained if electrowetting is observed as a global phenomena affected by the detailed geometry of the system. Within this framework it is predicted that reversed electrowetting is also possible (contact angle grows with the voltage). The mechanisms proposed include the thermodynamic limit,^[358] charge trapping in the dielectric layer,^[359] internal flow in the droplet,^[360] breakdown of the air near the contact line,^[361] large electrical resistivity of the liquid,^[362] and dielectric breakdown.^[363] This behavior is reversible and the CA returns back to its initial value after reducing the applied bias. At relatively high voltages breakdown of the dielectric occurs and the leakage current attains high values; air bubbles appear within the droplet indicating electrolysis of the liquid. From this point on, no reliable measurements can be made. On the contrary no reversibility was recorded in the case of the microstructured **sample A**. As shown in **Figure 5.24(b)**, the apparent CA decreases as the bias voltage increases until it saturates when the CA change becomes $\sim 70^\circ$. EWOD experiments performed on **sample B** show similar qualitative and quantitative characteristics to those of **sample A**. Again, no reversibility was observed and the corresponding CA change before saturation was $\sim 80^\circ$.

The inset of **Figures 5.24(a)** shows the cosine of the CA as a function of the square of the applied voltage for flat Si. The line is a fit to the data according to the linear behavior predicted by the Lippmann-Young equation (**Eq. 5.15**). For the fit we have used in **Eq. 15** the measured oxide thickness d (shown in **Table 1**), the silicon oxide dielectric constant $\epsilon_r = 3.941$ and $\gamma_{lv} = 65.7 \text{ mN/m}$. The fit indicates that the experimentally observed behavior is in good agreement to the one predicted by **Eq. 15** until CA saturation occurs. On the contrary, this is not true for the corresponding CA (V) dependencies measured on the structured samples, suggesting that a proper modification of **Eq 5.15** is required in order to account for the effect of roughness on the EWOD behavior.

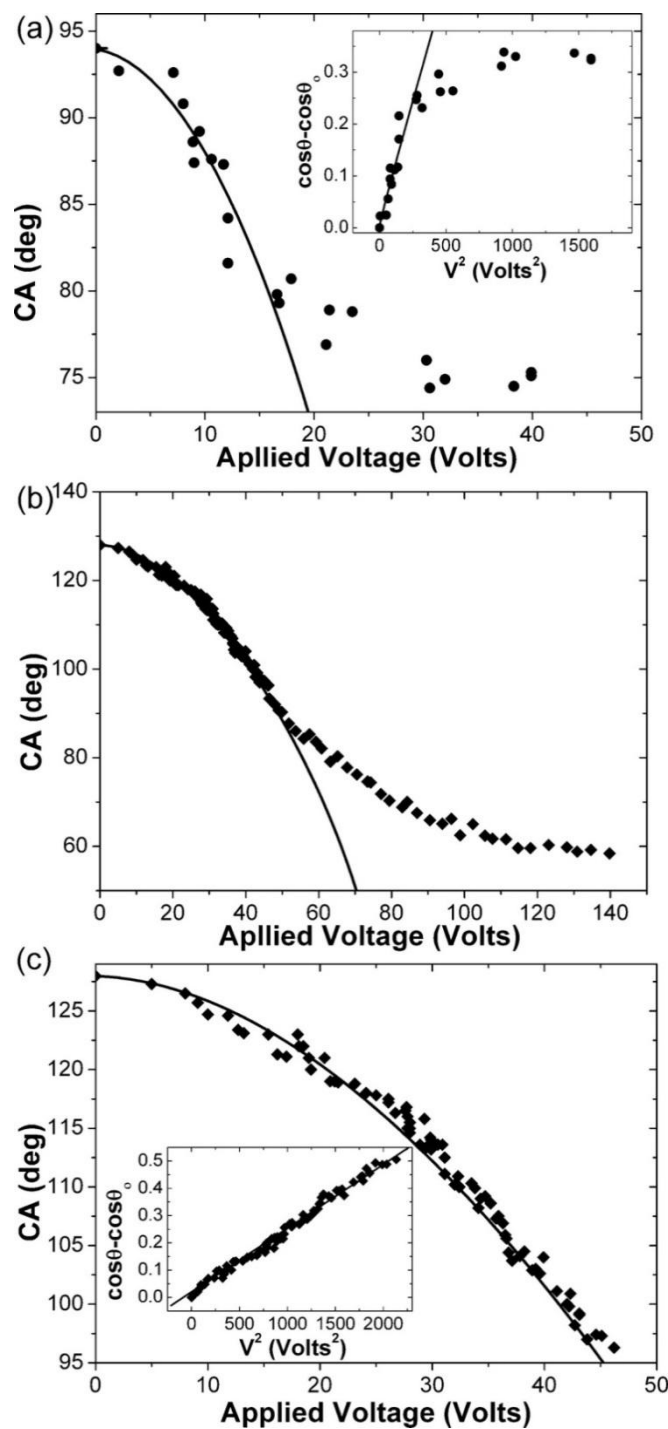


Figure 5.24: Contact angle of a 85% glycerol drop as a function of applied voltage for **(a)** a flat Si surface and **(b)** a structured Si surface prepared at low laser fluence. The lines represent fits to the Lippman-Young equation with parameters shown in the text. **(c)** Higher magnification of **(b)** at low voltages. Insets: The cosine of the contact angle as a function of the square of the applied voltage is shown. The line is a fit of the experimental data to the Lippmann-Young equation.

The effect of the macroscopic surface roughness on wettability has been explained by two different states described in **chapter 5.2.2**. Summing up in the Wenzel or “impalement” state,^[364] the liquid is assumed to completely penetrate within the rough surface and the apparent contact angle, θ_w , is given by the following equation: $\cos\theta_w = r \cos\theta_o$. In contrast, Cassie and Baxter assumed^[365] that the liquid does not completely impale the roughened solid. As a result, air pockets are trapped inside the features underneath the liquid, which sits above a composite surface made of solid and air (see also **Section 5.4**). For the Cassie state, the contact angle, θ_{CB} , is an average between the value on air (that is, 180°) and on the flat solid (that is, θ_o) and is given by $\cos \theta_{CB} = -1 + f + r_f f \cos \theta_o$. From energy considerations, it has been shown that the Cassie-Baxter state is often metastable.^[366] In practice this means that the drop will transit from a Cassie-Baxter state to the Wenzel state if it is subjected to an external perturbation, for example, as in our case, to an EWOD potential. Usually the external perturbation is quantified by the external pressure needed to provoke the droplet impalement. For a single-sized structure of pillars of radius d , this critical pressure is of the order of $P_c = (2\sigma\cos\theta_o)/d$, according to the Washburn equation, where σ is the liquid surface tension. To increase P_c , hence the resistance of the Cassie-Baxter state, a multiple-scale roughness has been proposed, inspired from the structure of the lotus leaf.^[367,368]

ii. Electrowetting on superhydrophobic surfaces

Figure 5.25(a), (b), shows the detailed evolution of the apparent CA during the EWOD process. The behavior is partly reversible as the contact angle returns back to the receding CA value after lowering the applied bias to 0 V. Reversibility is preserved upon several repetition cycles provided that the applied voltage falls within 0 and 44 V. This reversible electrowetting induced CA modification is $\sim 40^\circ$ ($\sim 150^\circ$ to 110°) in air environment is larger than that achieved ($\sim 23^\circ$) by Brunet et al.^[369] At higher voltages, however, the EWOD effect becomes irreversible though the apparent CA further decreases until it saturates when the CA change is $\sim 95^\circ$. At this state the contact angle hysteresis is significant as the sliding angle measured exceeds 30° .

In the case of the superhydrophobic surface we follow the approach described in **section 5.4.2** for the rough surface. Since $f < 1$ in **Eq. 14**, the EWOD effect is much weaker on highly hydrophobic surfaces than on normal ones. However the maximum change of the apparent CA is limited by the critical pressure of the surface which is reached when the microscopic CA between the liquid membrane and spike walls falls below 90° . In this case a wetting transition from the Cassie-Baxter to the Wenzel state occurs and the spikes are filled with liquid due to capillary forces. Until that critical limit of the apparent CA, θ_c , is reached the apparent CA as a function of voltage is approximately given by **Eq 5.18**

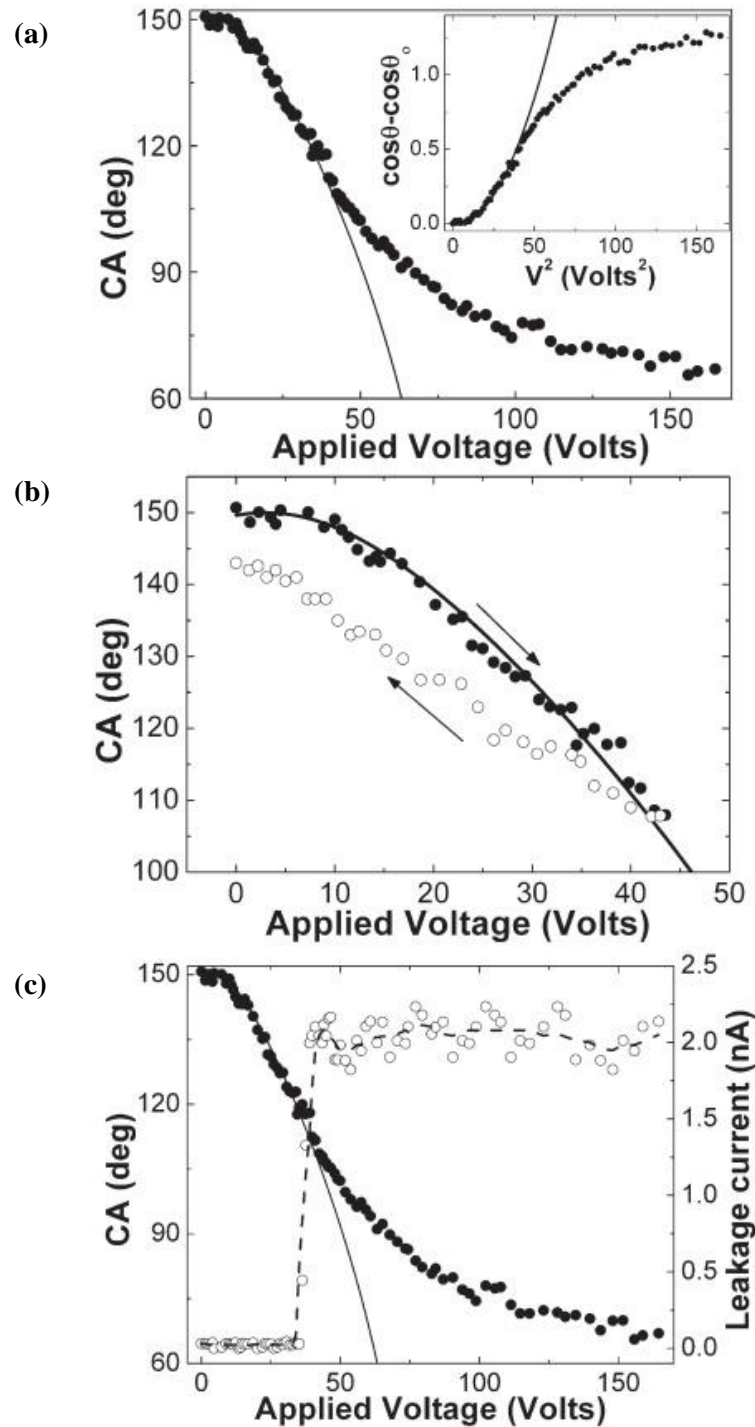


Figure 5.25 : (a) Contact angle of a 85% glycerol drop as a function of applied voltage for a black Si surface prepared at high laser fluence. Inset: The cosine of the contact angle as a function of the square of the applied voltage. The lines represent fits to the Lippman-Young equation with parameters shown in the text. (b) Reversibility of the EWOD effect; the arrows indicate decrease / increase of applied bias respectively (c) CA (on the left y axis) and leakage current (on the right y axis) dependence on the applied voltage. The solid line is a fit to the Lippmann-Young equation with parameters shown in the text; the dash line is a guide for the eye.

5.6.6 Critical value of applied voltage – CA saturation

When the applied field exceeds the critical value for which the wettability transition occurs, the apparent contact angle tends to saturate. **Figure 5.25(c)** shows the recorded leakage current through the EWOD device as a function of the applied voltage. A large jump in the leakage current was observed at about the same voltage where the onset of saturation takes place. Much higher applied voltage causes dramatic increase of the current, which is also indirectly detected by the bubbles rising inside the liquid drop, indicating hydrolysis. Our results are consistent with dielectric breakdown behavior regarding reversibility.^[370] Silicon oxide breakdown is a local effect, appearing as small spots of the order of 10 nm on the dielectric surface^[371] and it is found to be reversible as long as the leakage current is kept low.^[372] When excessive current is passed, e.g., due to high applied voltage, breakdown propagates and thermal damage is caused.^[373,374]

5.6.7 Reversibility of the electrowetting process

Summarizing the above results, reversibility of the electrowetting process occurred only on flat and superhydrophobic Si surfaces (**Sample C**). No reversibility was observed on hydrophobic surfaces. An example of the reversibility of the process on superhydrophobic surfaces is illustrated in **Figure 5.26** where the corresponding snapshots of glycerol droplets on the surface at different voltages are shown.

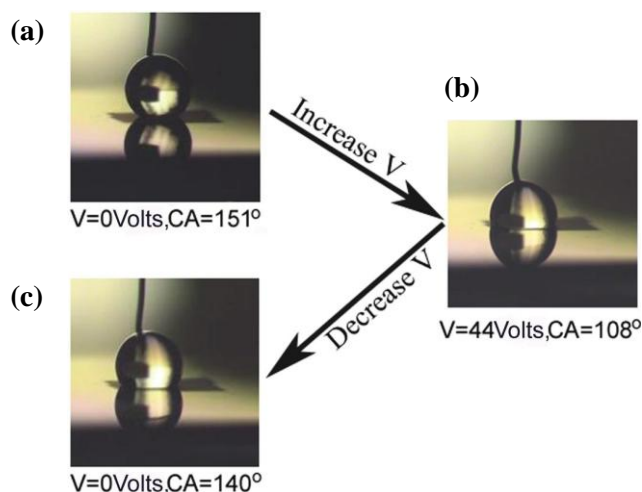


Figure 5.26: Reversibility of an EWOD system based on a super-hydrophobic black Si surface **(a)** before the application of voltage (0 V), **(b)** maximum contact angle change upon the application of 40.3 V, and **(c)** decrease of the voltage to 18.1 V, where the voltage to 18.1 V, where the system reaches contact angles close to the initial one.

The CA at 0 V equals to 151° and reaches down to 108° at 44 V. Decreasing the voltage back to 0 brings the drop close the initial CA ($\sim 140^\circ$) where the corresponding snapshots of glycerol droplets on the surface at different voltages are shown.

The insets of **Figures 5.24(c)** and **5.25(a)** show the best fits to **Eq. 5.18** for the black Si surfaces, with the f value being the only adjustable parameter. The corresponding best-fit f values, shown in **Table 1**, are similar among different samples indicating that the deterioration of the EWOD effect is not affected by the variations of the roughness ratio. On the other hand θ_c varies systematically among samples showing that the critical pressure limit and thus the droplet impalement state are reached at higher apparent angles as the roughness ratio is increased. This comes in accordance to the EWOD experiments of Lappiere et al. performed on superhydrophobic nanowire surfaces.^[375] More importantly, in **sample C**, θ_c coincides with the apparent angle above which EWOD reversibility can be attainable. This suggests that the irreversibility phenomenon may be attributed and associated to the wettability transition. When $\theta_{CB} > \theta_c$, the droplet is in the Cassie state and thus the CA can be reverted to its initial value once the applied voltage is removed. This is reasonable considering that the Cassie state is characterized by a minimal liquid/solid contact area and thus low hysteresis. Upon further increase of the applied voltage, the droplet switches to the Wenzel state and completely wets the interspike grooves. Once droplet impalement occurs, the CA becomes irreversible because the solid/liquid surface energy is lower than that of air/liquid, and thus it is energetically favorable for the system to preserve this state. Besides the solid/liquid contact area significantly increases leading to high contact angle hysteresis and thus to droplet pinning.^[376] The above indicate a relation between contact angle hysteresis and EWOD reversibility which is further supported from the observation that the only surface showed reversibility, i.e., **sample C**, exhibits the lowest hysteresis values. In conclusion, EWOD experiments suggest that surfaces of low contact angle hysteresis show higher resistance to liquid impalement.

Table 1. Morphological Characteristics, Wetting, and Electrowetting Properties of the Si Surfaces Studied

sample	spike density (cm ⁻²)	spike height, h (μ m)	d (nm)	contact angle (deg)	sliding angle (deg)	θ_a (deg)	θ_r (deg)	f	critical angle, θ_c (deg)	threshold velocity, v_t (m/sec)	critical velocity, v_c (m/sec)	critical pressure, P_c (kPa)
A	2×10^6	1	210 ± 5	128 ± 1	> 30			0.20	90	0.18 ± 0.01	3.10	9.60
B	5×10^5	7	205 ± 5	150 ± 1	14 ± 2	157 ± 1	148 ± 1	0.19	96	0.16 ± 0.01	3.83	14.70
C	3×10^5	10	190 ± 5	151 ± 1	7 ± 2	157 ± 1	152 ± 1	0.21	108	0.16 ± 0.01	> 5.0	> 25.00
Flat Si			210 ± 5	94 ± 1	> 30							

5.6.8 Alternative method for further investigation of the wettability transition via dynamic experiments.

In order to further investigate the relation between the EWOD behavior on superhydrophobic surfaces and the wettability transition we have used an alternate method to test the resistance to impalement. Drop impact is a method through which high pressures can be applied when a free-falling liquid droplet bounces on the surface under study. Neglecting any viscous effect, the dynamical pressure acting on the liquid interface is equal to $P = \rho v^2$, where ρ is the liquid density and v is the impact velocity. Bouncing experiments were performed on all samples studied and **Figure 5.27** presents a selected time sequence of snapshots of 10 μL (radius of $R \sim 1.35$ mm) water droplets impacting on **sample A**. Initially, it is observed that the drop shape changes significantly during impact as its kinetic energy transforms into stored energy due to surface deformation. Subsequently, due to the hydrophobicity of the surface, it retracts and under certain conditions bounce off the surface as illustrated in **Figure 5.27(a)**. The elasticity of such collisions is quantified by the determination of the restitution coefficient, $e = v'/v$, defined as the ratio of the center of mass velocity just after impact, v' , to that just before impact, v . Elasticity arises from the efficient interchange between kinetic and surface energy during drop deformation.^[377]

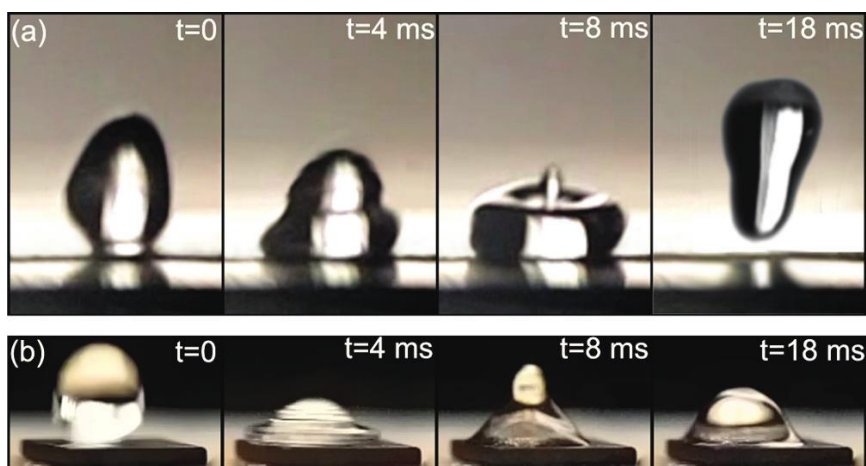


Figure 5.27: (a) Impact of a 10 μL water droplet on the black Si surface structured at the highest fluence used (**sample C**). The impact speed is 3.10 m/s and the droplet bounces off the surface. (b) Impact on the black Si surface structured at the lowest fluence used (**sample A**) at the same speed as in (a). The water droplet remains stuck on the surface.

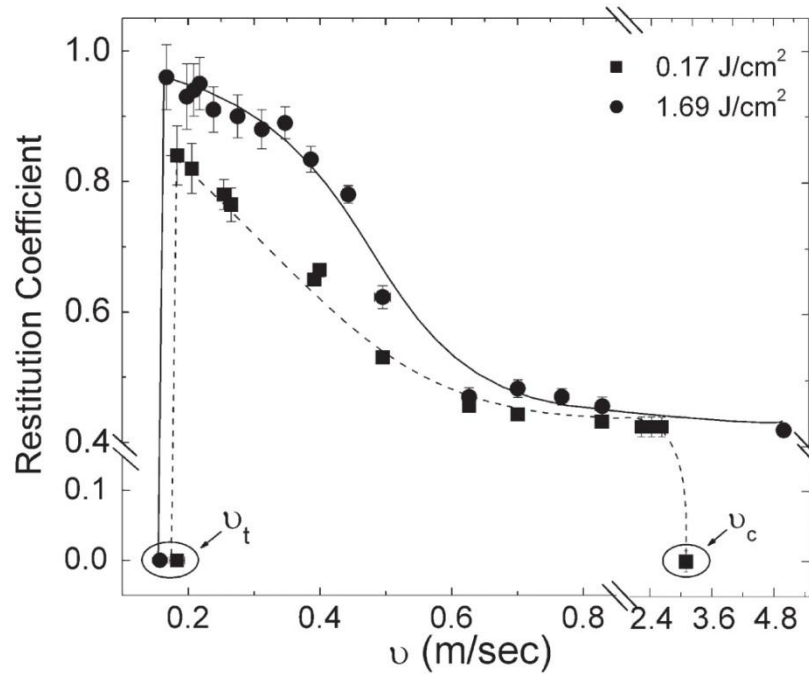


Figure 5.28: Restitution coefficient as a function of the impact velocity for the black Si samples structured at high (solid circles) and low (solid squares) laser fluence respectively. The lines are guides to the eye.

The restitution coefficient for **samples A** and **C**, deduced from the recorded video images is shown in **Figure 5.28** as a function of the impact velocity v . Looking more carefully at the retraction dynamics represented by the restitution coefficient we observe that, in the case of **sample A**, the droplet bounces back only for a range of impact velocities ($v_t < v < v_c$) and thus three distinct velocity regimes can be identified. For small velocities, e decreases abruptly with decreasing v and reaches zero at a velocity threshold v_t defined as the lowest velocity sufficient for droplet repellence; the smaller this velocity, the more water repellent the surface is.^[378] At intermediate velocities the drop bounces off the surface and several bouncing events can be observed. Upon increasing the velocity in this regime the droplet deformation becomes larger, the contact line hardly retracts and the elasticity of collisions is decreased. Finally, there exists an upper velocity, v_c , above which significant penetration of the liquid inside the structures occurs and, as a result, the contact line does not retract and the droplet remains stuck on the surface.^[379] This strong pinning effect is clear evidence that the liquid has penetrated within the microstructure and that the critical pressure, $P_c = \rho v_c^2$, for impalement has been reached. The values for v_t , v_c , and P_c , determined for the different samples studied are summarized in **Table 1**. It is interesting that **sample C** is found to be resistant to water penetration over the entire range of attainable impact velocities (0.16 - 5.00 m/s). This means that such surfaces resist pressures larger than ~ 25 kPa. Note that the surface was thoroughly examined after each experiment with a high resolution CCD optical system to confirm the

absence of any sign of water impalement. On the contrary **sample A** exhibits the lowest impalement pressure while its corresponding e values are lower than those of surface **C** for the whole range of v_s as liquid impalement causes a dramatic decrease of the respective bouncing heights. Both bouncing to non bouncing transitions arise due to the presence of surface defects, such as roughness or chemical heterogeneities^[380] that become the main source of kinetic energy dissipation. The contact line pins on such defects leading to a difference between the advancing and receding contact angles, i.e., in contact angle hysteresis. This suggests that the impalement effect may cause massive kinetic energy dissipation, due to the large value of the contact angle hysteresis at the vicinity of the moving contact line, during the spreading and receding processes. On the contrary, at the bouncing threshold regime the liquid does not penetrate the structure and the dissipation should only be due to pinning on top of the spikes, which constitute a small effective area and thus a lower mean number of surface defects. In this case, the pinning force per unit length is^[381,382] $F = \gamma_{LV}(\cos \theta_r - \cos \theta_a) = \gamma_{LV}\Delta(\cos \theta)$, with γ_{LV} the liquid surface tension and θ_a and θ_r the advancing and receding contact angles, respectively; the energy dissipated will, thus, scale as $\gamma_{LV}R^2\Delta(\cos \theta)$. The drop will bounce provided that its kinetic energy, which scales as $\rho R^3 v^2$, can overcome this dissipation. An estimate of the threshold velocity for water repellency can be obtained by equating the two energies. For a drop with radius $R \sim 1.35$ mm, the estimated threshold velocity is calculated as ~ 0.07 and ~ 0.12 m/s for **samples C** and **B** respectively. These threshold velocity values close to those observed experimentally.

5.6.9 Conclusions

In summary the EWOD properties of dual rough black Si surfaces with different micro and nano morphological characteristics were investigated. The EWOD induced CA change on these surfaces shows reversible or nonreversible behavior depending on the geometry of the surface structures. Reversibility is observed when the double-scale roughness becomes more and more pronounced leading to small values of contact angle hysteresis, low water repellence thresholds, and high values of critical pressures for impalement. Our results therefore indicate a clear relation between reversibility and surface water repellence properties. Furthermore, our results show at least two potential advantages of using dual rough black Si instead of planar Si in EWOD applications. On one hand, the roughened surface provides extension of the available EWOD voltages that can be applied before breakdown occurs and on the other hand, the changes in the CA, before the systems reaches saturation, are higher. In conclusion, our EWOD system exhibits remarkable CA reversibility in air environment as well as superior water repellence properties and may constitute dual rough black Si an important material in integrated microfluidic systems.^[383]

5.7 Reversible Photoinduced Wettability Transition of Hierarchical ZnO Structures

5.7.1 Introduction

Functional surfaces that can be reversibly switched between hydrophobicity and hydrophilicity under the action of external stimuli have aroused great interest due to a wide range of potential applications including intelligent microfluidic and laboratory-on-chip devices, controllable drug delivery, and self-cleaning surfaces.^[384,385,386] Among other materials, the wetting properties of metal oxides, mainly of ZnO and TiO₂, have been widely studied, since their wettability can be reversibly switched between superhydrophobicity and superhydrophilicity by alternation of ultraviolet (UV) irradiation and dark storage.^[387,388,389] In the present study, a two-step approach is developed in order to obtain a ZnO surface exhibiting roughness at two length scales. Microscale roughness, in the shape of spikes, is achieved on a Si wafer by structuring with femtosecond laser pulses (see **Section 2.4.1** and **3.3**). Nanoscale roughness is subsequently realized by coating the laser-structured surface with ZnO nanograins grown by pulsed laser deposition (PLD).^[390] Consequently, an enhancement of the nanoscale roughness is realized, and the final ZnO surface comprises hierarchical microstructures and nanostructures.

5.7.2 Surface characteristics and measurements

A two-step method was developed for the fabrication of ZnO nanostructures on Si spikes. Two surfaces were fabricated as described in **section 2.5.1** with laser fluence 0.17 and 2.1 J/cm². Following a thin ZnO film was deposited on each surface as described in **section 2.5.4**. Three types of substrates, namely, **sample A** (the Si microstructure prepared at 0.17 J/cm²), **sample B** (the Si microstructure prepared at 2.1 J/cm²), and a nanostructured thin film. The morphology of the samples' surfaces, prior as well as after the deposition of ZnO, was characterized by field emission scanning electron microscope (FE-SEM, JEOL 7000) equipped with an energy dispersive X-ray spectrometer (EDX).

Static contact angle (CA) measurements were performed by an automated tension meter as described in **section 2.7**, using the sessile drop method. The contact angle was found to remain the same, within experimental error, for droplets in the 1-5 μ L volume range. A minor decrease of 3° was measured in the case of a 0.5 μ L droplet. Therefore, a 2 μ L distilled deionized millipure water droplet was gently positioned on the surface using a microsyringe, and images were captured to measure the

angle formed at the liquid-solid interface. The contact angle hysteresis (CAH), defined as the difference between the advancing and receding angles, has also been measured. Light induced hydrophilicity was studied by irradiating the samples for certain time intervals using selective femtosecond-pulsed UV laser irradiation (248nm), with an intensity of 14 mW cm^{-2} . A monochromatic pulsed laser source is a preferable alternative to conventional UV lamps in terms of photoconversion efficiency because the process can be significantly accelerated, while avoiding a wider spectral distribution that often includes unwanted visible wavelengths known to inhibit the photoinduced transition.^[391] After each irradiation interval, a 2 μL water drop was placed on the irradiated area, and the corresponding contact angle was measured. Following irradiation, the samples were either stored in the dark at room temperature or annealed for 1 h at 200 °C under ambient conditions. Subsequently, the respective time-dependent contact angle variations were determined.

Figure 5.29(a) shows FE-SEM pictures of the microstructured silicon surfaces. Laser irradiation creates a surface morphology comprising a highly uniform and densely packed array of micrometer-sized conical structures (spikes). At higher laser fluence, the spike aspect ratio increases, resulting in a significant enhancement of the overall roughness.^[392] As we have previously reported,^[393] femtosecond laser structuring at different fluences allows one to control the wetting properties of Si surfaces. The water contact angle increases with laser fluence from 65° (flat Si) to ~129° for the surface prepared at 0.17 J/cm² and to ~150° for the surface prepared at 2.1 J/cm².

Surface morphology of a ZnO thin film deposited on a flat Si substrate is presented in **Figure 5.29(b)**. It consists of nanosized grains of average diameter of approximately 50 nm, with a regular, hexagonal shape. The corresponding cross-sectional view depicts the columnar structure of the grains, suggesting that the film growth has a preferred orientation, perpendicular to the substrate plane. X-ray diffraction analysis confirmed that the as-deposited ZnO film is highly oriented along the (002) direction. Other orientations corresponding to (100) and (101) are present with very low relative intensities. In the as-deposited state, the ZnO film is hydrophilic, exhibiting a contact angle close to 80°.

Panels c and d of Figure 5.29 depict FE-SEM images of the morphology of **samples A (Figure 5.29(a))** and **B (Figure 5.29(b))**, as acquired after the deposition of the nanograined ZnO film. As clearly seen, a significant enhancement of the nanoscale roughness is attained. The micrometer scale spikes have been decorated by nanosized protrusions, resulting in a hierarchically rough surface. The nanoscale

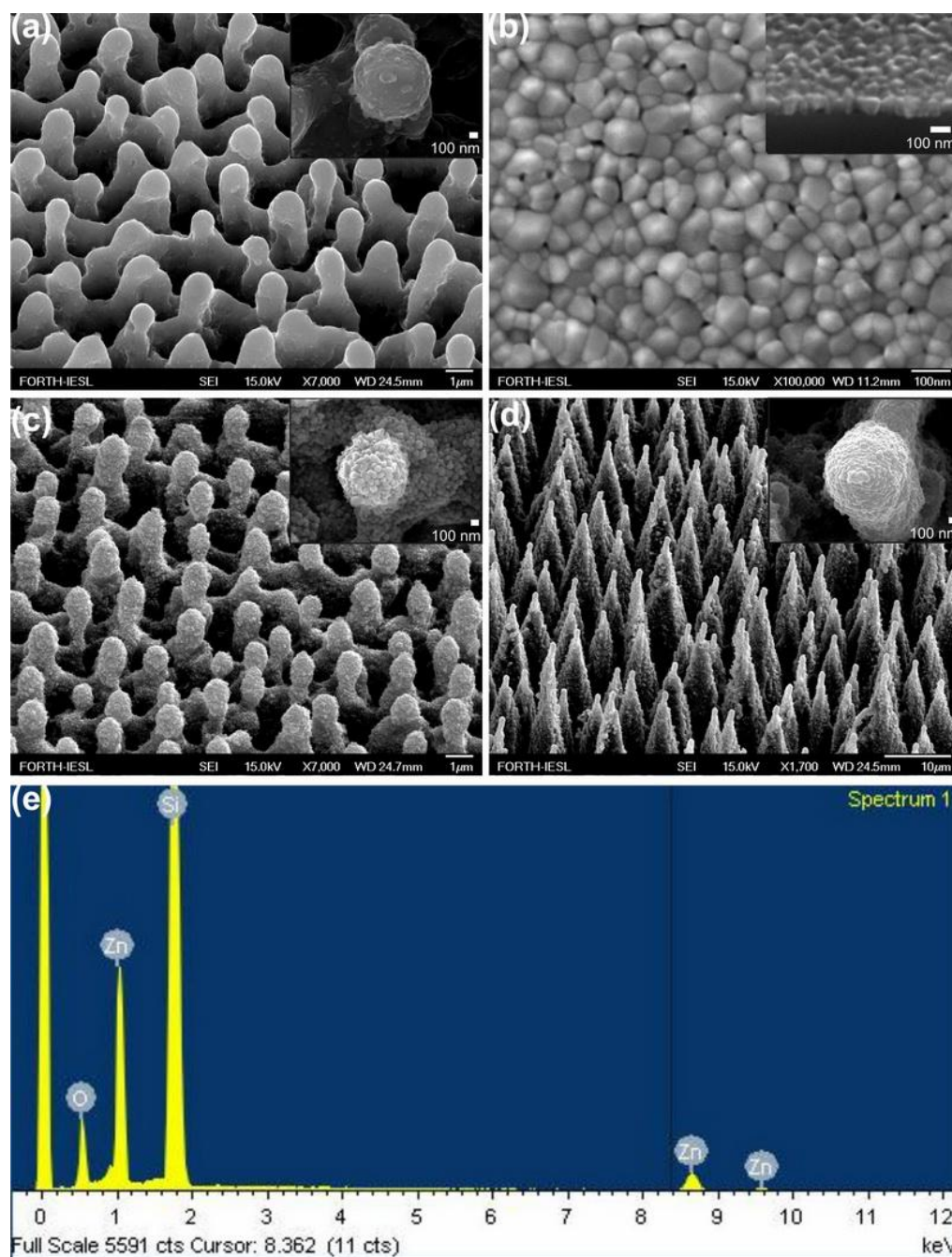


Figure 5.29: (a) Side SEM view of Si surfaces structured by femtosecond irradiation at a laser fluence of 0.17 J/cm^2 . The inset shows a higher magnification of the top of a single microcone. (b) Top SEM view of a nanogained ZnO film prepared by PLD on a flat Si substrate. A cross-sectional image of the film is shown in the inset. (c) Side SEM view of a ZnO-coated Si surface structured by femtosecond irradiation at a laser fluence of 0.17 J/cm^2 . Higher magnification of the top of a single microcone (scale bar is 100 nm), shown in the inset, reveals the double-scale roughness of the structures. (d) The same as in (c) but at a laser fluence of 2.1 J/cm^2 . (e) Typical EDX spectrum from a ZnO-coated Si spike surface. Elemental analysis showed a 1.0:1.05 molar ratio of Zn:O2.

features are more pronounced in **sample A** than those in **sample B**. The corresponding contact angle and CAH values were measured for sample A ($CA = 120 \pm 1^\circ$ and $CAH = 48 \pm 2^\circ$) and for **sample B** ($CA = 140 \pm 1^\circ$ and $CAH = 37 \pm 2^\circ$). The high CAH values denote that the droplet is strongly pinned to the surface; thus, the initial state of the droplet is stable.^[394] Stoichiometry of the ZnO protrusions was confirmed by EDX measurements performed on different positions on the structured surfaces (**Figure 5.29(e)**). Elemental analysis of the EDX spectrum was found to be similar to that obtained in the flat part of the sample outside of the spiked area. In both cases, the ZnO coating was deposited under conditions identical to those used for the nanostructured thin film shown in **Figure 5.29(b)**.

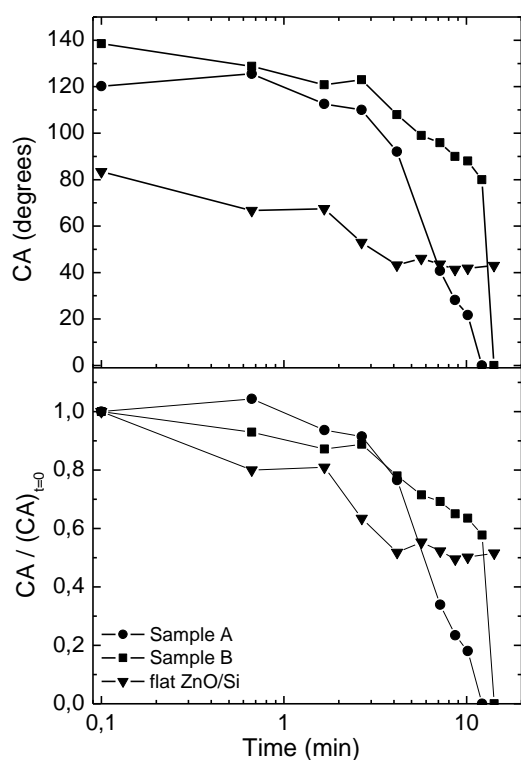


Figure 5.30: Dependence of the water contact angle on the UV illumination time for the flat and the structured ZnO samples studied. The corresponding evolution of the ratio of the respective contact angles to their initial values is also plotted for comparison.

Alternatively, thermal heating at 200 °C for 1 h can return all surfaces to their original hydrophobic state, speeding the reversibility process. All samples were subjected to numerous switching cycles (**Figure 5.31(c)**), without observing any deterioration of the irradiation efficiency or the reversibility behavior.

Figure 5.30 depicts the contact angle evolution with UV irradiation time for the different ZnO structures employed. Both structured samples exhibit a significant photoinduced transition to superhydrophilicity, reaching a nearly zero contact angle in short time. More importantly, the contact angle reduction rate, being a measure of the efficiency of the light-induced process, is higher than that observed in other ZnO structures.^[395,396] Counter intuitively, this rate is lower for sample B, which exhibits a higher total roughness (shown later). On the contrary, the nanostructured ZnO thin film shows a weak response to UV irradiation, as the wetting angle change in this case is much smaller for the same irradiation time. It should be emphasized that the aforementioned wettability changes are reversible because both dark storage and thermal heating reconvert the superhydrophilic surfaces to their original states (**Figure 5.31(a)**). After UV irradiation, the samples were placed in the dark. Hydrophobicity for **samples A** and **B** was restored within 24 h, whereas the flat sample required 7 days storage in order to return to its initial wetting state (**Figure 5.31(b)**).

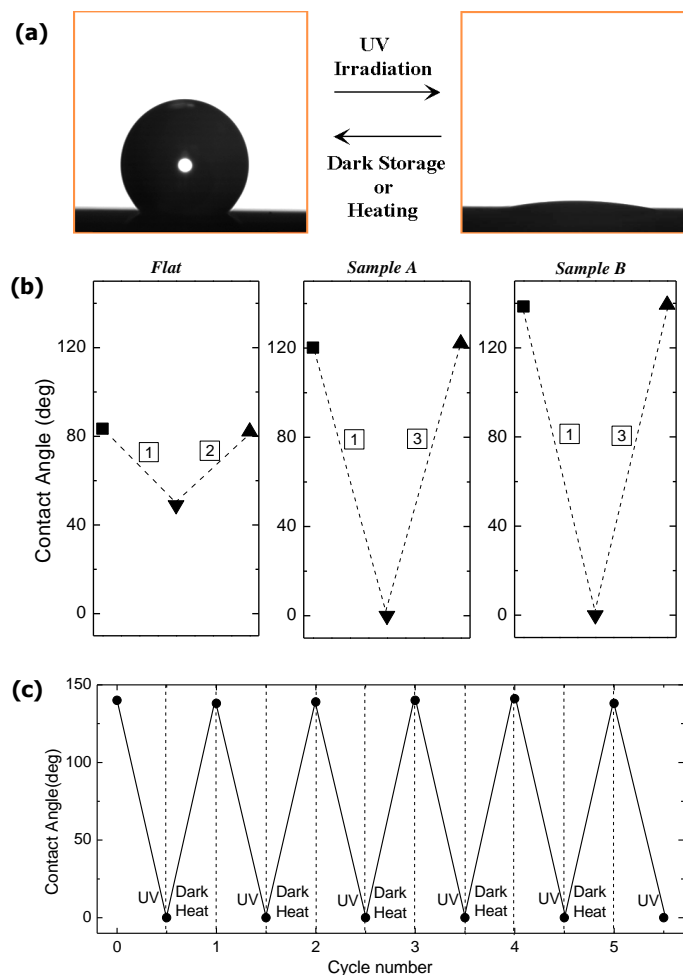


Figure 5.31: (a) Photographs of the shape of a water droplet on Sample B before (left) and after (right) UV illumination. The transition from hydrophobicity to superhydrophilicity is reversible upon dark storage or thermal heating (see (b) and (c)). (b) Restoration of the UV light-induced wettability conversion upon sample storage in the dark. The processes 1, 2 and 3 denote UV illumination for 20min and dark storage for 7 and 1 days respectively. In all cases, the surface can be switched several times between the two states, under the alternation of UV irradiation and dark storage. (c) Reversible switch from hydrophobicity to super-hydrophilicity for the Sample B, under the alternation of UV irradiation and thermal heating at 200 °C for 1 hour. Sample A exhibits similar response.

5.7.3 Transition from Cassie – Baxter to Wenzel state

Taking into account the theory described in **section 5.3** we analyze the response of the surfaces. The effect of double-scale roughness on wettability has been recently addressed.^[397,398,399] Assuming that the two types of roughness are homothetic^[400] meaning that they occupy the same fraction of surface, f , the Cassie-Baxter equation is modified as follows

$$\cos \theta_{CB} = -1 + f^2 (1 + \cos \theta) \quad (\text{eq 5.19})$$

As $f < 1$, the comparison of **Eq. 5.12** and **5.14** shows that the contact angle of the dual roughness surface is always higher than in the single roughness case. There are many theoretical and experimental reports on the transition between the two basic wetting states described above under the action of various external stimuli.^[401,402,403,404] However, to our knowledge, there are limited theoretical and no experimental reports for the effect of this transition.

The initial contact angle of the flat ZnO sample is always lower than 90° , indicating that the as-deposited grains are hydrophilic. Following the results presented in **Figure 5.30**, it is obvious that the original contact angle values measured for the structured samples are consistent with the CB model because contrary to the Wenzel model, it predicts a rise in the wetting angle upon increasing the roughness of an initially hydrophilic ($\theta < 90^\circ$) surface. Assuming that the intrinsic contact angle θ is measured on the flat film ($\theta = 83.4^\circ$), **Eq 5.12** is used for the estimation of the f parameter for the two samples in their as-deposited state. The result is $f \sim 0.7$ for **sample A** and $f \sim 0.5$ for **sample B**. This means that **sample B** exhibits higher total roughness and, being in a Cassie-Baxter state, is less wetted by the water drop.

As also shown in **Figure 5.30**, in both samples the evolution of contact angles is gradual at short illumination times, followed by an abrupt change taking place at wetting angles lower than $\sim 90^\circ$. This sharp transition toward superhydrophilicity suggests that the wetting state of the drop switches from the Cassie-Baxter state to the Wenzel state, as the latter is the model predicting the possibility of superhydrophilicity for very rough surfaces. The corresponding evolution of the composite roughness factor f up to the transition to the Wenzel state can be monitored using **Eq 5.14** and the contact angle values of **Figure 5.30**. This is plotted in **Figure 5.32**, where each point of the factor f had been obtained by substitution in **Eq 5.19** of the respective contact angle values for any given exposure time. As can be seen from this plot, the transition takes place when f equals values higher than unity, rendering the Cassie-Baxter model invalid.

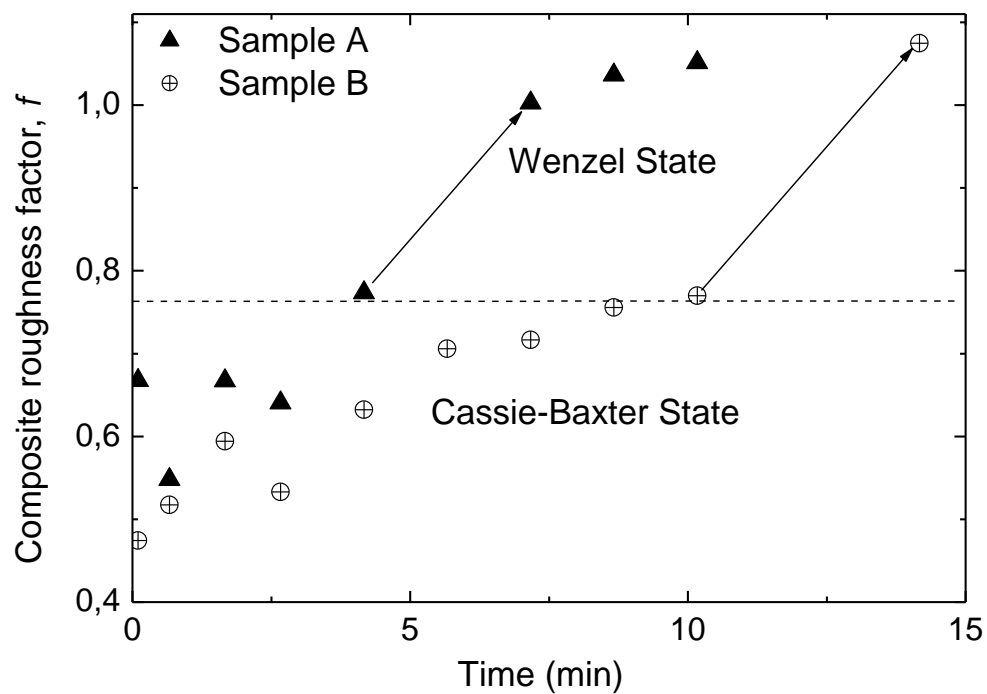
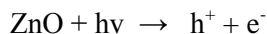


Figure 5.32: Dependence of composite roughness factor, f , on the UV-irradiation time for the samples A and B, respectively. The transition from the Cassie Baxter to the Wenzel state occurs at a critical f denoted by the dashed line.

5.7.4 Mechanism of the transition

Then the semiconductors are illuminated with energy greater than their bandgap energy E_g . Excited high-energy states of electrons and hole pairs^[405] (e^-/h^+) are produced



Some of the holes react with lattice oxygen to form surface oxygen vacancies, while the electrons can react with the metal ions (Zn^{2+}) present in the lattice, forming Zn^+ defective sites. Meanwhile, water and oxygen may compete to dissociatively adsorb on these vacancies. The Zn^+ defective sites are kinetically more favorable for hydroxyl adsorption than oxygen adsorption. As a result, the surface hydrophilicity is improved, and the water contact angle is significantly reduced. It has also been demonstrated that the surface becomes energetically unstable after hydroxyl adsorption. Because oxygen adsorption is thermodynamically favored, it is more strongly bonded on the defect sites than on the hydroxyl groups.^[406] Therefore, the hydroxyl groups adsorbed on the defective sites can be replaced gradually by oxygen atoms when the UV-irradiated samples are placed in the dark. Subsequently, the surface evolves back to its original state (before any UV irradiation), and the wettability is reconverted. Heat treatment accelerates the elimination of surface hydroxyl groups, and as a result, the hydrophilic surface converts quickly to a hydrophobic surface.^[407] On the basis of the above analysis, it can be concluded that the reversible switching between hydrophobicity and superhydrophilicity is related to the synergy of the surface chemical composition and the surface roughness. The former provides a photosensitive surface, which can be switched between hydrophilicity and hydrophobicity, and the latter further enhances these properties.

As is shown in **Figures 5.30** and **5.31**, the final step to superhydrophilicity is more abrupt in the case of **sample B** where the microscale roughness is higher. This suggests that microscale roughness plays a major role in the transition from the Cassie-Baxter to the Wenzel state as it contributes more to the total roughness. In contrast, the transition to the Wenzel state occurs in shorter times for sample A, where the nanoscale roughness is more pronounced. This indicates that nanoscale roughness plays a more important role in the efficiency of the light-induced process. This may be attributed to the fact that the surface to volume ratio is higher in this case, and as a result, the total interface between water and the grown ZnO structures is high. This leads to an effective increase in photoactive defect sites, which are in contact with water molecules.

5.7.5 Conclusions

In conclusion, we have developed a two-step method to prepare ZnO structures showing hierarchical architectures combining microscale and nanoscale features. Such ZnO structures were found to exhibit a remarkable reversible transition to superhydrophilicity after exposure to UV light. We conclude that this technique can be employed to control the structural and morphological properties of ZnO structures, resulting in reversible efficient wettability changes. Such capability may be useful for self-cleaning coatings and microfluidic applications, as well as for studying the wettability of biological surfaces and its relation to microstructures and nanostructures.

5.8 Smart Polymer-Functionalized Surfaces

5.8.1 Introduction

Attempts to develop substrates with dual-scale roughness have created surfaces with high contact angles (CA) ($\sim 150\text{-}160^\circ$) and low contact angle hysteresis (CAH, defined as the difference between the advancing and receding CA) ($2.5\text{-}5^\circ$),^[408,409,410] both of which are particularly important with respect to water repellency.^[411,412,413] Functionalization of an artificially roughened substrate with a responsive coating has resulted in surfaces that can, in principle, switch between super-hydrophobicity and super-hydrophilicity in response to appropriate stimuli. The possibility of multi-responsive surfaces has been explored as well.^[414,415] Polymer brushes created by end-grafting stimuli-sensitive polymers onto surfaces with hierarchical micro/nano roughness have been frequently utilized for the development of such smart surfaces. For responsive surfaces, only the static CA has been used to describe the superhydrophobic state whereas achieving low values of CAH was not illustrated.^[411] The dynamic behavior of droplets impinging on such smart surfaces remains unexplored as well. To date polymers that become superhydrophobic at low pH and anionic and superhydrophilic at high pH have been reported;^[414] however, that imposes certain limitations for many applications, e.g., the anionic polymer surfaces cannot interact with DNA, enzymes, and polyanionic drugs by attractive electrostatic interactions.

In the present section, we utilize these surfaces to develop polymer functionalized pH-responsive substrates that can reversibly switch between superhydrophilicity at low pH and superhydrophobicity / water repellency at high pH. The switching behavior of the surface is driven by the combined effects of the polymer chemical response and the dual-scale roughness. Herein, we quantify the water repellency of the surfaces in their superhydrophobic state by drop elasticity measurements. Moreover, we demonstrate that the water repellent state of the surfaces requires appropriate hydrophobicity of the functionalizing polymer, whereas for the first time we characterize the CAH along with the static CA in the superhydrophobic state of the responsive surfaces.

5.8.2 Functionalizing the silicon structured surfaces

Silicon structured surfaces were prepared by laser irradiation as described in **section 2.4.1 and Figure 5.5.1**. These artificial surfaces, possessing hierarchical micro- and nano- structures are able to quantitatively mimic both the structure and the water repellence of Lotus leaf. The responsive surfaces were prepared by “grafting from” poly(2-(diiso-propylamino)ethyl methacrylate), PDPAEMA, brushes, at anchoring density $\sigma=0.78$ chains/nm², onto the dual-length-scale roughened substrates using surface-initiated atom transfer radical polymerization (ATRP). Both the microscale conical features and the nanoscale protrusions are evident following the functionalization process verifying that the polymerization reaction did not perturb the hierarchical surface roughness. PDPAEMA homo-polymer is a pH-responsive weak polybase, which undergoes reversible protonation/deprotonation upon changing the solution pH.

5.8.3 Switching the hydrophobicity via the PH sensitive coating

The switching behavior of the surface is driven by the combined effects of the polymer chemical response and the dual-scale roughness. Herein, we quantify the water repellency of the surfaces in their superhydrophobic state by drop elasticity measurements. Moreover, we demonstrate that the water repellent state of the surfaces requires appropriate hydrophobicity of the functionalizing polymer, whereas for the first time we characterize the CAH along with the static CA in the superhydrophobic state of the responsive surfaces.

Images of a water droplet lying on the PDPAEMA functionalized artificial surface are shown in **Figure 5.33** following successive immersions in solutions at pH 8.5 and pH 2.5. The complete wetting (superhydrophilicity) following the immersion at pH 2.5 and the superhydrophobic behavior (CA $154 \pm 1^\circ$) following the immersion at pH 8.5 are due to the reversible protonation/deprotonation of DPAEMA (the pK_a of PDPAEMA is 6.3). **Figure 5.33** also shows the respective behavior for a dual-scale roughened surface, functionalized with a poly(2-(diethylamino)ethyl methacrylate), PDEAEMA, brush (the pK_a of PDEAEMA is 7.3). The responsive behavior is evident in this case as well; however, the behavior after immersion at pH 10 is far from super-hydrophobic with the CA reaching only $\sim 126 \pm 1^\circ$. It is noted that the water CA on a PDPAEMA brush on a flat Si surface is

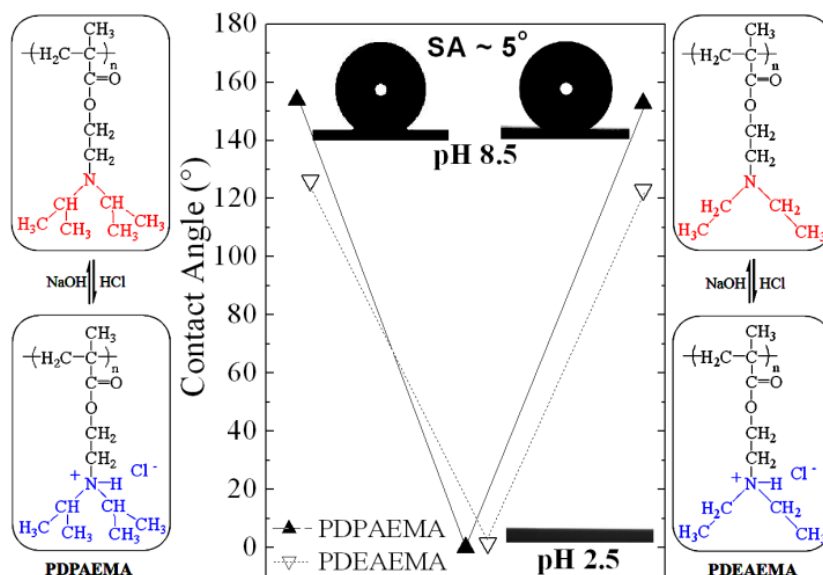


Figure 5.33: Characteristic images of water droplets residing on the PDPAEMA functionalized hierarchically structured surface following immersion at pH 8.5, pH 2.5 (complete wetting) and again at pH 8.5 (▲). The CA values for the PDEAEMA functionalized surface at pH 10 and pH 3 are shown for comparison (▽). The schemes on the two sides show the protonation / deprotonation process of PDPAEMA and PDEAEMA.

$\sim 88 \pm 1^\circ$ whereas that on a PDEAEMA brush on a flat Si surface is $\sim 83 \pm 1^\circ$ (both in the deprotonated state). It is, therefore, the combined effect of the dual-scale roughness and the sufficient hydrophobicity of the material^[416] that is necessary in order for a surface to become superhydrophobic; the incorporation of only two extra methyl groups per monomer unit (**Figure 5.33**) can lead to a “hydrophobic enough” material.

The average CAs of water drops residing on the PDPAEMA functionalized artificially structured surface are shown in **Figure 5.34(a)** following successive immersions at pH 8.5 and pH 2.5. It is evident that the responsiveness of the functionalized hierarchically-structured surface holds for at least ten cycles, with very stable values of the CAs of both the superhydrophobic and the superhydrophilic state. It is, thus, proven that the polymer brush synthesized onto the dually-roughened surface is resilient to pH variations, which is especially important since the brush is immersed in basic and strongly acidic solutions. The PDPAEMA brush synthesized onto a flat Si surface is responsive as well (**Figure 5.34(b)**) with CA value variations, however, that are only within $\sim 30^\circ$.

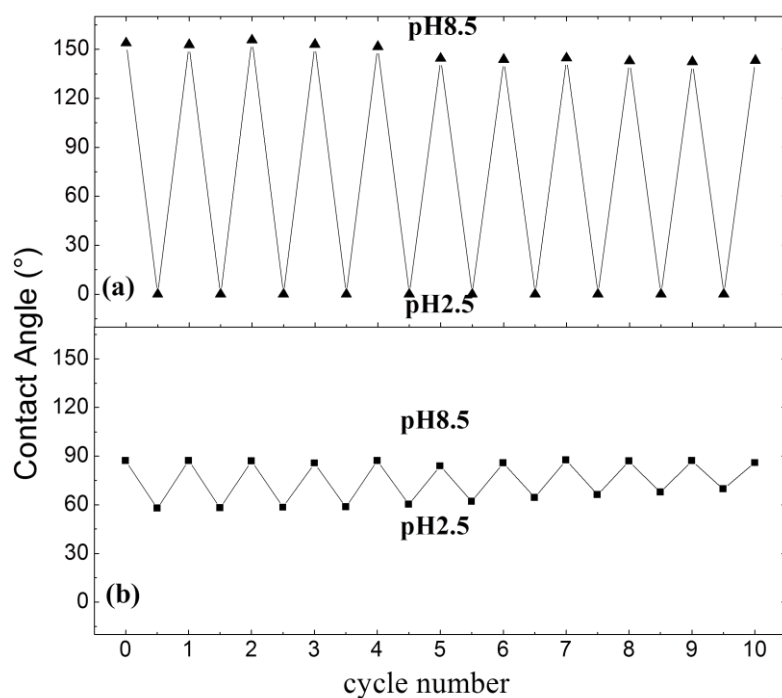
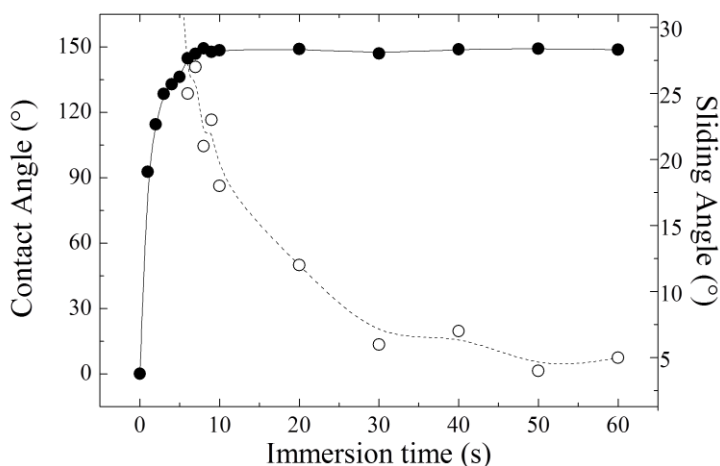


Figure 5.34: (a) Average CA values of water drops residing on the PDPAEMA functionalized hierarchically structured and (b) flat surfaces following successive immersions at pH 8.5 and pH 2.5.

The kinetics of the hydrophilic/hydrophobic transition determines the speed of the surface responsiveness. **Figure 5.35** shows the average CAs of water droplets on the PDPAEMA functionalized artificial surface following immersions in a solution at pH 8.5 together with the respective **sliding angles** (SA^{endnote-i}) for 10 μ L drops as a function of immersion time. It is clearly seen that, although the equilibrium value of the CA of $\sim 154^\circ$ is reached after only about 10s, the

- ii. The SA, α , is defined
criterion for assessing
 $\gamma_{LV}(\cos\theta_r - \cos\theta_a) = \gamma_{LV}$
advancing and receding
sliding angle of 5° corr
- i. The Weber number is d



d surface; it is used as a
equation $mg\sin(\alpha)/2R =$
al constant, θ_a and θ_r the
lume) and for $\theta_a=154^\circ$, a
locity.

Figure 5.35: Average CA (filled symbols) and SA (open symbols) values for a PDPAEMA functionalized hierarchically structured surface as a function of immersion time in a solution at pH 8.5.

equilibrium value of the SA of $\sim 5^\circ$, which results in water repelency, is only reached after much longer times of ~ 40 - 50 s. Most probably, although the incomplete deprotonation of the polymer brush can be sufficient to result to an apparent hydrophobicity of the surface ($CA > 150^\circ$), the presence of even few charged monomer units can lead to chemical heterogeneities^[417,418] that cause contact line pinning and, thus, high CAH.^[411] The inset of **Figure 5.36** presents selected snapshots of a free-falling water droplet (radius 1.35 mm) impinging on the PDPAEMA functionalized artificial surface following its immersion to a pH 8.5 solution. The drop impacts the surface with a velocity that corresponds to a dimensionless Weber number of $We=3.5$.^[endnote-ii] The surface is so water-repellent that the drop bounces back numerous times and selected maxima of its trajectory are shown as a function of time. The drop finally comes to rest on the surface after ~ 250 ms.. The elasticity of the

collisions on the PDPAEMA brush-functionalized artificially-structured surface indicates a high degree of repellency. A direct measure of this elasticity is the restitution coefficient, $\varepsilon = V'/V$, defined as the ratio of the center of mass velocity of a droplet just after impact, V' , to that just before impact, V . This coefficient is deduced from the recorded video images and is shown in **Figure 5.36** as a function of the impact velocity V in comparison with that of the natural Lotus leaf.^[410] The highest elasticity is observed at intermediate velocities, from ~ 0.18 m/sec to ~ 0.30 m/sec, where the

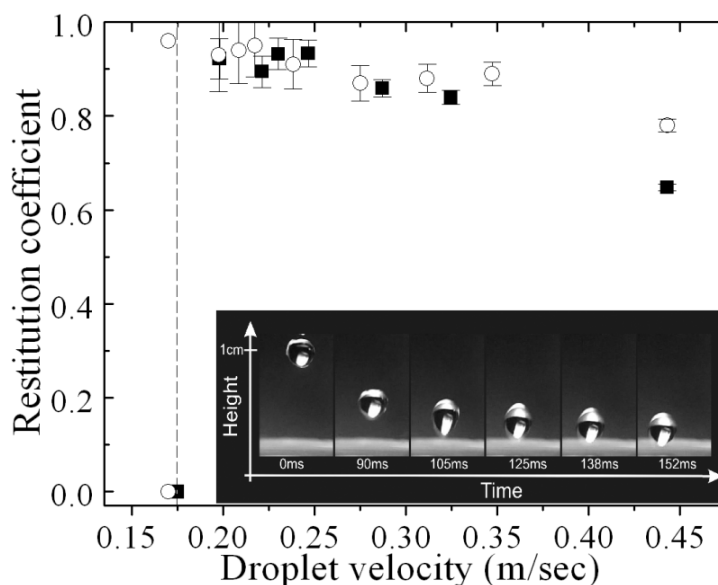


Figure 5.36: Restitution coefficient as a function of the impact velocity for the PDPAEMA functionalized surface, after immersion at pH 8.5 (filled squares), and a natural Lotus leaf surface^[410] (open circles). The dashed line signifies the threshold velocity. Inset: Selected snapshots of a water drop impinging on the surface for $We=3.5$.^[24] Maxima of the drop trajectory are shown as a function of time.

restitution coefficient exceeds 0.90. For small velocities, ε decreases abruptly with decreasing V and reaches zero at a certain velocity (0.17 m/s). This is the threshold that quantifies the water repellency of the surface; the smaller this velocity, the more water repellent the surface is. The similarity of the restitution coefficient (to our knowledge, is among the highest ever reported^[411]) as well as the threshold velocity value (necessary to avoid sticking of the drops) between the functionalized artificial and the Lotus leaf surface is evident. It is considered that the bouncing to non-bouncing transition arises from the presence of surface defects; the contact line pins on defects resulting in a difference between advancing and receding CA, θ_a and θ_r , i.e., in hysteresis. The pinning force per unit length is $F = \gamma_{LV}(\cos\theta_r - \cos\theta_a) = \gamma_{LV} \Delta(\cos\theta)$,^[281] the energy dissipated will, thus, scale as $\gamma_{LV}R^2\Delta(\cos\theta)$. The drop will bounce provided that its kinetic energy scaling as ρR^3V^2 can overcome

this dissipation. An estimate of the threshold velocity for water repellency can be obtained by equating the two energies. The relative CA were measured as $\theta_a=154\pm1^\circ$ and $\theta_r=149\pm1^\circ$ for the PDPAEMA superhydrophobic surface. For a drop with radius $R\sim 1.35$ mm, the estimated threshold velocity is calculated as ~ 0.07 m/sec, a value close to that observed experimentally.

5.8.4 Conclusions

In summary, pH-responsive surfaces were developed, which can reversibly switch between superhydrophilic at low pH and superhydrophobic and water repellent at high pH. The surfaces were developed by “grafting from” a pH-sensitive polymer brush onto controlled hierarchically micro- and nano-structured substrates, which mimic the hierarchical morphology of natural water repellent surfaces. The responsive behavior is due to the combined effect of the hierarchical micro- and nano-roughness and the appropriate hydrophobicity of the functionalizing polymer brush. We show the kinetic behavior for achieving low values of the CAH, which, together with high values of the static CA, are required for superhydrophobicity and water repellency.

C) Biological Applications

Introduction

The eventual goal of artificial cell culture scaffold design is to mimic the natural extracellular environment features, in a way that cells can function as if they in vivo. In this respect, designing surfaces for controlling cell–material interactions is a considerably interesting subject, highly significant in the development and eventual success of implantable medical devices and engineered tissues.^[419,420,421] Using different approaches, various materials have been surface engineered in order to guide cell adhesion and modulate cell–biomaterial interactions,^[422,423,424] indicating that cell growth, division and migration are highly dependent on their immediate culture substrate. Hence, surface chemistry,^[425,426,427] wettability^[428,429] and roughness^[2,430,431] are found to be three of the most important factors influencing biological reactions at biomaterial surfaces.^[432] In spite of such numerous investigations, an intrinsic and deep understanding of the factors governing attachment of cells to biomedical surfaces, is still limited^[433-434]. Most studies have been using substrates covering only a small range of roughness, while the effects of nanoscale or microscale roughness were in most cases separately investigated.^[2,435,436,437,438,439] There is, however, increasing evidence indicating that cell–surface interactions occur at multiple length scales.^[6] Indeed, in the context of a natural environment, the cells included in a tissue are surrounded by a three-dimensional (3D) dynamic extracellular matrix (ECM), which provides instructive cues at meso-micro- and nano- scales necessary to maintain cell phenotype and behaviour. Therefore, in order to reach the level of ECM complexity, biomedical substrates must interlace hierarchically organized multiple-scale structures. Due to such demanding design requirements, cell response on sub-micrometer as well as micrometer scale rough substrates, has not yet been systematically studied. Thus, the production of surface engineering schemes enabling controlled and reproducible structuring of biomaterials at both micro- and nano-scales, is required.^[440]

Another limiting parameter of the so far available literature includes the instability of chemical composition of the surfaces, which by changing deliberately or unintentionally during the micro/nano structuring process, damage the cells, since they are inherently sensitive to variations of surface chemistry

[6]. Consequently, most of studies raise the question of whether cell behaviour, related to viability, proliferation, motility, adhesion, morphology, cytoskeletal arrangement and gene expression, is influenced by the topographical features and/or the surface chemistry of a scaffold, parameters that determine the surface tension and wettability.^[441,442] In order to overcome such controversies, it is crucial to find pathways to discriminate among the different effects. In this respect, the ability (a) to control the surface chemistry, while keeping the same micro/nano morphology or vice versa and (b) to tune surface wettability from super-hydrophobicity to super-hydrophilicity are highly important tools allowing successful attachment of fully functional cells to biomedical surfaces.

5.9 Tuning cell adhesion of fibroblasts

5.9.1 Introduction

In this Section we demonstrate the ability to tune cell adhesion using biomimetic artificial substrates in a 3D-design, comprising hierarchical micro- and nanostructures produced by ultrafast laser patterning of silicon (Si). Tailoring of the structures' morphological features can be advantageously achieved by varying certain fabrication parameters. This capability allows one to control the wetting properties and thus, surface tension of the Si substrates. Further control over wettability can be achieved by altering the surface chemistry through coating the structures with various conformal layers, while keeping the same morphology. As a consequence, it is possible to preferentially tune the wettability of the artificial substrates from super-hydrophobicity to super-hydrophilicity through a proper combination of surface topography and chemistry. In this respect, it was demonstrated that the patterned Si substrates can be potentially used as model scaffolds for the systematic exploration of the role of 3D micro/nano morphology and/or surface energy on cell adhesion and growth. The different structures obtained by this method can be transferred to various types of polymeric materials as well through replication molding techniques.^[443] The simplicity of the structuring process and the flexibility of fast patterning by laser beam scanning, together with its potential to tailor the wettability of different classes of materials, are certainly useful for creating patterned interfaces on biomaterials devices.

5.9.2 Methodology

Four different Silicon structured surfaces were fabricated as described in section 2.5.1. Depending of the laser fluence each of these samples posse a 3D-design and exhibit different roughness having both micrometer and nanometer length scales. **Figure 5.37(a),(b)** presents the SEM images of the silicon structured surfaces. Starting from flat silicon (a-i) and increasing the laser fluence remarkable changes in the structures ragarding ratio, dimension and density can be archieved. Besides directly affecting the micrometer-scale surface topology, increasing fluence is also crucial to induce a more pronounced sub-micrometer decoration on the spikes walls. In particular, the spikes height varied from one to ten micrometers, while the size of nano-protrusions ranged from tens to a few hundreds of nanometers, providing a double length-scale pattern on the silicon surface (**Figure 5.37(b)**).

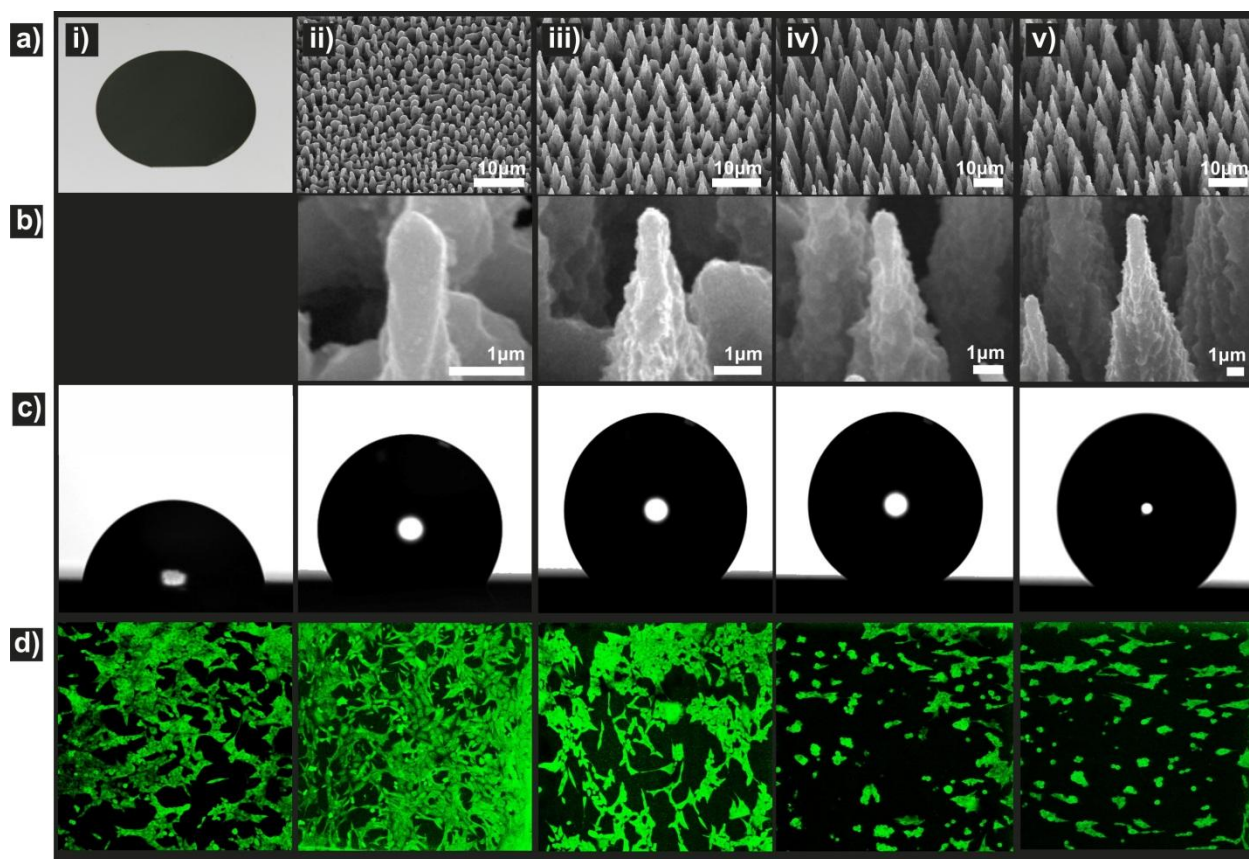


Figure 5.37: (a) Picture of a polished Si wafer (i) and side SEM views of the as-prepared Si spikes surfaces structured at four different laser fluencies (ii) 0.34 J/cm^2 (A1), (iii) 0.56 J/cm^2 (A2), (iv) 0.90 J/cm^2 (A3), and (v) 1.69 J/cm^2 (A4); (b) high magnification SEM images of the corresponding Si cones obtained; (c) photographs of water droplets on the patterned Si surfaces; and (d) confocal laser microscopy pictures of fibroblast cells cultured for three days on the respective surfaces.

Sample	Flat Si	Oxidized Flat Si	A1	B1	A2	B2	A3	B3	A4	B4
Laser fluence (J/cm^2)	–	–	0.34	0.34	0.56	0.56	0.90	0.90	1.69	1.69
Roughness ratio	0	0	2.6	2.6	3.3	3.3	6.0	6.0	6.9	6.9
Wetting angle ($^\circ$)	67	25	105	20	121	20	152	0	154	0

Table 1: General properties of the different samples used for this study. Series A denote as-prepared patterned Si surfaces and series B denote the patterned surfaces after thermal oxidation treatment.

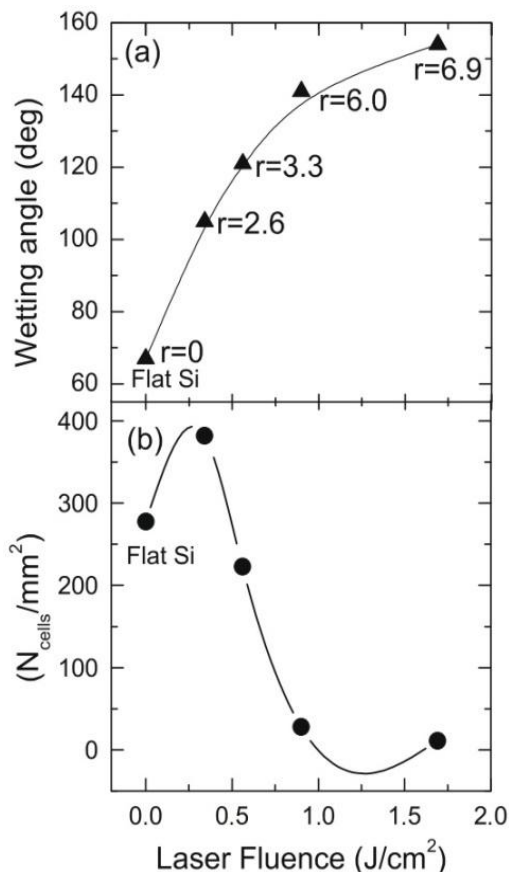


Figure 5.38: (a) Relation between the laser fluence and surface wettability for the series A patterned Si substrates; the corresponding roughness ratio for each sample is also indicated; (b) cell density after 72 h incubation as a function of the surface wettability for the flat Si and structured surfaces of series A. All experiments were done on triplicates and the cell density values plotted are the calculated mean values. The lines serve as a guide for the

The micrometer-scale features, together with the nanoscale protrusions resulted into a significant increase of the overall roughness. Consequently, these etched substrates should allow more 3D free space perpendicular to the culture plane and should also provide physical cues to facilitate cell adhesion and spreading.

In this study, three series of substrates were tested: **Type A** corresponds to the, as-prepared, patterned Si surfaces comprising four samples with gradient roughness ratios, denoted as **A1–A4**; **Type B** corresponds to the same substrates coated with a hydrophilic thermally grown oxide layer (**B1–B4**); (c) **Type C** corresponds to the same substrates coated by a hydrophobic silane layer. **Types A** and **C** samples had shown the same qualitative results and will be considered as equivalent cases thereafter. In all series, the corresponding flat surfaces were tested as control samples. The principal properties of the above substrate types are summarized in **Table 1**. Images of water droplets lying on flat and as-prepared micro-structured Si surfaces are shown in **Figure 5.37c**. The corresponding dependence of the wetting angle (WA) on the laser fluence and roughness ratio attained is plotted in **Figure 5.38(a)**. It is evident that the laser assisted texturing of Si induced a remarkable increase in its hydrophobicity which was more pronounced at high fluences.^[444] This was a direct consequence of the hierarchical morphology of the artificial structures, which mimicked that of the natural super-hydrophobic surfaces.^[445] Indeed, the WA of the patterned surface

structured at the highest fluence was 154° , which is close to the average WA measured on the most popular natural ultrahydrophobic surface – the Lotus (*nelumbo nucifera*) leaf.^[446]

5.9.3 Cell culture, spreading and viability

In order to investigate whether these surfaces were able to modulate cellular responses, cell adhesion experiments were performed using the fibroblast NIH/3T3 cell line. The experimental methodology (Cell culture, viability assay, Staining) used to culture the fibroblast cell on the silicon surfaces can be found in **section 2.10**. Optical and SEM photomicrographs of NIH/3T3 fibroblasts, seeded on patterned surfaces, showed that both the cell concentration and shape are different depending on the culture substrate (**Figures 5.37(d)** and **5.39**, respectively). The number of attached cells per unit area decreased as the roughness ratio and WA increased, denoting that cell attachment was favoured on more hydrophilic surfaces. Concurrently, cell morphology changed from a well spread polygonal phenotype on smoother surfaces to a round-shaped phenotype on highly rough super-hydrophobic substrates and a smaller cell size, indicative of poor adhesion.

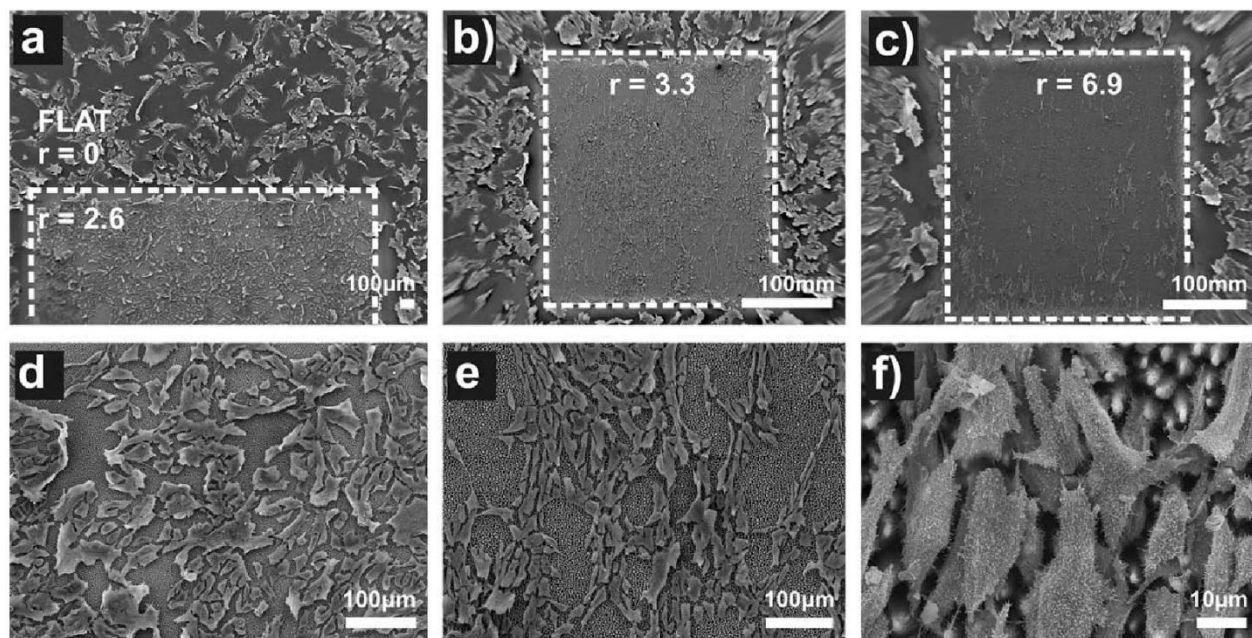


Figure 5.39: SEM micrographs of NIH/3T3 cells cultured on (a) flat and A1 (a and d), A2 (b and e), A4 (c and f) patterned Si substrates with low, mid and high roughness ratio respectively. The corresponding roughness ratios are also shown. The dashed lines indicate the border between flat and patterned regions.

Additionally, the SEM micrographs of **Figure 5.39** showed that in super-hydrophobic substrates, cells appeared to accumulate and form multilayers, probably due to limited opportunity for sufficient traction and stretch out in order to minimize unfavourable contacts with the substrate. This layer of elongated cells could serve as a basal structure for other cells to populate that region, resulting in the formation of cell multilayers (**Figure 5.39(f)**). The extent of cells spreading on a material provides a visual qualitative indicator of the strength of the cell–surface interaction.^[23] Polygonal cell spreading implies extensive interaction between the surface and the cells, whereas weak cell–surface interaction results in cell clustering.^[23,447]

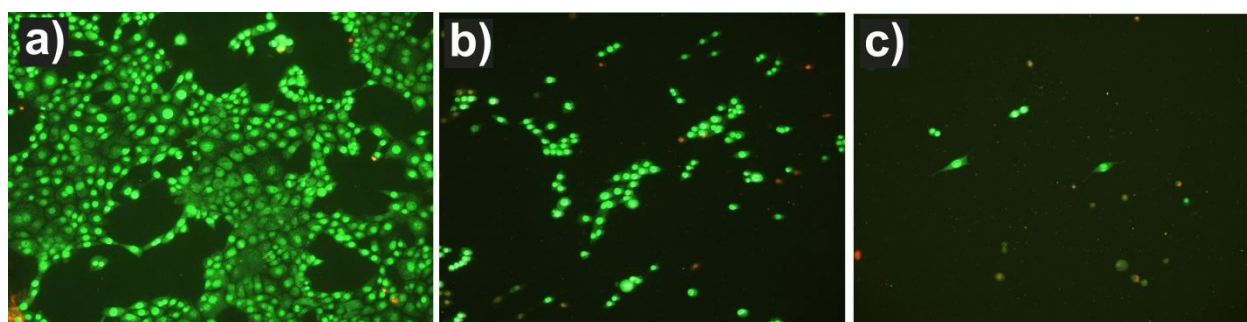


Figure 5.40: Fluorescence microscopy images of live (green) and dead (yellow–red) cells cultured on A1 (a), A2 (b) and A4 (c) patterned Si substrates.

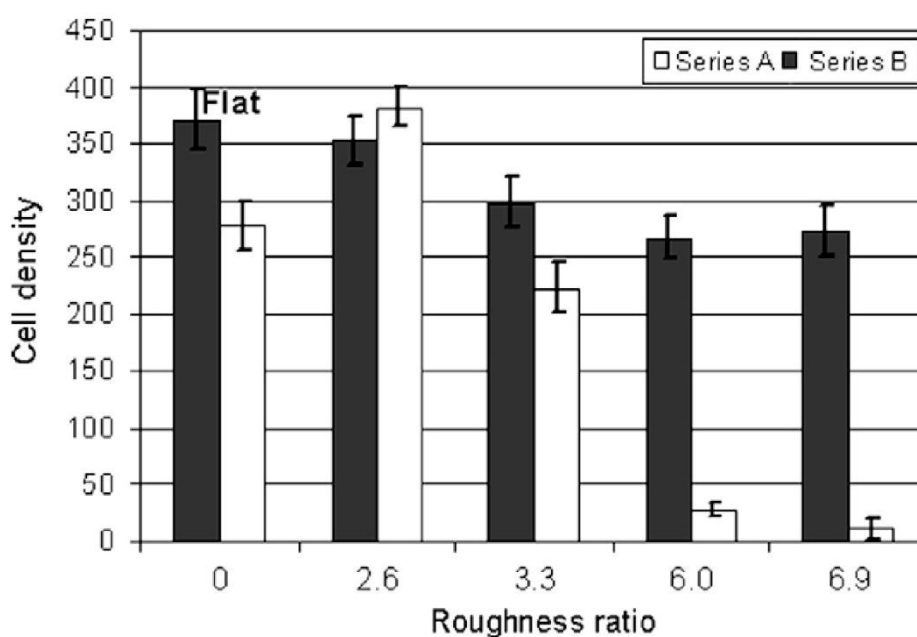


Figure 5.41: Cell density of fibroblasts on flat and oxidized Si, the as-prepared (series A) and oxidized (series B) patterned Si surfaces after 72 h incubation. All experiments were done on triplicates and the cell density values shown are the calculated mean values.

Cell viability of the attached cells on the different surfaces was assessed using the ‘live-dead’ kit (**Figure 5.40**). This staining protocol facilitates counting the number of live (depicted as green) and dead cells (depicted as red/yellow) per unit area. According to this test cell cultures on hydrophilic surfaces (A1) represented a very low percentage of dead cells, equal to 2%. This percentage seemed to increase proportional to the roughness ratio, namely on surfaces **A2** and **A4** the particular percentages were 17% and 42%, respectively. The corresponding dependence of the live cell density on the laser fluence and surface wettability is presented in **Figures 5.40** and **5.41**, respectively. It is obvious that the induction of roughness facilitated cell spreading up to an optimum roughness ratio. On the contrary, cell spreading was inhibited on highly rough and super-hydrophobic substrates. Furthermore, hydrophobization of substrates using a hydrophobic silane coating, failed to reverse the inhibition of cell spreading. In order to further characterize the principal surface property determining cell response, the wettability of the substrates was modified by coating the structures with a hydrophilic oxide layer. As a result, all the structured surfaces were converted to super-hydrophilic, without altering their initial morphology (**Figure 5.42(a)->(β)**).

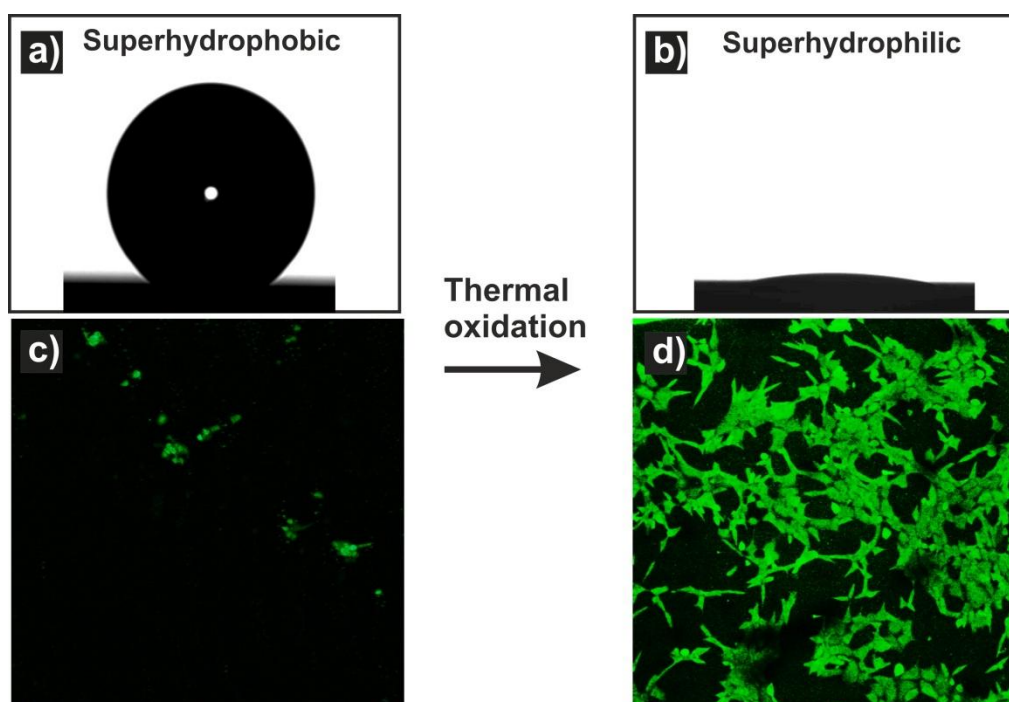


Figure 5.42: Images of water droplets placed on: (a) the roughest patterned Si surface (A4) and (b) on the same surface coated with a hydrophilic silicon oxide layer (B4). The corresponding confocal microscopy pictures of fibroblast cells cultured for three days on these surfaces are also shown. After thermal oxidation, the super-hydrophobic substrate becomes super-hydrophilic. As a direct consequence, the culture substrate switches from fibroblast-phobic to fibroblast-philic.

In this case, a remarkable change in cell behaviour was obtained, since they spread well in the highly rough oxidized surfaces, **B3** and **B4** (**Figure 5.42(b)**). Similar results were obtained by culturing HeLa cells on the above mentioned surfaces (data not shown). Following the corresponding evolution of cell densities for the hydrophobic and hydrophilic surface chemistries (**Figures 5.41** and **5.43**), it can be argued that the cell response is not solely dependent on surface morphology or surface chemistry, but on their combination, which represents surface energy. Thus, fibroblasts preferentially adhered to high surface energy or hydrophilic substrates. The ability to tune the surface energy of the patterned Si substrates, by changing either the total roughness or chemistry, could allow advantageous manipulation of the cell behaviour and vice versa.

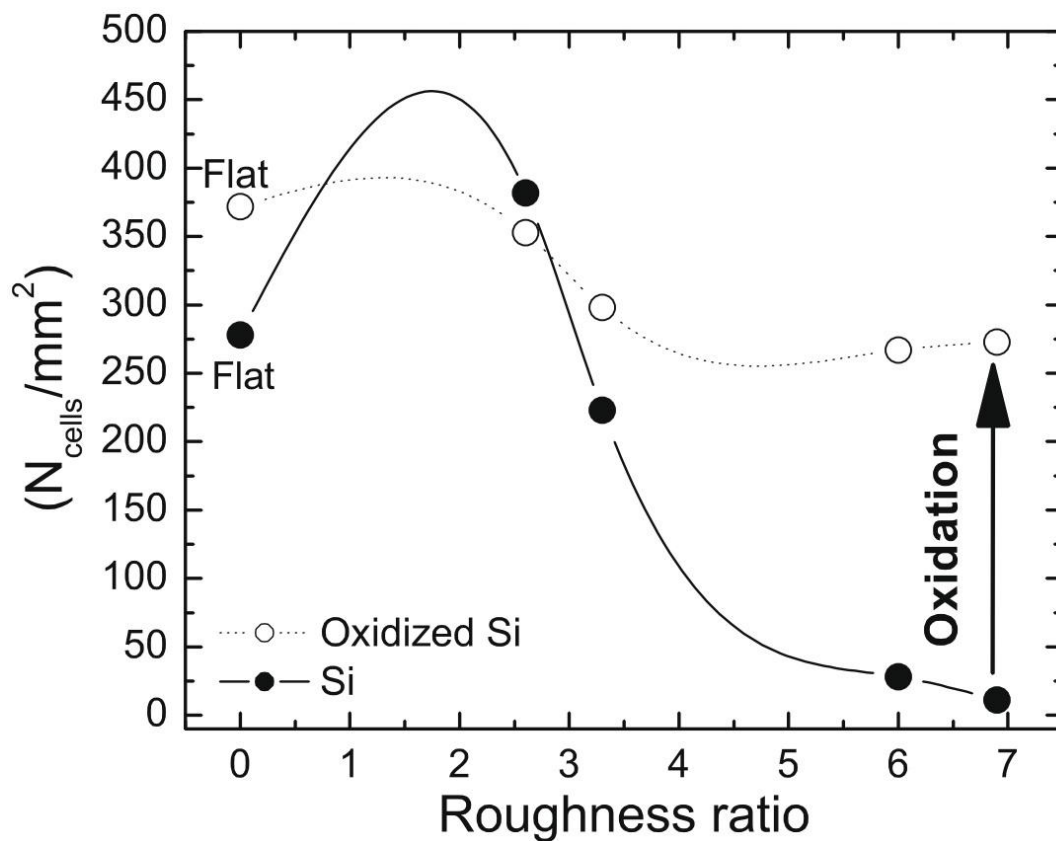


Figure 5.43: (a) Relation between cell adhesion and surface wettability for the flat and patterned Si surfaces of series A and series B. All experiments were done on triplicates and the cell density values plotted are the calculated mean values. The lines serve as a guide for the eye.

5.9.4 Cell adhesion

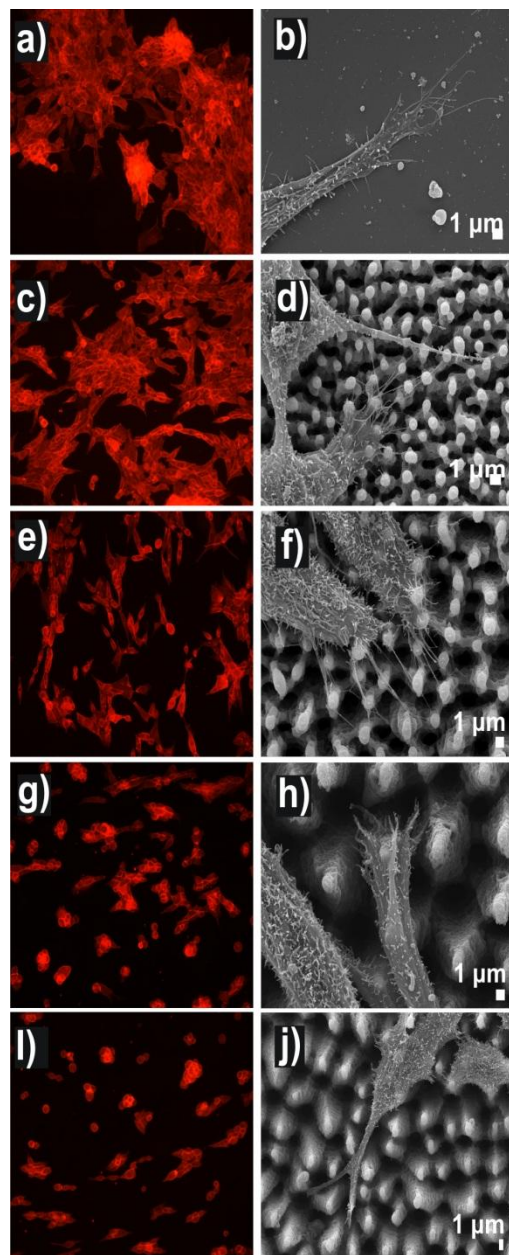


Figure 5.44: (a), (b) Fluorescent microscopy images of fibroblasts, showing actin cytoskeletal networks on flat silicon surface and ((c), (e), (g), and (i)) on patterned surfaces. The corresponding SEM micrographs of fibroblast cell adhering to flat (b) and to patterned surfaces ((d), (f), (h), and (j)) are also shown; (c and d: A1 surfaces; e and f: A2 surfaces; g and h: A3 surfaces; i and j: A4 surfaces).

Once fibroblasts detect their target location using the filopodia on their leading edge, the formation of lamellipodia facilitates the cell movement to the desired site.^[448] While a lot of studies have reported that cells are sensitive to micro/nanoscale topography,^[17,449,450] it is generally accepted that cells use filopodia for spatial sensing in their movement and spread on structured surfaces. Thus, the ability of fibroblast cells to recognize and adhere to the different surfaces described here was examined.

Confocal microscopy analysis, following actin distribution in the cells growing on the different structured surfaces, clearly showed morphological changes in the various cases tested here (**Figure 5.44**). Thus, fibroblast cells growing on more hydrophobic surfaces were mostly rounded (**Figure 5.44(g)** and **5.44(i)**), while a significantly larger number of cells growing on that surface (**Figure 5.44(c)** and **5.44(e)**) as well as on flat control (**Figure 5.44(a)**) had produced lamellae. In all cases the actin filaments were located at the cell periphery. The high magnification SEM images confirmed the differences in lamellipodium formation, also showing that cells on less hydrophobic structured areas were polarized with areas of dense filopodia extension (**Figure 5.44(d)** and **5.944(f)**). Some of these cells were showing a kind of flattening, but reduced size as compared to cells growing on the flat controls (**Figure 5.44(b)**). These processes were spread in multiple planes perpendicular to the patterned area, suggesting a 3D cell proliferation mode (**Figure 5.44(d)** and **5.944(f)**).

On the contrary, cells growing on the super-hydrophobic surfaces seemed to be smaller, with decreased number of filopodia extensions. This type of morphology could therefore be used to assess the quality of cell–surface interactions. Furthermore, the numeral processes developed between cells should facilitate cell–cell interaction and communication.

In order to evaluate the ability of fibroblasts to adhere on 3D structured surfaces, the expression of vinculin protein was examined. The membrane expression of vinculin, which is a member of focal adhesions molecules, indicates the existence of strong cell–substrate adhesion. As shown in **Figure 5.45**, vinculin was expressed in fibroblasts cultured on **A1** surfaces (**Figure 5.45(a)**) and co-localized with actin at the edges of filopodias (**Figure 5.45(c)**). Similar results were obtained after double staining of cells cultured on the highest roughness ratio oxidised substrates (**B4**). On the other hand the weak cell–substrate adhesion on super-hydrophobic surfaces is evidenced by the low vinculin expression (**A4**; **Figure 5.45(d)**).

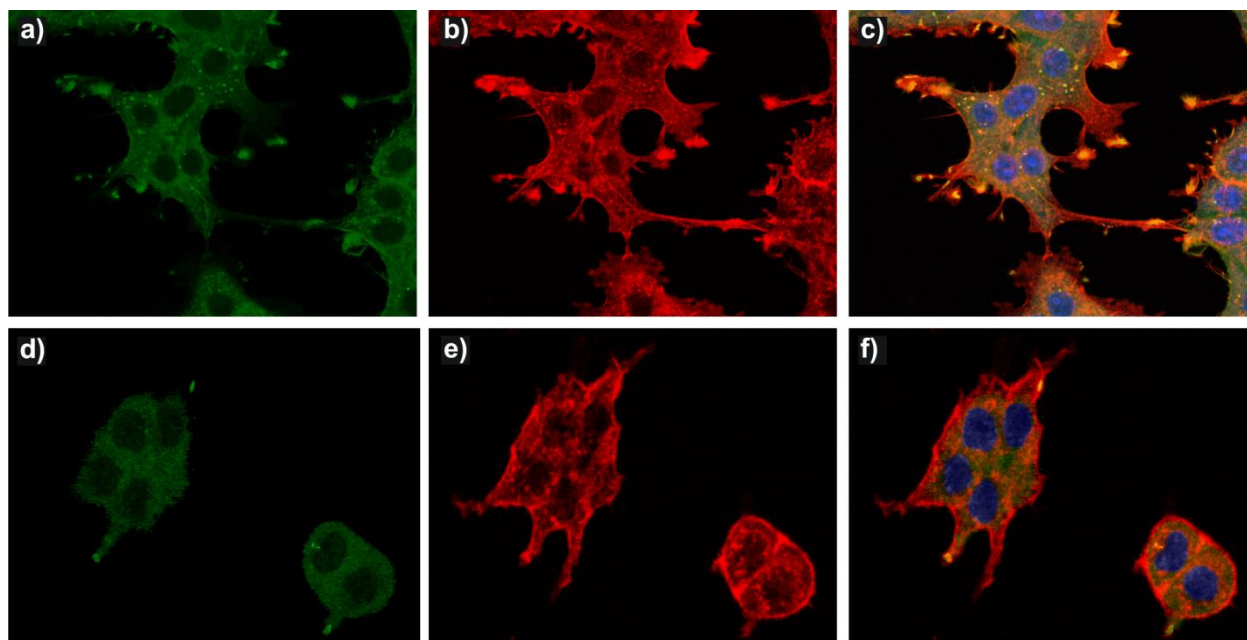


Figure 5.45: Confocal images showing the distribution of actin (red) and vinculin (green) in fibroblasts cultured for 3 days: (**a–c**) on the low-rough patterned surface (A1), (**d–f**) on the highly-rough patterned surface (A4). Double stained images are also shown.

The correlation between the substrate characteristics and cell adhesion highly depends on the level of surface free energy.^[451] Originally, Baier suggested that the amount of bioadhesion does not correlate well with the surface energy of the substrate.^[452] He reported the existence of a surface energy window with minimal adhesion, while substrates exhibiting surface energies outside the defined range

could absorb considerable amounts of biomass. In contrast, Schakenraad et al. found a sigmoidal dependence of cell spreading on surface energy, indicating a sharp transition at low surface energies between poor and good adherence.^[453] However, in these studies the adhesion dependence was measured on a large number of different polymers and glasses and not on one substratum type, modified to display different WAs. Thus, it cannot be excluded that in some cases, specific substrate chemical effects may determine adhesion and not the wettability itself. The physical behaviour of hydrolyzed living cells may be regarded as a drop of liquid. The adhesion of this cell liquid can be affected by the surface wettability due to the increased or decreased contact area, which is proportional to the solid–liquid interfacial adhesive force. Alternatively, a living cell can be described by tensegrity models^[454] which consider that cellular shape and adhesion are largely influenced by the cytoskeleton; the cell tends to form focal adhesions in locations that balance cytoskeletal forces. In this respect surface wettability is crucial as it describes to what extent the surface is exposed to culture medium and subsequent protein adsorption. A reduction in adhesive protein adsorption due to a decreased liquid–surface interfacial area may detrimentally affect the ability of cells to form adhesions. In any case, the surface energy influences the contact area of the cell membrane with the substrate, while the profile of membrane could change depending on the wettability of the adjacent solid. In order to understand the cell response on substrates with different roughness, one has to consider the effect of the macroscopic roughness on wettability, which has been theoretically approached by two different models. In the Wenzel model,^[455] the liquid is assumed to wet the entire rough surface, without leaving any air pockets underneath it. The apparent WA, θ_w , is given as already discussed in **section 5.4 (Eq. 5.12)** by the following equation:

$$\cos \theta_w = r_w \cos \theta_o \quad \text{Eq. 5.20}$$

where r_w is the ratio of the unfolded surface to the apparent area of contact under the droplet, and θ_o is the contact angle on a flat surface of the same nature as the rough. Since r_w is always greater than unity, this model predicts that the contact angle will decrease/increase with surface roughness for an initially hydrophilic ($\theta_o < 90^\circ$)/hydrophobic ($\theta_o > 90^\circ$) surface. In contrast, Cassie and Baxter (**section 5.4.2, Eq. 5.14**) (CB) assumed^[456] that the liquid does not completely permeate the rough surface because air pockets get trapped underneath it.

The liquid is thus said to be in a ‘fakir’ or the Cassie–Baxter state and the apparent WA, θ_w CB, is an average of the flat surface, θ_o , and the value for full hover over the flat surface (that is, 180°) and is given by:

$$\cos \theta_{CB} = -1 + f(1 + \cos \theta_o) \quad \text{Eq. 5.21}$$

where f defines the fraction of the projected solid surface that is wet by the liquid. As f is always lower than unity, this model always predicts enhancement of hydrophobicity, independently of the value of the initial contact angle θ_o . The lower the value of f , the smaller the solid–liquid contact area and the higher the increase in the measured contact angle. Following the results presented in **Figure 5.38(a)**, it is obvious that the WA values measured for the structured substrates are consistent with the CB model because, in contrast to the Wenzel model, it predicts a rise in the WA upon enhancement of the roughness of an initially hydrophilic ($\theta < 90^\circ$) surface. Hence, for the super-hydrophobic substrates, where the solid–liquid contact area is minimal, water cannot penetrate the roughness elements and therefore an intervening air layer persists. This resembles the case of many aquatic and semi-aquatic arthropods (insects and spiders) which are rendered water repellent due to a rough, waxy exterior festooned with hairs.^[457] Owing this super-hydrophobic integument, the respiratory demands of these species are facilitated by a thin intervening layer of trapped air, which is called ‘plastron’ and maintained along their body surface. This air layer is visible at non-zero reflection angles and is responsible for the silvery underwater reflections from aquatic species. Indeed, as shown in **Figure 5.46**, when a water repellent spike-substrate is immersed in water or cell culture liquid, it glistens with a silvery sheen, indicating that a sheathing film of air remains on the submerged surface.

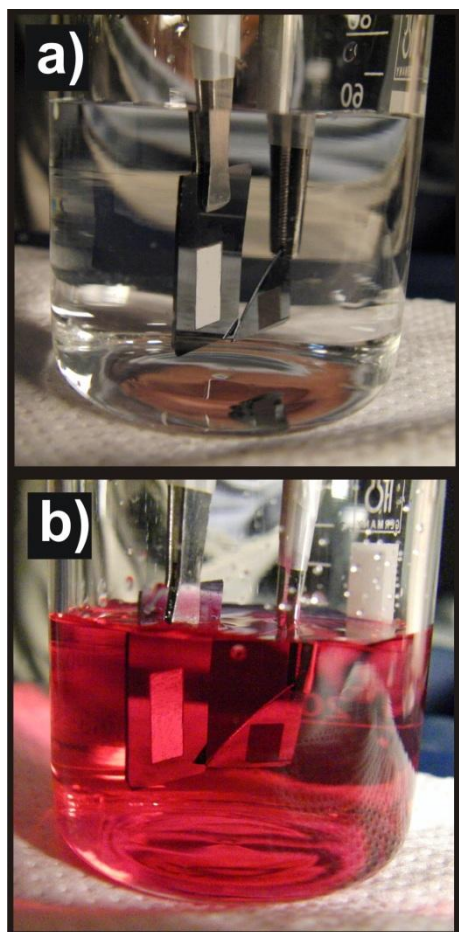


Figure 5.46: Pictures of the as-prepared super-hydrophobic (sample A1, on the left) and oxidized super-hydrophilic (sample B4, on the right) patterned regions immersed in water (a) and cell culture medium (b) respectively. The silvery shine is visible only on the super-hydrophobic patterned region of the A1 sample while it is absent on flat regions and the less hydrophobic patterned area of the B4 sample.

Conversely, for more hydrophilic substrates, the fraction of the wetted area increases and the surface glistening disappears, as a result of increasing liquid penetration. Finally for super-hydrophilic substrates, the contact area is maximized and water completely penetrates the roughness elements. Therefore, taking into account that cell culture medium is aqueous, the interaction of cell membrane with the underlying substrate may be governed by the degree of surface wettability and thus surface energy. Fibroblast spreading is promoted on hydrophilic or high surface energy rough substrates due to the permeation of the culture liquid in the structures, allowing cells to take advantage of the high surface-area-to-volume ratio offered by the structured substrates. On the contrary, fibroblast adhesion is almost impossible on ultrahydrophobic or low surface energy rough substrates, as the penetration of the culture liquid on the structures is inhibited. The results presented in **Figure 5.41** suggest the existence of a switching function for the structured Si surface characteristics, from fibroblast adhesive to fibroblast repulsive, when a critical combination of roughness and wettability, and thus surface energy, is attained. This switching effect agrees with the sigmoidal dependence suggested by Baier and may be attributed to the critical transition from the Wenzel to Cassie–Baxter states.^[458] Further support to this statement is coming from the results obtained after substrate oxidation, where the highly rough substrate is converted from ultrahydrophobic to ultrahydrophilic and accordingly the wettability switches from Cassie–Baxter to Wenzel states. This transition is again followed by a corresponding enhancement in cell spreading, where the surface switches from cell-phobic to cell-philic. We can thus conclude that the sharp transition from superhydrophobicity to superhydrophilicity is accompanied by a similar transition in cell adherence as well. This sharp transition between the two extreme wetting states may be potentially a useful tool towards controlling cell behaviour on culture substrates. Furthermore, a non-monotonic dependence of fibroblast adhesion on wettability could be detected (**Figure 5.41**), which is qualitatively in accordance to the Baier model. Optimum cell adhesion was obtained for small roughness ratios, independently of the WA values and surface chemistry (**Figure 5.43**). This observation was also supported by the SEM images of **Figure 5.44**, where the total number of filopodial processes was much higher in surfaces with low roughness. The proliferation and immigration of adhesion depended cells was realised though exertion of contact strain.^[459] The filopodia of growth cones play an important role in feeling the environment. On a surface exhibiting a suitable roughness, the cell soma and the processes would adopt a shape complementary to the surface profile, achieving maximum contact area, and therefore, interfacial force. This force will benefit cell adhesion and spreading on the substrate surface, so that cells recognize and migrate to areas of optimum roughness.

There have been a lot of reports on studying the effect of roughness and surface energy on cellular responses. Both discrete specimens and surface energy gradients were used in these studies and

many different outcomes have been observed. In some cases, cell functions are enhanced on hydrophilic surfaces^[33,460,461,462,463,464] whereas, in other cases, cell functions are enhanced on hydrophobic surfaces.^[465,466,467,468,469] While in other cases, surface energy has no effect on cell functions^[51] or cell functions have a maximum at an intermediate surface energy.^[45,53,470,471] This broad range of outcomes is possibly a result of the wide variability in experimental conditions such as cell types, incubation times, culture conditions, surface chemistries and topographies. In this study, it is attempted to discriminate among the different effects by studying the effect of surface energy for the whole range of contact angles, from superhydrophobicity to superhydrophilicity, while keeping the same micro/nano morphology or vice versa. In this respect, the main outcome of the current study is that cell response shows a non-monotonous dependence on the surface energy, in accordance to some previous observations.^[48,51–53] Besides this, there are various studies on the effect of surface roughness on cell response. Most studies investigate the separate effect of nano- or micro-roughness respectively.^[472,473,56,57] On the contrary, due to demanding design requirements, the synergistic effect of roughness at micro and nano-scales on cell response has been limitedly studied.^[474] The present study focuses on cell response on surfaces possessing micro/nano topography (i.e. microstructures decorated by secondary nano-features), thus investigating the synergistic effect of micro- and nano-scale roughness on cell adhesion and viability. It is shown that a dual rough surface amplifies hydrophilicity towards superhydrophilicity or hydrophobicity towards water repellency and accordingly enhances cell-phobicity or cell-philicity for the culture substrate.

The cell spreading dependence on surface energy has an important heuristic impact in the area of biomaterials research and it is crucial to understand this dependence on a molecular basis. Mechanistically, one has to go back to the first reaction between a biomaterial and the organism, which is protein adsorption. At high WAs, i.e. in the hydrophobic range different proteins are adsorbed compared to the hydrophilic range. The adsorbed protein layers comprising different proteins on the surface could therefore result in differential tissue reactions, which would lead to stronger bioadhesion. The investigation of protein adsorption to these artificial surfaces needs further exploration.

5.9.5 Conclusions

In summary it is shown that laser structured Si micro and nano rough spike scaffolds with controllability of roughness ratio and surface chemistry can serve as a novel means to elucidate the 3D cell–biomaterials interactions *in vivo*. It is demonstrated that the wettability of such artificial substrates can be preferentially tuned from super-hydrophobic to super-hydrophilic through independently controlling roughness ratio and surface chemistry. The dependency of fibroblast cell response on the artificial structures was systematically investigated and clarified that a fundamental parameter that determines cell adhesion on 3D substrates is not solely the degree of roughness or surface chemistry but the synergy of both, which determines the wettability or surface energy of the culture substrate. Indeed, a proper change in the surface energy for the same degree of roughness can switch the behaviour from cell-phobic to cell-philic and vice versa and this transition is always accompanied by a similar sharp transition in surface wettability. However, and in accordance to previous theoretical models describing cell response, a non-monotonic dependence of fibroblast adhesion on wettability is found. Although it appears to be a general tendency that adhesion is favoured on hydrophilic substrates, it is observed that cells' spreading becomes optimum on low-rough substrates, independently of their wettability. This indicates that cell attachment is further enhanced and facilitated by a proper form and size of surface topography.

The silicon scaffold material design is crucial as it affects cellular attachment and provides tools for micro- and nanoscale addressability of material architectures which allow to precisely position and explore the complex interaction phenomena of anchorage-dependent cells with their *in vitro* environment. Hierarchical roughness should provide physical cues for cell orientation and spreading, while etched pores may provide room for remodeling of tissue structures. Further studies on the behavior of different cell types are ongoing to better understand the interactions between artificial structures and adhesion proteins, but this approach offers a potent method for tuning cell–material interactions at the molecular level. We envisage that the multi-variant platforms offered by the biomimetically modified substrates described here, will find potential applications in bioengineering, especially in guiding cell adhesion, motility and differentiation as well as in the development of tissue scaffolds and cell microarrays, in which the ability to switch from strong to weak cell–substrate adhesion is beneficial.

5.10 3D primary neuronal cells culture

5.10.1 Introduction

In this section we study the culture of primary neuronal cells on the Silicon structured surfaces. Neurons depend on surface support more than other cells, but readily adhere to surfaces coated with ECM proteins. Moreover, brain development and neuronal networks formation depend on an intricate blueprint of axon guidance, dendritic arborization, and synapse formation cues. The challenge to comprehend the multitude of cues neurons receive, process, and direct, in vivo, and to simulate 3D cultures in vitro, has been addressed; however, the results are limited.^[475,476] Recently, Pautot et al. addressed this subject developing the first 3D neuronal network on silica beads. The importance of 3D neuronal cultures can be realized if one thinks that the dimensionality of the network has a strong impact on its connectivity, and therefore plays an important role for its possible behavior.^[477] In this study, we have utilized silicon (Si) micro-structured substrates to enable neurons to grow in 3D, without coating, synthetic ECM, or chemotropic factors.

5.10.2 Methodology

Silicon structured surfaces ($2 \times 2 \text{ mm}^2$) were fabricated as described in **section 2.5.1** with a fluence of $0.21 \text{ J}=\text{cm}^2$ and cleaned afterwards (**section 2.4.1**). Following samples were oxidized as described in **section 2.5.2**. An example of the Si structures are presented in **Figure 5.47**

A detailed methodology about the neuron cell preparation can be found in **section 2.10.3**.

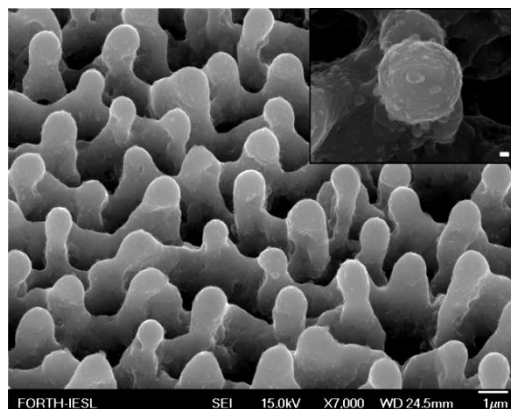


Figure 5.47: Side FESEM view of Si spikes. The inset shows a higher magnification of the top of a single spike. (scale bar 100nm)

5.10.3 Promoting neuron cell adhesion

Microstructured roughness in the form of spikes promoted the adhesion of single or clusters of neurons to the substrate (**Figure 5.48(a)**). In contrast, only few cells survived on a flat Si substrate used as a control (**Figure 5.48(b)**) to verify the role of roughness in absence of synthetic ECM. The cells developed into a dynamic cellular aggregate, with long neurites sprouting over the spikes' surface (**Figure 5.48(c)**). The integrity and uniform sprouting observed suggest the biocompatibility of the neuronal population with the surface. The protrusions of the neurolemma grow over the spikes, engulfed their top (**Figure 5.48(d)**), and incorporated them to form a web. Moreover, a network of nanoscale thin neuritic extensions was formed along the third dimension (-z axis) utilizing the space toward the base of the spikes (**Figure 5.48(e)**). A SEM micrograph cross section demonstrates the mechanically sheared cell membrane and the engulfed Si spikes (**Figure 5.48(f)**). Having enveloped the top of the spike, the thicker extensions appeared (~550 nm) and the processes continued toward the bottom, with thinner nanoextensions (~35 nm). A Si substrate with nonperiodical spikes exemplifies the ergonomic way of neuritic sprouting, because neuritic extension is dictated by the shortest intraspikes distance (**Figure 5.48(h)**). In addition, multiple protrusions extended along the z-axis from one single neurite.

A snapshot of the formation of nonsubstrate-constrained growth cone filopodium-like structures is shown in **Figure 5.48(g)**. A blindly winding end (indicated by the arrow) has reached the closest adhesion point and the process was limited by a final adhesion step (asterisk). Such filopodia may grow to physically bridge the distance between the membranes aiming to construct a network. This observation is supported by the Hammarback and Letoumeau guide post-hypothesis that growth cones quickly cross a low-adhesivity substrate gap in vitro, when this gap is spanned by even a single filopodium establishing contact on a distant high-adhesivity substrate.^[478]

With the cell membrane being amphiphilic, surface chemistry is also an important factor for cell attachment. The importance of surface chemistry on neuronal survival was tested utilizing a geometrically identical Si substrate, following thermal oxidation. Neurons sensed the vertical microstructured roughness and adhered. However, a prominent feature on the spike area was the extended cellular death. Although the oxidized Si spikes maintained the same geometrical microenvironment as the bare Si spikes, they did not allow long-term cell survival.

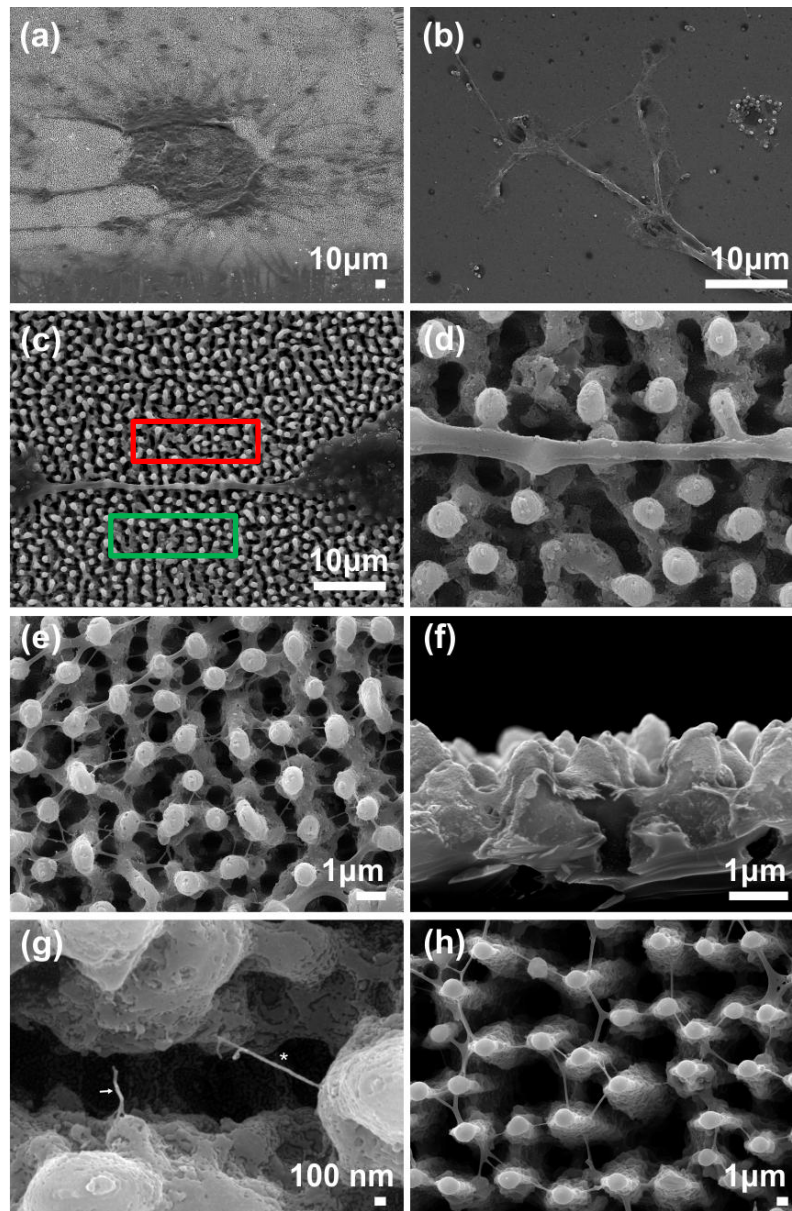


Figure 5.48: (a) Neuronal cluster on the Si spikes area. The neurons are shown to have attached over a large area of spikes. (b) Flat Si substrate used as a growth control surface. Scale bar 10 mm. The neurons do not adhere as readily on the flat substrate as they do on the microstructured one. Only a few cells survived, demonstrated also by the cellular debris that remained attached. (c) Detail corresponding to red lined inset of (c), showing a long neurite that has attached and grown over the spikes. (d) Protrusions of neurolemma growing over and engulfing the top of the spikes. (e) Detail corresponding to green-lined inset of (c), showing the three-dimensional web of cytoplasmic processes growing along the z direction, toward the base of the spikes. (f) Cross section of substrate, demonstrating the engulfed Si spikes and the mechanically sheared membrane. (g) A microstructured substrate comprising irregularly spaced Si spikes. The cytoplasmic processes are lead toward the closest adhesion point. The arrows indicate how multiple processes may initiate from one neurite. (h) The arrow on the left indicates a serpentine filopodial-like process that explores its microenvironment for the closest adhesion point. The extension is limited by a final stretching (asterisk). Si, silicon.

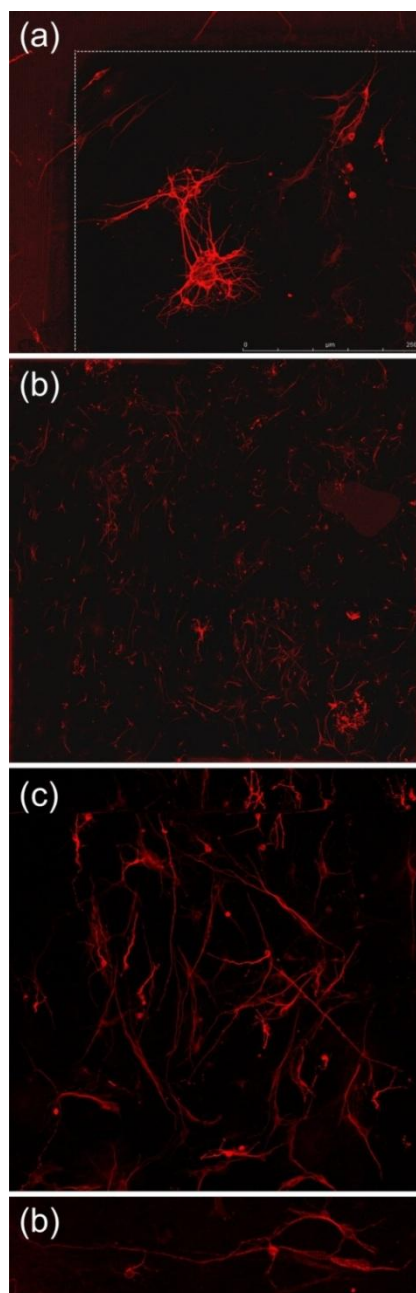


Figure 5.49: (a) Neuron-specific immunohistochemistry and confocal microscopy, using anti-beta III tubulin primary antibody. Corner of spike area showing some cells in a cluster (scale bar 250 mm); (b) full spike area photo. Square indicating lengthy axonal fiber extension; (c) magnification of inset from (b); (d) lengthy extension comparable with the results of other studies¹⁷ (two-dimensional scale bar 450 mm).

A possible explanation is that Si spikes covered with silicon oxide are super hydrophilic (contact angle less than 5°), whereas bare Si spikes are hydrophobic, with contact angles close to 130°. Consequently, biomaterial roughness is not a stand-alone prerequisite for neuronal survival and growth, but it rather requires the synergistic effect of surface chemistry.^[479] The importance of these findings is multifaceted.

The culture conditions used favored the sole growth of primary neurons, and the confocal microscopy was employed to confirm the immunofluorescence of tubulin beta III, which is specific for mature neurons. The cells used here were beta III tubulin immunopositive, and the comparable immuno-fluorescence (**Figure 5.49(a)**) and SEM (**Figure 5.47(a)**) pictures confirm that there was no glial feeder layer on the substrates under study. Hence, the immunostaining enabled us to confirm the neuronal specificity of our cultures, to verify the shape of adhesion on the substrates, and to measure a significant increase in length for some of the neurons^[480] (**Figure 5.49(b)–(d)**). In addition, primary neuronal cultures were stained with specific antibodies both for beta III tubulin (red) and GFAP (blue) at 5 days in vitro, as shown in **Figure 5.50**. The attached to the Si microstructured substrates. It is worth emphasizing that when the cells were plated on the oxidized Si substrates, adhesion was limited. The wet culture conditions did not compromise the stability of the substrates. In addition, neuronal adhesion was not superficial. This was established by the attachment, growth, and elongation of neurites on the substrates, in all three dimensions. The undeniable proof of outstanding adhesion properties was derived from the electron micrographs demonstrating how the neuronal membranes incorporated the tips of the spikes as their own. Besides promoting neuronal adhesion, the microscale roughness in synergy with the surface chemistry allowed the formation of an exquisitely organized 3D neuritic network. The use

of hydrophobic, Si microstructures enabled the “autografting” of these structures by the neurons, meaning that the neurons cloaked the spikes, thus self-grafting the area. The ability of the neurons to adjust their shape via dynamic cytoskeletal remodeling is intrinsic. Nevertheless, these intracellular processes that drive membrane extensions, such as migration or filopodial lengthening, work against the membrane’s mechanical properties. In this study, we demonstrated that inherent neuronal guidance cues were sufficient to win over steady-state membrane mechanics. The outcome was to allow the filopodia of growth cones to explore this permissive 3D microenvironment, and to “decide” its direction depending on the shortest distance.

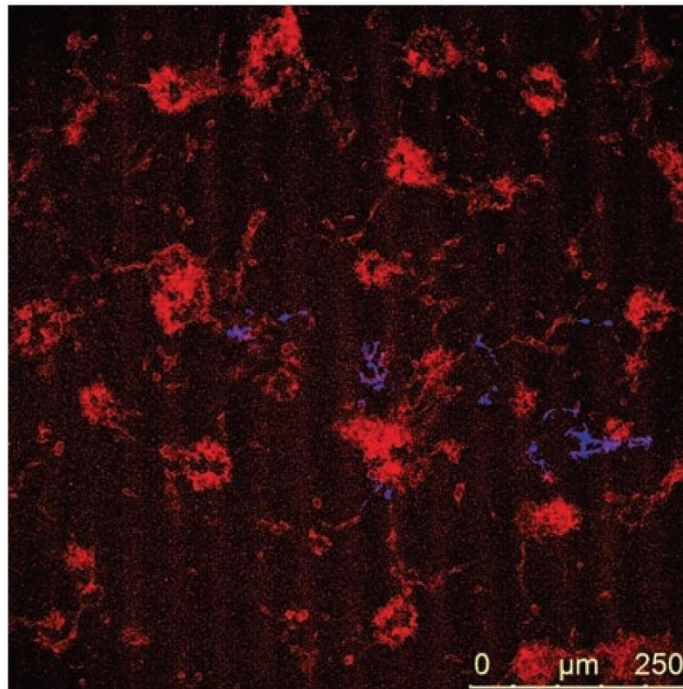


Figure 5.50: Primary neuronal culture immunostained both for beta III tubulin (red) and GFAP (blue) at 5 days in vitro. The micrograph demonstrates the low numbers of GFAP-immunopositive cells and staining colocalization.

5.10.3 Conclusions

In this section we have presented a novel approach that utilizes Si-microfabricated substrate to support growth, 3D development of primary neuronal cultures, in the absence of chemotropic factors or synthetic ECM. This approach provides a functional platform allowing the study of nervous system properties, including the ability of repair with potential usefulness in biomedical investigations.

Chapter 6

Formation of metallic nanosurfaces and nanoparticles via fs laser ablation in liquid media.

6.1 Introduction

Laser initiation of phase transitions at the solid-liquid interface results in the formation of self-organized **nanostructures** (NS) on the solid surface. Recent experimental results on the properties of such NS are described in this section of the thesis. Phase transitions at the solid-liquid interface, exposed to short laser pulses at an energy density sufficient to melt the solid, can be traced owing to modifications of the solid surface induced by the laser pulses. In case of a metallic target, the laser radiation is absorbed by free electrons, and the lattice temperature starts to increase due to electron-phonon relaxation process. If the absorbed energy is sufficiently high, the metal target melts, so that a layer of the liquid that surrounds it is heated up due to heat transfer from the metal. As a result of the high pressure of the adjacent medium that contacts the melt, the latter can be modified. In particular, the liquid vapors that surround the molten layer induce in it viscous flows giving rise to the formation of various structures.

The characteristic thickness of the modified layer of the solid target strongly depends on the melt thickness, and therefore, on both the laser fluence and its duration. The thickness of the molten layer h_m can be estimated by the heat diffusion length during the laser pulse as follows: $h_m \sim (at_p)^{1/2}$, where t_p

stands for pulse duration, and a stands for heat diffusion coefficient of the solid. This estimation is valid only for laser fluence close to the melting threshold of the solid. If the duration of the laser pulse is less than the time of electron-phonon relaxation, then the heating of the lattice occurs within the depth of the absorption of laser radiation. For typical metals the mean free path of excited electrons during the relaxation process is too short, and the melt thickness does not exceed a fraction of micrometer even for nanosecond (ns) laser pulses. As a result this layer of material may be re-distributed into one or another kind of nano-structures (NS) due to the recoil pressure of the liquid medium adjacent to it.

Melting of the target surface is a necessary condition for structures formation; however the adjacent medium is responsible for the actual type of structures. The morphology of the structures that are left in the target surface after melt solidification can provide valuable information about the phase transitions taking place at the solid-liquid interface. In a sense, the observed NS are the “fingerprints” of nano-scale inhomogeneities of the medium in its supercritical state that surrounds the target.

Laser ablation of solids in liquids is also leads to surface texturing of the target, however in this case different mechanisms prevail, owing to fact that the liquid adjacent to the melted surface undergoes a phase transition. Short laser pulses give rise not only to superheated liquid but also to a transient zone of elevated pressure close to the target, which may bring the surrounding medium to a supercritical state. As a result of the interaction of the pressure wave with the melt layer on the target surface, its morphology is changed. This surface profile is frozen upon cooling before being smeared by the surface tension of the melt. Typically the structures of this type have circular symmetry. Depending on the experimental conditions, such as laser peak power, target material, surrounding liquid, etc., these two types of structures – ripples and spherical features may coexist. Here we shall designate the spherical structures formed on materials surface as nano-structures (NS).

6.2 Morphology of NS and NP under laser ablation of planar surfaces

NS imaging using scanning probe microscopes, e.g., Atomic Force Microscope (AFM) indicates that they are densely packed nano-cones. This is illustrated in **Figure 6.1** for the case of NS grown on an Ag target under its ablation in water with picoseconds laser pulses.^[481] Note that both the lateral dimensions of NS and their period are much smaller than the laser spot size on the target, which in typical experimental conditions is of order of hundreds of micrometers. The estimated density of NS in **Figure 6.1** amounts to 10^{10} cm^{-2} . Therefore, the expanding vapors of the liquid that surrounds the target are unstable. Pressure difference appears within initially smooth vapor pocket above the molten layer of the target. This pocket is split into periodic cells, and the pressure difference within these cells pushes the melt from high to low pressure areas. Solidified NS on the target are just the imprints of those cells in the adjacent to target medium in which the phase transition takes place.

This type of NS is observed under ablation of solids with sufficiently short laser pulses. The upper limit of the laser pulse duration at which the NS are observed is around 300 – 400 ps. Longer pulses do not favor the formation of NS in the whole range of laser fluencies, from melting threshold to intense ablation. In the other hand, NS are readily observed under ablation with shorter laser pulses down to fs ones.

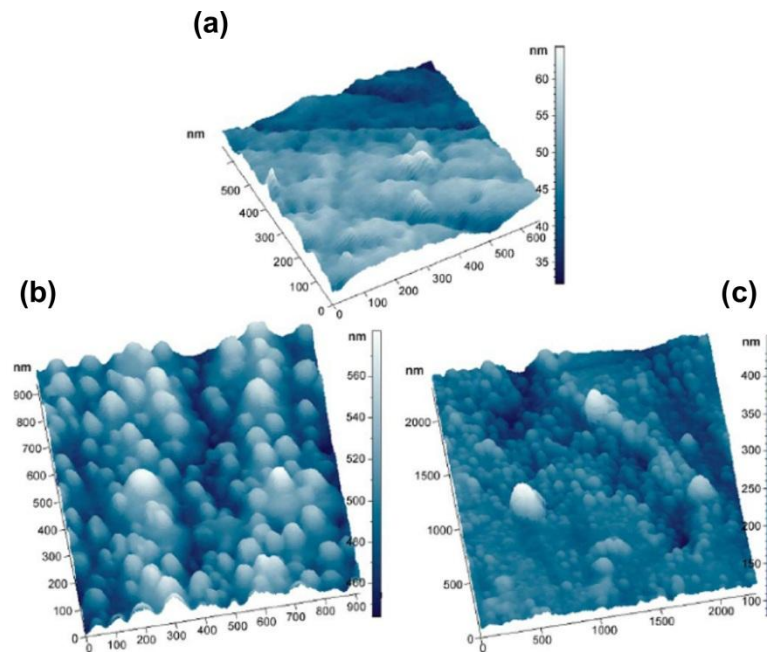


Figure 6.1: AFM view of NS on an Ag plate generated by its ablation in water under exposure to a 350 ps Nd:YAG laser radiation. (a) Pristine surface, (b) NS after laser ablation in water, (c) concentration of NS in micro-depressions of the relief.

The laser wavelength needed for NS formation is not very important as soon as metal targets are considered. This is because of the fact that optical constants of most metals are nearly the same in the range of wavelengths where lasers usually emit.

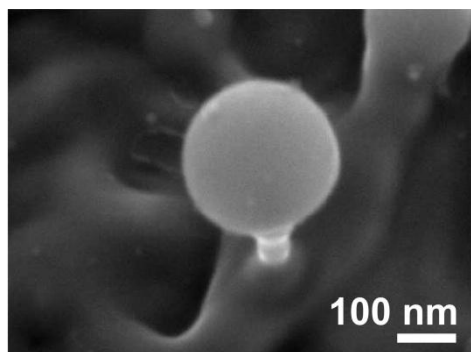


Figure 6.2: Enlarged view of a single NS on Ta produced by its ablation in water with 350 ps laser pulses of a Nd:YAG lasers.

NS obtained on any other metals, such as Au, Ti, Ta, etc., look very much alike though they have different periods and lateral sizes. However, later studies showed that scanning probe microscopes are not suitable for adequate imaging of NS formed. This is due to the complex profile of NS that are realized under these conditions. In reality, NS generated via laser ablation are often just solidified drops of the melting material that is attached to the target via a thin “neck.” This morphology can only be revealed with the help of high resolution scanning electron microscopy (SEM). A typical Field Emission SEM (FESEM) view of a

NS on Ta target obtained via its ablation in water with a 350 ps Nd:YAG laser is presented in **Figure 6.2**.

One can see that the shape of NS is mushroom-like, so that their lateral size is a non-monotonous function of the coordinate.^[482] **Figure 6.3** shows subsequent positions of an AFM tip along the surface containing NS presented above. The tip cannot approach the base of the NS, and the resulting profile deduced from scanning is a cone-like NS. Therefore, scanning electron microscopy provides more adequate information on the NS morphology. However, scanning probe microscopy is quite convenient for characterization of lateral dimensions of NS and their period. This also concerns any type of probe microscopes, AFM or Scanning tunnel microscope (STM).

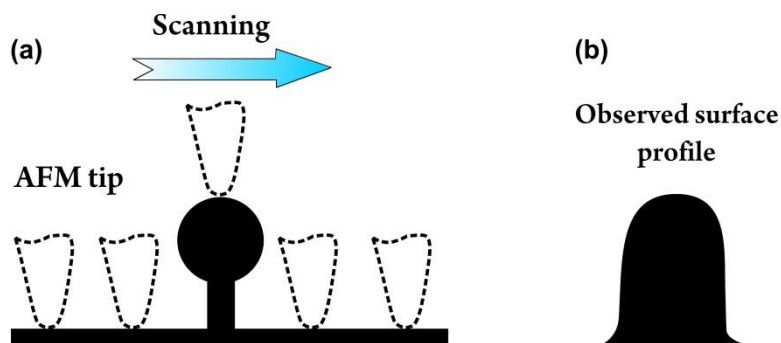


Figure 6.3: Imaging of NS with the help of a probe microscope. **(a)** Sequence of tip positions upon scanning the NS. **(b)** Registered profile of the NS.

Figure 6.4 (a)-(c) shows the FE SEM view of NS on Ag Au, and Zn targets ablated in water with ps laser radiation. Most of NS have a mushroom shape similar to that observed for Ta NS. Note that for both metals the temperature of the adjacent to the surrounding liquid layer is around 1000 K. As soon as the shock wave propagates toward the free surface of the liquid, the pressure in it remains

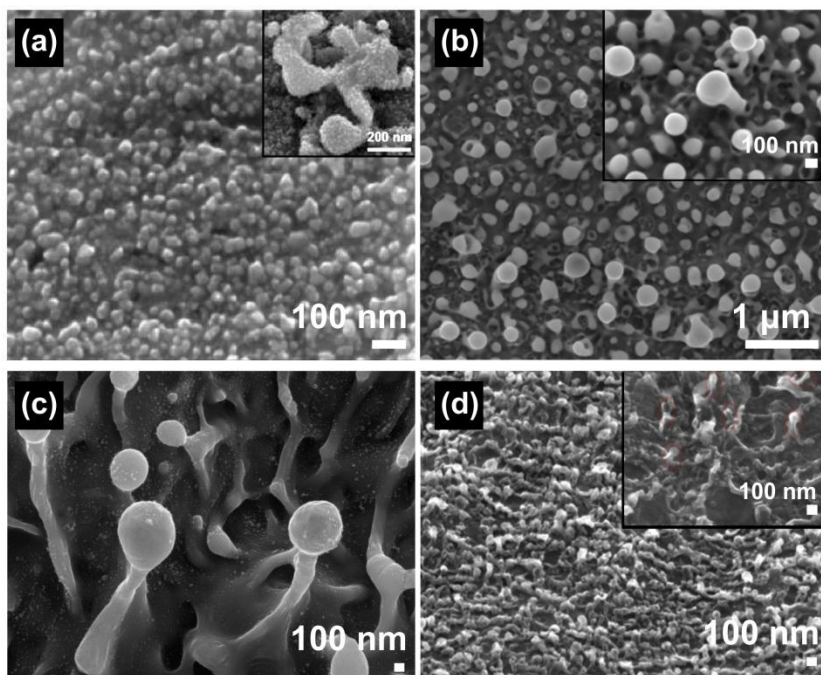


Figure 6.4: FE SEM view of NS on (a) Ag and (b) Au targets produced by their ablation in water with radiation of a 5 ps KrF laser, wavelength of 248 nm. Insets show the view at different scale. (c) Zn NS obtained by ablation of bulk Zn in ethanol with a 150 ps laser radiation, wavelength of 1064 μm . (d) NS on bulk Al ablated with 100 fs pulses of a Ti:sapphire laser in ethanol.

high, but when it reaches the liquid surface, the pressure above the target abruptly drops. Usually the shock wave in liquids propagates in it with the speed of sound (1497 m/s). This means that, for 1 mm thick liquid layer, the time of propagation of the shock wave is in order of microseconds, which is much longer than both the pulse duration and electron phonon relaxation time.

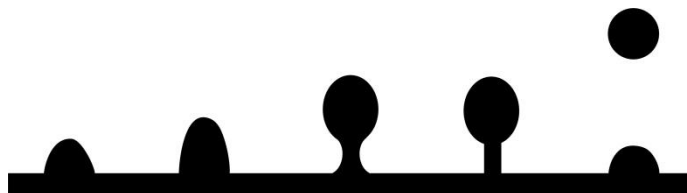


Figure 6.5: Possible types of NS morphology. The last right scheme corresponds to detachment of the molten drop that becomes a nanoparticles suspended in the surrounding liquid.

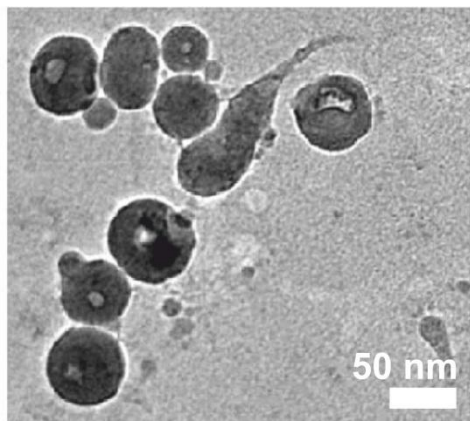


Figure 6.6: Transmission Electron Microscope view of nanoparticles of aluminum generated by ablation of a bulk Al target in ethanol using 100 fs Ti:sapphire laser pulses at a wavelength of 800 nm

As a result, all kinds of structures shown in **Figure 6.5** can be formed and this is corroborated by the NS images presented above. On the other hand, NS that were detached from the melt do not always take on a spherical shape. For instance, in case of Al **Figure 6.5(d)** ablation with femtosecond laser pulses either in water or ethanol, the nanoparticles (NP) found in liquid have a shape of a drop with “tails” as shown in the following **Figure 6.6** from a TEM microscope. It is pertinent to note that this kind of NPs morphology was not observed so far on any other metals under their laser ablation in liquids.^[483] This unique morphology can be due to the interplay of the melt viscosity and cooling rate of ejected nanodrops.

6.3 Generation of Al nanoparticles and nanostructures via ablation of bulk Al in liquids with short laser pulses

6.3.1 Introduction

Aluminum *nanostructures* (NSs) and *nanoparticles* (NPs) are considered as a possible fuel in advanced energetic materials applications such as propellants and pyrotechnics, as they feature high surface area which provides enhanced heat release during their exothermal oxidation.^[484,485,486] Furthermore, nanosized aluminum has recently attracted interest as building blocks for high-capacity hydrogen storage materials.^[487,488,489] This is due to the ability of metallic aluminum to form hydrogen upon reaction with water. Finally, Al NSs and NPs are found to exhibit distinctive optical characteristics for optoelectronic applications, such as surface-enhanced Raman scattering (SERS), metal-enhanced fluorescence for the label-free detection of biomolecules and broad-band wire-grid polarizers. Several methods for the generation of Al NPs have been tested so far, among them is wet-chemical synthesis, arc discharge, laser ablation in vacuum and calcinations of Al hydride dispersed on fibrous substrates at elevated temperature. One of the major impediments, especially for energetic applications, is that bare Al is highly reactive while oxide coated Al significantly decreases overall performance. This effect becomes more pronounced as particle size decreases, since the oxide layer represents a significant fraction of its mass. Much effort has been devoted to the synthesis of small aluminum nanoparticles that are stabilized by coatings or organic surface passivation agents for protection from rapid oxidation to aluminum oxide under ambient conditions.^[490,491,492,493] Nevertheless, synthesis of stable Al NPs exhibiting minute oxide thickness has remained a challenge.

Our approach to synthesis of metallic Al NPs and NSs is the use of laser ablation of bulk Al immersed into liquid. This technique provides the possibility of generating a large variety of NPs that are free of both surface-active substances and counter-ions. During laser ablation in liquid a quenching of the ejected hot plasma from the target to the liquid occurs. As a result the plasma formed reacts with both the liquid and air oxygen dissolved in it. However, the high reactivity of Al with ambient oxygen can partially be compensated by ablating using short laser pulses due to faster quenching which could minimize the formation of either oxide or hydroxide on the particle surface. Furthermore, the oxidation of NPs generated by this technique can be additionally suppressed by carefully outgassing the air trapped in liquid and/or replacement of it by a neutral gas.

6.3.2 Methodology

The generation of Al NPs and NSs was performed by laser ablation of an Al target supplied by Fluka with 99.9% purity. The surface of Al pellet was mechanically flattened and grinded with sandpaper to a μm roughness. The target was placed into a Pyrex cell and covered by a layer of absolute ethanol. The typical thickness of the liquid above the target was 1-2 mm. The cell was mounted on a computer-driven X-Y stage and translated during laser exposure. The ablation was performed using the beam of a fs Ti:sapphire laser emitting at 800nm, focused onto the target through the ethanol layer. The free surface of ethanol was exposed to air. Details of the experimental setup can be found also in **section 2.4.3**. It was found that the rate of NPs generation with 40 fs laser pulses at 800 nm is extremely low. This is mostly due to the fact that the peak power is so high that laser radiation is strongly absorbed by the liquid itself through non-linear processes (self-focusing effect). As a result, the fraction of laser energy that finally reaches the surface of the target is very small. Therefore, most of the experiments described below have been performed using 200 fs pulses. The typical spot size on the target was approximately 500 μm , corresponding to laser fluence of 0.2 J/cm² at the target surface. Finally the exposure time was about 10 minutes at the laser repetition rate of 1 kHz.

Alternatively, two ps Nd:YAG lasers at a wavelength of 1.06 μm , 10 Hz repetition rate were used for generation of Al NPs and NSs in either identical to the fs or anaerobic conditions. Their pulse widths were 30 and 150 ps, the former is used for ablation in anaerobic conditions and the latter for ablation in air. For the ablation in anaerobic conditions the target was placed into a sealed-off Pyrex cell, filled with ethanol and outgassed with a vacuum pump following several cycles of cell freezing with liquid nitrogen. The cell was filled with Ar prior to laser exposure minimizing thus the air content both in the cell and liquid. Laser radiation was focused through the Pyrex cap and liquid layer on the target and the typical exposure time was approximately 1 hour. Details about the morphological characterization can be found in **section 2.6.1**.

6.3.3 Characterization of Al nanoparticles.

The colloidal solutions obtained by ablation of an Al target with two types of lasers are different in appearance; the colloids produced with fs laser ablation look yellow in transmission, while those obtained with ps radiation look grey. In both cases the solutions are slightly opalescent and their opalescence increases upon increasing the laser fluence. All the colloids prepared were stable

against sedimentation for at least several months with no addition of any surface-active substances. Ablation of the same Al target in purified water, at fluencies of $0.2 - 0.5 \text{ J/cm}^2$, leads to opalescent colorless solutions. This should be attributed to chemical interaction of molten Al with water.

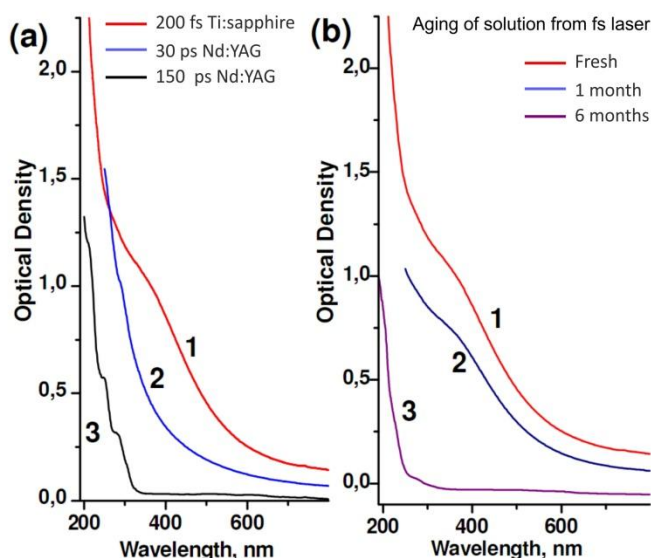


Figure 6.7: (a) Optical density spectrum of Al nanoparticles generated in ethanol after ablation of an Al target using two different laser sources: 200 fs Ti:sapphire laser (curve 1), 30 ps Nd:YAG laser (curve 2), and 150 ps Nd:YAG laser (curve 3). (b) Aging of the colloidal solution of NPs prepared with a fs laser radiation: freshly prepared colloidal solution (curve 1), 1 month storage upon contact in air (curve 2) and 6 months storage upon contact with air (curve 3).

decomposition (**Figure 6.7 (a)**, curve 3). NPs produced with fs pulses are hardly oxidized by air oxygen as indicated by the evolution of the corresponding absorption spectrum over several months (**Figure 6.7(b)**). The same is true for those produced with ps radiation, however only if the solution is saved without contact with air in a sealed-off container.

A TEM image of the Al NPs produced by fs laser ablation is presented in **Figure 6.8** indicating that a significant number of nanoparticles feature a tail. Although this tail has lower contrast in TEM compared to the high-contrast core, a high number of such tails are shown on the image background. The NPs show no distinct diffraction pattern in TEM, so that they are mostly

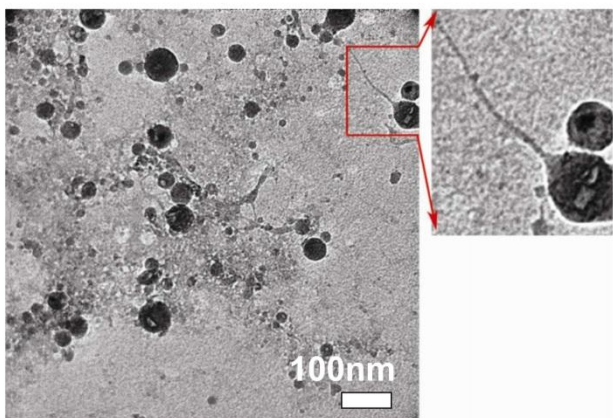


Figure 6.8: TEM view of nanoparticles generated via ablation of a bulk Al target in ethanol using fs laser radiation.

amorphous. This is confirmed by HRTEM characterization presented below. On the other hand, NPs generated using ps laser pulses are more round in shape. The colloidal solution in this case contains a significant amount of nanometer-sized debris that envelope NPs. Such debris have low contrast upon imaging and are probably non-metallic.

Size distribution of NPs obtained with different laser sources is presented in **Figure 6.9**. One can see that the size distribution is rather wide with the majority of NPs having size between 10 and 60 nm. It should be mentioned that the size of NPs determined using the dynamic light scattering (DLS) technique is always higher than that visible in **Figure 6.9** and for the same colloids is around 100-120 nm. This is attributed to the complex shape of NPs, shown in **Figure 6.8**. Therefore, the presence of low-contrast tails of NPs contributes to DLS measurements, while distributions in **Figure 6.9** correspond to high-contrast metallic NPs.

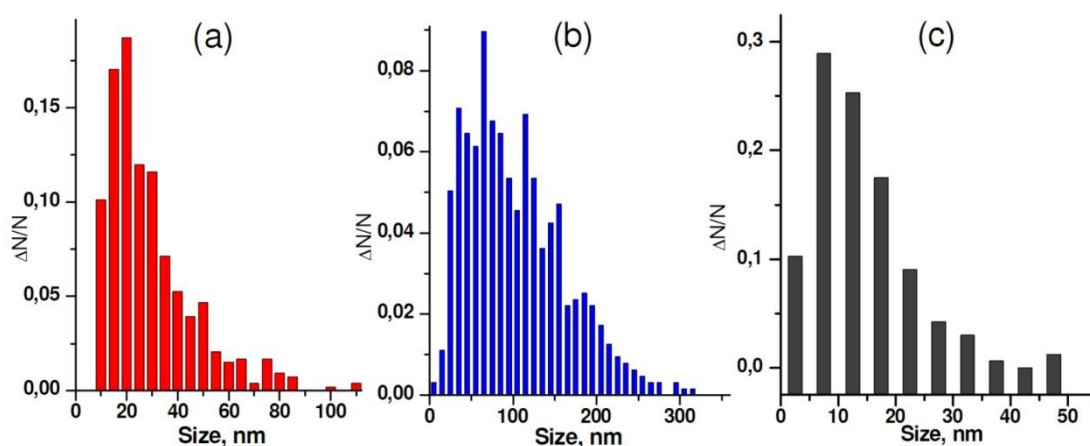


Figure 6.9: Distribution of NP size calculated from TEM images. (a) Ablation using a Ti:sapphire fs laser at fluence of 0.4 J/cm^2 , (b) a 30 ps Nd:YAG laser at fluence of 8 J/cm^2 in anaerobic conditions, (c) and a 150 ps Nd:YAG laser at fluence of 1.5 J/cm^2 . Following synthesis all three solutions were stored in a sealed-off container. The NP size was measured as the core diameter.

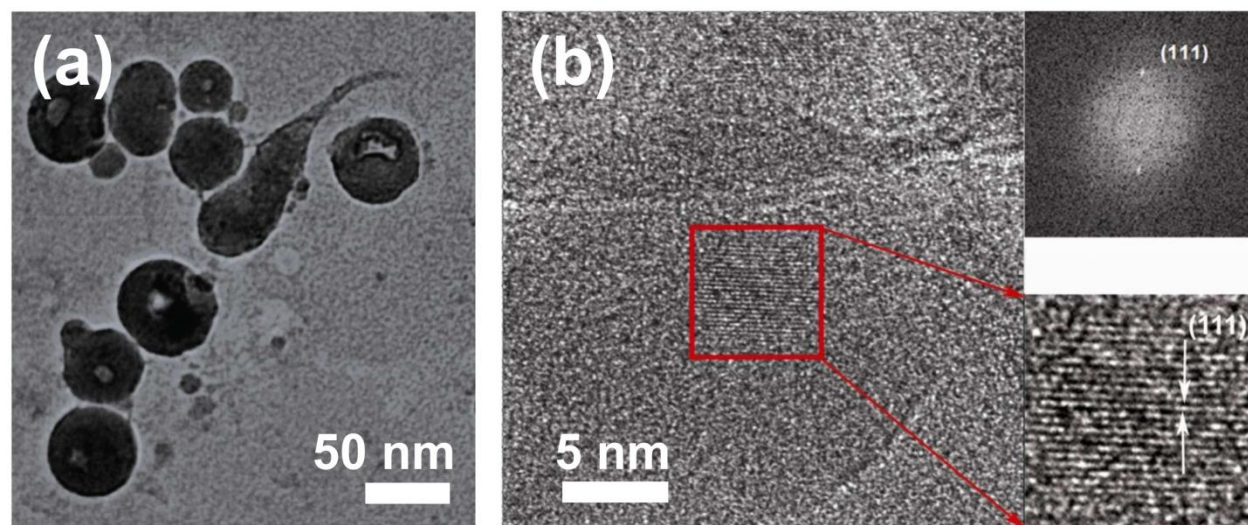


Figure 6.10: (a) TEM view of NPs generated by ablation of Al with 200 fs laser radiation, showing distinct areas inside NPs. (b) HRTEM image of a NP generated by laser ablation of Al target in ethanol using a Ti:sapphire fs laser. Red square indicates the visible crystallographic planes. Inset: numerical diffraction pattern corresponding to the selected zone in the HRTEM image, the spots correspond to the (111) planes of aluminum (distance of 0.233 nm).

A higher magnification TEM image, shown in **Figure 6.10(a)**, reveals that a distinct feature of Al NPs is the presence of a well-defined roundish area into their body. In most cases this area is situated close to the center of the particle and can be either brighter or darker than the rest of it. In some cases the same NP contains both dark and bright areas.

HRTEM images show crystalline inclusions within the Al nanoparticles (**Figure 6.10(b)**). Qualitatively, the fraction of crystallized areas of Al NPs is higher in case of ablation with ps laser (**Figure 6.11**) under anaerobic conditions. The lattice plane distances measured on the HRTEM images

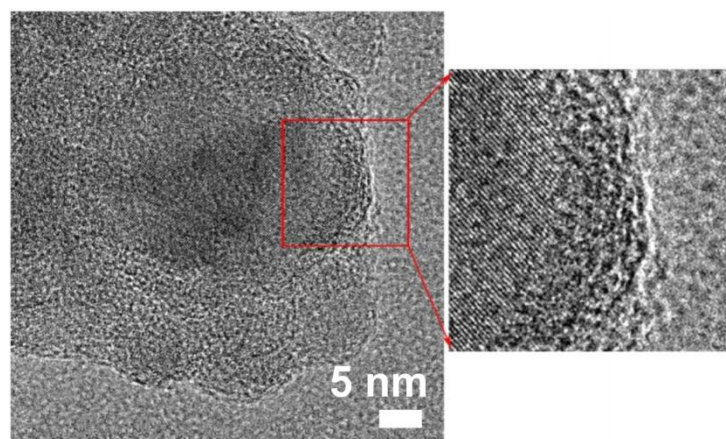


Figure 6.11: HRTEM image of a NP generated by laser ablation of Al target in ethanol using a Nd:YAG 30 ps laser.

are 0.233 and 0.202 nm which correspond to the (111) and (200) planes of metallic aluminum. It suggests that the nanoparticles are mostly amorphous but contain metal crystalline inclusions the proportion of which depending on the quenching rate of the nanoparticles. Longer pulses interact with NPs and therefore alter their quenching time. The darker areas inside the NPs on the HRTEM

images showed in **Figure 6.10(a)** can correspond to a diffraction contrast of the crystallized inclusions or to the absorption contrast of thicker zones. On the other hand the bright areas visible inside the NPs in **Figure 6.10(a)** can only correspond to a thinner zone and suggest a porosity of the Al NPs. A possible reason for appearance of these pores inside the Al NPs is the dissolution of the surrounding gas in the molten NP during laser ablation. The solubility of gases in metals increases by a factor of ten upon their melting.^[494] Fast solidification of NP ejected from the target quenches the dissolved gas, so that it becomes over-saturated. This over-saturation results in the formation of a gas-filled cavity inside the NP. Alternatively, these cavities can also be due to the chemical interaction of molten Al with traces of water in ethanol. In this case the cavities are filled with hydrogen, though this hypothesis requires further studies. In any case, the observation of this cavity is unique for laser-assisted generation of Al NPs and has never been reported so far for NP of other metals.^[495]

Electron Energy Loss Spectroscopy (EELS, not presented here) data confirm the metallic Al nature of the NPs obtained. The Al K-edge located at 1560 eV presents a near edge structure consistent with aluminium metal. In case of alumina particles the Al K-edge would be very different with a sharp line that characterizes aluminium oxide.^[496] A broad peak located at 531 eV corresponds to the O K-edge. The weak intensity of this peak confirms that the particles are mainly metallic certainly with a thin oxide layer at the surface, also indicated by the slow evolution of the

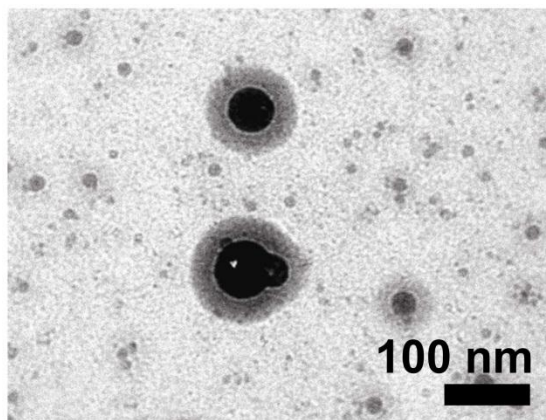


Figure 6.12: TEM view of NPs generated by ablation of bulk Al target in ethanol with a 150 ps Nd:YAG laser without using anaerobic conditions.

absorption spectrum with time. This layer is not clearly visible in TEM and HRTEM images of NPs produced using fs pulses, indicating that its thickness does not exceed the one of natural Al oxide and passivates Al NPs against further oxidation. On the other hand presence of an oxide layer is well seen on TEM images of NPs produced by ablation with ps pulses without using anaerobic conditions. This is illustrated in **Figure 6.12** where the NPs generated using 150 ps pulses have a core-shell structure with metallic core. The low-contrast shell is better visible on large NPs though is apparently presented on smaller ones.

One may deduce that laser ablation of a bulk Al target in ethanol results in the formation of metallic Al NPs. These NP are characterized by a plasmon resonance in near UV range. Absence of resonance peak in case of NP generated with ps laser radiation may be assigned to their larger size. In general, the average size of NPs is determined by the laser fluence on the target and not by the duration of

the laser pulse.^[497] The oxidation of NPs generated by laser ablation is closely related to the laser pulse width. Indeed, sufficiently short laser pulses produce mostly metallic NPs without the oxide shell observable with TEM. The NPs are oxidized slowly due to diffusion of air oxygen into the colloidal solution. On the contrary, the longer pulse duration of 150 ps leads to visible oxidation of as-generated NPs. However, in the latter case this oxide shell may provide better stability of NPs against further oxidation by air oxygen serving as a protective layer.

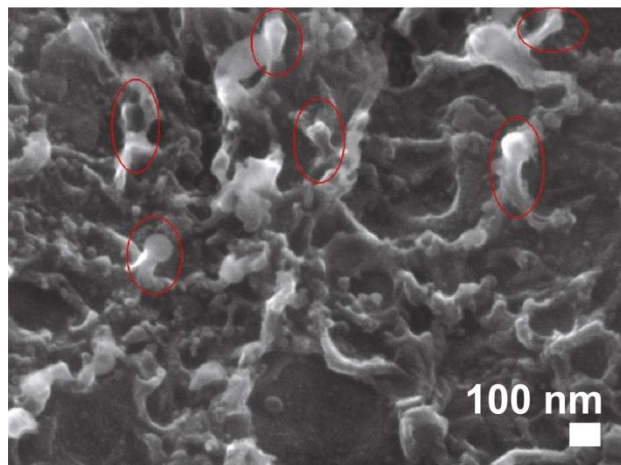


Figure 6.13: SEM micrograph of a nanostructured surface prepared by fs laser ablation of Al into ethanol. The red ellipses indicate mushroom-like NSs formed on the ablated surface

The elongated shape of Al NPs (tails) observed in case of ablation with a fs laser is closely related to the formation of nanostructures (NSs) on bulk Al targets under their ablation in liquids with short laser pulses.^[498,499] NSs are formed under the recoil pressure of the vapours of the liquid that surrounds the target. At the same time, a fraction of the molten layer of the target is dispersed into the liquid as NPs. Accordingly the tails of NPs observed in the resent work are due to detachment of liquid nano-drops from the molten layer. Finally, the nano-drops that fail to detach from the melt remain on the solidified surface as mushroom-like structures.^[500] Such structures are apparent in FESEM images of nanostructured Al surfaces, an example of which is shown in **Figure 6.13** (also see **Figure 6.5**). The close relationship between Al NSs and Al NPs can also be deduced from the proximity of the plasmon resonance of Al NPs reported in this work and the maximum of absorption of nanostructured Al surface.^[501]

The theoretical position of the plasmon resonance of Al NPs of 10 nm in diameter in water calculated in Ref ^[502], and the maximum of absorption lies around 200 nm. However, it is red shifted for NPs of higher diameters.^[503,504] Oxidation of Al NPs would also cause a red shift of their plasmon resonance, since its oxide, Al_2O_3 , has higher refractive index in the UV range than water. Indeed, theoretical calculations performed by Lukyanchuck et. al.^[505] are in good agreement with our results, as they calculated a large absorption peak between 300 and 400 nm for Al NPs with size 30-60 nm. The same is shown by Hornyak et al.,^[506] utilizing dynamical Maxwell-Garnett effective medium theory. Both laser wavelengths used in this study (800 and 1064 nm) are largely detuned from the plasmon resonance of Al NPs. This is an advantage for the generation of metallic Al NPs, since NPs

formed can be weak absorbers at the laser wavelength. On the contrary, UV wavelengths are close to the plasmon resonance of generated Al NPs, which can thus be efficiently heated by the ablation beam. This leads to enhanced interaction with the environment and eventual oxidation. Therefore, UV laser sources are not appropriate for generation of Al NPs.

The data on the morphology of Al NPs generated by laser ablation of an Al target shed new light on the mechanism of their formation. A number of experiments on laser-assisted formation of NPs have been reported and the modeling of NPs growth is described in terms of nucleation of the target material in the expanding plasma plume.^[507] Such approach shows good agreement with experimental data,^[508,509] especially in case of carbon ablation in liquid environment with nanosecond laser pulses. Presence of a molten layer on the target made of carbon is still under question. Al is a metal with low melting point, and the presence of a melt layer during laser ablation affects the size distribution of ejected NPs. Indeed, the specific shape of Al NPs observed in the present work (see **Figure 6.10**) and nano-protrusions left on the surface of the target (**Figure 6.13**) resemble each other. At a given laser fluence some protrusions leave the molten surface and become nanoparticles. Therefore NPs leave the melt as nano-entities and are not condensed in the plasma plume from smaller clusters or atoms. The dispersion of the melt occurs due to hydrodynamic instability that develops at the melt- vapor interface of the liquid that surrounds the target.^[510] The maximal amount of the target material that can be dispersed is determined by the melt thickness and is of order of $(at_p)^{1/2}$, where a stands for the heat diffusion coefficient of the target material, t_p is the laser pulse duration. Melt thickness also depends on the laser fluence in a linear way as soon as it exceeds the threshold fluence needed to melt the target material. In case of femtosecond laser the melting and dispersion of the melt starts when the laser pulse is over, after completion of the electron-phonon relaxation. The melt thickness in this case is determined by the absorption depth of laser radiation in the target material and the size of NPs is almost independent on the pulse duration, since the diffusion length of electrons excited in the material into the target is negligible.

6.4 Optical properties of nanostructures.

The visible manifestation of NS formation after laser irradiation of a metallic target is the coloration of exposed areas. A representative example is shown in **Figure 6.14**, which shows the yellow colored Al surface obtained after its ablation by fs pulses in water. This coloration should be distinguished from surface oxidation, since some oxides have absorption bands in the visible. However, a thin oxide layer

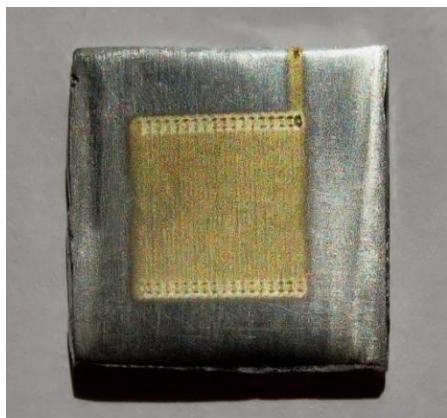


Figure 6.14: Macro view of an Al target exposed in water to radiation of 180 fs Ti:sapphire laser. The yellow square at the center corresponds to the exposed area

cannot be responsible for intense coloration of the target. The optical properties of NS are closely related to the spectral features of corresponding nanoparticles (NP). This is due to the fact that electrons are confined within NS just like in NP.^[511,512] The interesting feature of the reflectivity of a surface with NS is that the color is visible only in case of mirror-like reflection. This confirms the participation of electrons in NS to the observed coloration.

Exposure of an Al target at short laser pulses in liquid results in the yellowish coloration of the metal, being visible at angles close to mirror reflection (**Figure 6.15**). The coloration is most pronounced in the case of exposure into ethanol, where it appears just after only a few pulses at a fluence of as low as 0.05 J/cm^2 . At lower fluences, virtually no changes of the Al surface are observed, even with elevated number of laser shots. This color change is permanent, for instance, the target may be wiped by a wet tissue without any change of the color and it is observed independently of the purity of Al target with Al content ranging from 75% through 95%. Hence, this coloration should be assigned to structuring of the Al surface at the nanometre scale similarly to NS on both Ag and Au.^[513,514] **Figure 6.15** presents the absorption spectra of Al surfaces structured with different laser sources. In the blue and near UV region the absorption of the exposed samples exceeds that of the initial surface while in the NIR range, the samples ablated into liquid show lower absorption. In all cases, the absorption maximum is situated around 300 nm, which is justified by the yellow coloration of the corresponding exposed areas. This peak is shifted to lower wavelengths upon aging. When the Al target is exposed into liquids the latter takes on a yellow color as well, indicating the formation of Al particles dispersed in the liquid. As shown in the spectrum of **Figure 6.17**, these NP dispersions show a characteristic absorption peak close to 300 nm. The lateral size of NS on Al produced by its ablation in water with 350 ps laser radiation is 200 – 300 nm. The coloration of the exposed surface in this case is not visible at all. Comparison of laser ablation of bulk

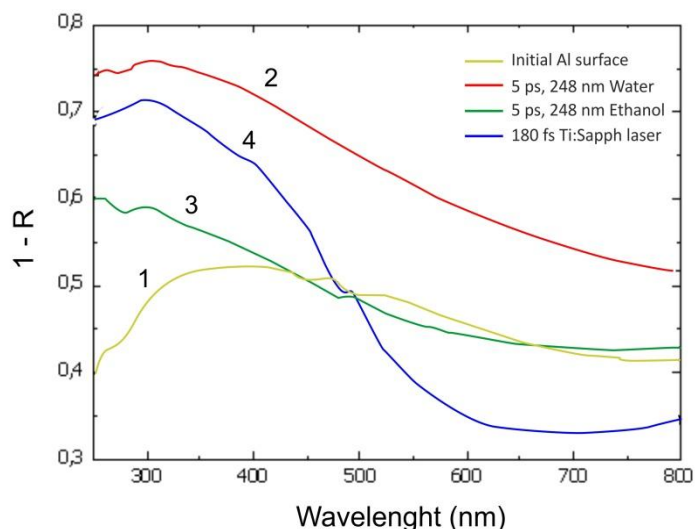


Figure 6.15: Absorption spectra of the (1) initial Al surface (2) of those exposed to the radiation of a 5 ps laser at 248 nm in water and (3) in ethanol. The curve (4) corresponds to exposure of Al in water to 180 fs-Ti:sapphire laser.

Al target in air and liquids has been reported recently.^[515] It is found that coloration of Al is gained under laser action in both media. However, in case of laser exposure in air the target surface is covered by significant amount of sputtered material. NS generated in air are less compact presumably due to higher amount of oxide. The similarity of the spectrum under ablation of Al in air and in liquids suggests that the mechanism governing the NS formation is the same, independently on the medium. In all cases NS are formed due to spatial instability of the evaporation and appear as a result of action of recoil pressure onto a thin molten

layer on Al. When the exposure is performed in liquids this pressure is the pressure of vapor of the surrounding liquid. In case of exposure in air this pressure is due to fast evaporation of the molten layer itself. That is why the laser fluence required to produce NS on Al in liquid is several times lower than in case of air exposure. NS in this case are formed owing to recoil pressure of metal vapors. Apparently, this process is also characterized by evaporation instability leading to formation of self-organized nano-sized areas within the evaporation cloud.

Formation of Ag and Au NS under laser ablation of corresponding metallic targets in liquids is extensively studied, as the plasmon resonance of NS from these two metals lies in the visible. Therefore the successful formation of such NS is extremely important for optoelectronic applications. Laser exposure of Ag in liquids leads to significant modifications of the plasmon spectrum of this metal. Coloration of Al surface exposed to femtosecond laser radiation has been also reported by C. Guo et al.^[516] It is observed that after ablation at sufficiently high laser fluence in air, the target takes on a gold-yellow tint. Later, this coloration has been attributed to the formation of NS on Al surface under its ablation with fs laser pulses either in air or in liquid environment.^[517] The authors attribute the yellow coloration of Al to the formation of periodic ripples decorated with NS. The spectral reflectivity of the laser-treated sample is measured at near-normal incidence with poor resolution, so the UV features of Al NS presented in the present work were not observed. Coloration is ascribed either to different ripple periods or just to grooving the Al surface with various periods.

The optical characteristics of an Al surface after its ablation in liquids can be again explained by a plasmon resonance absorption mechanism. The theoretical position of plasmon resonance of Al NPs of 10 nm in diameter in water was calculated in ref.^[518], and the maximum of absorption lies around 200 nm (more precisely – in vacuum UV region). However, it is red-shifted for NP of higher diameters.^[519] Also, oxidation of Al NP would also cause a red shift of their plasmon resonance, since its oxide, Al_2O_3 , has higher refractive index in the UV range than water. It should be noted that alumina itself has no absorption in the range of study since its absorption only commences from 250 nm and even shorter wavelength, depending on its impurities. The presence of aluminum oxide is indicated by fluorescence measurements performed on the exposed surfaces. This oxide layer may be formed by fast oxidation of the irradiated surface upon solidification and efficiently passivates the surface of NS against further oxidation, so they are chemically stable to provide permanent coloration of Al surface. No fluorescence is detected in the case of a pristine Al target.^[520]

It is pertinent to note that the most probable effect caused by nano-structuring of a metallic surface is its yellow coloration. Plasmon frequencies for majority of metallic NPs are situated in UV with the exception of only three metals, Ag, Au, and Cu. Therefore, nano-structured metallic surface may show enhanced absorption in the blue region of spectrum, which is closer to UV. Enhanced absorption in the blue region corresponds to yellow coloration of the surface that is what is observed for Al and Ag. Of course, quadruple plasmon resonance of electrons in NS is usually shifted to the red region compared to the dipole one. However, the intensity of this absorption band is much weaker.

6.5 Applications of Nanostructures

Besides evident fundamental interest, NS that are formed under laser-induced phase transitions at the solid-liquid interface possess promising potential for different applications. Nano-sized metal features are responsible for so called *Surface-Enhanced Raman Scattering* (SERS) due to local amplification of the electromagnetic waves in the their vicinity. As a result, the intensity of a pumping laser beam is enhanced giving rise to a corresponding amplification of the intensity of the weak Raman-shifted scattering signal. The total enhancement factor amounts to 10^5 - 10^6 .

Here we present that laser nanotexturing of metals can find applications for the increase of emission properties of cathodes made of this metal. Nano-protrusions with small radius of curvature serve as an efficient emitter of electrons since the electric field near them is higher than on a flat surface. Therefore, the potential barrier for electrons near these protrusions is lower, and the efficient work function of nano-structured surface is lower than that of a flat one. **Figure 6.16(a),(b)** shows the image of W cathode before and after laser ablation in ethanol with pulse duration of 180 fs.^[521] The surface of the Tungsten target is covered by ripples with period about 350 nm. The surface protrusions are situated on top of

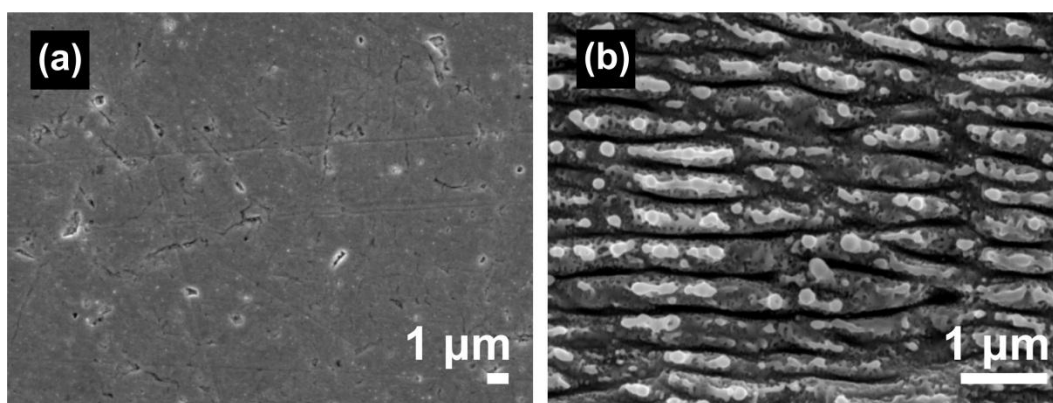


Figure 6.16: FESEM image of (a) the initial surface of W cathode and (b) NS with ripples on it after ablation in ethanol. NS are located on top of ripples. Pulse duration of 180 fs, wavelength of 800 nm.

periodic ripples. Their lateral size is between 50 and 150 nm. The cathode made of W was subjected to double exposure with linear polarization of the laser radiation. The sample was turned for 90° between the exposures.^[522] The morphology of W cathode after double laser exposure in ethanol is shown in **Figure 6.17**. Average lateral size of squared texture is about 150-250 nm. Spherical NS are located on top of square areas. Their size varies from 50 to 200 nm, and density of NS is 8×10^8 per 1 cm^2 . Following the work function of cathode with thermal emission was measured. **Figure 6.18** shows the dependence of the work function of both initial and nanotextured cathodes on temperature. The work function of

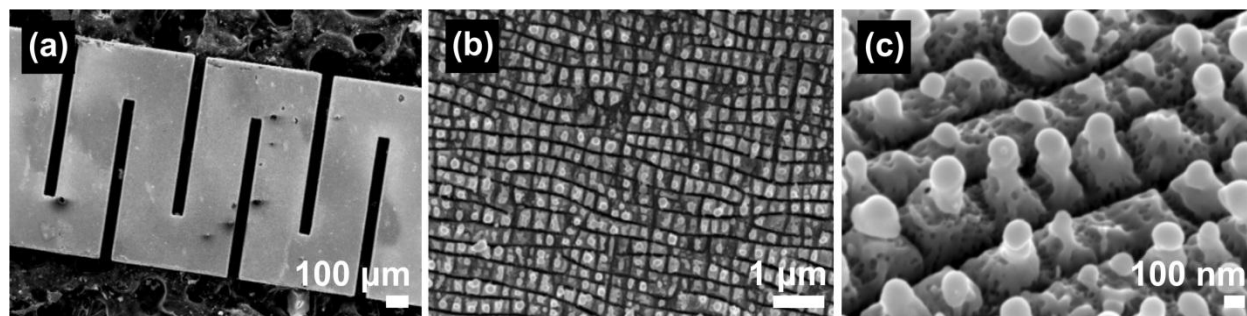


Figure 6.17: FE SEM view of (a) W cathode, general view, (b) top view of two-dimensional array obtained by double laser exposure in ethanol with sample rotation by 90°, (c) view tilted for 25

nanotextured cathode decreases by 2.5% with the increase of temperature. Initial cathode does not show such changes. Also presented data indicate the decrease of work function for the structured surfaces of the cathode by 8 % with respect to the initial sample. It is about 0.3eV. Since the density of the electron current depends on the work function exponentially, this result is very promising. Nanostructuring of W allows working at lower temperature at the same emission current that allows increasing the lifetime of the device.

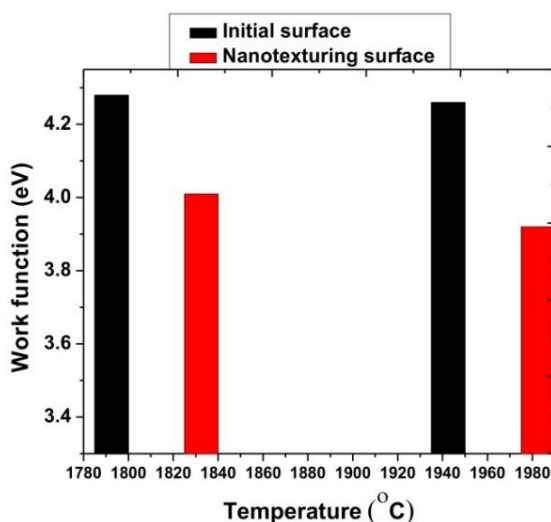


Figure 6.18: Dependence of the work function on temperature for initial and nanotextured W cathode. Ti:sapphire laser, wavelength of 800 nm, pulse duration of 180 fs, double laser exposure in ethanol.

6.6 Conclusion

It is shown that laser-induced phase transitions at the solid-liquid interface are characterized by instability in evaporation of the liquid that surrounds the solid. Smooth temperature profile leads to formation of regions with different pressure and velocity gradients within the evaporated liquid. The melting of underlying target serves as a recording medium to visualize these regions. This can be achieved only with sufficiently short laser pulses, since surface tension of the melt tends to dump nano-sized perturbations of its surface. Provided that the cooling rate of the target is sufficiently high, then these perturbations can be “frozen” as nanostructures.

Laser ablation of a bulk Al targets in ethanol leads to the formation of metallic Al NPs. In case of fs laser ablation the process can be carried out in open air. Generated Al NPs exhibit minimal oxide cladding and are pretty stable as they become slowly oxidized by air oxygen. Both are highly desirable properties for advanced energetic applications. Laser ablation with longer pulses in anaerobic conditions also results in metallic NPs, while NPs generated in open air are of core-shell type due to partial oxidation. The average size of Al NPs formed lies between 10 and 60 nm, depending on the experimental conditions. In all cases, the NPs produced are mostly amorphous with few single crystalline inclusions per NP.

As a rule, the average lateral size of NS decreases with the decrease of laser fluence towards the melting threshold of the target material. Formation of NS under laser-induced phase transitions at the solid-liquid interface is accompanied by modification of the reflectivity of the target. As a result, the surface of Al with NS becomes yellow colorized due to plasmon resonance of free electrons in NS.

NS that are formed under laser-induced phase transitions at the solid-liquid interface possess promising potential for different applications. Here we present that laser nanotexturing of metals can find applications for the enhancement of thermionic emission properties of nanostructured cathodes made of this metal.

Concluding Remarks

This dissertation has presented a detailed study on femtosecond laser structuring of solid surfaces. In particular, fundamental aspects of the interaction of single and temporally shaped double femtosecond pulses with Si and ZnO surfaces have been investigated. The special case of fs laser nanostructuring of metallic surfaces in the presence of liquid media has been additionally studied. The second part of the dissertation is focused on the importance of femtosecond laser structured surfaces for novel practical applications, including electronic, microfluidic and biological.

The main findings of this thesis are summarized below.

A) Laser Induced Periodic Surface Structure formation.

We present a detailed experimental and theoretical investigation of the interaction of single and double femtosecond pulses with Si, focusing in the normal boiling regime, where material removal is minimal and ablation can be excluded. In order to shed light on the formation mechanism of the final surface profile attained, a detailed theoretical model that takes into account heat transfer components and hydrodynamic description of the material melting and resolidification process has been developed. The model also accounts for the periodic surface structure formation (ripples) observed during semiconductor irradiation with femtosecond laser pulses. The success of our model to predict the experimentally observed surface profile, and ripple characteristics indicates and suggests that the hydrodynamic factor is of significant importance. Therefore it should be always taken into account towards understanding the physics of fs laser-solid interaction. **B) The effect of temporally designed double femtosecond pulses on Si and ZnO**

We have demonstrated the evolution of the surface morphology of Si upon irradiation with femtosecond laser double pulses for a fluence region close to the normal boiling regime. For low number of pulses the creation of wavelength ripples occurs independently of the time delay between pulses. On the other hand, the spot depth and area show a gradual decrease upon increasing pulse separation. To

account for these experimental findings our theoretical model has been modified to describe the double-pulse irradiation process. It is shown that, the spot area evolution with delay time predicted by the model, comes in fair agreement with the experimental findings. Finally, experiments performed in the ablation regime showed a suppression of the crater formed in the spot centre, in accordance to previous works performed on metallic surfaces.

Our study was then focused on femtosecond laser processing of transparent semiconductors and in particular to the study of the fundamentals of laser induced periodic structures (ripples) formation on ZnO surfaces irradiated with femtosecond delayed double pulses. It is found that by proper choice of laser fluence and time delay one can alter the ripples periodicity on demand from LSFR to M/HSFR and vice versa. Based on these results we propose the use of femtosecond laser double pulses as a novel method of controlling the large area formation of LSFR or M/HSFR ripple patterns on ZnO surfaces.

C) Application of femtosecond laser structured Silicon.

In this part we have demonstrated femtosecond laser structured Si surfaces to be superior platforms for various practical applications, including electronic, microfluidic and biological. In particular:

- We have systematically studied the characteristics of cold electron emission from fs-laser fabricated silicon spikes passivated with metallic and nano-carbon coatings. It is found that the emission characteristics, stability and durability of those cathodes are by far superior compared to conventional Si microcathodes.
- It is demonstrated that femtosecond laser fabricated hierarchically micro/nano structured surfaces are excellent platforms for the realization of responsive surfaces, the wettability of which can be switched on demand under the action of various external stimuli. It is shown that depending on the conformal functional coating deposited onto such surfaces efficient and stable electro-, photo- and pH- responsive surfaces can be attained.
- Finally, it is shown that femtosecond laser structured Si micro/nano structured surfaces can be used as scaffolds that promote cell adhesion and growth. It is demonstrated that the ability to precisely control the surface roughness, chemistry and thus the surface energy of those scaffolds can serve as a novel means to tune cell adhesion and thus elucidate the 3D cell–biomaterials interactions.

D) Formation of metallic nanosurfaces and nanoparticles via ablation in liquid media

We have investigated the formation of metallic nanoparticles (NPs) and nanostructures (NSs) produced upon femtosecond laser ablation of metallic surfaces in the presence of a liquid medium. It is shown that, contrary to the use of long laser pulses, the application of femtosecond pulses can give rise to metallic NPs and NSs exhibiting minimal oxide thickness, close to the native one. This is a highly desirable property for advanced applications of metallic nanostructures.

Relevant Publications

1. **M. Barberoglou**, M. Karalaki, D. Grey, E. Magoulakis, C. Fotakis, E. Stratakis, P. A. Loukakos, "High and Low Spatial frequency control of ripples on ZnO films with ultrashort double pulses." in preparation
2. **M. Barberoglou**, G. D. Tsibidis, P. A. Loukakos, E. Stratakis, C. Fotakis, "The influence of femtosecond double pulse laser irradiation on the morphology of Si surfaces" in preparation
3. G. D. Tsibidis, **M. Barberoglou**, P. A. Loukakos, E. Stratakis, C. Fotakis, "Ultrashort pulsed laser surface modification on silicon after cooling of a superheated liquid" *Physical Rev. B* **86**, 115316 (2012)
4. E. Stratakis, A. Mateescu, **M. Barberoglou**, M. Vamvakaki, C. Fotakis, and S. H. Anastasiadis, "From superhydrophobicity and water repellency to superhydrophilicity: smart polymer-functionalized surfaces," *Chem Commun* **46**, 4136-4138 (2010).
5. **M. Barberoglou**, V. Zorba, A. Pagozidis, C. Fotakis, and E. Stratakis, "Electrowetting Properties of Micro/Nanostructured Black Silicon," *Langmuir* **26**, 13007-13014 (2010).
6. A. Ranella, **M. Barberoglou**, S. Bakogianni, C. Fotakis, and E. Stratakis, "Tuning cell adhesion by controlling the roughness and wettability of 3D micro/nano silicon structures," *Acta Biomater* **6**, 2711-2720 (2010).
7. E. L. Papadopoulou, A. Samara, **M. Barberoglou**, A. Manousaki, S. N. Pagakis, E. Anastasiadou, C. Fotakis, and E. Stratakis, "Silicon Scaffolds Promoting Three-Dimensional Neuronal Web of Cytoplasmic Processes," *Tissue Eng Part C-Me* **16**, 497-502 (2010).
8. E. L. Papadopoulou, A. Pagkozidis, **M. Barberoglou**, C. Fotakis, and E. Stratakis, "Electrowetting Properties of ZnO and TiO(2) Nanostructured Thin Films," *Journal of Physical Chemistry C* **114**, 10249-10253 (2010).
9. E. V. Barmina, **M. Barberoglou**, V. Zorba, A. V. Simakin, E. Stratakis, C. Fotakis, and G. A. Shafeev, "Laser control of the properties of nanostructures on Ta and Ni under their ablation in liquids," *J Optoelectron Adv M* **12**, 495-499 (2010).
10. E. Stratakis, R. Giorgi, **M. Barberoglou**, T. Dikonimos, E. Salernitano, N. Lisi, and E. Kymakis, "Three-dimensional carbon nanowall field emission arrays," *Appl Phys Lett* **96** (2010).
11. E. Spanakis, **M. Barberoglou**, V. Zorba, P. Tzanetakis, and C. Fotakis, "Metal coated silicon spike cold-electron emitters show improvement of performance with operation," *Appl Phys Lett* **96** (2010).

12. **M. Barberoglou**, V. Zorba, E. Stratakis, E. Spanakis, P. Tzanetakis, S. H. Anastasiadis, and C. Fotakis, "*Bio-inspired water repellent surfaces produced by ultrafast laser structuring of silicon*," *Appl Surf Sci* **255**, 5425-5429 (2009).
13. E.V. Barmina, **M. Barberoglu**, V. Zorba, A.V. Simakin, E. Stratakis, C. Fotakis, G.A. Shafeev "*Surface nanotexturing of tantalum by laser ablation in water*" *Quantum Electronics* 39 (1) 89 - 93 (2009)
14. **M. Barberoglou**, V. Zorba, E. Stratakis, E. Spanakis, P. Tzanetakis, S. H. Anastasiadis, and C. Fotakis, "*Bio-inspired water repellent surfaces produced by ultrafast laser structuring of silicon*," *Appl Surf Sci* **255**, 5425-5429, (2009).
15. E. Stratakis, V. Zorba, **M. Barberoglou**, E. Spanakis, S. Rhizopoulou, P. Tzanetakis, S. Anastasiadis, and C. Fotakis "*Laser structuring of water-repellent biomimetic surfaces.*" *SPIE* 10.1117/2.1200901.1441(2009)
16. Evie L. Papadopoulou, **Marios Barberoglou**, Vassilia Zorba, Aleka Manousaki, Alexios Pagkozidis, Emmanuel Stratakis and Costas Fotakis, "*Reversible photoinduced wettability transition of hierarchical ZnO structures*" *J. Phys, Chem C* **113** p. 2891 (2009)
17. E. L. Papadopoulou, **M. Barberoglou**, V. Zorba, A. Manousaki, A. Pagkozidis, E. Stratakis, and C. Fotakis, "*Reversible Photoinduced Wettability Transition of Hierarchical ZnO Structures*," *Journal of Physical Chemistry C* **113**, 2891-2895 (2009).
18. E. Stratakis, V. Zorba, **M. Barberoglou**, C. Fotakis, and G. A. Shafeev, "*Laser writing of nanostructures on bulk Al via its ablation in liquids*," *Nanotechnology* **20** (2009).
19. V. Zorba, E. Stratakis, **M. Barberoglou**, E. Spanakis, P. Tzanetakis, S. H. Anastasiadis, and C. Fotakis, "*Biomimetic Artificial Surfaces Quantitatively Reproduce the Water Repellency of a Lotus Leaf*," *Adv Mater* **20**, 4049-+ (2008).
20. V. Zorba, E. Stratakis, **M. Barberoglou**, E. Spanakis, P. Tzanetakis, C. Fotakis, "*Tailoring the wetting response of silicon surfaces via fs laser structuring*" *Appl Phys A* **93** 819 (2008)

Reference

-
- [1] B.C. Stuart, et al., J. Opt. Soc. Am. B **13**, 459 (1996).
 - [2] B.N. Chichkov, et al., Appl. Phys. A-Mater **63**, 109 (1996).
 - [3] W.S. Fann, R. Storz, H.W.K. Tom, J. Bokor, Phys. Rev. B **46**, 13592 (1992).
 - [4] J. Hohlfeld, et al., Chem. Phys. **251**, 237 (2000).
 - [5] K. Sugioka et al. (eds.), Laser Precision Microfabrication, Springer Series in Materials Science 135, DOI 10.1007/978-3-642-10523-4__7
 - [6] E. Stratakis, E. Ranella and C. Fotakis, Biomicrofluidics, **5**, 0113411 (2011).
 - [7] Kabashin A.V., Meunier M., in Recent Advances in Laser Processing of Materials p. 1 (Amsterdam: Elsevier, 2006)
 - [8] Arnold B.G., Pique A. MRS Bull., **32**, 9 (2007).
 - [9] Prasad P.N. Introduction to Biophotonics (Boston: Wiley-Interscience, 2003).
 - [10] Shafeev G.A., Laser-based formation of nanoparticles, in: Lasers in Chemistry, Volume 2: Influencing matter. Edited by M. Lackner, Wiley VCH Verlag GmbH&Co, KGaA, Weinheim, 713 – 741 (2008).
 - [11] D. Bauerle, *Laser Processing and Chemistry* (2nd edition), Springer, Berlin (1996).
 - [12] E. Magoulakis, E. L. Papadopoulou, E. Stratakis, C. Fotakis, and P. A. Loukakos, Appl.Phys. A. **98**, 701 (2010).
 - [13] A. Ranella, M. Barberoglou, S. Bakogianni, C. Fotakis, and E. Stratakis, Acta Biomaterialia **6**, 2711 (2010).
 - [14] E. Stratakis, A. Ranella, M. Farsari, and C. Fotakis, Progress in Quantum Electronics **33**, 127 (2009).
 - [15] V. Zorba, L. Persano, D. Pisignano, A. Athanassiou, E. Stratakis, R. Cingolani, P. Tzanetakis, and C. Fotakis, Nanotechnology **17**, 3234 (2006).
 - [16] V. Zorba, E. Stratakis, M. Barberoglou, E. Spanakis, P. Tzanetakis, S. H. Anastasiadis, and C. Fotakis, Advanced Materials **20**, 4049 (2008).
 - [17] V. Zorba, P. Tzanetakis, C. Fotakis, E. Spanakis, E. Stratakis, D. G. Papazoglou, and I. Zergioti, Appl. Phys. Lett. **88** (2006).

-
- [18] E. Stratakis, A. Ranella, and C. Fotakis, *Biomicrofluidics* **5** (2011).
- [19] J. C. Diels and W. Rudolph, *Ultrashort Laser Pulse Phenomena: Fundamentals, Techniques, and Applications on a Femtosecond Time* (2nd edition), Academic Press, Burlington, MA, (2006).
- [20] R. F. W. Herrmann, J. Gerlach, and E. E. B. Campbell, *Appl. Phys A* **66**, 35 (1998).
- [21] D. Bäuerle, *Laser Processing and Chemistry* (2011)
- [22] S.K. Sundaram, E. Mazur, *Nat. Mat.* **1**, 217, (2002)
- [23] S. H. Lee, J. S. Lee, S. Park, and Y. K. Choi, *Numerical Heat Transfer Part a-Applications* **44**, 833 (2003).
- [24] S. I. Anisimov, Kapeliov.BI, and T. L. Perelman, *Zhurnal Eksperimentalnoi I Teoreticheskoi Fiziki* **66**, 776 (1974).
- [25] P. P. Pronko, P. A. VanRompay, C. Horvath, F. Loesel, T. Juhasz, X. Liu, and G. Mourou, *Phys. Rev. B*, **58**, 2387 (1998).
- [26] H. M. van Driel, *Phys. Rev. B*, **35**, 8166 (1987).
- [27] N. M. Bulgakova, I. M. Burakov, Y. P. Meshcheryakov, R. Stoian, A. Rosenfeld, and I. V. Hertel, *Journal of Laser Micro Nanoengineering* **2**, 76 (2007).
- [28] M. M. Martynyuk, *Zh Fiz Khim+* **57**, 810-821 (1983).
- [29] A. Miotello, and R. Kelly, *Appl Phys a-Mater* **69**, S67-S73 (1999).
- [30] M.M. Martynyuk, *Sov. Phys. Tech.-Phys.* **19**, 793 (1974)
- [31] M.M. Martynyuk, *Phys. Combust. Explosions* **13**, 178 (1977)
- [32] M. Birnbaum, *J. Appl. Phys.* **36**, 3688 (1965)
- [33] D. C. Emmony, R. P. Howson, L. J. Willis, *Appl. Phys. Lett.* **23**, 598 (1973)
- [34] H. J. Leamy, G. A. Rozgonyi, T. T. Sheng, G. K. Celler, *Appl. Phys. Lett.* **32**, 535 (1978)
- [35] P. M. Fauchet, A. E. Siegman, *Appl. Phys. Lett.* **40**, 824 (1981)
- [36] T. E. Zavecz, M. A. Saifi, *Appl. Phys. Lett.* **26**, 165 (1975)
- [37] J. C. Koo, R. E. Slusher, *Appl. Phys. Lett.* **28**, 614 (1976)
- [38] N. R. Isenor, *Appl. Phys. Lett.* **31**, 148 (1977)
- [39] A. K. Jain, V. N. Kulkarni, D. K. Sood, J.S. Uppal, *J. Appl. Phys.* **52**, 4882 (1981)
- [40] P. A. Temple, M. J. Soileau, *IEEE J. Quant. Elec.* **QE-17**, 2067 (1981)
- [41] M. Huang, F. L. Zhao, Y. Cheng, N. S. Xu, and Z. Z. Xu, *ACS Nano* **3**, 4062 (2009).

-
- [42] A. Latif, M.S. M.A. Aleem, M.S. Rafique, M. Khaleeq-Ur-Rahman, M. Laser and Particle Beams, **27**, 129, (2008).
- [43] J. Bonse, M. Munz, H.J. Sturm, H. J. Appl. Phys., **97**, 013538, (2005).
- [44] E.M. Hsu, T.H.R. Crawford, H.F. Tiedje, H.K. Haugen, Appl. Phys. Lett., **91**, 111102, (2007).
- [45] D. C. Emmony, R. P. Howson and L. J. Willis, Appl. Phys. Lett. **23**, 598 (1973).
- [46] J. E. Sipe, J. F. Young, J. S. Preston, and H. M. van Driel, Phys. Rev. B **27**, 1141 (1983).
- [47] Z. Guosheng, P. M. Fauchet and A. E. Siegman, Phys. Rev. B **26**, 5366 (1982).
- [48] A. Boronic, H. K. Haugen, Appl. Phys. Lett. **82**, 4462-4464 (2008)
- [49] E. M. Usu, T. H. R. Crawford, H. F. Tiedje, H. K. Heugen, Appl. Phys. Lett. **91**, 111102, (2007)
- [50] T. Tomita, K. Kinoshita, S. Matsuo, S. Hachimoto, Appl. Phys. Lett. **90**, 153115, (2007)
- [51] T. Tomita, Y. Fukumori, K. Kinoshita, S. Matsuo, S. Hashimoto, Appl. Phys. Lett. **92**, 013104, (2008)
- [52] H. Varel, M. Wahmer, A. Rosenfeld, D. Ashkenasi, and E. E. B. Campbell, Appl. Surf. Sci. **127–129**, 128 (1998)
- [53] A. M. Ozkan, A. P. Malshe, T. A. Railkar, W. D. Brown, M. D. Shirk, and P. A. Molian, Appl. Phys. Lett. **75**, 3716 (1999)
- [54] D. Dufft, A. Rosenfeld, S. K. Das, R. Grunwald, and J. Bonse J. Appl. Phys. **105**, 034908 (2009)
- [55] Jenneck, Ann. Phys. Leipz. **23**, 846-866 (1907)
- [56] R. H. Ritchie, Phys. Rev. **106**, 874–881 (1957)
- [57] M. Huang, F. L. Zhao, Y. Cheng, N. S. Xu, and Z. Z. Xu, ACS Nano **3**, 4062 (2009).
- [58] S. Sakabe, M. Hashida, S. Tokita, S. Namba, and K. Okamuro, Phys. Rev. B **79**, 033409 (2009).
- [59] A. Borowiec, and H. K. Haugen, Appl Phys Lett **82**, 4462-4464, (2003).
- [60] T. Q. Jia, H. X. Chen, M. Huang, F. L. Zhao, Q. Jr, R. X. Li, Z. Z. Xu, X. K. He, J. Zhang, and H. Kuroda, Phys Rev B **72** (2005).
- [61] D. Dufft, A. Rosenfeld, S. K. Das, R. Grunwald, and J. Bonse J. Appl. Phys. **105**, 034908 (2009)
- [62] G. D. Tsibidis, M. Barberoglou, P. A. Loukakos, E. Stratakis, C. Fotakis' <http://arxiv.org/abs/1109.6780> (submitted 2011)
- [63] Wood, R. W. *Philysophical magazine* **4**, 396-40, (1902).
- [64] L. D. Landau and E. M. Lifshitz, *Fluid Mechanics* (2nd Edition) (1987).

-
- [65] C. Froehly, B. colombeau, M. Vampouille, Prog. Opt. **20**, 65-153, (1983).
- [66] A. M. Weiner, Rev. Sci. Instrum. **71**, 1929-60, (2000).
- [67] A. M. Weiner, J. P. Heritage, E. M. Kirschner, J. Opt. Soc. Am. **5**, 1563-72, (1988).
- [68] T. Brixner, G. Gerber, Opt. Lett. **26**, 557-9, (2001).
- [69] T. Feurer, J. C. Vaughan, R. M. Koehl, K. A. Nelson, Opt. Lett. **27**, 652-4, (2002).
- [70] A. Monmayrant, S. Weber, B. Chatel, J. Phys. B **43**, 103001 (2010)
- [71] D. Oner, T. J. McCarthy, Langmuir **16**, 7777 (2000).
- [72] R. C. Smith, D. C. Cox, and S. R. P. Silva, Appl. Phys. Lett. **87**, 1031121 (2005)
- [73] D. Bauerle, *Laser Processing and Chemistry* (2nd edition), Springer, Berlin (1996).
- [74] J. C. Diels and W. Rudolph, *Ultrashort Laser Pulse Phenomena: Fundamentals, Techniques, and Applications on a Femtosecond Time* (2nd edition), Academic Press, Burlington, MA, (2006).
- [75] E. Magoulakis, E. L. Papadopoulou, E. Stratakis, C. Fotakis, and P. A. Loukakos, Applied Physics a-Materials Science & Processing **98**, 701 (2010).
- [76] A. Ranella, M. Barberoglou, S. Bakogianni, C. Fotakis, and E. Stratakis, Acta Biomaterialia **6**, 2711 (2010).
- [77] E. Stratakis, A. Ranella, M. Farsari, and C. Fotakis, Progress in Quantum Electronics **33**, 127 (2009).
- [78] A. Y. Vorobyev and C. L. Guo, Optics Express **18**, 6455 (2010).
- [79] V. Zorba, L. Persano, D. Pisignano, A. Athanassiou, E. Stratakis, R. Cingolani, P. Tzanetakis, and C. Fotakis, Nanotechnology **17**, 3234 (2006).
- [80] V. Zorba, E. Stratakis, M. Barberoglou, E. Spanakis, P. Tzanetakis, S. H. Anastasiadis, and C. Fotakis, Advanced Materials **20**, 4049 (2008).
- [81] V. Zorba, P. Tzanetakis, C. Fotakis, E. Spanakis, E. Stratakis, D. G. Papazoglou, and I. Zergioti, Applied Physics Letters **88**, 081103 (2006).
- [82] E. Stratakis, A. Ranella, and C. Fotakis, Biomicrofluidics **5** (2011).
- [83] F. He, Y. Cheng, L. L. Qiao, C. Wang, Z. Z. Xu, K. Sugioka, K. Midorikawa, and J. Wu, Applied Physics Letters **96** (2010).
- [84] R. F. W. Herrmann, J. Gerlach, and E. E. B. Campbell, Applied Physics a-Materials Science & Processing **66**, 35 (1998).
- [85] C. B. Arnold and E. McLeod, Nature Nanotechnology **3**, 413 (2008).
- [86] N. M. Bulgakova, I. M. Burakov, Y. P. Meshcheryakov, R. Stoian, A. Rosenfeld, and I. V. Hertel, Journal of Laser Micro Nanoengineering **2**, 76 (2007).

-
- [87] R. Kelly and A. Miotello, *Applied Surface Science* **96-8**, 205 (1996).
- [88] N. M. Bulgakova and I. M. Bourakov, *Applied Surface Science* **197**, 41 (2002).
- [89] N. M. Bulgakova, A. V. Bulgakov, I. M. Bourakov, and N. A. Bulgakova, *Applied Surface Science* **197**, 96 (2002).
- [90] V. Semak and A. Matsunawa, *Journal of Physics D-Applied Physics* **30**, 2541 (1997).
- [91] X. H. Ye and X. Chen, *Journal of Physics D-Applied Physics* **35**, 1049 (2002).
- [92] L. J. Zhang, J. X. Zhang, G. F. Zhang, W. Bo, and S. L. Gong, *Journal of Physics D-Applied Physics* **44** (2011).
- [93] G. D. Tsibidis, E. Stratakis, and K. E. Aifantis, *Journal of Applied Physics* **111** (2012).
- [94] E. Stratakis, A. Ranella, and C. Fotakis, *Biomicrofluidics* **5** (2011).
- [95] J. Bonse, M. Munz, and H. Sturm, *Journal of Applied Physics* **97**, 013538 (2005).
- [96] Y. H. Han and S. L. Qu, *Chemical Physics Letters* **495**, 241 (2010).
- [97] M. Huang, F. L. Zhao, Y. Cheng, N. S. Xu, and Z. Z. Xu, *ACS Nano* **3**, 4062 (2009).
- [98] J. E. Sipe, J. F. Young, J. S. Preston, and H. M. Vandriel, *Physical Review B* **27**, 1141 (1983).
- [99] B. Tan and K. Venkatakrishnan, *Journal of Micromechanics and Microengineering* **16**, 1080 (2006).
- [100] G. S. Zhou, P. M. Fauchet, and A. E. Siegman, *Physical Review B* **26**, 5366 (1982).
- [101] V. Semak and A. Matsunawa, *Journal of Physics D-Applied Physics* **30**, 2541 (1997).
- [102] X. H. Ye and X. Chen, *Journal of Physics D-Applied Physics* **35**, 1049 (2002).
- [103] L. J. Zhang, J. X. Zhang, G. F. Zhang, W. Bo, and S. L. Gong, *Journal of Physics D-Applied Physics* **44** (2011).
- [104] R. F. W. Herrmann, J. Gerlach, and E. E. B. Campbell, *Applied Physics a-Materials Science & Processing* **66**, 35 (1998).
- [105] J. Bonse, M. Munz, and H. Sturm, *Journal of Applied Physics* **97**, 013538 (2005).
- [106] R. Stoian, M. Boyle, A. Thoss, A. Rosenfeld, G. Korn, and I. V. Hertel, *Applied Physics a-Materials Science & Processing* **77**, 265 (2003).
- [107] J. Zhang, Q. Lin, G. Piredda, R. W. Boyd, G. P. Agrawal, and P. M. Fauchet, *Applied Physics Letters* **91** (2007).

-
- [108] H. M. van Driel, *Physical Review B* **35**, 8166 (1987).
- [109] T. Held, T. Kuhn, and G. Mahler, *Physical Review B* **44**, 12873 (1991).
- [110] G. D. Tsibidis, E. Stratakis, and K. E. Aifantis, *Journal of Applied Physics* **111** (2012).
- [111] H. M. van Driel, *Physical Review B* **35**, 8166 (1987).
- [112] J. K. Chen, D. Y. Tzou, and J. E. Beraun, *International Journal of Heat and Mass Transfer* **48**, 501 (2005).
- [113] R. E. Russo, S. S. Mao, X. L. Mao, and R. Greif, *Applied Surface Science* **127**, 206 (1998).
- [114] R. E. Russo, X. L. Mao, H. C. Liu, J. H. Yoo, and S. S. Mao, *Applied Physics a-Materials Science & Processing* **69**, S887 (1999).
- [115] C. P. Grigoropoulos, R. H. Buckholz, and G. A. Domoto, *Journal of Applied Physics* **60**, 2304 (1986).
- [116] T. R. Anthony and H. E. Cline, *Journal of Applied Physics* **48**, 3888 (1977).
- [117] J. Zhou, H. L. Tsai, and P. C. Wang, *Journal of Heat Transfer-Transactions of the Asme* **128**, 680 (2006).
- [118] V. Semak and A. Matsunawa, *Journal of Physics D-Applied Physics* **30**, 2541 (1997).
- [119] X. H. Ye and X. Chen, *Journal of Physics D-Applied Physics* **35**, 1049 (2002).
- [120] L. J. Zhang, J. X. Zhang, G. F. Zhang, W. Bo, and S. L. Gong, *Journal of Physics D-Applied Physics* **44** (2011).
- [121] H. Y. Zhao, W. C. Niu, B. Zhang, Y. P. Lei, M. Kodama, and T. Ishide, *Journal of Physics D-Applied Physics* **44** (2011).
- [122] J. H. Cho, D. F. Farson, J. O. Milewski, and K. J. Hollis, *Journal of Physics D-Applied Physics* **42** (2009).
- [123] L. D. Landau and E. M. Lifshitz, *Fluid Mechanics* (2nd Edition) (1987).
- [124] R. Kelly and A. Miotello, *Applied Surface Science* **96-8**, 205 (1996).
- [125] R. Kelly and A. Miotello, *Applied Surface Science* **96-8**, 205 (1996).
- [126] J. K. Chen, D. Y. Tzou, and J. E. Beraun, *International Journal of Heat and Mass Transfer* **48**, 501 (2005).
- [127] R. E. Russo, S. S. Mao, X. L. Mao, and R. Greif, *Applied Surface Science* **127**, 206 (1998).
- [128] N. M. Bulgakova and I. M. Bourakov, *Applied Surface Science* **197**, 41 (2002).

-
- [129] N. M. Bulgakova, A. V. Bulgakov, I. M. Bourakov, and N. A. Bulgakova, *Applied Surface Science* **197**, 96 (2002).
- [130] N. M. Bulgakova, A. V. Bulgakov, I. M. Bourakov, and N. A. Bulgakova, *Applied Surface Science* **197**, 96 (2002).
- [131] C. A. J. Fletcher, *Computational techniques for fluid dynamics* (Springer-Verlag, Berlin ; New York, 1991).
- [132] H. M. van Driel, *Physical Review B* **35**, 8166 (1987).
- [133] C. A. J. Fletcher, *Computational techniques for fluid dynamics* (Springer-Verlag, Berlin ; New York, 1991).
- [134] Y. Wang and H. L. Tsai, *International Journal of Heat and Mass Transfer* **44**, 2067 (2001).
- [135] T. S. Chung, *Journal of Applied Physics* **60**, 55 (1986).
- [136] J. H. Cho, D. F. Farson, J. O. Milewski, and K. J. Hollis, *Journal of Physics D-Applied Physics* **42** (2009).
- [137] P. Solana and G. Negro, *Journal of Physics D-Applied Physics* **30**, 3216 (1997).
- [138] Y. Morinishi, O. V. Vasilyev, and T. Ogi, *Journal of Computational Physics* **197**, 686 (2004).
- [139] Y. Morinishi, T. S. Lund, O. V. Vasilyev, and P. Moin, *Journal of Computational Physics* **143**, 90 (1998).
- [140] M. Spivak, *A comprehensive introduction to differential geometry* (Publish or Perish, Inc., Houston, 1999).
- [141] D. S. Ivanov and L. V. Zhigilei, *Physical Review Letters* **98** (2007).
- [142] D. S. Ivanov and L. V. Zhigilei, *Physical Review B* **68** (2003).
- [143] V. Semak and A. Matsunawa, *Journal of Physics D-Applied Physics* **30**, 2541 (1997).
- [144] L. D. Landau and E. M. Lifshitz, *Fluid Mechanics* (2nd Edition) (1987).
- [145] T. R. Anthony and H. E. Cline, *Journal of Applied Physics* **48**, 3888 (1977).
- [146] J. Bonse, M. Munz, and H. Sturm, *Journal of Applied Physics* **97**, 013538 (2005).
- [147] R. Stoian, M. Boyle, A. Thoss, A. Rosenfeld, G. Korn, and I. V. Hertel, *Applied Physics a-Materials Science & Processing* **77**, 265 (2003).
- [148] J. Bonse, M. Munz, and H. Sturm, *Journal of Applied Physics* **97**, 013538 (2005).
- [149] G. S. Zhou, P. M. Fauchet, and A. E. Siegman, *Physical Review B* **26**, 5366 (1982).
- [150] Y. H. Han and S. L. Qu, *Chemical Physics Letters* **495**, 241 (2010).
- [151] M. Huang, F. L. Zhao, Y. Cheng, N. S. Xu, and Z. Z. Xu, *ACS Nano* **3**, 4062 (2009).

-
- [152] J. E. Sipe, J. F. Young, J. S. Preston, and H. M. Vandriel, *Physical Review B* **27**, 1141 (1983).
- [153] C. S. Madi, E. Anzenberg, K. F. Ludwig, and M. J. Aziz, *Physical Review Letters* **106** (2011).
- [154] J. Bonse, M. Munz, and H. Sturm, *Journal of Applied Physics* **97**, 013538 (2005).
- [155] T. H. Her, R. J. Finlay, C. Wu, S. Deliwala, and E. Mazur, *Applied Physics Letters* **73**, 1673 (1998).
- [156] S.I Dolgaev, S.V. Lavrishev, A.A. Lyalin, A.V. Simakin, V.V. Voronov, G.A. Shafeev, *Appl. Phys. A* **73**, 177 (2001).
- [157] J.E.Carey, C.H.Crouch, E.Mazur, *Optics and Photonics News*, 32, 2/2003.
- [158] J.D.Fowlkes, A.J.Pedraza, D.H.Lowndes, *Appl. Phys. Lett.* **77**, 1629 (2000).
- [159] F.Sanchez, J.L.Morenza, R.Aguiar, J.C.Delgado, M.Varela, *Appl. Phys. Lett.* **69**, 620 (1996).
- [160] F.Sanchez, J.L.Morenza, R.Aguiar, J.C.Delgado, M.Varela, *Appl. Phys. A* **66**, 83 (1996).
- [161] A.J.Pedraza, J.D.Fowlkes, D.H.Lowndes, *Appl. Phys. Lett.* **74**, 2322 (1999).
- [162] J.D.Fowlkes, A.J.Pedraza, D.H.Lowndes, *Appl. Phys. Lett.* **77**, 1629 (2000).
- [163] A.A. Evtukh, E.B. Kaganovich, V. G. Litovchenko, Yu.M. Litvin, D.V. Fedin, E.G. Manoilov, S.V. Svechnikov, *Semiconductor Physics, Quantum Electronics & Optoelectronics*, 3(4), 474 (2000).
- [164] A.V. Karabutov, V.D. Frolov, E.N. Loubnin, A.V. Simakin, G.A. Shafeev, *Appl. Phys. A* **76**, 413 (2003) .
- [165] A. V. Karabutov, V. D. Frolov, A. V. Simakin, G. A. Shafeev, *J. Vac. Sci. Technol. B* **21**, 449 (2003).
- [166] T-H.Her, R.J.Finlay, C.Wu, S.Deliwala, E.Mazur, *Appl. Phys. Lett.* **73**, 1673 (1998).
- [167] T-H.Her, R.J.Finlay, C.Wu, E.Mazur, *Appl. Phys. A* **70** 383 (2000).
- [168] C. H. Crouch, J. E. Carey, J. M. Warrender, M. J. Aziz, E. Mazur and F. Y. Genin *Appl. Phys. Lett.* **84**, 1850 (2004).
- [169] K. Seeger and R.E. Palmer, *Appl. Phys. Lett.* **74**, 1627 (1999).
- [170] R. Ortega Martinez, T. R. Verhey, P.K. Boyer, and J.J. Rocca, *J. Vac. Sci. Technol. B* **6**, 1581 (1988).
- [171] Callan, J. P. in *Ultrafast Dynamics And Phase Changes In Solids Excited By. Femtosecond Laser Pulses 59–104 Thesis, Harvard Univ., Cambridge, (2000)*
- [172] A. M. Weiner Femtosecond pulse shaping using spatial light modulators review of scientific instruments vol 77, 5, (2000)
- [173] R. Sattmann, V. Sturm, R. Noll, , *J. Phys., D. Appl. Phys.* **28**, 2181–2187, (1995).

-
- [174] A.C. Forsman, P.S. Banks, M.D. Perry, E.M. Campbell, A.L. Dodell, M.S. Armas, , J. Appl. Phys. **98**, (033202(1–6)) (2005).
- [175] D.E. Roberts, A. du Plessis, L.R. Botha, Appl. Surf. Sc. **256**, 1784-1792, (2010).
- [176] A. Semerok, C. Dutouquet,, Thin Solid Films **453–454**, 501–505, (2004).
- [177] M. E. Povarnitsyn, T. E. Itina, K. V. Khishchenko, P. R. Levashov, Phys. Rev. Lett. **104**, 059902(E) (2010)
- [178] M. E. Povarnitsyn, T. E. Itina, P. R. Levashov, K. V. Khishchenko, appl surf. Sc. **257**, 5168-5171, (2011).
- [179] A. Klini, P. A. Loukakos, D. Gray, A. Manousaki, and C. Fotakis Optics Express, **16**,. 11300-11309 (2008)
- [180] D. Agassi, Journal of Applied Physics **55**, 4376. (1984).
- [181] A. Semerok, C. Dutouquet,, Thin Solid Films **453–454**, 501–505, (2004).
- [182] F. Korte, S. Nolte, B. N. Chichkov, T. Bauer, G. Kamlage, T. Wagner, C. Fallnich, and H. Welling, "Far-field and near-field material processing with femtosecond laser pulses," Appl Phys a-Mater 69, S7-S11 (1999).
- [183] Bauerle 2011
- [184] S. Kawata, H. B. Sun, T. Tanaka, and K. Takada, "Finer features for functional microdevices -Micromachines can be created with higher resolution using two-photon absorption., " Nature 412, 697-698 (2001).
- [185] M. Deubel, G. Von Freymann, M. Wegener, S. Pereira, K. Busch, and C. M. Soukoulis, "Direct laser writing of three-dimensional photonic-crystal templates for telecommunications," Nat Mater 3, 444-447 (2004).
- [186] M. Huang, F. L. Zhao, Y. Cheng, N. S. Xu, and Z. Z. Xu, "Origin of Laser-Induced Near-Subwavelength Ripples: Interference between Surface Plasmons and Incident Laser," Acs Nano 3, 4062-4070 (2009).
- [187] E. V. Barmina, E. Stratakis, K. Fotakis, and G. A. Shafeev, "Generation of nanostructures on metals by laser ablation in liquids: new results," Quantum Electron+ 40, 1012-1020 (2010).
- [188] A. Y. Vorobyev, V. S. Makin, and C. L. Guo, "Periodic ordering of random surface nanostructures induced by femtosecond laser pulses on metals," J Appl Phys 101 (2007).
- [189] J. Bonse, H. Sturm, D. Schmidt, and W. Kautek, "Chemical, morphological and accumulation phenomena in ultrashort-pulse laser ablation of TiN in air," Appl Phys a-Mater 71, 657-665 (2000).
- [190] Y. Shimotsuma, P. G. Kazansky, J. R. Qiu, and K. Hirao, "Self-organized nanogratings in glass irradiated by ultrashort light pulses," Physical Review Letters 91 (2003).
- [191] M. Bolle, and S. Lazare, "Characterization of Submicrometer Periodic Structures Produced on Polymer Surfaces with Low-Fluence Ultraviolet-Laser Radiation," J Appl Phys 73, 3516-3524 (1993).
- [192] M. Olbrich, E. Rebollar, J. Heitz, I. Frischauf, and C. Romanin, "Electroporation chip for adherent cells on photochemically modified polymer surfaces," Appl Phys Lett 92 (2008).
- [193] A. Y. Vorobyev, V. S. Makin, and C. L. Guo, "Brighter Light Sources from Black Metal: Significant Increase in Emission Efficiency of Incandescent Light Sources," Physical Review Letters 102 (2009).

-
- [194] R. Stoian, M. Boyle, A. Thoss, A. Rosenfeld, G. Korn, I. V. Hertel, and E. E. B. Campbell, "Laser ablation of dielectrics with temporally shaped femtosecond pulses," *Appl Phys Lett* 80, 353-355 (2002).
- [195] M. Huang, F. L. Zhao, Y. Cheng, N. S. Xu, and Z. Z. Xu, "Origin of Laser-Induced Near-Subwavelength Ripples: Interference between Surface Plasmons and Incident Laser," *Acs Nano* 3, 4062-4070 (2009).
- [196] R. Stoian, A. Mermillod-Blondin, S. W. Winkler, A. Rosenfeld, I. V. Hertel, M. Spyridaki, E. Koudoumas, P. Tzanetakis, C. Fotakis, I. M. Burakov, and N. M. Bulgakova, "Temporal pulse manipulation and consequences for ultrafast laser processing of materials," *Opt Eng* 44 (2005).
- [197] A. Klini, P. A. Loukakos, D. Gray, A. Manousaki, and C. Fotakis, "Laser Induced Forward Transfer of metals by temporally shaped femtosecond laser pulses," *Opt Express* 16, 11300-11309 (2008).
- [198] A. C. Forsman, P. S. Banks, M. D. Perry, E. M. Campbell, A. L. Dodell, and M. S. Armas, "Double-pulse machining as a technique for the enhancement of material removal rates in laser machining of metals," *J Appl Phys* 98 (2005).
- [199] M. E. Povarnitsyn, T. E. Itina, K. V. Khishchenko, and P. R. Levashov, "Suppression of Ablation in Femtosecond Double-Pulse Experiments (vol 103, art no 195002, 2009)," *Physical Review Letters* 104 (2010).
- [200] V. Schmidt, W. Husinsky, and G. Betz, "Ultrashort laser ablation of metals: pump-probe experiments, the role of ballistic electrons and the two-temperature model," *Appl Surf Sci* 197, 145-155 (2002).
- [201] 20. A. Semerok, and C. Dutouquet, "Ultrashort double pulse laser ablation of metals," *Thin Solid Films* 453, 501-505 (2004).
- [202] M. Li, S. Menon, J. P. Nibarger, and G. N. Gibson, "Ultrafast electron dynamics in femtosecond optical breakdown of dielectrics," *Physical Review Letters* 82, 2394-2397 (1999).
- [203] I. H. Chowdhury, X. F. Xu, and A. M. Weiner, "Ultrafast double-pulse ablation of fused silica," *Appl Phys Lett* 86 (2005).
- [204] N. M. Bulgakova, R. Stoian, A. Rosenfeld, I. V. Hertel, and E. E. B. Campbell, "Electronic transport and consequences for material removal in ultrafast pulsed laser ablation of materials," *Phys Rev B* 69 (2004).
- [205] P. F. Carcia, R. S. McLean, and M. H. Reilly, "High-performance ZnO thin-film transistors on gate dielectrics grown by atomic layer deposition," *Appl Phys Lett* 88 (2006).
- [206] R. L. Hoffman, B. J. Norris, and J. F. Wager, "ZnO-based transparent thin-film transistors," *Appl Phys Lett* 82, 733-735 (2003).
- [207] D. K. Hwang, M. S. Oh, J. H. Lim, and S. J. Park, "ZnO thin films and light-emitting diodes," *J Phys D Appl Phys* 40, R387-R412 (2007).
- [208] Q. M. Pan, L. M. Qin, J. Liu, and H. B. Wang, "Flower-like ZnO-NiO-C films with high reversible capacity and rate capability for lithium-ion batteries," *Electrochim Acta* 55, 5780-5785 (2010).
- [209] J. B. Chu, S. M. Huang, D. W. Zhang, Z. Q. Bian, X. D. Li, Z. Sun, and X. J. Yin, "Nanostructured ZnO thin films by chemical bath deposition in basic aqueous ammonia solutions for photovoltaic applications," *Appl Phys a-Mater* 95, 849-855 (2009).

-
- [210] F. Garrelie, J. P. Colombier, F. Pigeon, S. Tonchev, N. Faure, M. Bounhalli, S. Reynaud, and O. Parriaux, "Evidence of surface plasmon resonance in ultrafast laser-induced ripples," *Opt Express* 19, 9035-9043 (2011).
- [211] M. Huang, F. L. Zhao, Y. Cheng, N. S. Xu, and Z. Z. Xu, "Origin of Laser-Induced Near-Subwavelength Ripples: Interference between Surface Plasmons and Incident Laser," *Acs Nano* 3, 4062-4070 (2009).
- [212] F. Garrelie, J. P. Colombier, F. Pigeon, S. Tonchev, N. Faure, M. Bounhalli, S. Reynaud, and O. Parriaux, "Evidence of surface plasmon resonance in ultrafast laser-induced ripples," *Opt Express* 19, 9035-9043 (2011).
- [213] D. Dufft, A. Rosenfeld, S. K. Das, R. Grunwald, and J. Bonse, "Femtosecond laser-induced periodic surface structures revisited: A comparative study on ZnO," *J Appl Phys* 105 (2009).
- [214] M. Huang, F. L. Zhao, Y. Cheng, N. S. Xu, and Z. Z. Xu, "Origin of Laser-Induced Near-Subwavelength Ripples: Interference between Surface Plasmons and Incident Laser," *Acs Nano* 3, 4062-4070 (2009).
- [215] Wood, R. W, "On a remarkable case of uneven distribution of light in a diffraction grating spectrum." *Philosophical magazine* 4, 396-402, (1902).
- [216] C. B. Li, D. H. Feng, T. Q. Jia, H. Y. Sun, X. X. Li, S. Z. Xu, X. F. Wang, and Z. Z. Xu, "Ultrafast dynamics in ZnO thin films irradiated by femtosecond lasers," *Solid State Commun* 136, 389-394 (2005).
- [217] M. A. M. Versteegh, T. Kuis, H. T. C. Stoof, and J. I. Dijkhuis, "Ultrafast screening and carrier dynamics in ZnO: Theory and experiment," *Phys Rev B* 84 (2011)
- [218] Furthermore theoretical (M. A. M. Versteegh, T. Kuis, H. T. C. Stoof, and J. I. Dijkhuis, "Ultrafast screening and carrier dynamics in ZnO: Theory and experiment," *Phys Rev B* 84 (2011).
- [219] E. Koudoumas, M. Spyridaki, R. Stoian, A. Rosenfeld, P. Tzanetakis, I. V. Hertel, and C. Fotakis, "Influence of pulse temporal manipulation on the properties of laser ablated Si ion beams," *Thin Solid Films* 453, 372-376 (2004).
- [220] R. Stoian, M. Boyle, A. Thoss, A. Rosenfeld, G. Korn, and I. V. Hertel, "Dynamic temporal pulse shaping in advanced ultrafast laser material processing," *Appl Phys a-Mater* 77, 265-269 (2003).
- [221] M. E. Povarnitsyn, T. E. Itina, K. V. Khishchenko, and P. R. Levashov, "Suppression of Ablation in Femtosecond Double-Pulse Experiments," *Physical Review Letters* 103 (2009).
- [222] A. Borowiec, and H. K. Haugen, *Appl Phys Lett* **82**, 4462-4464 (2003).
- [223] A.Y. Vorobyev, V.S. Makin, and C. Guo *J. Appl. Phys.* **101**, 034903, (2007)
- [224] L. Qi, K. Nishii,² and Y. Namba *Optics let.*, 34, 12 (2009)
- [225] M. Huang, F. L. Zhao, Y. Cheng, N. S. Xu, and Z. Z. Xu, *ACS Nano* **3**, 4062 (2009).
- [226] R. Gomer, *Field Emission and Field Ionization* (Harvard University Press, Massachusetts, US, 1961)
- [227] F. Causa, P.A. Netti, L. Ambrosio, *Biomaterials*, **28**, 5093, (2007)

-
- [228] D. Falconnet, G. Csucs, H.M. Grandin, M. Textor, *Biomaterials*, **27**, 3044, (2006)
- [229] L. Cen, W. Liu, L. Cui, W.J. Zhang, Y.L. Cao, *Pediatric Res* **63**,492, (2008)
- [230] A. Kurella, N.B. Dahotre, Review paper. *J Biomater Appl*, **20**, 5,(2005).
- [231] D. Temple, *Mater. Sci. Eng. R.* **24** (1999) 185
- [232] T.Utsumi. *IEEE Trans. Electron. Dev.* **38** (1991) 2276.
- [233] R. H. Reuss, B. R. Chalamala, *J. Vac. Sci. Technol. B* **21** (2003) 1187.
- [234] D. G. Pflug, PhD Thesis at MIT “Low Voltage Field Emitter Arrays through Aperture Scaling” (2000).
- [235] W. P. Dyke, J. K. Trolan, W. W. Dolan, G. Barnes, *Appl. Phys.* **24**, 570 (1953)
- [236] Y. Endo, I. Honjo S. Goto, *J. Vac. Sci. Technol. B* **16** (1998) 3082.
- [237] T.Utsumi. *IEEE Trans. Electron. Dev.* **38**, 2276 (1991).
- [238] K. Grossman and M. Peckecar, *Nanotechnology* **5** (1994) 179.
- [239] A. E. Ennos, *Br. J. Appl. Phys.* **5** (1954) 27.
- [240] C. A. Spindt, I. Brodie, L. Humphrey and E.R Westerberg, *J. Appl. Phys.* **47**, 5248, (1976).
- [240] S. Yamamoto, *Rep. Prog. Phys.* **69**, 181, (2006).
- [241] S. Yamamoto, *Rep. Prog. Phys.* **69**, 181, (2006).
- [242] J. Ishikawa, H. Tsuji , Y. Gotoh, T. Sasaki, T. Kaneko, M. Nagao and K. Inoue *J. Vac. Sci. Technol. B* **11**, 403 (1993).
- [243] M. Ding, H. Kim, and A. I. Akinwande, *Appl. Phys. Lett* **75**, 823 (1999)
- [244] S. Johnson, A. Markwitz, M. Rudolphi, H. Baumann, S.P. Oei, K.B.K Teo and W.I. Milne, *Appl. Phys. Lett.* **85**, 3277 (2004).
- [245] K.C.Kao and H. Hwang, *Electrical Transport in Solids* (Pergamon, London, 1981) p.150.
- [246] K.C.Kao and H. Hwang, *Electrical Transport in Solids* (Pergamon, London, 1981) p.150.
- [247] D. Temple, *Mater. Sci. Eng. R.* **24**, 185 (1999).
- [248] Y. Endo, I. Honjo and S. Goto, *J. Vac. Sci. Technol. B* **16**, 3082 (1998).
- [249] W. Wurker, J. Roy and J. Hesse, *Mat. Res. Bull.* **9**, 971 (1974).
- [250] S.M. Sze, *Physics of Semiconductor Devices* (Wiley, New York, 1981) p. 68.

-
- [251] A.V. Karabutov, V.D. Frolov, E.N. Loubnin, A.V. Simakin and G.A. Shafeev, *Appl. Phys. A* **76**, 413 (2003).
- [252] Y. Endo, I. Honjo and S. Goto, *J. Vac. Sci. Technol. B* **16**, 3082 (1998).
- [253] Y. Wei, B. R. Chalamala, B.G. Smith, C.W. Penn, *J. Vac. Sci. Technol. B* **17**, 233 (1999).
- [254] Y. H. Wu, P. W. Qiao, T. C. Chong, and Z. X. Shen, *Adv. Mater.* **14**, 64, (2002).
- [255] H. Hiraki, A. Hiraki, N. Jiang, and H. X. Wang, *J. Korean Phys. Soc.* **49**, 1276, (2006).
- [256] C. Li, G. Fang, L. Yuan, N. Liu, L. Ai, Q. Xiang, D. Zhao, C. Pan, and X. Zhao, *Nanotechnology* **18**, 155702 (2007).
- [257] A. T. H. Chuang, J. Robertson, B. O. Boskovic, and K. K. K. Koziol, *Appl. Phys. Lett.* **90**, 123107 (2007).
- [258] Th. Dikonimos, L. Giorgi, R. Giorgi, N. Lisi, E. Salernitano, and R. Rossi, *Diamond Relat. Mater.* **16**, 1240 (2007).
- [259] V. Zorba, P. Tzanetakis, C. Fotakis, E. Spanakis, E. Stratakis, D. G. Papazoglou, and I. Zergioti, *Appl. Phys. Lett.* **88**, 081103, (2006).
- [260] E. Stratakis, E. Kymakis, E. Spanakis, P. Tzanetakis, and E. Koudoumas, *Phys. Chem. Chem. Phys.* **11**, 703 (2009).
- [261] E. Minoux, O. Groening, K. B. K. Teo, S. H. Dalal, L. Gangloff, J.-P. Schnell, L. Hudanski, I. Y. Y. Bu, P. Vincent, P. Legagneux, G. A. J. Amaratunga, and W. I. Milne, *Nano Lett.* **5**, 2135, (2005).
- [262] W. J. Zhao, W. Rochanachivapar, and M. Takai, *J. Vac. Sci. Technol. B* **22**, 1315 (2004).
- [263] S. Wang, J. Wang, P. Miraldo, M. Zhu, R. Outlaw, K. Hou, X. Zhao, B. C. Holloway, D. Manos, T. Tyler, O. Shenderova, M. Ray, J. Dalton, and G. McGuire, *Appl. Phys. Lett.* **89**, 183103, (2006).
- [264] A. Modinos, *Field, Thermionic, and Secondary Electron Emission Spectroscopy* Plenum, New York, (1984).
- [265] V. V. Zhirmov, E. I. Givargizov, and P. S. Plekhanov, *J. Vac. Sci. Technol. B* **13**, 418, (1995).
- [266] J. M. Bonard, N. Weiss, H. Kind, T. Stockli, L. Forro, K. Kern, and A. Chatelain, *Adv. Mater.* **13**, 184, (2001).
- [267] T. Utsumi, *IEEE Trans. Electron Devices* **38**, 2276, (1991).
- [268] L. Nilsson, O. Groening, C. Emmenegger, O. Kuettel, E. Schaller, L. Schlapbach, H. Kind, J. M. Bonard, and K. Kern, *Appl. Phys. Lett.* **76**, 2071, (2000).
- [269] F. H. Read and N. J. Bowring, *Nucl. Instrum. Methods Phys. Res. A* **519**, 305, (2004).
- [270] J. M. Bonard, N. Weiss, H. Kind, T. Stockli, L. Forro, K. Kern, and A. Chatelain, *Adv. Mater.* **13**, 184, (2001).
- [271] J. M. Bonard, N. Weiss, H. Kind, T. Stockli, L. Forro, K. Kern, and A. Chatelain, *Adv. Mater.* **13**, 184, (2001).

-
- [272] M.A. Cohen Stuart, W.T.S. Huck, J. Genzer, M. Müller, C. Ober, M. Stamm, G.B. Sukhorukov, I. Szleifer, V.V. Tsukruk, M. Urban, F. Winnik, S. Zauscher, I. Luzinov, S. Minko, *Nat. Mater.* 2010, **9**, 101.
- [273] B. Zhao, J. S. Moore, D. J. Beebe, *Science*, **291**, 1023, (2001).
- [274] D.J. Beebe, J.S. Moore, Q. Yu, R.H. Liu, M.L. Kraft, B.-H. Jo, C. Devadoss, *Proc. Natl. Acad. Sci. U.S.A.*, **97**, 13488, (2000).
- [275] D.A. LaVan, T. McGuire, R. Langer, *Nat. Biotechnol.*, **21**, 1184-1191, (2003)
- [276] K. Christian, H. Andreas, S. Wolfgang, *Anal. Chem.*, **74**, 355, (2002).
- [277] I. Roy, M.V.S. Rao, M.N. Gupta, *Biotechnol. Appl. Biochem.*, **37**, 9, (2003).
- [278] J.-I. Edahiro, K. Sumaru, Y. Tada, K. Ohi, T. Takagi, M. Kameda, T. Shinbo, T. Kanamori, Y. Yoshimi, *Biomacromolecules*, **6**, 970, (2005).
- [279] I. Tokarev and S. Minko, *Adv. Mater.*, **21**, 241, (2009).
- [280] C. M. Ruan, K. G. Ong, C. Mungle, M. Paulose, N. J. Nickl, C. A. Grimes, *Sens. Actuators B*, **96**, 61, (2003).
- [281] R. Blossey, *Nat. Mater.*, **2**, 301, (2003).
- [282] T. P. Russell, *Science*, **297**, 964, (2002).
- [283] S. H. Anastasiadis, H. Retsos, S. Pispas, N. Hadjichristidis, S. Neophytides, *Macromolecules*, **36**, 1994, (2003).
- [284] W. Jiang, G. Wang, Y. He, X. Wang, Y. An, Y. Song, L. Jiang, *Chem. Commun.*, **28**, 3550, (2005).
- [285] Athanassiou, M. I. Lygeraki, D. Pisignano, K. Lakiotaki, M. Varda, C. Fotakis, R. Cingolani, S. H. Anastasiadis, *Langmuir*, **22**, 2329, (2006).
- [286] A T. N. Krupenkin, J. A. Taylor, E. N. Wang, P. Kolodner, M. Hodes, T. R. Salamon, *Langmuir*, **23**, 9128, (2007).
- [287] P. F. Xia, Y. Zhu, L. Feng, L. Jiang, *Soft Matter*, **5**, 275, (2009).
- [288] P. Roach, N. J. Shirtcliffe, M. I. Newton, *Soft Matter*, **4**, 224, (2008).
- [289] X. Zhang, F. Shi, J. Niu, Y. G. Jiang and Z. Q. Wang, *J. Mater. Chem.*, **18**, 621, (2008).
- [290] F. Xia, L. Jiang, *Adv. Mater.*, **20**, 2842, (2008).

-
- [291] W. Barthlott, C. Neinhuis, *Planta*, **202**, 1, (1997).
- [292] W. Lee, M. K. Jin, W. C. Yoo, J. K. Lee, *Langmuir* **20**, 7665 (2004).
- [293] G. S. Watson, J.A. Watson: *Appl. Surf. Sci.* **235**, 139 (2004).
- [294] T. L. Sun, L. Feng, C. F. Gao, L. Jiang, *Acc. Chem. Res.*, **38**, 644, (2005).
- [295] X.-M. Li, D. Reinhoudt, M. Crego-Calama, *Chem. Soc. Rev.*, **36**, 1350, (2007).
- [296] D. Quéré, *Rep. Prog. Phys.*, **68**, 2495, (2005).
- [297] J.-Y. Shiu, C.-W. Kuo, P. Chen C.-Y. Mou : *Chem. Mater.* **16**, 561 (2004).
- [298] P. N. Bartlett, J. J. Baumberg, P. R. Birkin, M. A. Ghanem, M. C. Netti: *Chem. Mater.* **14**, 2199 (2002).
- [299] I. Woodward, W. C. E. Schofield, V. Roucoules, J. P. S. Badyal: *Langmuir* **19**, 3432 (2003).
- [300] V. Zorba, L. Persano, D. Pisignano, A. Athanassiou, E. Stratakis, R. Cingolani, P. Tzanetakis, C. Fotakis: *Nanotechnology* **17**, 3234 (2006).
- [301] N. S. Murthy, R. D. Prabhu, J. J. Martin, L. Zhou, , R. L Headrick.: *J. Appl. Phys.* **100**, 023528 (2006).
- [302] D. Bäuerle: *Laser Processing and Chemistry*. (Springer, Berlin 2000).
- [303] S.I. Dolgaev, S.V. Lavrishev, A.A. Lyalin, A.V. Simakin, V.V. Voronov, G.A. Shafeev: *Appl. Phys. A* **73**, 177 (2001).
- [304] P.G. De Gennes, *Rev. Mod. Phys.* **57**, 827 (1985).
- [305] L. Leger, J.F. Joanny, *Rep. Prog. Phys.* **55**, 431 (1992).
- [306] R. N. Wenzel, *Ind. Eng. Chem.* **28**, 988 (1936).
- [307] Cassie ABD, Baxter S. *Trans Faraday Soc* 1944;40:546.
- [308] A. Lafuma, D. Quere, *Nat. Mater.* **2**, 457 (2003)
- [309] M. Morita, T. Ohmi, E. Hasegawa, M. Kawakami, K. Suma, *Appl.Phys.Lett.* **55**, 562 (1989).
- [310] H. Shimizu, C. Munakata, *Semicond.Sci.Technol.* **5**, 842 (1990).
- [311] D. Richard, C. Clanet, D. Quere, *Nature*, **417**, 811, (2002)
- [312] D. Richard, D. Quere, *Europhys. Lett.*, **48**, 286 (1999)
- [313] W. Barthlott, C. Neinhuis, *Planta*, **202**, 1,(1997)

-
- [314] V. Zorba, P. Tzanetakis, C. Fotakis, E. Spanakis, E. Stratakis, D. G. Papazoglou, I. Zergioti, *Appl. Phys. Lett.*, **88**, 081103, (2006)
- [315] T.-H. Her, R. J. Finlay, C. Wu, S. Deliwala, E. Mazur, *Appl. Phys. Lett.*, **73**, 1673, (1998)
- [316] D. Bäuerle in *Laser Processing and Chemistry*, Springer, Berlin, 2000.
- [317] N. S. Murthy, R. D. Prabhu, J. J. Martin, L. Zhou, R. L. J. Headrick, *Appl. Phys. A*, **100**, 023528 (2006).
- [318] A. Bensaoula, C. Boney, A. Pillai, G. A. Shafeev, A. V. Simakin, D. Starikov, *Appl. Phys. A*, **79**, 973, (2004).
- [319] S. R. Wasserman, Y.-T. Tao, G. M. Whitesides, *Langmuir*, **5**, 1074, (1989)
- [320] W. R. Ashurst, C. Carraro, R. Maboudian *IEEE Transactions on device and materials reliability*, **3**, 173 (2003)
- [321] D. Richard, D. Quere, *Europhys. Lett.*, **50**, 769, (2000).
- [322] D. Richard, D. Quere, *Europhys. Lett.* 2000, 50, 769.
- [323] A.-L. Biance, F. Chevy, C. Clanet, G. Lagubeau, D. Quere, *J. Fluid Mech.*, **554**, 47, (2006)
- [324] P. G. de Gennes, *Rev. Mod. Phys.*, **57**, 827, (1985)
- [325] M. Reyssat, A. Pepin; A. Marty, Y. Chen, D. Quere, *Europhys. Lett.*, **74**, 306, (2006)
- [326] D. Bartolo, F. Bouamrine, E. Verneuil, A. Buguin, P. Silberzan, S. Moulinet, *Europhys. Lett.*, **74**, 299, (2006)
- [327] R. Mukhopadhyay, *Anal. Chem.*, **78**, 1401, (2006).
- [328] F. Mugele, J.-C. J. Baret, *Phys.: Condens. Matter*, **17**, R705, (2005).
- [329] H. H. Girault, *Nat. Mater.*, **5**, 851, (2006).
- [330] M. G. Pollack, A. D. Shenderov, R. B. Fair, *Lab Chip*, **2**, 96, (2002).
- [331] J. S. Kuo, P. Spicar-Mihalic, I. Rodriguez, D. T. Chiu, *Langmuir*, **19**, 250, (2003).
- [332] H. Ren, R. B. Fair, M. G. Sens Pollak, *Actuators B*, **98**, 319, (2004).
- [333] J. Fowler, H. Moon, C.-J. Kim, *IEEE 15th Int. Conf. MEMS, Las Vegas, NV*, pp97-100 (2002).
- [334] R. B. Fair, V. Srinivasan, H. Ren, P. Paik, V. K. Pamula, M. G. Pollack, *Technical Digest IEEE International Electron Dev. Meeting*, p 779 (2003).
- [335] V. Srinivasan, V. K. Pamula, R. B. Fair, *Lab Chip*, **4**, 310, (2004).
- [336] S. K. Cho, H. J. Moon, C. J. J. Kim, *Microelectromech. Syst.*, **12**, 70, (2003).
- [337] Fouillet, Y.; Achard, J. L. *C. R. Phys.*, **5**, 577, (2004).

-
- [338] B. Berge, J. Peseux, *Eur. Phys. J. E*, **3**, 159, (2000).
- [339] R. A. Hayes, B. J. Feenstra, *Nature*, **425**, 383, (2003).
- [340] B. R. Acharya, T. Krupenkin, S. Ramachandran, Z. Wang, C. C. Huang, J. A. Rogers, *Appl. Phys. Lett.*, **83**, 4912, (2003).
- [341] J. Lee, C. J. J. Kim, *Microelectromech. Syst.*, **9**, 171, (2000).
- [342] F. Mugele, J.-C. J. Baret, *Phys Condens. Matter*, **17**, R705, (2005).
- [343] A. Torkelli, Ph.D. Thesis; Helsinki University of Technology: Helsinki, 2004.
- [344] T. Nishino, M. Meguro, K. Nakamae, M. Matsushita, Y. Ueda, *Langmuir*, **15**, 4321, (1999).
- [345] D. L. Herbertson, C. R. Evans, N. J. Shirtcliffe, G. McHale, M. I. Newton, *Sens. Actuators, A*, **130-131**, 189–193 (2006).
- [346] T. N. Krupenkin, J. A. Taylor, T.M. Schneider, S. Yang, *Langmuir*, **20**, 3824–3827, (2004).
- [347] M. S. Dhindsa, N. R. Smith, J. Heikenfeld, P. D. Rack, J. D. Fowlkes, M. J. Doktycz, A. V. Melechko, M. L. Simpson, *Langmuir*, **22**, 9030–9034, (2006).
- [348] N. Verplanck, E. Galopin, J. C. Camart, V. Thomy, Y. Coffinier, R. Boukherroub, *Nano Lett.*, **7**, 813, (2007).
- [349] P. Brunet, F. Lapierre, V. Thomy, Y. Coffinier, R. Boukherroub, *Langmuir*, **24**, 11203, (2008).
- [350] T. N. Krupenkin, J. A. Taylor, T.M. Schneider, S. Yang, *Langmuir*, **20**, 3824–3827, (2004).
- [351] N. Verplanck, E. Galopin, J. C. Camart, V. Thomy, Y. Coffinier, R. Boukherroub, *Nano Lett.*, **7**, 813, (2007).
- [352] S. R. Wasserman, Y.-T. Tao, G. M. Whitesides, *Langmuir*, **5**, 1074, (1989).
- [353] W. R. Shurst, C. Carraro, R. Maboudian, *IEEE Trans. Device Mater. Reliab.*, **3**, 173, (2003).
- [354] V. Zorba, E. Stratakis, M. Barberoglou, E. Spanakis, P. Tzanetakis, C. Fotakis, *Appl. Phys. A*: **93**, 819–825, (2007).
- [355] M. Vallet, M. Vallade, B. Berge, *Euro. Phys. J. B*, **11**, 583, (1999).
- [356] B. Shapiro, H. Moon, R.L. Garrell, C.J. Kim, C. J.; *J. App. Phys.*, **93**, 5794, (2003)
- [357] D. Klarman, D. Andelman, and M. Urbakh, "A Model of Electrowetting, Reversed Electrowetting, and Contact Angle Saturation," *Langmuir* **27**, 6031-6041, (2011).
- [358] V. Peykov, A. Quinn, J. J. Ralston, *Colloid Polym. Sci.*, **278**, 789, (2000).
- [359] H. J. J. Verheijen, M. W. J. Prins, *Langmuir*, **15**, 6616, (1999).
- [360] J. Lin, G. Lee, Y. Chang, K. Lien, *Langmuir*, **22**, 484, (2006).
- [361] M. Vallet, M. Vallade, B. Berge, *Eur. Phys. J. B*, **11**, 583, (1999).

-
- [362] B. Shapiro, R. L. Moon, R. L. Garell, C.-J. J. Kim, *Appl. Phys.*, **93**, 5794, (2003).
- [363] A.G. Papathanasiou, A.G. Boudouvis, *Appl. Phys. Lett.*, **86**, 164102, (2005).
- [364] R. N. Wenzel, *Ind. Eng. Chem.*, **28**, 988, (1936).
- [365] A. B. D. Cassie, S. Baxter, *Trans. Faraday. Soc.*, **40**, 546, (1944).
- [366] D. Quere, *Rep. Prog. Phys.*, **68**, 2495, (2005).
- [367] N. A. Patankar, *Langmuir*, **20**, 8209, (2004).
- [368] B. Bhushan, M. Nosonovsky, Y. C. J. R. Jung, *Soc. Interface*, **4**, 643, (2007).
- [369] P. Brunet, F. Lapierre, V. Thomy, Y. Coffinier, R. Boukherroub, *Langmuir*, **24**, 11203, (2008).
- [370] M. Reyssat, A. Pepin, A. Marty, Y. Chen, D. Quere, *Europhys. Lett.*, **74**, 306, (2006).
- [371] E. Stratakis, N. Misra, E. Spanakis, D. J. Hwang, C. P. Grigoropoulos, C. Fotakis, P. Tzanetakis, *Nano Lett.*, **8**, 1949, (2008).
- [372] M. Nafria, J. Sune, X. J. Aymerich, *Appl. Phys.*, **73**, 205, (1993).
- [373] E. Stratakis, N. Misra, E. Spanakis, D. J. Hwang, C. P. Grigoropoulos, C. Fotakis, P. Tzanetakis, *Nano Lett.*, **8**, 1949, (2008).
- [374] M. Nafria, J. Sune, X. J. Aymerich, *Appl. Phys.*, **73**, 205, (1993).
- [375] F. Lapierre, V. Thomy, Y. Coffinier, R. Blossey, R. Boukherroub, *Langmuir*, **24**, 11203, (2008).
- [376] G. McHale, N. J. Shirtcliffe, M. I. Newton, *Langmuir*, **20**, 10146–10149, (2004).
- [377] D. Richard, D. Quere, *Europhys. Lett.*, **48**, 286, (1999).
- [378] V. Zorba, E. Stratakis, M. Barberoglou, E. Spanakis, P. Tzanetakis, S. H. Anastasiadis, C. Fotakis, *Adv. Mater.*, **20**, 4049, (2008).
- [379] D. Bartolo, F. Bouamrine, E. Verneuil, A. Buguin, P. Silberzan, S. Moulinet, *Europhys. Lett.*, **74**, 299, (2006).
- [380] R. E. Johnson, R. H. J. Dettre, *Phys. Chem.*, **68**, 1744, (1964).
- [381] C. G. L. J. Furmidge, *Colloid Sci.*, **17**, 309, (1962).
- [382] M. Reyssat, A. Pepin, A. Marty, Y. Chen, D. Quere, *Europhys. Lett.*, **74**, 306, (2006).
- [383] G. M. Whitesides, *Nature*, **442**, 368, (2006).
- [384] O. D. Velev, B. G. Prevo, K. H. Bhatt, *Nature*, **426**, 515, (2003).
- [385] N. Verplanck, Y. Coffinier, V. Thomy, R. Boukherroub, *Nanoscale Res. Lett.*, **2**, 577, (2007).

-
- [386] V. Zorba, E. Stratakis, M. Barberoglou, E. Spanakis, P. Tzanetakakis, S. H. Anastasiadis, C. Fotakis, *Adv. Mater.*, **20**, 4049, (2008).
- [387] X. Feng, L. Feng, M. Jin, J. Zhai, L. Jiang, D. J. Zhu, *Am. Chem. Soc.*, **126**, 62, (2004).
- [388] X. Feng, J. Zhai, L. Angew. Jiang, *Chem., Int. Ed.*, **44**, 5115, (2005).
- [389] G. Kenanakis, E. Stratakis, K. Vlachou, D. Vernardou, E. Koudoumas, N. Katsarakis, *Appl. Surf. Sci.*, **254**, 5695, (2008).
- [390] E. L. Papadopoulou, M. Varda, K. Kouroupis-Agalou, M. Androulidaki, E. Chikoidze, P. Galtier, G. Huyberechts, E. Aperathitis, *Thin Solid Films*, **516**, 8141, (2008).
- [391] V. Rico, C. Lopez, A. Borrás, J. P. Espinos, A. R. Gonzalez-Elipé, *Sol. Energy Mater. Sol. Cells*, **90**, 2944, (2006).
- [392] V. Zorba, E. Stratakis, M. Barberoglou, E. Spanakis, P. Tzanetakakis, C. Fotakis, *Appl. Phys. A*, **93**, 819, (2008).
- [393] V. Zorba, E. Stratakis, M. Barberoglou, E. Spanakis, P. Tzanetakakis, C. Fotakis, *Appl. Phys. A*, **93**, 819, (2008).
- [394] M. Nosonovsky, B. Bhushan, *Microelectron. Eng.*, **84**, 382, (2007).
- [395] G. Kenanakis, E. Stratakis, K. Vlachou, D. Vernardou, E. Koudoumas, N. Katsarakis, *Appl. Surf. Sci.*, **254**, 5695, (2008).
- [396] M. Nosonovsky, B. Bhushan, *Microelectron. Eng.*, **84**, 382, (2007).
- [397] M. Nosonovsky, B. Bhushan, *Ultramicroscopy*, **107**, 969, (2007).
- [398] N. A. Patankar, *Langmuir*, **20**, 8209, (2004).
- [399] S. Shibuichi, T. Onda, N. Satoh, K. J. Tsujii, *Phys. Chem.*, **100**, 19512, (1996).
- [400] N. Verplanck, Y. Coffinier, V. Thomy, R. Boukherroub, *Nanoscale Res. Lett.*, **2**, 577, (2007).
- [401] A. Lafuma, D. Quere, *Nat. Mater.*, **2**, 457, (2003).
- [402] M. Sbragaglia, A. M. Peters, C. Pirat, B. M. Borkent, R. G. H. Lammertink, M. Wessling, D. Lohse, *Phys. Rev. Lett.*, **99**, 15601, (2007).
- [403] E. Bormashenko, R. Pogreb, G. Whyman, M. Erlich, *Langmuir*, **23**, 6501, (2007).
- [404] C. Dorner, J. Ruhe, *Langmuir*, **23**, 3820, (2007).
- [405] E. Spanakis, E. Stratakis, P. Tzanetakakis, H. Fritzsche, S. Guha, J. Yang, *J. Non-Cryst. Solids* **299–302**, 521, (2002).
- [406] R. Sun, A. Nakajima, A. Fujishima, T. Wanatabe, K. J. Hashimoto, *Phys. Chem. B*, **105**, 1984, (2001).

- [407] M. Miyauchi, N. Kieda, S. Hishita, T. Mitsuhashi, A. Nakajima, T. Watanabe, K. Hashimoto, *Surf. Sci.*, **511**, 401, (2002).
- [408] M. Miwa, A. Nakajima, A. Fujishima, K. Hashimoto, T. Watanabe, *Langmuir*, **16**, 5754, (2000).
- [409] N. J. Shirtcliffe, G. McHale, M. I. Newton, G. Chabrol, C. C. Perry, *Adv. Mater.*, **6**, 1929, (2004).
- [410] V. Zorba, E. Stratakis, M. Barberoglou, E. Spanakis, P. Tzanetakis, S. H. Anastasiadis, C. Fotakis, *Adv. Mater.*, **20**, 4049, (2008).
- [411] M. Callies, D. Quéré, *Soft Matter*, **1**, 55, (2005).
- [412] D. Quéré, *Ann. Rev. Mater. Res.*, **38**, 71, (2008).
- [413] C. W. Extrand, *Langmuir*, **18**, 7991, (2002).
- [414] F. Xia, H. Ge, Y. Hou, T. Sun, L. Chen, G. Z. Zhang, L. Jiang, *Adv. Mater.*, **19**, 2520, (2007).
- [415] F. Xia, L. Feng, S. Wang, T. Sun, W. Song, W. Jiang, L. Jiang, *Adv. Mater.*, **18**, 432, (2006).
- [416] Q. Jiang, F. Xia, T. Sun, W. Song, T. Zhao, M. Liu, L. Jiang, *Chem. Commun.*, **31**, 1199, (2008).
- [417] R. E. Johnson Jr., R. H. Dettre, *Adv. Chem. Ser.*, **43**, 112, (1964).
- [418] R. E. Johnson Jr., R. H. Dettre, *J. Phys. Chem.*, **68**, 1744, (1964).
- [419] F. Causa, P.A. Netti, L. Ambrosio, "A multi-functional scaffold for tissue regeneration: the need to engineer a tissue analogue" *Biomaterials*, **28**, 5093, (2007).
- [420] D. Falconnet, G. Csucs, H.M. Grandin, M. Textor, "Surface engineering approaches to micropattern surfaces for cell-based assays." *Biomaterials*, **27**, 3044, (2006).
- [421] D.W. Hutmacher, "Scaffolds in tissue engineering bone and cartilage." *Biomaterials*, **21**, 2529, (2000).
- [422] L. Cen, W. Liu, L. Cui, W.J. Zhang, Y.L. Cao, "Collagen tissue engineering: development of novel biomaterials and applications." *Pediatric Res*, **63**, 492, (2008).
- [423] A. Kurella, N.B. Dahotre, "Review paper: surface modification for bioimplants: the role of laser surface engineering." *J. Biomater. Appl.*, **20**, 5, (2005).
- [424] M.M Stevens, J.H. George, "Exploring and engineering the cell surface interface." *Science*, **310**, 1135, (2005).
- [425] L.A. Cyster, K.G. Parker, T.L. Parker, D.M. Grant, "The effect of surface chemistry and nanotopography of titanium nitride (TiN) films on 3T3-L1 fibroblasts." *J. Biomed. Mater. Res. Part A*, **67A**, 138, (2003).
- [426] L.A. Cyster, K.G. Parker, T.L. Parker, D.M. Grant. "The effect of surface chemistry and nanotopography of titanium nitride (TiN) films on primary hippocampal neurones." *Biomaterials*, **25**, 97, (2004).

-
- [427] J.Y. Suh, B.C. Jang, X.L. Zhu, J.L. Ong, K. Kim, "Effect of hydrothermally treated anodic oxide films on osteoblast attachment and proliferation." *Biomaterials*, **24**, 347, (2003).
- [428] L. Backman, "Shape changes of the human red-cell studied by aqueous 2-phase partition. " *Febs Lett.* **262**, 107, (1990).
- [429] D.S. Salloum, S.G. Olenych, T.C.S. Keller, J.B. Schlenoff Vascular smooth muscle cells on polyelectrolyte multilayers: hydrophobicity-directed adhesion and growth. *Biomacromolecules*, **6**, 161, (2005).
- [430] R.G. Flemming, C.J. Murphy, G.A. Abrams, S.L. Goodman, P.F. Nealey, "Effects of synthetic micro- and nano-structured surfaces on cell behavior." *Biomaterials* **20**, 573, (1999).
- [431] Teixeira AI, Nealey PF, Murphy CJ. Responses of human keratocytes to micro- and nanostructured substrates. *J. Biomed. Mater Res. Part A*, **71A**, 369, (2004).
- [432] J. Reichert, S. Brukner, H. Bartelt, K.D. Jandt. "Tuning cell adhesion on PTFE surfaces by laser induced microstructures." *Adv Eng Mater.* **9**, 1104, (2007).
- [433] E.J. Lee, J.M. Cuddihy, N. Kotov, "Three-dimensional cell culture matrices: state of the art." *Tissue Eng: Part B*, **14**, 61, (2008).
- [434] S.K. Seidlits, J.Y. Lee, C.E. Schmidt, "Nanostructured scaffolds for neural applications." *Nanomedicine*, **3**, 183, (2008).
- [435] C.H. Choi, S.H. Hagvall, B.M. Wu, J.C.Y. Dunn, R.E. Beygui, C.J. Kim, "Cell interaction with three-dimensional sharp-tip nanotopography." *Biomaterials*, **28**, 1672, (2007).
- [436] Z.W. Ma, M. Kotaki, R. Inai, S. Ramakrishna, "Potential of nanofiber matrix as tissue-engineering scaffolds." *Tissue Eng.*, **11**, 101, (2005).
- [437] G.A. Silva, C. Czeisler, K.L. Niece, E. Beniash, D.A. Harrington, J.A. Kessler, "Selective differentiation of neural progenitor cells by high-epitope density nanofibers." *Science*, **303**, 1352, (2004).
- [438] P. Roach, D. Eglin, K. Rohde, C.C. Perry, "Modern biomaterials: a review-bulk properties and implications of surface modifications." *J. Mater. Sci-Mater Med.*, **18**, 1263, (2007).
- [439] K. Ghosh, D.E. Ingber. "Micromechanical control of cell and tissue development: implications for tissue engineering." *Adv Drug Deliv. Rev.* **59**, 1306, (2007).
- [440] E. Stratakis, A. Ranella, M. Farsari, C. Fotakis. "Laser based micro/nano- engineering for biological applications." *Progr. Quant. Electron.* **33**, 127, (2009).
- [441] F. Grinnell, "Cellular adhesiveness and extracellular substrate." *Int. Rev. Cytol.*, **65**, (1978).
- [442] J.Y. Wong, Leach JB, Brown XQ. Balance of chemistry, topography, and mechanics at the cell–biomaterial interface. Issues and challenges for assessing the role of substrate mechanics on cell response. *Surf. Sci*, **570**, 119, (2004).
- [443] C. Reinhardt, S. Passinger, V. Zorba, B.N. Chichkov, C. Fotakis, "Replica molding of picosecond laser fabricated Si microstructures." *Appl Phys A-Mater Sci Process*, **87**, 673, (2007).

-
- [444] V. Zorba, E. Stratakis, M. Barberoglou, E. Spanakis, P. Tzanetakis, C. Fotakis, "Tailoring the wetting response of silicon surfaces via fs laser structuring." *Appl Phys A-Mater Sci Process* **93**, 819, (2008).
- [445] V. Zorba, E. Stratakis, M. Barberoglou, E. Spanakis, P. Tzanetakis, S.H. Anastasiadis, "Biomimetic artificial surfaces quantitatively reproduce the water repellency of a lotus leaf." *Adv. Mater.* **20**, 4049, (2008).
- [446] M. Barberoglou, V. Zorba, E. Stratakis, E. Spanakis, P. Tzanetakis, S.H. Anastasiadis, "Bio-inspired water repellent surfaces produced by ultrafast laser structuring of silicon." *Appl. Surf. Sci.* **255**, 5425, (2009).
- [447] J.Y. Lim, M.C Shaughnessy, Z.Y. Zhou, H. Noh, E.A. Vogler, H.J. Donahue, "Surface energy effects on osteoblast spatial growth and mineralization." *Biomaterials*, **29**, 1776, (2008).
- [448] A.S. Andersson, F. von Euler A Backhed, A. Richter-Dahlfors, D. Sutherland, B. Kasemo B. Nanoscale features influence epithelial cell morphology and cytokine production. *Biomaterials*, **24**, 3427, (2003).
- [449] J.L. Charest, A.J. Garcia, W.P. King, "Myoblast alignment and differentiation on cell culture substrates with microscale topography and model chemistries." *Biomaterials*, **28**, 2202, (2007).
- [450] M.J. Dalby, M.O. Riehle, D.S. Sutherland, H. Agheli, A.S.G. Curtis, "Changes in fibroblast morphology in response to nano-columns produced by colloidal lithography." *Biomaterials*, **25**, 5415, (2004).
- [451] J.M. Schakenraad, editor. *Biomaterials science*. Academic Press, (1996).
- [452] R.S. Manly, editor, "Adhesion in biological systems." New York: Academic Press; (1970).
- [453] J.M. Schakenraad, H.J. Busscher, C.R.H. Wildevuur, J. Arends, "The influence of substratum surface free-energy on growth and spreading of human-fibroblasts in the presence and absence of serum-proteins." *J. Biomed. Mater. Res.*, **20**, 773, (1986).
- [454] D.E. Ingber, "Cellular tensegrity: defining new rules of biological design that govern the cytoskeleton." *J. Cell Sci.*, **104**, 613, (1993).
- [455] R.N. Wenzel RN. *Ind Eng Chem*, **28**, 988, (1936).
- [456] A.B.D. Cassie, S. Baxter S. *Trans. Faraday Soc.*, **40**, 546, (1944).
- [457] M.R. Flynn, J.W.M. Bush, "Underwater breathing: the mechanics of plastron respiration." *J. Fluid Mech.* **608**, 275, (2008).
- [458] A. Lafuma, D. Quere, Superhydrophobic states. *Nature Mater.* **2**, 457, (2003).
- [459] M. Dembo, Y.L. Wang. "Stresses at the cell-to-substrate interface during locomotion of fibroblasts." *Biophys. J.* **76**, 2307, (1999).
- [460] N.J. Hallab, K.J Bundy, K. O'Connor, R.L. Moses, J.J. Jacobs. "Evaluation of metallic and polymeric biomaterial surface energy and surface roughness characteristics for directed cell adhesion." *Tissue Eng.* **7**, 55, (2001).
- [461] S.J. Lee, G. Khang, Y.M. Lee, H.B. Lee. "The effect of surface wettability on induction and growth of neurites from the PC-12 cell on a polymer surface." *J. Colloid. Interf. Sci.* **259**, 228, (2003).

-
- [462] T.G. Ruardy, J.M. Schakenraad, H.C. Vandermei, H.J. Busscher. "Adhesion and spreading of human skin fibroblasts on physicochemically characterized gradient surfaces." *J. Biomed. Mater. Res.*, **29**, 1415, (1995).
- [463] P. Vandervalk, A.W.J. Vanpelt, H.J. Busscher, H.P. Dejong, C.R.H. Wildevuur, J. Arends. "Interaction of fibroblasts and polymer surfaces – relationship between surface free-energy and fibroblast spreading." *J Biomed Mater Res.*, **17**, 807, (1983).
- [464] P.B. Vanwachem, T. Beugeling, J. Feijen, A. Bantjes, J.P. Detmers, W.G. Vanaken. "Interaction of cultured human–endothelial cells with polymeric surfaces of different wettabilities." *Biomaterials*, **6**, 403, (1985).
- [465] Lee JH, Jeong BJ, Lee HB. "Plasma protein adsorption and platelet adhesion onto comb-like PEO gradient surfaces." *J. Biomed. Mater. Res.*, **34**, 105, (1997).
- [466] J.H. Lee, G. Khang, J.W. Lee, H.B. Lee, "Platelet adhesion onto chargeable functional group gradient surfaces." *J. Biomed. Mater. Res.* **40**, 180, (1998).
- [467] J.H. Lee, S.K. Lee, G. Khang, H.B. Lee, "The effect of fluid sheer stress on endothelial cell adhesiveness to polymer surfaces with wettability gradient." *J. Colloid. Interf. Sci.*, **230**, 84, (2000).
- [468] S.A. Redey, S. Razzouk, C. Rey, D. Bernache-Assollant, G. Leroy, M. Nardin, G.Cournot, "Osteoclast adhesion and activity synthetic hydroxyapatite, carbonated hydroxyapatite, and natural calcium carbonate: relationship to surface energies." *J. Biomed. Mater. Res.* **45**, 140, (1999).
- [469] T.G. Ruardy, H.E Moorlag, J.M. Schakenraad, H.C. Vander Mei, H.J Busscher, "Growth of fibroblasts and endothelial cells on wettability gradient surfaces." *J. Colloid. Interf. Sci.* **188**, 209, (1997).
- [470] S.B. Kennedy, N.R. Washburn, C.G. Simon, E.J. Amis. "Combinatorial screen of the effect of surface energy on fibronectin-mediated osteoblast adhesion, spreading and proliferation." *Biomaterials*, **27**, 3817, (2006).
- [471] J.H. Lee, J.W Lee, G.. Khang, H.B. Lee. "Interaction of cells on chargeable functional group gradient surfaces." *Biomaterials*, **18**, 351, (1997).
- [472] M. Jager, C. Zilkens, K. Zanger, R. Krauspe. "Significance of nano- and microtopography for cell–surface interactions in orthopaedic implants." *J. Biomed. Biotechnol.* (2007).
- [473] M.S. Kim, G. Khang, H.B. Lee. "Gradient polymer surfaces for biomedical applications." *Progr. Polym. Sci.* **33**, 138, (2008).
- [474] G. Zhao, A.L. Raines, M. Wieland, Z. Schwartz, B.D. Boyan. "Requirement for both micron- and submicron scale structure for synergistic responses of osteoblasts to substrate surface energy and topography." *Biomaterials*, **28**, 2821, (2007).
- [475] J. Lee, M.J. Cuddihy, N.A. Kotov. "Three dimensional cell culture matrices: state of the art." *Tissue Eng.* **B 14**, 61, (2008).
- [476] S. Pautot, C. Wyart, E.Y. Isacoff. "Colloid guided as-sembly of oriented 3D neuronal networks." *Nat. Methods* **5**, 735, (2008).
- [477] J. P. Eckmann, O. Feinerman, L. Gruendlinger, E. Moses, J. Soriano, and T. Tlusty, *Phys Rep* **449**, 54 (2007). "The physics of living neural networks." *Phys Rep* **449**, 54, 2007.
- [478] J.A. Hammarback, P.C. Letourneau. "Neurite extension across regions of low cell-substratum adhesivity: implications for the guidepost hypothesis of axonal pathfinding." *Dev. Biol.* **117**, 655, (1986).

-
- [479] J.M. Schakenraad, B.D. In: Ranter, A.S. Hoffman, F.J. Schoen, J.E. Lemons. “eds.” Biomaterials Science. Academic Press, **141** 5, (1996).
- [480] J. S. Goldner, J. M. Bruder, G. Li, D. Gazzola, D. Hoffman-Kim, Biomaterials, **27**, 460 (2006).
- [481] Zavedeev E.V. Petrovskaya A.V.; Simakin A.V.; and Shafeev G.A.; *Quan. Electr.*, **36**(10), 978, (2006).
- [482] Barmina E.V.; Barberoglou M.; Zorba V.; Simakin A.V.; Stratakis E.; Fotakis C.; and Shafeev G.A.; Quantum Electronics, **39**(1) 89-93 (2009).
- [483] Shafeev G.A., in: Lasers in Chemistry, Volume 2: Influencing matter. Edited by M. Lackner, Wiley VCH Verlag GmbH&Co, KGaA, Weinheim, ISBN: 978-3-527-31997-8, 713 – 741, (2008).
- [484] I. K. Park, D. Lee, A. Rai, D. Mukherjee, and M. R. Zachariah, J. Phys. Chem. B, **109** (15), 7290 -7299, (2005).
- [485] L. Galfetti, L. T. De Luca, F. Severini, L. Meda, G. Marra, M. Marchetti, M. Regi, and S. Bellucci, J. Phys.: Condens. Matter **18**, S1991–S2005, (2006).
- [486] H. Tyagi, P. E. Phelan, R. Prasher, R. Peck, T. Lee, J. R. Pacheco, P. Arentzen, Nano Lett., **8**, 1410, (2008).
- [487] P. J. Roach, W. H. Woodward, A. W. Castleman, Jr., A. C. Reber, S. N. Khanna, Science **323**, 492 (2009)
- [488] Balde, C. P.; Hereijgers, B. P. C.; Bitter, J. H.; de Jong, K. P. J. Am. Chem. Soc., **130**, 6761–6765, (2008).
- [489] Zheng, S. Y.; Fang, F.; Zhou, G. Y.; Chen, G. R.; Ouyang, L. Z.; Zhu, M.; Sun, D. L. Chem. Mater. **20**, 3954–3958, (2008).
- [490] R. J. Jouet, A. D. Warren, D. M. Rosenberg, V. J. Bellitto, K. Park, and M. R. Zachariah, Chem. Mater., **17**, 2987-2996, (2005).
- [491] L. G. Guo, W.L. Song, C.S. Xie, X.T. Zhang, M.L. Hu, Mater. Lett., **61**, 3211–3214, (2007)
- [492] T. J. Foley, C. E. Johnson, K. T. Higa, Chem. Mater., **17**, 4086–4091, (2005).
- [493] Y. S. Kwon, A. A. Gromov, J. I. Strokova, Appl. Surf. Sci., **253**, 5558–5564, (2007).
- [494] V. Dembovský, “Thermodynamics of dissolution and liberation of gases in the atomization of molten metals by plasma-induced expansion,” J. Mater. Process. Technol. **64**(1-3), 65–74, (1997).
- [495] G. A. Shafeev, Formation of nanoparticles under laser ablation of solids in liquids, in: Nanoparticles:New Research, editor Simone Luca Lombardi, Nova Science Publishers Inc., pp. 1 –37 (2008).
- [496] J. C. Sanchez-Lopez, A. Caballero, and A. Fernandez, “Characterisation of passivated aluminum nanopowders: An XPS and TEM/EELS study,” J. Eur. Ceram. Soc. **18**(9), 1195–1200, (1998).
- [497] G. A. Shafeev, Formation of nanoparticles under laser ablation of solids in liquids, in: Nanoparticles:New Research, editor Simone Luca Lombardi, Nova Science Publishers Inc., pp. 1 –37 (2008).
- [498] E. Stratakis, V. Zorba, M. Barberoglou, C. Fotakis, and G. A. Shafeev, “Laser writing of nanostructures on

- bulk Al via its ablation in liquids,” *Nanotechnology* **20**(10), 105303–105311 (2009).
- [499] E. Stratakis, V. Zorba, M. Barberoglou, C. Fotakis, and G. A. Shafeev, “Femtosecond laser writing of nanostructures on bulk Al via its ablation in air and liquids,” *Appl. Surf. Sci.* **255**(10), 5346–5350 (2009).
- [500] J. C. Sanchez-Lopez, A. Caballero, and A. Fernandez, “Characterisation of passivated aluminum nanopowders: An XPS and TEM/EELS study,” *J. Eur. Ceram. Soc.* **18**(9), 1195–1200, (1998).
- [501] E. Stratakis, V. Zorba, M. Barberoglou, C. Fotakis, and G. A. Shafeev, “Laser writing of nanostructures on bulk Al via its ablation in liquids,” *Nanotechnology* **20**(10), 105303–105311 (2009).
- [502] J. A. Creighton, and D. G. Eadon, “Ultraviolet-visible absorption spectra of the colloidal metallic elements,” *J. Chem. Soc., Faraday Trans.* **87**(24), 3881, (1991).
- [503] J. A. Creighton, and D. G. Eadon, “Ultraviolet-visible absorption spectra of the colloidal metallic elements,” *J. Chem. Soc., Faraday Trans.* **87**(24), 3881 (1991).
- [504] Y. Ekinici, H. H. Solak, and J. F. Löffler, “Fabrication and characterization of metallic nanostructures for surface-enhanced Raman spectroscopy,” *J. Appl. Phys.* **104**, 083107, (2008).
- [505] B. S. Luk'yanchuk and M. I. Tribelsky, “Anomalous Light Scattering by Small Particles and inverse hierarchy of optical resonances” Collection of papers devoted to memory of Prof. M. N. Libenson. The St.-Petersburg Union of the Scientists, Russia, pp. 101–117 (2005).
- [506] G. L. Hornyak, K. L. N. Phani, D. L. Kunked, V. P. Menon, and C. R. Martin, “Fabrication, characterization and optical theory of aluminum nanometal/nanoporous membrane thin film composites,” *Nanostruct. Mater.* **6**(5-8), 839–842 (1995).
- [507] G. W. Yang, “Laser ablation in liquids: Applications in the synthesis of nanocrystals,” *Prog. Mater. Sci.* **52**(4), 648–698 (2007).
- [508] C. X. Wang, P. Liu, H. Cui, and G. W. Yang, “Nucleation and growth kinetics of nanocrystals formed upon pulsed-laser ablation in liquid,” *Appl. Phys. Lett.* **87**(20), 201913–201915 (2005).
- [509] P. Liu, Y. L. Cao, C. X. Wang, X. Y. Chen, and G. W. Yang, “Micro- and nanocubes of carbon with C8-like and blue luminescence,” *Nano Lett.* **8**(8), 2570–2575 (2008).
- [510] G. A. Shafeev, Formation of nanoparticles under laser ablation of solids in liquids, in: *Nanoparticles: New Research*, editor Simone Luca Lombardi, Nova Science Publishers Inc., pp. 1–37 (2008).
- [511] Stratakis E.; Zorba V.; Barberoglou M.; Fotakis C.; and Shafeev G.A.; *Appl. Surf. Sci.* **255**, 5346–5350, (2009).
- [512] Stratakis E.; Zorba V.; Barberoglou M.; Fotakis C.; and Shafeev G.A.; *Nanotechnology*, **20**, 105303-7, (2009).
- [513] Zavedeev E.V.; Petrovskaya A.V.; Simakin A.V.; and Shafeev G.A.; *Quantum Electronics*, **36** (10) 978, (2006).
- [514] Lau Truong S. ; Levi G.; Bozon-Verduraz F.; Petrovskaya A.V.; Simakin A.V.; and Shafeev G.A. ; *Appl. Surf. Sc.* **254**, 1236, (2007).

-
- [515] Stratakis E. Zorba V. Barberoglou M. Fotakis C. and Shafeev G.A. Appl. Surf. Sci. **255**, 5346–5350, (2009).
- [516] Creighton J.A. and Eadon D.G.; *J. Chem. Soc. Faraday Trans.*, **87** 3881, (1991).
- [519] B. S. Luk'yanchuk and M. I. Tribelsky, Collection of papers devoted to memory of Prof. M. N. Libenson. The St.-Petersburg Union of the Scientists, Russia, pp. 101–117 (2005).
- [520] Stratakis E.; Zorba V.; Barberoglou M.; Fotakis C.; and Shafeev G.A.; *Nanotechnology* **20**, 105303-7 (2009).
- [521] E.V. Barmina, E. Stratakis, Fotakis, Stolyarov V. N., Stolyarov I. N., and G.A. Shafeev, Applied Surface Science, to be published
- [522] 522 E. Freysz, J. Degert, N. Lascoux, and G. Shafeev, in *Conference on Lasers and Electro-Optics/Quantum Electronics and Laser Science and Photonic Applications Systems Technologies*, Technical Digest (Optical Society of America, 2005), paper JTuC45.